THESIS FOR THE DEGREE OF DOCTOR OF PHILOSOPHY

Topographical Impact on Space Charge Injection, Accumulation and Breakdown in Polymeric HVDC Cable Interfaces

ESPEN H. DOEDENS

High Voltage Engineering
Department of Electrical Engineering

CHALMERS UNIVERSITY OF TECHNOLOGY

Gothenburg, Sweden 2020

Topographical Impact on Space Charge Injection, Accumulation and Breakdown in Polymeric HVDC Cable Interfaces
ESPEN H. DOEDENS
ISBN 978-91-7905-379-6

Doktorsavhandlingar vid Chalmers tekniska högskola
Ny serie nr 4846
ISSN 0346-718X

High Voltage Engineering
Department of Electrical Engineering
Chalmers University of Technology
SE-412 96 Gothenburg
Sweden
Telephone + 46 (0)31-772 1000

Cover:
HVDC extruded cable end ready for jointing, with its key features addressed in detail in section 2.1. Inset illustrations (top to bottom): Scanning electron microscopy of an abraded surface (section 4.1.1), surface field distribution towards the abraded surface (section 6.1.1), observed charge packets/fluctuations in space charge measurements (section 4.2.1.2), and microscopic discharge traces from a DC breakdown (section 4.2.2.1). The background illustration is a private photo taken at the beach of the Redwood creek picnic area, Reading rock state marine conservation area, California, USA. This illustration is not an actual installation of an extruded HVDC cable system.

Chalmers Bibliotek, Reproservice
Gothenburg, Sweden 2020

“There is no more important rule of conduct in the world than this: attach yourself as much as you can to people who are abler than you and yet not so very different that you cannot understand them.”
Notebook F (1776-1779)

Georg Christoph Lichtenberg

Abstract

Extruded HVDC cable systems feature a variety of interface types, for which physio-chemical properties will depend on the type of application. Such applications can be joints, terminations or the cable itself, all introducing different material combinations and manufacturing methods. To ensure beyond 40 years of faultless cable system operation, the interface's design and quality control procedures are essential. Interfacial control requires detailed knowledge on how measurable physio-chemical properties of polymer surfaces relate to their electrical performance, through features such as localized electric field strength, space charge injection and breakdown strength. This work aims to expand such understanding by assessing polymer surfaces created with different, industrialized preparation methods, featuring different degrees of surface roughness. Surface preparation was carried out on real HVDC cable prototypes, from which cable peelings were extracted, ensuring replication of the material's bulk and interfacial natures into the small-scale tests. Also, DC breakdown tests on medium voltage cables revealed a strong impact of surface roughness, pinpointing the need for accurate roughness evaluation.

While chemical characterization assessed certain features brought about in the preparation, physical assessments such as optical profilometry quantified the surfaces' topographies. It was found that the topography, featuring micrometer and sub-micrometer geometrical variation, could be readily adopted in a mesoscopic modelling approach. Thereby, the geometric impact on local quantities of field strength, charge density and injection current density was estimated. Also, a set of roughness enhanced charge injection equations were derived for charge injection types such as Schottky, Fowler-Nordheim and hopping injection mechanisms. Such equations, featuring surface-specific field (β) parameters, were employed in a one-dimensional bipolar charge transport model. Through careful model calibration against the results of space charge measurements, the parameters for roughness enhanced charge injection, together with parameters for charge transport, trapping, detrapping and recombination, were estimated. This calibration verified roughness enhanced injection and generated a description of the density of states in the material's bulk. Furthermore, DC breakdown tests performed on the cable peelings for establishing the relationship between surface roughness and breakdown strength. An adopted multi-scale simulation approach, based on the calibrated parameter set, estimated local field strength, charge density and other quantities in the surface domain.

Conclusively, surface topography causes a local redistribution of the electric field, in turn locally increasing charge injection due to its strong field dependency at the rough asperities. Ultimately, coinciding high field strength and high charge density, at repeated positions along the surface, yields a lower breakdown strength. Such knowledge allows for tailoring the methodologies of surface preparation and quality control in HVDC cable systems, and other HV apparatuses. Control over mesoscopic surface effects will allow engineers to design ever more advanced and long-lasting HV components, meeting humanity's renewable energy transmission needs for decades to come.

Keywords: HVDC, extruded cable, XLPE, interfaces, polymer surfaces, cable peelings, DC breakdown, PEA, space charge, roughness, field enhancement factor, charge injection, roughness enhanced charge injection.

Sammanfattning

I extruderade HVDC-kablar och tillhörande kabelsystem finner man olika typer av gränsytor, vars önskade egenskaper beror på komponenten i fråga. Sådana komponenter, som skarvar, termineringar eller själva kabeln, innefattar en rad olika materialkombinationer och tillverkningsmetoder. För att säkerställa minst 40 års felfri drift av kabelsystemet, är rätt design och noggrann kvalitetsäkerställning viktigt. Detta kräver goda kunskaper om hur mätbara fysiska och kemiska parametrar av polymeriska gränsytor påverkar elektriska egenskaper som elektriskt fältstyrka, injektion av rymdladdningar samt elektriskt hållfasthet. Detta arbete syftar till att öka denna förståelse genom att utvärdera polymeriska ytor, från ett antal olika industriellt gångbara tillverkningsmetoder som ger upphov till olika grader av ytråhet. Tunna provfilmer erhölls genom att ytskiktet på kabeltermineringar skalades av så att ytprepareringen blev kvar på den ena sidan och kunde utvärderas. Eftersom provprepareringen utfördes på riktiga HVDC-kabelprototyper replikerades materialets bulk och gränssnittskaraktär i de småskaliga testerna. Hållfasthetstester med likström utförda på mellanspänningskablar visade också en stark inverkan av ytråheten och fastställde behovet att noggrant utvärdera denna ytparameter.

Medans kemisk karakterisering bedömde inverkan av ytprepareringen, så lyckades fysiska mätningar som optisk profilometri kvantifiera ytornas topografier. Det visade sig att topografin, med geometrisk variation i mikro- och sub-mikrometer skala, kunde införas direkt i en mesoskopisk modell. Olika mesoskopiska beräkningar, med den uppmätta topografin i full upplösning, kunde kvantifiera den geometriska effekten på lokal fältstyrka, laddningstäthet och injektionsströmtäthet. Detta genererade en uppsättning ekvationer med ytråhetskorrigering för injektionsmekanismer såsom Schottky, Fowler-Nordheim och hopping. Dessa ekvationer, med en ytspecifik fältparametrar (β) användes i en endimensionell transportmodell för bipolär laddning. Genom noggrann modellkalibrering mot resultaten av rymdladdnings mätningar uppskattades parametrarna för ytråhetskorrigerad laddningsinjektion, samt för laddningstransport, laddnings-infångning, excitering av laddningsbärare och laddningsrekombination. På detta sätt utvärderades injektionsegenskaperna och en beskrivning av tillståndstätheten i materialet genererades. Dessutom etablerade hållfasthetstester med likström utförda på kabelskalningarna sambandet mellan ytråhet och elektrisk hållfasthet. En multiskalig simuleringsmetod, baserad på ovan nämnda kalibrerade parametrar, uppskattade den lokala fältstyrkan, laddningstätheten och andra kvantiteter i gränssnittets delregion.

Kort sammanfattat har topografi och dess relation till elektrisk hållfasthet beskrivits i detalj. Detta möjliggör skräddarsydd yttillverkning samt kvalitetskontroll i HVDC-kabelsystem samt andra högspänningskomponenter. Kontroll över mesoskopiska yteffekter ger ingenjören möjligheten att utforma allt bättre och mer långlivade komponenter som möter mänsklighetens behov att överföra förnybar energi under decennier framöver.

Acknowledgements

Nexans Norway AS is greatly acknowledged for the opportunity they have provided for this work, and the funding thereof. The Nexans Research Centre (NRC) in Lyon is also acknowledged for collaboration and realization of the space charge measurements. Furthermore, the Materials Testing Lab (MTL) associated with the Nexans Halden plant is acknowledged for the carried out physico-chemical characterizations. Chalmers University of Technology is acknowledged for support and accepting the research proposal made in 2014, allowing for this dedicated study to take place.

I would like to thank my wife, Louise Doedens, for her love and positive support throughout the thesis. Additionally, her effort on raising our son Kelvin during my long nightly work schedule, cannot be understated and deserves my deepest gratitude. I would like to thank my parents, Folkert Barkhuyzen and Geertje Doedens, supplying me with a solid theoretical and practical foundation. I would also like to thank Maja Lif for putting a roof over our heads and her help with raising our son.

Next, I would like to express my gratitude towards my mentors who have contributed greatly to my personal development. Here, Jan Varreng is deeply acknowledged for his mentorship and positive attitude towards research in high voltage engineering. Dr. Christian Frohne is acknowledged for his contributions and support for the realization of this project. Professor Stanislaw Gubanski is acknowledged for aid with theoretical understanding of the subject. Professor Yuriy V. Serduk is acknowledged for helping with understanding and developing the space charge models. I would also like to thank Dr. E. Markus Jarvid for his theoretical insights, helpful reviews and supervision of this thesis. To Jan, Christian, Stanislaw, Yuriy and Markus, I dedicate the earlier listed quote from Prof. Lichtenberg.

For giving me the opportunity to realize and focus on this research, I would like to thank my manager, Per-Arne Osborg and project managers of the Norwegian HVDC extruded team, Dr. Roberto Gaspari and Torunn Lund Clasen.

For aid with execution and interpretation of the space charge measurements, I would like to thank Dr. Raphael Guffond. I would also like to thank Jan-Are Sundby for carrying out the FTIR-ATR measurements and Andreas Nyborg for carrying out the HPLC analysis in this thesis. I would also like to acknowledge Dr. Dimitri Charrier for aid in further testing the impact of rough surface geometry. Also, Dr. Xiangdong Xu is acknowledged for theoretical discussions and for creating the software used in the DCBD test cell. Heine Pettersen and Tormod Foss Johansen are acknowledged for their work spent on the DCBD measurements of cables.

Brynjar Jacobsen and Nils-Bertil Frisk are acknowledged for executing of my past role in the extruded HVDC project, allowing me to fully focus on this thesis. All other members of the Nexans extruded HVDC project are also acknowledged for their research contributions.

Thank you!

Espen Doedens
Gothenburg, Sweden
September 2020

List of abbreviations

HVDC – High Voltage Direct Current
HVAC – High Voltage Alternating Current
MI – Mass Impregnated
XLPE – Crosslinked Polyethylene
LDPE – Low Density Polyethylene
HDPE – High Density Polyethylene
PDP – Peroxide Decomposition Products
CB – Carbon Black
GIS – Gas Insulated Switchgear
3D – Three-Dimensional
FEM – Finite Element Method
DOS – Density of States
PD – Partial Discharges
FEF – Field Enhancement Factor
SFE – Surface Free Energy
SE – Schrödinger's Equation
PF – Poole-Frenkel (effect)
FN – Fowler-Nordheim (injection)
MWS – Maxwell-Wagner-Sillars (polarization)
SCLC – Space Charge Limited Current
MV – Medium Voltage
SEM – Scanning Electron Microscopy
RMS – Root Mean Square
HPLC – High Performance Liquid Chromatography
FTIR – Fourier Transform Infrared Spectroscopy
ATR – Attenuated Total Reflection
PEA – Pulsed Electro-Acoustic (measurement/method)
DCBD – Direct Current Breakdown
IPL – Inverse Power Law
BDF – Backward Differentiation Formula
SPD – Surface Potential Decay

Table of Contents

Chapter 1

Introduction

The fraction of global energy consumption originating from renewable resources increased from a meager 8.4% to 9.3% in 2018 [1]. Increasing this renewable energy resource usage is paramount for protecting the intrinsic value of our environment (mainly by reducing CO_2 emissions). Furthermore, preserving fossil fuels for non-substitutable materials in future products increases intra-generational justice. The world's reserves of crude oil are estimated to last for only ~43 years [1], at current consumption rates. Also, according to a recent energy outlook [1], the electric power sector comprises only ~42% of the total energy used, while the transport sector constitutes 19%. Thus, while the transport sector's electrification is essential, it will shift the energy source to the electric power sector. It is therefore crucial to increase supply and push for a renewable shift in electric power generation, ensuring a renewable origin in all global energy consumption, regardless of sector. The amount of renewable integration in the power grid stands in direct relation to the amount of greenhouse gas emission equivalents per produced kilowatt-hour, which is shown below in Figure 1 for north-western Europe.

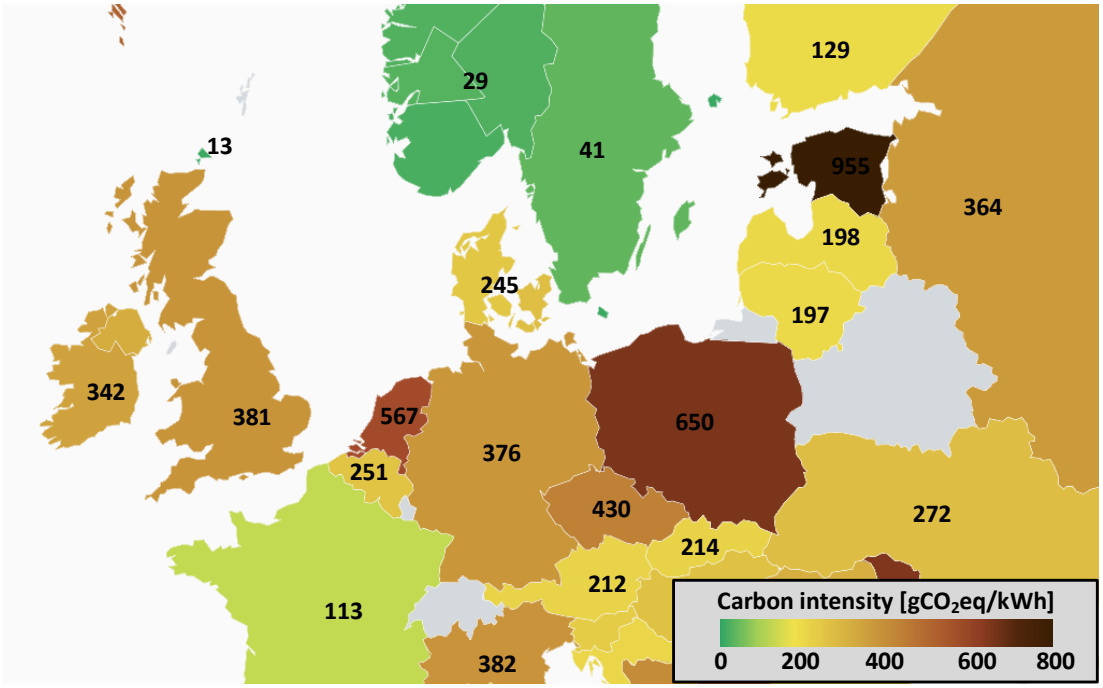

Figure 1. CO_2 intensity of north-western European electric power generation on 19/11-2019 adapted from "www.electricitymap.org" [2]. *The values and color bar indicate the degree of CO_2 emissions in gCO_2eq/kWh for power generated per country or region respectively.*

As seen in Figure 1, large geographical discrepancies arise in the carbon intensity, corresponding in part to the degree of renewable implementation in electric power generation. Such geographic variations appear since widespread, large-scale implementation of renewables has multiple difficulties to be overcome, being:

1. Short-term or seasonal fluctuations in power output
2. Resource remoteness to urban areas of major power consumption
3. Long investment pay-back times for the technologies

Land and submarine high voltage direct current (HVDC) transmission links are key for overcoming the above challenges. The benefit of using HVDC is that transmission losses for HVDC links are typically lower than for conventional high voltage alternating current (HVAC) systems, especially when long transmission distances are needed. Also, HVDC links exert full control over the direction of power flow. HVDC links can thereby connect separate power grids over long distances, leveling out arising supply-demand imbalances over large geographical areas. This is further exemplified in Figure 2, showing planned and operational HVDC cable systems in north-western Europe. Major cities are also shown, indicating how densely populated regions will be further interconnected with regions dense in renewable generation in the upcoming years.

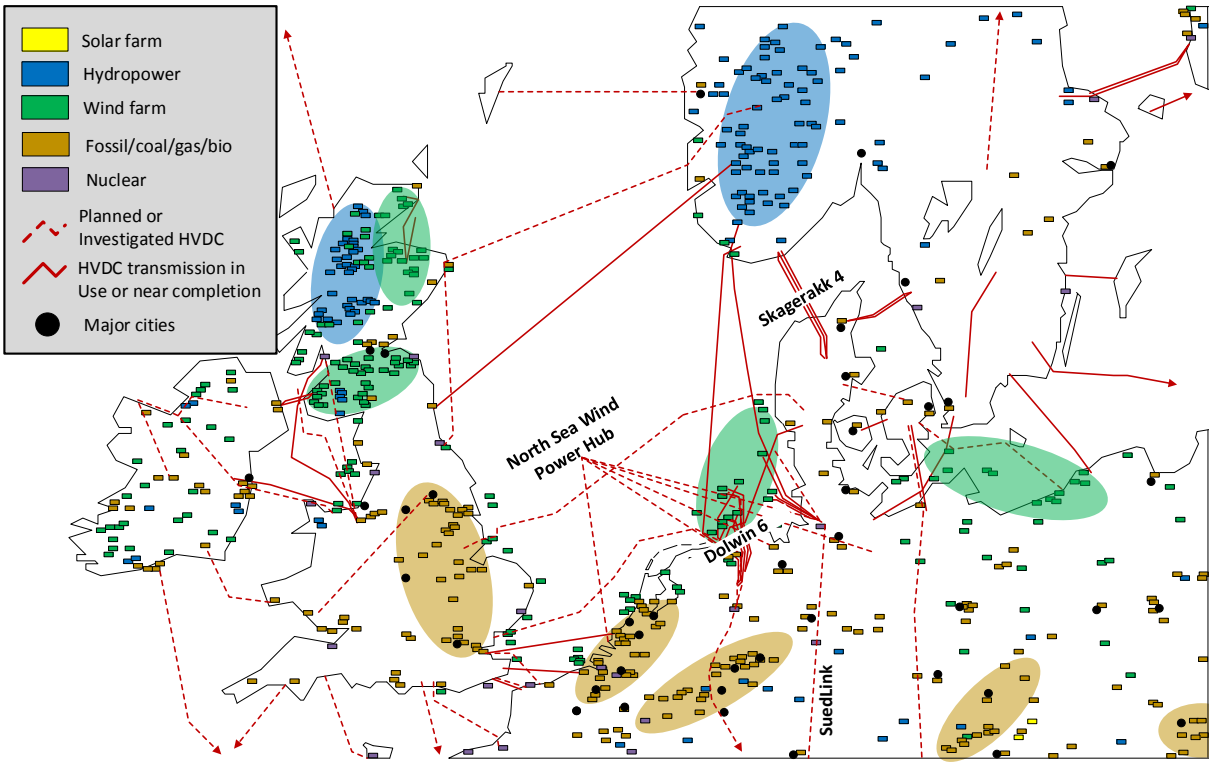

Figure 2. HVDC transmission systems in use, under construction, or planned in north-western Europe before 2040, adopted from [3]. *Renewable energy generation is shown (yellow, blue, green) highlighting the production remoteness to major European urban areas, in comparison to CO_2 emitting generation (brown). Land AC transmission infrastructure is not shown.*

As shown in Figure 2, north-western Europe is seeing an unprecedented expansion of HVDC cable transmission systems, adding up to approximately 10.200 km submarine and 2.400 km land cable, to be installed until 2035 [3]. These links will connect remote wind- and hydro based electricity generation with end-users in urban population centers, ensuring maximal renewable energy resource utilization in the power grid.

Four different examples of typical HVDC cable systems are mentioned by name in Figure 2, being:

- The recently installed submarine interconnector: “Skagerrak 4”, 239 km, 700 MW
- The to-be-installed offshore wind integrator: “Dolwin 6”, 90 km, 900 MW [4]
- The by 2025 planned land-based interconnector: “SuedLink”, 700 km, 4 GW [3]
- The by 2035 planned renewable integrator and interconnector, currently under consideration: “North Sea Wind Power Hub”, 2258 km, 12 GW [3]

Conventional mass-impregnated, non-draining (MI) HVDC cable systems have been around for decades and account for the bulk of today's submarine transmission infrastructure. MI HVDC systems have service-proven reliability, exceeding 40 years of operational lifetime. For this reason, the Skagerrak transmission system shown in Figure 2, was recently expanded with its forth MI cable link, Skagerrak 4, boosting its total transmission capacity to 6 GW.

High voltage cables utilizing crosslinked polyethylene (XLPE) as insulating material, such as HVDC extruded cable systems, have recently entered the market. Thanks to development of voltage source converter technology, polarity reversals are no longer required for power flow inversion. This breakthrough, along with improvements to the insulation system's base material, has facilitated the recent development of 320, 400, and 525 kV HVDC cable technologies [5], [6], with additional technological breakthroughs waiting around the corner. This new HVDC extruded technology is very cost competitive compared to traditional MI systems, owing to its higher operation temperature and faster jointing methods in the field. Based on such advantages, the 320 kV Dolwin 6 cable link will rely on HVDC extruded technology [4] and will be installed in bipole configuration (two cables in parallel).

While using HVDC cables instead of overhead lines is the only practical solution for long submarine transmission lengths, it is also a good choice on land as it has less impact on the local environment. Therefore, the upcoming German land-based interconnector SuedLink, is specifically requesting extruded HVDC cable technology at 525 kV [6]. Also, projects of an even larger scale are being considered, such as the North Sea Wind Power Hub, interconnecting a massive geographical area with a staggering total capacity of 12 GW [3]. Future ambitions do not stop at such scales either, HVDC super-grids are being evaluated, supporting massive inter-continental power flow exchanges. The ever-growing demand for HVDC infrastructure, with origins in the renewable generation shift, will drastically alter the complexity of our power grid. Reliability is therefore a key design factor in all cable projects, being closely related to the investment pay-back time and availability of transmission. It is thus paramount to ensure long-term reliability in all components and interfaces comprising the cable systems.

1.1 Background

An extruded HVDC cable link is incomplete without its cable accessories, which are tailor-made for the installation's requirements. Numerous types of cable accessories are required, as depicted for two submarine link types in Figure 3.

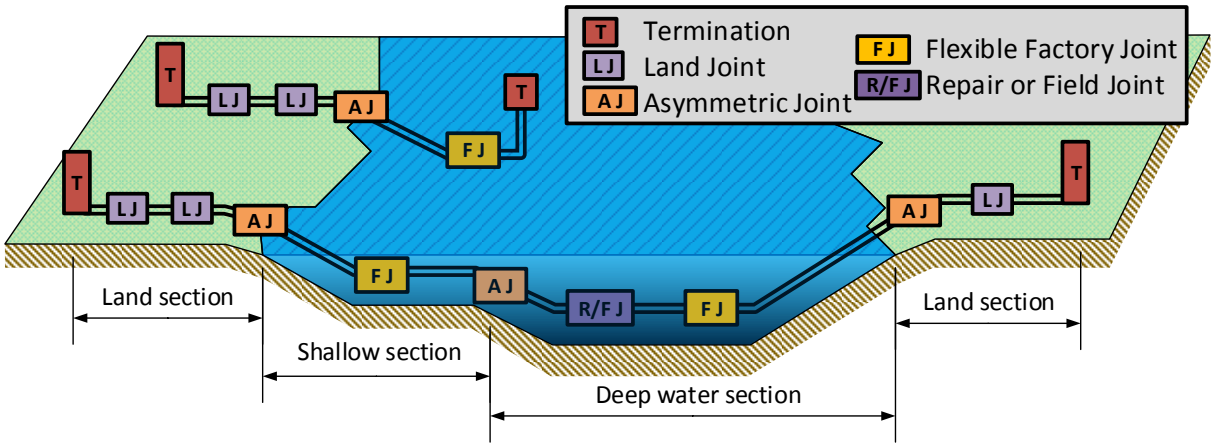

Figure 3. Generic illustration of different cable accessories required in extruded HVDC cable systems. The top link illustrates a bipole system integrating an offshore wind farm. The bottom link illustrates a bipole submarine interconnector.

The cable systems shown in Figure 3, generally require the following number of accessories:

- Two terminations per pole/cable
- Approximately one land joint per each kilometer of land cable
- One asymmetric joint per encountered transition in environment per cable
- One flexible factory joint per each 20-30 km of submarine cable
- One field joint per each 150-250 km of submarine cable
- Two repair joints for each repair carried out during the submarine cable life-time

These accessories introduce material interfaces into the complex electrical system. Such interfaces, if poorly designed, can introduce weak points in the system, ultimately leading to premature failure forcing an outage of the entire cable system. While flexible asymmetric or factory joints make use of in factory molded and bonded layers, all other accessories listed above rely on a pre-molded body that is installed onto the cable's surface. The installation requires removing the outer layers from the cable end and preparing the insulation surface at the installation site. The here created interface, referred to as a physical interface [7], must be ensured to be of high quality. From the previously listed joint occurrences, the Dolwin 6 link can be estimated to introduce around 90 joints containing this physical interface, while the SuedLink project could introduce more than 1400 joints. If assuming that all considered links in Figure 2 [3] will use extruded HVDC technology, an excess of 4900 joints are to be installed in north-western Europe alone, all containing this type of physical interface. The difficulty is that the nature of this material interface is still far from fully understood, which makes specifying the procedures for its manufacturing and quality assurance a challenging task. Understanding physical cable interfaces better is thus important for realizing a renewable energy transition while maintaining the reliability of supply.

1.2 Purpose

The main purpose of the work described in this thesis is to further investigate the impact of physical surface preparations on the performance of cable accessories. A simplification of real accessory geometry into cable peelings is made, allowing a larger number of experiments leading to a high statistical certainty in the results. To maintain identical interfacial and bulk characteristics in this downscaling, the samples themselves have been extracted from full-scale cable ends provided by Nexans Norway AS. Also, tests on medium voltage sized cables were performed to ensure the scalability and applicability of the test results.

From the characterizations of different physical, chemical and electrical surface parameters, this research aims to develop a theoretical framework that better anticipates surface performance under DC stress. This is achieved by determining the inter-related effects between measurable quantities. The novelty within this framework is that it encompasses not only effects at the molecular and macroscopic scales, but additionally mesoscopic effects are resolved as accurately as possible. Thereby, measurable quantities can be understood such that the reliability of physical interfaces can be ensured even when the manufacturing takes place in the field.

While a large set of surface parameters was initially assessed and identified, the focus of the research work concentrated on studying the impact of surface roughness on complex electrical phenomena. This narrowed scope allowed for the development of a theoretical framework based on the accurately defined mesoscopic topography of the surface. Given the complexity of charge transport in highly disordered insulators, a large effort has been placed on the

development of a bipolar charge transport model, providing both a better interpretation of measurement results and having predictive capability in case of future changes to the system.

1.3 Outline of the thesis

Chapter 2 commences with an introduction of the HVDC extruded cable, its insulation system and its accessories. After defining the mesoscopic gap, a review is made on bipolar charge transport effects and injection processes determining the electrical behavior of the system. Thereafter, the characteristics of the insulation surface are described by listing its key features. Furthermore, relevant aging, degradation and breakdown phenomena are addressed. This allows identifying simplifications of the accessory's features, ruling out certain effects for studying its performance with accuracy, listed at the end of the chapter.

Chapter 3 describes the measurement methods adopted to study the HVDC cable accessory's interface and practical aspects and test setups used in the experimental part of the study are explained. The chapter is divided into physio-chemical and electrical characterizations.

Chapter 4 presents the physico-chemical and electrical measurement results and findings obtained within this work. It contains an analysis of sample surface structure followed by chemical analysis results and surface free energy measurements. This is followed by results of electrical measurement consisting of space charge measurements and breakdown tests on cylindrical (cable) and planar geometries.

Chapter 5 presents the physical background of the bipolar charge transport model and the effects it simulates. Such effects are thereafter summarized and their impacts on the evolution of current density and field strength are listed. It ends by describing the methodologies of the different simulation approaches.

Chapter 6 presents the calculation and simulation results, beginning with estimations of the surface field distribution, making use of measured surface profiles. Thereafter, such field distributions are used to estimate the impact on the injection of charge carriers, deriving a set of roughness enhanced charge injection equations. Thereafter a one-dimensional bipolar charge transport model is formulated, making use of the roughness enhanced injection expressions. The injection behavior and rates of bulk conduction processes are calibrated against the space charge measurements, verifying the simulated effects. Lastly, a unique multi-scale approach is presented providing further insight into the complex carrier evolution in the irregular surface domain.

Chapter 7 discusses bulk conduction and charge injection from the perspective of observations made in measurement and simulation. This is followed by a description of the theoretical framework of surface topographical impact, and its theoretical evidence found in experiments. Thereafter follows a discussion on other factors contributing to surface performance.

Chapter 8 concludes the findings of the thesis, being the relations between topography, the surface field distribution and space charge injection.

Chapter 9 contains the suggested future work. Resolving mesoscopic effects may allow for improved understanding of the great complexity arising from irregular attributes in the polymer.

1.4 List of publications

The following publications were prepared and presented during the project work:

E. H. Doedens, N. B. Frisk, M. Jarvid, L. Boyer, and S. Josefsson, "Surface preparations on MV-sized cable ends for ramped DC breakdown studies," in *IEEE Conference on Electrical Insulation and Dielectric Phenomena (CEIDP)*, Oct. 2016, pp. 360–362, doi: 10.1109/CEIDP.2016.7785475.

E. Doedens, M. Jarvid, S. Gubanski, and C. Frohne, "Cable surface preparation: chemical, physical and electrical characterization and impact on breakdown voltage," in *International Symposium on HVDC Cable Systems (Jicable-HVDC)*, 2017.

E. Doedens, M. Jarvid, Y. V. Serdyuk, R. Guffond, and D. Charrier, "Local surface field- and charge distributions and their impact on breakdown voltage for HVDC cable insulation," in *International Conference on Insulated Power Cables (Jicable)*, 2019, p. F2.24.

E. Doedens, E. M. Jarvid, C. Frohne, and S. M. Gubanski, "Enhanced charge injection in rough HVDC extruded cable interfaces," *IEEE Transactions on Dielectrics and Electrical Insulation*, vol. 26, no. 6, pp. 1911–1918, Dec. 2019, doi: 10.1109/TDEI.2019.008213.

E. Doedens, E. M. Jarvid, R. Guffond, and Y. V. Serdyuk, "Space Charge Accumulation at Material Interfaces in HVDC Cable Insulation Part I—Experimental Study and Charge Injection Hypothesis," *Energies*, vol. 13, no. 8, p. 2005, Apr. 2020, doi: 10.3390/en13082005.

E. Doedens, E. M. Jarvid, R. Guffond, and Y. V. Serdyuk, "Space Charge Accumulation at Material Interfaces in HVDC Cable Insulation Part II—Simulations of Charge Transport," *Energies*, vol. 13, no. 7, p. 1750, Apr. 2020, doi: 10.3390/en13071750.

E. H. Doedens and E. M. Jarvid, "Considerations on the impact of material mesostructure on charge injection at cable interfaces," *IEEE Electrical Insulation Magazine*, vol. 36, no. 5, pp. 43–51, Aug. 2020, doi: 10.1109/mei.2020.9165698.

Presented and awaiting publication:

E. Doedens, E. M. Jarvid, and Y. V. Serdyuk, "Roughness Enhanced Charge Injection and Field Dependent Conduction Mechanisms for Bipolar Charge Transport Models," in *International Conference on Dielectrics (ICD)*, 2020.

Contribution to additional papers not included in this thesis:

N-B. Frisk, R. Gaspari, E. Doedens, Q. Eyssautier and C. Frohne, "Qualification of 400 and 525 kV HVDC XLPE cable systems including a multitude of accessory configurations," in *International Conference on Insulated Power Cables (Jicable)*, 2019.

Chapter 2

Literature review and background

This chapter summarizes present knowledge relevant to the thesis, to better understand the nature of cable interfaces and their environment. First, a description is made of the cable system, its accessories, and encountered interface types in the system. After defining the mesoscopic gap, bipolar charge transport is summarized, allowing for a subsequent description of mesoscopic surface properties that govern the electrical nature of the interface. The chapter ends by addressing relevant degradation phenomenon and ultimately concludes by listing adaptations made to reduce complexity in the methodology.

2.1 High voltage cable systems

Each high voltage cable is tailor-made for its application and its installation environment [8]. As many tons of expensive materials are required for making a cable link, the design of an HV cable involves detailed engineering. There, the design is optimized to exceed project-specific requirements such as power transmission rating, voltage rating and transient withstand capability while minimizing the amounts of materials required. The optimization process also accounts for the local thermal environment along the designated route. For this reason, no two HV cables are exactly alike.

An extruded HVDC cable is a type of cable made with an extrudable, polymeric insulation system specifically designed for HVDC applications. It is possible to further divide the family of extruded HVDC cables into land-based and submarine applications. Their major differences arise in the used water blocking technology, mechanical strength, installation methods and jointing operations. In Figure 4, an illustration of a submarine extruded HVDC cable is shown, listing the different layers used in its design.

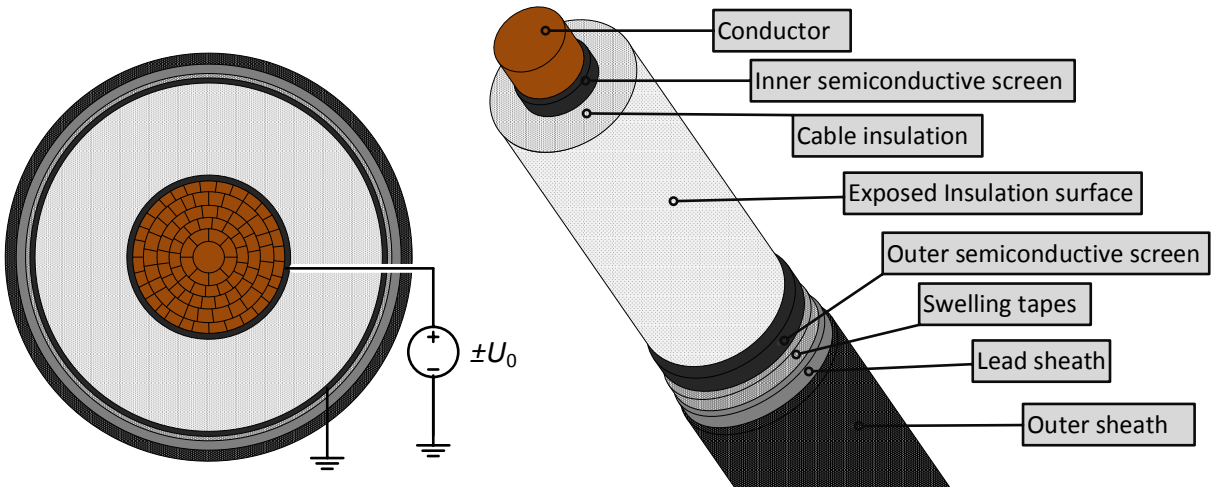

Figure 4. Cross-sectional illustration of a submarine extruded HVDC cable (left) and illustration of a prepared cable end ready for accessory mating (right).

As seen in Figure 4, submarine extruded HVDC cables are constructed as follows:

- A copper (Cu) or aluminum (Al) **conductor** is used for carrying the high current during operation. It is stranded layer by layer in a single production line. The cross-sectional design may be round-wired, sector-shaped (as illustrated), Milliken or solid depending on the application. The conductor's dimensions are designed through ampacity and mechanical calculations.
- The **inner semi-conductive layer** (or conductor screen) normally consists of carbon black loaded XLPE. The smoothness of this layer is essential, as any asperities into the insulation will form electric field enhancements. This layer is extruded simultaneously with the insulation layer and outer semi-conductive layer through a triple extrusion process, to minimize any possible contamination.
- The **insulation layer** is extruded along with the inner and outer semi-conductive layer in a vertical or horizontal extrusion line. Directly after extrusion, the cable passes through a long and pressurized heat-controlled zone, crosslinking all three layers, called a continuous vulcanization (CV) line. The thickness of the insulation layer is designed according to its rated voltage level U_0, and design stress (electric field strength).
- The **exposed insulation surface**, as shown in Figure 4, is only uncovered for a certain length when a joint or termination is to be manufactured.
- The **outer semi-conductive layer** is extruded over the insulation to again ensure a geometrically smooth contact preventing field enhancements. After the triple extrusion and crosslinking process, the cable is normally spooled to a drum or turntable for degassing, which removes chemical residues such as by-products originating from the cross-linking process.
- **Swellable tapes** are lapped over the cable core just before applying the lead sheath. These tapes prevent longitudinal transport of moisture in the case of water ingress, in case of mechanical damage to the radial water barrier during operation.
- The **lead sheath** is extruded over the cable and serves as its radial water blocking barrier. This metallic barrier is crucial as even tiny amounts of water, which would permeate through polymeric materials, will change the insulation's properties significantly. Deep installation depths for submarine cables also put mechanical requirements on the water barrier as external seawater pressure will reach high levels.
- The **outer sheath** is an extruded polymeric sheath, which serves as mechanical protection for the metallic barrier underneath.
- **Additional layers**, not displayed in Figure 4, may comprise armoring layers covered with polypropylene-yarns. The armoring is designed specifically to withstand the mechanical loading for a certain installation depth and is protected from corrosion with bitumen. The polypropylene yarns prevent wash-out of bitumen and can serve as individual cable identification through different combinations of colored yarns. Further layers and design choices may exist, omitted here for the sake of simplicity.

Land cables are constructed similarly with the same cable layers displayed in Figure 4, though some design changes resulting from its different environment may be encountered. For example, they generally require a larger conductor cross-section to reduce heat generation because of less efficient natural cooling. Armoring layers are also not required, and their sheaths can be made of a thin layer of aluminum, due to their less strenuous installation process. While submarine cables can be installed campaign-wise in long sections from an installation vessel, land cables are shipped to the site on drums, limiting their sectional length to 1-3 km depending on weight and drum size. The insulation system (inner and outer semiconductors and the insulation layer) is identical in design for submarine and land cables, with only minorly different manufacturing methods of the sectional lengths.

2.1.1 Materials in the insulation system

The insulation material used in this thesis is commercial grade XLPE tailor-made for DC applications [9]. XLPE is a semi-crystalline polymeric material with low conductivity and high dielectric breakdown strength [10]. Its complex semi-crystalline nature can be better understood when compared to the structures of low-density polyethylene (LDPE) and high-density polyethylene (HDPE). Such materials are made by reacting the same monomer *(CH_2=CH_2)* and therefore the polymeric chains consist of the same *-(CH_2-CH_2)$_n$-* repeat units. However, the used polymerization reaction differs significantly, yielding the different polymer chain configurations shown in Figure 5.

LDPE is typically manufactured through free-radical addition polymerization[11]. First, an initiator decomposes at high temperature and transfers a free radical to a monomer. Thereafter, chain growth ensues from the activated monomer, where monomer after monomer adds itself to the growing chain. This reaction is carried out under high temperature and pressure, and polymerization occurs throughout the mixture. LDPE has frequent short side-chain branches (around three side branches per 100 main-chain carbon atoms [10]) in addition to the long side branches shown in Figure 5A. Short branching originates from chain backbiting when the growth point (the free radical) on the end of the growing polymer chain relocates itself backward along the chain in the polymerization process. Short side-branches are thus formed every time backbiting occurs. Additionally, long side branches are formed through a chain transfer reaction, when the free radical is transferred to a neighboring chain, and growth ensues from the neighbor chain.

For HDPE, on the other hand, polymerization is initiated on the surface of a Ziegler-Natta catalyst [10]. The catalyst allows not only for polymerization to occur at lower temperature and pressure, it additionally controls the polymerization reaction. Chain growth is now limited to only ensue on the surface of the catalyst, limiting the chain transfer reactions. This results in more linear chain growth, with infrequent side branching as shown in Figure 5B.

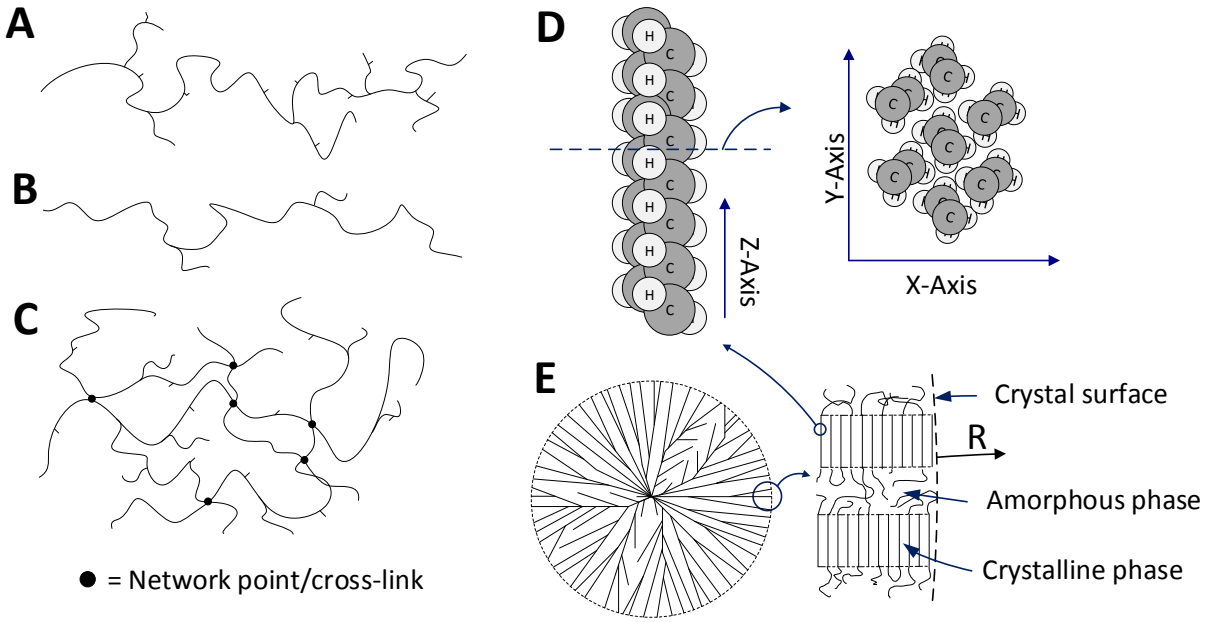

Figure 5.Molecular structure of LDPE (A), HDPE (B), XLPE (C). Conformation of the polymer chain and close packing arrangement within lamellae (D). Shape of a spherulite crystal (E) consisting of lamellae with amorphous interstitial areas. Crystal growth direction is indicated with R.

XLPE, shown in Figure 5C, is created through a crosslinking process. One way of attaining such a crosslinked material is by adding Dicumyl-peroxide (DCP) to LDPE. After forming the shape of the material, additional heating is applied which thermally decomposes the DCP. The DCP then subtracts hydrogen atoms from the polymer chains, creating macroradicals (vacancies). These vacancies become points where polymer chains bind to vacancies on neighboring chains. This results in a linked network with improved thermal stability at elevated temperatures referred to as a thermoset.

The amount of side branches present on the polymer chain affects the degree of crystallinity in the material. When cooling from the melt, polymer chains arrange in a manner to minimize the free energy (often by occupying as little space as possible). Polyethylene crystallizes in an all trans-zigzag form [11], representing the lowest energy state, as shown in Figure 5D. These linear chain sections stack into dense crystals, referred to as lamellae. As further growth of lamellae occurs outwards in the *x-y* plane, the structure originates from a growth point, with the lamellae branching on outwards. This forms a spherical superstructure with growth radius *R*, as shown in Figure 5E, referred to as a spherulite. In between the lamellae, amorphous regions are frozen in, therefore the spherulite consists of many lamellar and amorphous layers as shown in Figure 5E. Side branching on the chain inhibits the formation of ordered structures to some degree, as such branches cannot be present within the lamellae. This results in different degrees of crystallinity for LDPE and HDPE. For XLPE, similar crystallization occurs as in base polymer before introducing the cross-links. However, upon increasing its crosslink density, the formation of perfect spherulites as shown in Figure 5E is inhibited. Like branches, also network points cannot be contained within the perfect crystal structure in the lamellae. Increased crosslink density, therefore, leads to the formation of axialites and less ordered lamellae stacks at higher crosslinking densities [12]. The crystallization process starts when cooling below the melt temperature T_m, with crystallization starting at T_c (located slightly below T_m), and its rate decreases with temperature until it is fully prohibited below the glass transition temperature T_g. The degree of crystallinity achieved in a specific material sample can be measured by means of Differential Scanning Calorimetry (DSC), allowing also to deduce the size distribution of lamellae [4]. Additionally, certain features, such as the *C-H* stretch vibration, can be detectable in Infrared Spectroscopy, which relates to crystallinity and the degree of regularity in the backbone structure [13].

As shown in Figure 5D, the degree of packing is dense in the crystalline regions of the material, resulting in low solubility of chemical impurities in these areas. This can result in a higher impurity concentration at the spherulite surface, as these impurities are pushed outwards as the spherulite grows [14], [15]. Also, different concentration levels between the amorphous and crystalline phases within the spherulite itself are likely to be present. Conduction processes can thus differ significantly between the amorphous phase, crystalline phase and crystalline boundary as both molecular structure and impurity concentration differ in these regions.

The drawback of the thermoset forming crosslinking process (i.e. creating XLPE) is the generated byproducts, commonly referred to as peroxide decomposition products (PDP). These impurities, being α-Cumyl alcohol, Acetophenone, α-Methylstyrene, water and methane, have a negative impact on dielectric performance [16]. Thus, a degassing process is required for improved performance. Additionally, several useful additives may be included in the material, such as antioxidants, stabilizers, scorch retarders, crosslinking boosters, acid or ion scavengers, processing aids and fillers [9]. For example, antioxidants inhibit ageing by neutralizing radicals, through hydrogen donation to the polymer chain. However, antioxidants may contribute negatively to space charge accumulation and dielectric performance [17]. The degree of

crosslinking and additives in any DC grade XLPE is thus a complex trade-off between thermal stability, ageing resistance and electrical performance, amongst other factors. However, for the specific DC grade XLPE used, improved crosslinking is contradictorily achieved with low DCP content. Vinyl groups are attached to the base polymer, boosting crosslinking efficiency which facilitates lower DCP usage, allowing for significantly lower residual PDP concentrations after the thermoset is formed [9]. This material has shown excellent performance during cable system qualifications at 320 kV [4], 400 kV and 525 kV [6]. Furthermore, semi-conductive layers in HVDC cables typically consist of non-polar XLPE doped with carbon black (CB) particles. The CB particles predominantly originate from furnace or acetylene black. The choice of semiconductor material with regards to its CB type, its loading and choice of the base matrix is known to strongly affect space charge accumulation in the HVDC cable [18], [19].

2.1.2 Cable accessories in high voltage cable systems

Different cable accessories are required as the cable is produced in certain production lengths, with maximal length limited by practical factors such as scorch onset in the extrusion line, or feasible drum sizes in land transport.

For submarine cables, flexible factory joints are utilized to connect production lengths prior to the armoring process [8]. Such factory joints connect several 20-30 km production lengths in series, creating an installation length of 150-250 km. Factory joint design requires flexibility and they are preferably of similar diameter to that of the cable. Thereby, further cable spooling and installation through the installation vessel's mechanical system is unaffected. These joints are therefore made under controlled factory conditions, by reconstructing the cable layer by layer, using identical materials, and performing stepwise local vulcanization of the inner-semiconductor, insulation and outer-semiconductor. The introduced interfaces in this joint are therefore chemically bonded in the crosslinking process.

The complete submarine installation length is shipped to the site and installed on the sea bottom. However, multiple installation lengths are often required, as the total link length can exceed the loading capabilities of the installation vessel. The cable is then installed in multiple campaigns, with each new installation length connected to the previous one through a submarine field joint. In rare cases, due to offshore external damages to the cable, an additional length is jointed in utilizing two submarine repair joints. In other cases, different cable designs are required along the installation route. Such transitions can be realized in advance by asymmetric factory joints or made offshore with asymmetric field joints. The main challenge in field and repair jointing is their offshore assembly, as weather windows during which the vessel can safely perform the work are limited in time. The design of such joints therefore focuses on a swift and reliable installation. These joints utilize a pre-manufactured insulation system which is slipped over a compressed or screwed conductor connection. Mechanical strength and water tightness are ensured by an outer casing and additional layers.

Connecting the submarine cable to a land section can be realized by a transition joint or asymmetric land joint. The land section will additionally have frequent land joints along its route, as onshore installation lengths are greatly limited by road transport capabilities. Such joints are installed in a bunker or joint pit, with a similar methodology to the submarine field joints. The electrical insulation systems of symmetric or asymmetric field, repair, and land joints are thus comparable, and the interfaces within them are of similar nature, as shown in Figure 6.

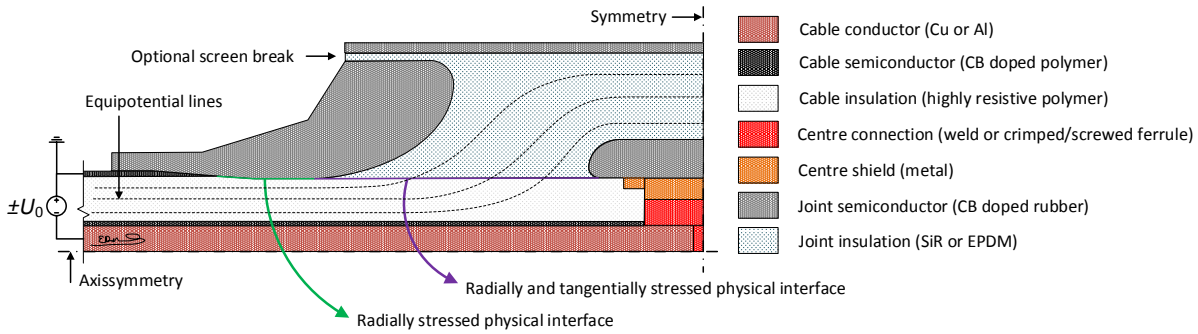

Figure 6. Generic illustration of an extruded HVDC cable joint utilizing a rubberized slip-on joint body (not to scale). For simplicity, only its electrical layers are shown, with the outer casing and additional layers not depicted.

The in Figure 6 shown pre-molded joint body, can thus be made to suit several types of cable accessories. It is usually made through an injection molding process, to create the complex shape required. The materials used in such components are rubbers, with ethylene propylene diene monomer (EPDM) and silicon rubber (SiR) being the most commonly used materials. Carbon black loaded materials are also introduced to create the complex geometry required for electric field control. The true advantage of this technology is its pre-manufactured electrical system, which is electrically tested prior to installation. Thereby, defects can be effectively avoided within the joint body. As both the cable and the joint body are in advance screened for defects, the only further required quality assurance is that of the interface created between them.

In the two ends of a finalized link, terminations are utilized to connect the cable to a bus bar, gas-insulated switchgear (GIS) or overhead lines. Terminations can contain dielectric fluids, gas or can be designed as a dry type. A simplified illustration of a gas or fluid-filled cable termination is shown in Figure 7.

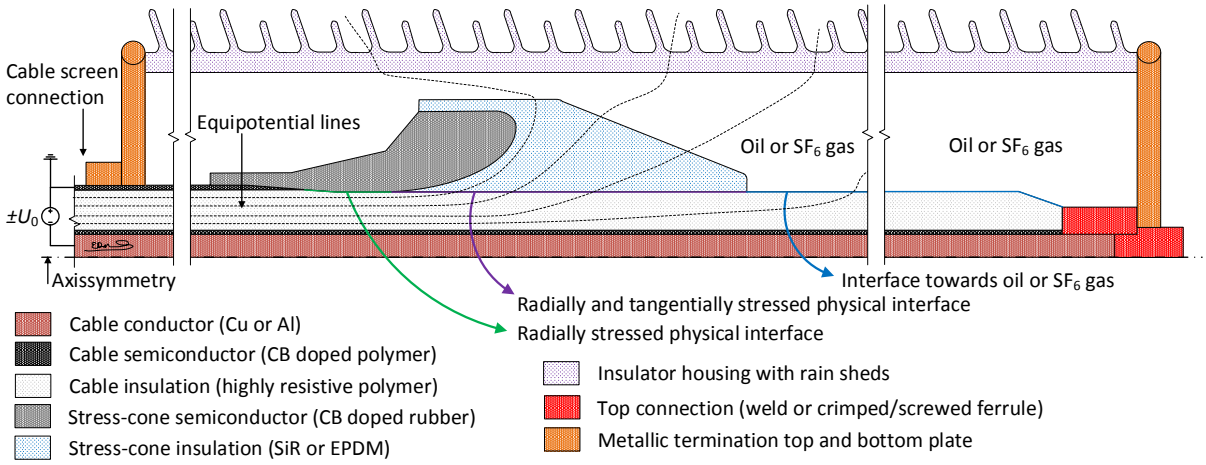

Figure 7 Generic illustration of an extruded HVDC cable termination with geometric field control using a slip-on stress relief cone (not to scale).

As seen in Figure 7, the stress-cone used for the geometrical field control in the termination is of similar design to that of the pre-manufactured joint. Comparable manufacturing and pre-installation testing often apply, which again allows for a swift installation of a pre-tested and defect free component. Also, in this case, the cable interface between the cable and component is the most difficult aspect to control during the installation of a termination. For this interface, any geometrical deviation can lead to air pockets. Such air pockets are prevented by the use of an interstitial medium such as grease or oil, improving the mating and allowing for slip-on of

the pre-molded accessory. Mechanical interface pressure additionally limits void size during the lifetime of the accessory and is commonly created through the elastic forces of the undersized pre-molded joint body. While a more detailed description of these cable accessories is made by Worzyk [8], the work's purpose is now to in detail investigate the nature of their interfaces.

2.1.3 Interface types in extruded cable accessories

Interfaces used within cable accessories can be divided into two categories, being chemical interfaces and physical interfaces [7]. The chemical interface is normally inseparable and consists of two materials joined together in an extrusion or injection molding process. The physical interface, on the other hand, is the on-site created mating between the cable and the pre-molded accessory body, or between other components in the accessory. Common chemical and physical interfaces present in HVDC cable accessories are listed in Table 1.

*Table 1. List of common interface types in HVDC extruded cable accessories subjected to electrical stress. Stress orientation is indicated, with normal being perpendicular and tangential being along the interface. *Physical interfaces in land, field and repair joints and terminations previously shown in Figure 6 and Figure 7.*

Accessory type	Interfacial nature	Inner material	Outer material	Field orientation
Flexible factory joint	Chemical	Joint semicon (molded XLPE + CB)	Joint insulation (molded XLPE)	Normal
	Chemical	Cable semicon (extruded XLPE + CB)	Joint insulation (molded XLPE)	Normal
	Chemical	Cable insulation (extruded XLPE)	Joint insulation (molded XLPE)	Normal and tangential
Land joint, field joint, repair joint and termination	Chemical	Accessory insulation (molded SiR or EPDM)	Accessory semicon (molded SiR or EPDM + CB)	Normal
	Chemical	Cable semicon (extruded XLPE + CB)	Cable insulation (extruded XLPE)	Normal
	Physical*	Cable insulation (extruded XLPE)	Accessory insulation (molded SiR or EPDM)	Normal and tangential
	Physical*	Cable insulation (extruded XLPE)	Accessory semicon (molded SiR or EPDM + CB)	Normal
Termination	Interface towards gas/liquid*	Cable insulation (extruded XLPE)	Insulating oil, SF_6 gas, or other dielectric fluid/gas	Normal and tangential
Dry-type termination	Physical	Accessory insulation (molded SiR or EPDM)	Spacer insulation (molded epoxy)	Normal and tangential

Limiting asperities, roughness and contamination are the main considerations during the production of all interfaces listed in Table 1. As such factors introduce small geometric deviations, they can locally distort the normal or tangential field at the interface. This work mainly focuses on the physical interface with the electric field in normal direction, located underneath the joint semiconductor as shown in Figure 6 and Figure 7. The results are also applicable to effects induced by the dominating normally oriented stress in the other interface types. For example, the chemical interface between semiconductor and insulation in the cable or the factory joint exhibits features shared with the studied physical interface.

What the physical interfaces in Table 1 have in common, is their creation through the removal of the outer semi-conductive layer from a section of cable. This process can be achieved with

different methodologies, referred to in this work as the cable preparation method. According to Sawyer et al. [20], the need for polymer machining and surface preparation arises when injection molding or extrusion is unsuitable for creating the specific geometry, or when high dimensional accuracy or surface finish is required, exceeding what can be shaped with injection molding or extrusion. This statement is certainly relevant for physical cable interfaces. The prepared cable surface requires a high-quality finish to be made in the field, preferably avoiding any complex procedures. This procedure should also be as repeatable as possible. For such reasons, different abrasion, cutting and remolding procedures are most suitable for the task. Such methods create different surface characteristics, to be investigated further in this thesis.

2.1.4 Cable surface preparation

As the polymer's nature affects machinability, the outcome of a certain preparation method can differ if substantial change is made in the insulation material. Mechanical parameters such as density, modulus and strength, originating from molecular structure, affect the effectiveness of surface preparation. For example, presence of crosslinks in the material restricts the material from ductile behavior (melt flow) when the melt temperature, T_m is locally exceeded during machining [21]. This may spawn different results when using the same preparation method on a thermoset or a thermoplastic material. The glass transition temperature T_g can also affect the preparation's outcome. Preparations carried out below T_g (note: local temperature at tool edge) remove material through a rupture or extreme fracture process. Preparation of LDPE, having T_g around -120 °C, exhibits instead a yielding process [22], when prepared at room temperature. Yielding of a polymer is described by the flow model of Eyring [10], expressing yield stress dependent on temperature and strain rate (cutting speed). Such parameters are thus crucial to control in preparation to create reproducibility in the field.

In abrasion, material removal is carried out through sharp Al_2O_3, SiC or diamond grains embedded on a substrate, which are rubbed along the polymer surface. It is common to start with a low grit size (thus larger abrasive grains) and work down until finalizing with the highest grit size. The use of coolant may facilitate better cooling and more effective removal of polymeric particles from the abrasive. When polymeric particles are pulled off from the polymer, certain peaks can be observed on the polymer surface [23]. Such peaks could originate from a yielding process as described by Eyring's flow model. The final surface texture should resemble a matte scratched surface originating from the latest used grit size, as shown in Figure 8A.

When cutting a polymer surface, a cutting blade moves along the surface, cutting off slices from the material. This process shares similarities with ordinary machining, except that the tool's rake angle is much lower for cutting. The rake angle is known to affect the fracture mode during preparation [21]. However, for preparing LDPE or XLPE at room temperature (above T_g), fracturing should not be the major form of material removal. The final surface texture should be a striated surface, with striations originating from the cutting edge's shape, as in Figure 8B.

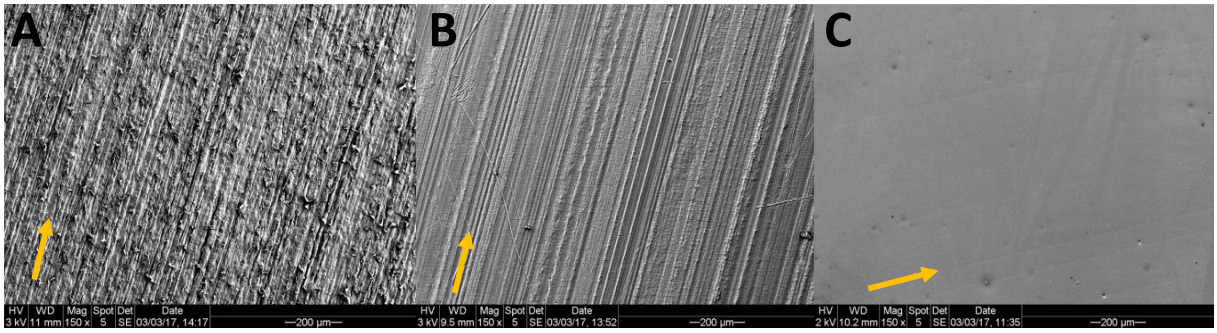

Figure 8. Texture of abraded (A), cut (B) and remolded (C) XLPE cable surfaces, with arrows indicating the texture's orientation.

When remolding a polymeric surface, a molding process is performed on the priory formed and crosslinked material surface. If crosslink density is sufficiently low, remolding should yield similar results to the molding of a thermoplastic film. The remolding procedure could impact morphology in the surface region, depending on temperature and film material used in the process [24]. The created texture is a replica of the surface texture on the contacting film, which is shown in Figure 8C. Here, the visible texture originates from the manufacturing of the press film. In this way, a surface texture resembling that of an extruded or molded material can be efficiently introduced in the field.

2.2 The mesoscopic gap

The relevant electrical effects and calculation methods are exemplified in Figure 9, arranged according to their geometric size.

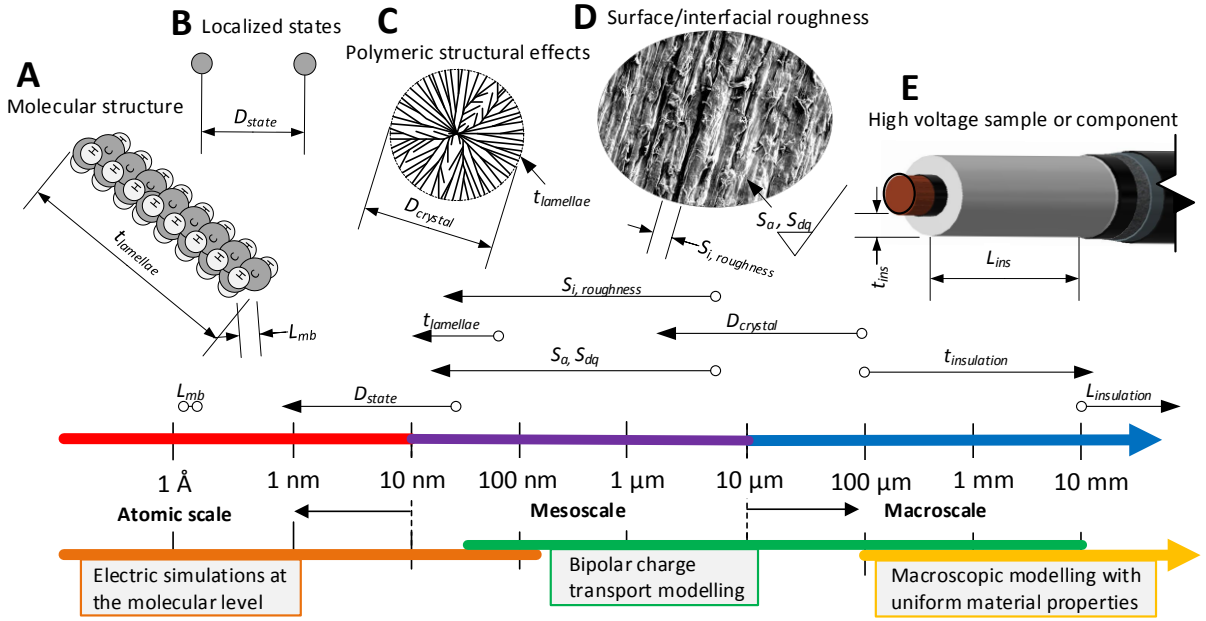

Figure 9. Geometrical scale of polymeric and interfacial structural effects. The mesoscale region is here regarded as the range in between the macroscopic and atomic scales. Indicated effects shown are: A) L_{mb} = length of (covalent) molecular bonds, B) D_{state} = relevant separations between localized states, C) $t_{lamellae}$ = lamellaer thickness and $D_{crystal}$ = Spherulite diameter, D) S_i = surface texture spacing and S_a, S_{dq} = surface roughness parameters, E) t_{ins} = insulation thickness and L_{ins} = the HV component's outer dimensions.

As observed in Figure 9, the geometric scale of relevance spans over several orders of magnitude, all the way from component size down to the size of atoms. Especially daunting is the in Figure 9 indicated mesoscale region [25], in which many three-dimensional (3D) effects occur. When unaccounted for, they may lead to faulty conclusions about the origin of observed macroscopic properties. The true challenge is thus to link macroscopic cable properties, to the complex atomic and mesoscopic effects in polymeric insulation.

Properties of the band gap (which will be introduced in section 2.3.1) and localized states in it, can be estimated through molecular modelling, (e.g. by means of Density Functional Theory (DFT)) [26]. Such simulations allow describing complex charge carrier-matrix interactions, accounting for the impact of molecular chain conformation and in-chain defects [26]. Such simulations are however limited in maximum domain size as the smallest simulated elements, covalent molecular bonds (indicated with L_{mb} in Figure 9), are many orders of magnitude smaller than the lower range of the mesoscale.

Meanwhile, in the macroscale, measurement techniques and computational methods are advancing allowing for a more accurate description of the analytical and theoretical properties of polyethylene, as when matching conductivity or space charge measurements with bipolar charge transport models [27]–[31]. The bipolar transport model needs to consider the entire insulation cross-section (indicated with t_{ins} in Figure 9), whose domain size is larger than 10 mm when describing an HV cable. At the same time, a nearly nanometer-sized mesh is required for accurately modelling the random by nature mesoscopic effects with Finite Element Method (FEM). Also, the localized state separations (indicated with D_{state}) define the lower scale at which the used equations can be regarded as continuous functions. Additionally, due to low charge densities to be modelled, they become fractional charge carriers in small local domains. Such challenges thus make constructing an all-encompassing macroscopic cable model difficult.

The difficulty in bringing these molecular and macroscopic approaches together, thus bridging the mesoscopic gap, is that computational performance is still insufficient. The limitation is thus clear, there is a discrepancy between the maximum molecular model domain size and the smallest element feasible in a full macroscopic simulation. This discrepancy makes accounting for certain effects occurring within the mesoscopic gap a specifically difficult task, and it explains why charge transport in polymers is far from fully understood. It is therefore the target of this research to provide further insight into local mesoscopic behavior utilizing different experimental and simulation procedures.

2.3 Bipolar charge transport

Before electrical surface properties can be addressed, a description of charge carrier transport and injection in insulators is required. The basis of the description relies on the band gap model, originating from semiconductor physics. It is described in detail in the works of Kittel [32], Neamen [33] and Dissado and Fothergill [34]. It begins by outlining the band gap specific to polyethylene. Thereafter, charge transport in polyethylene is described. This is followed by a description of space charge injection and extraction.

2.3.1 The band gap of polyethylene

Fully aligned (crystalline) polymeric chains, consisting of covalent bonds repeated at regular intervals, form a periodic (coulomb) lattice potential $V(x)$. Schrödinger's equation (SE) predicts the periodic potential's interaction with the electron's wavefunction, forming the forbidden

energy band (band gap) of the insulator. The simplest form of this band gap (E_g), between the valence band edge *(E_v)* and conduction band edge *(E_c)* is shown against spatial position *z* in Figure 10. For polyethylene, the level of the conduction band is above the energy of an electron in vacuum, yielding a negative electron affinity χ. For the crystalline phase, the electron affinity is thus in the range of -0.65 eV to -1 eV, and the band gap E_g is around 6-8 eV.

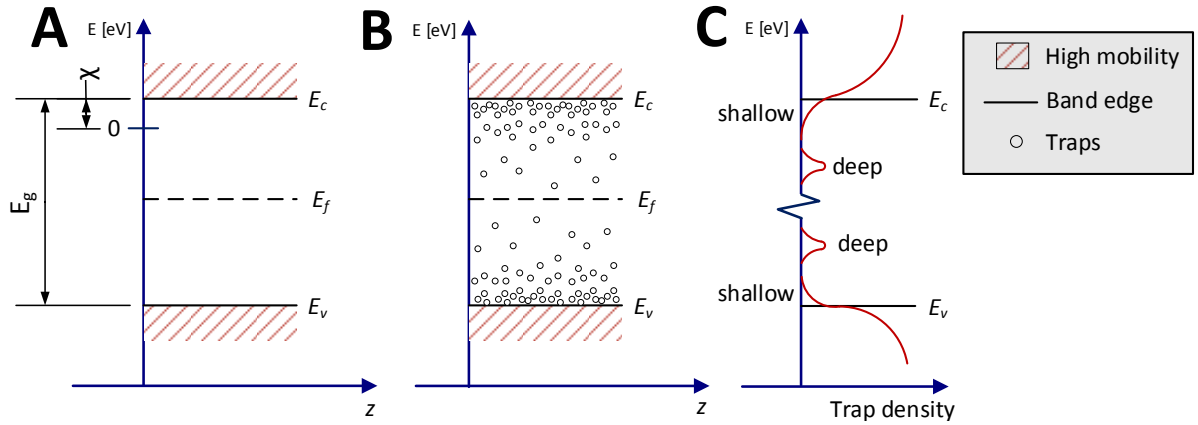

Figure 10. Schematic representations of the band gap of polyethylene. The ideal band gap (A). Realistic band gap with traps and variation in the position of the band edges (B). Density of states (DOS) assuming extended shallow states with an exponential distribution, and a gaussian distribution of deep traps (C), adopted from [35].

Only considering intra-chain conduction amongst fully aligned polymer chains, with its corresponding band gap shown in Figure 10 A, has its limitations. The predicted band gap mobility for intra-chain conduction is in the range of $1.2 \cdot 10^{-5}$ $m^2/(V \cdot s)$ [34]. Charge carriers in the conduction or valence band, are thus estimated to have too high mobilities, poorly describing the material's conduction properties. It is thus necessary to extend the model to inter-chain conduction and accounting for material imperfections, such as non-ideal polymer chain conformation, chain defects, vacancies (free volume) and non-ideal bonds. Such imperfections can be considered as a disruption of the periodic lattice potential *V(x)*, and thus result in a distribution of states within the band gap as shown in Figure 10 B. A simplified description of the DOS in polyethylene [35] including such imperfections is shown in Figure 10 C. This DOS can be further used for defining specific trap and transport levels, which allow for parameterization of charge transport rates. Such rates can be individually expressed for electrons and holes, which is identified by their respective subscripts (*e*,*h*).

2.3.2 Bulk conductive processes

This section describes properties and effects in the material bulk that impact the transport of charge carriers. Such processes, including (hopping) transport, trapping, detrapping, recombination and diffusion mechanisms for electronic charge carriers.

2.3.2.1 Hopping transport

Spatial movement of charge carriers is considered within the framework of a hopping mechanism that is essentially a thermally assisted tunneling between localized states in the material. Hopping thus governs hole inter-chain conduction through the weak Van-der-Waals bonds in between the polymer chains [36], or electron conduction in between nanometric low-density regions in between polymer chains [25]. The distance and energic levels between neighboring states dictate the probability that hopping can occur. Based on this description, the carrier's mobility in $m^2/(V \cdot s)$ can be expressed as:

$$\mu_{(e,h)}(E,T) = \frac{2va_{(e,h)}}{E} e^{-\frac{w_{hop(e,h)}}{k_B T}} \sinh\left(\frac{eEa_{(e,h)}}{2k_B T}\right) \quad (1)$$

where e is the elementary charge measuring $1.602 \cdot 10^{-19}$ C, k_B is the Boltzmann's constant, T is the temperature in K and E is the electric field strength in V/m. v is the attempt-to-jump/escape frequency (defined as $v = k_B T/h \approx 6.2 \cdot 10^{12}$ s^{-1} at 25 °C), and $w_{hop(e,h)}$ is the average encountered energy barrier for hopping in eV. $a_{(e,h)}$ is the average spacing between trap sites in meters. If a shallow trap density of 10^{27} /m^3 is assumed in a uniform cubic lattice, a trap separation $a_{(e,h)}$ of 1 nm is deduced. This parameter can be used for estimating the field limit in equation (1):

$$eEa_{(e,h)} \ll k_B T \quad or \quad E \ll \frac{k_B T}{ea_{(e,h)}} \quad (2)$$

Thus, with 1 nm trap separation, equation (2) estimates a field limit of approximately 26 kV/mm. Equation (1) can thus be simplified by eliminating the field dependency, expressing effective mobility as:

$$\mu_{eff}(T) = \mu_{0(e,h)} e^{-\frac{w_{hop(e,h)}}{k_B T}} \quad , \quad \mu_{0(e,h)} = e\frac{a_{(e,h)}{}^2}{h} \quad (3)$$

As equation (3) only requires the parameters μ_0 and w_{hop} for each carrier type, it makes model calibration more manageable and is therefore frequently used [37]–[44]. However, equation (3) expresses inaccurate transport rates above the field limit defined by equation (2). Also, the carrier drift velocity, m/s; can be expressed as:

$$\vec{v}_{d(e,h)} = \mu_{(e,h)} \vec{E} \quad (4)$$

The drift velocity expresses a linear field dependency below the field limit in equation (2), whereas above this limit it exhibits a stronger field dependency.

2.3.2.2 Trapping, detrapping and Poole-Frenkel effect

The deep traps in the distribution shown in Figure 10 C, may be of such depth that transport amongst such states occurs at a very low rate. Therefore, a certain fraction of charge carriers is effectively immobilized, yielding a trapping rate ($T_{(e,h)}$, s^{-1}) and a detrapping rate ($D_{(e,h)t}$, s^{-1}) between mobile and trapped carriers. These rates are extremely challenging to calibrate because the mobile-trapped charge ratio is unobservable in space charge measurement signals.

Poole-Frenkel (PF) effect describes a field-dependent barrier height for detrapping of carriers. It originates from coulomb field interaction between the charge carrier and an ionized (donor or acceptor) trap site. The coulomb field will superimposed with the background electric field result in a lowering of the detrapping barrier height, such that its maximum height is located a certain distance r_m, from the trap site as depicted in Figure 11.

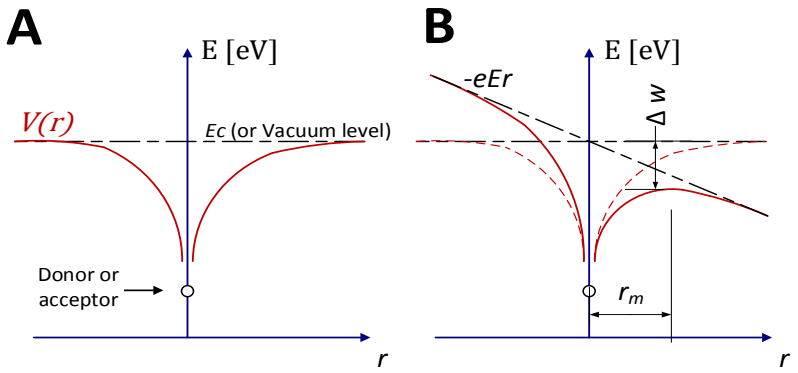

Figure 11. Coulomb electric potential (V(r)) near ionized donor site at no electric field (A) and strong electric field (B), defining the maximal barrier position r_m, and the barrier reduction Δw.

As seen in Figure 11, the maximal barrier position r_m, will exhibit a dependency on the background field, expressed as:

$$r_m = \sqrt{e/(4\pi\varepsilon_0\varepsilon_r E)} \tag{5}$$

where ε_0 is the vacuum permittivity with a value of $8.854 \cdot 10^{-12}$ F/m and ε_r is the unitless relative permittivity. This expression can be used to estimate the lowering of the potential barrier (in one dimension), in eV:

$$\Delta w(E) = \sqrt{e^3 E/(\pi\varepsilon_0\varepsilon_r)} \tag{6}$$

Thus, the lowering of the potential barrier will result in an increased detrapping rate expressed as:

$$D_{PF(e,h)}(E,T) = ve^{-\frac{w_{0(e,h)}-\Delta w(E)}{k_B T}} \tag{7}$$

Where $w_{0(e,h)}$ is the original barrier height, eV; and $\Delta w(E)$ is the barrier lowering expressed in equation (6). As equation (7) is derived for one dimension, the actual barrier lowering effect in three dimensions is lower [45], [46], as it accounts for barrier height in directions offset from the electric field orientation. This description ultimately yields a barrier lowering of approximately [47]:

$$\Delta w_{3D} = 0.3184 \Delta w_{1D} \tag{8}$$

Conclusively, both trapping and detrapping may exhibit temperature and field dependencies, which have been further evaluated in section 5.1.

2.3.2.3 Charge recombination

Recombination between carriers of opposite polarity may take place, neutralizing electron-hole pairs in the material (or ionic related pairs). Upon recombining, energy is released in the form of electroluminescence due to the large energetic difference between the opposite carriers. Because the rate of recombination (S, $m^3/(C \cdot s)$) is an unknown quantity, it has been calibrated against electroluminescence measurements [39], [40], [48]. Such calibration obtained recombination rates ($S = 3 \cdot 10^{-4}$) which have been adopted in many bipolar simulation approaches [37]–[44].

2.3.2.4 Diffusion of electronic carriers

The diffusion of electronic carriers, forming a transport rate dependent on their 3D gradient $\nabla n_{(e,h)}$, is dependent on the material's diffusion coefficients $D_{(e,h)}$, m^2/s. This coefficient, albeit difficult to quantify experimentally, can be derived from the mobility using the Einstein relation:

$$D_{(e,h)} = \frac{k_B T}{e} \mu_{(e,h)} \tag{9}$$

Equation (9) is valid for a semiconductor in steady-state. Thus, estimated diffusion rates may be less accurate for the insulator upon stepwise poling application.

2.3.2.5 Ionic transport

While the transport processes outlined so far describe the motions of electronic carriers (electrons and holes), the transport of larger charged species (ions) can also be considered. Such species are positioned in the bulk's free volume and at crystalline interfaces in the material. As such species (such as PDP) are polar, they can be ionized (or dissociated) under electric field application, resulting in a threshold field for their internal generation rate [44]. Their transport can be described with field-assisted drift and concentration gradient dependent diffusion, allowing for modelling such species with the previously outlined transport processes [44]. Instead of states within the band gap, hopping of ionized species makes use of the vacant sites in the material [34], and require thus different transport parameter values. The main differences between electronic and ionic processes are thus that the latter facilitates internal carrier generation (electron-ion, hole-ion or ion-ion pairs) and that the latter process can behave differently at the electrodes (with heterocharge formation), which will be described in the next section.

As ionizable species can have a strong influence on the conduction processes, it is desirable to keep polymeric high voltage materials as clean and dry as possible. This is normally the case for well-degassed ultra-clean XLPE used in cables or neat polyethylene materials used for studying space charge evolution, allowing for the elimination of ionic processes in the theoretical methodology.

2.3.3 Space charge injection and extraction

This section describes the injection and extraction processes at the material's electrodes. Such processes result in a flux of charge carriers perpendicularly oriented inwards or outwards from the material boundaries. Different injection mechanisms; Schottky injection, Fowler-Nordheim injection and hopping injection are described. Also, charge extraction is described at the end of this section.

2.3.3.1 Schottky injection

Schottky injection describes thermionic emission from ideally mated metal-semiconductor and metal-insulation contacts. The ideal Schottky barrier thus assumes injection from an infinitely smooth electrode, into a semiconductor or insulator devoid of any localized states in its band gap. For insulators, no significant majority carrier concentration exists, thus no significant band bending, nor alignment of Fermi levels occurs upon mating the electrode. Theoretically, the injection barrier height for electrons is defined by the energetic difference between the metal's

work function ϕ_m and the insulator's electron affinity χ in eV, as illustrated in Figure 12 and described in equation (10).

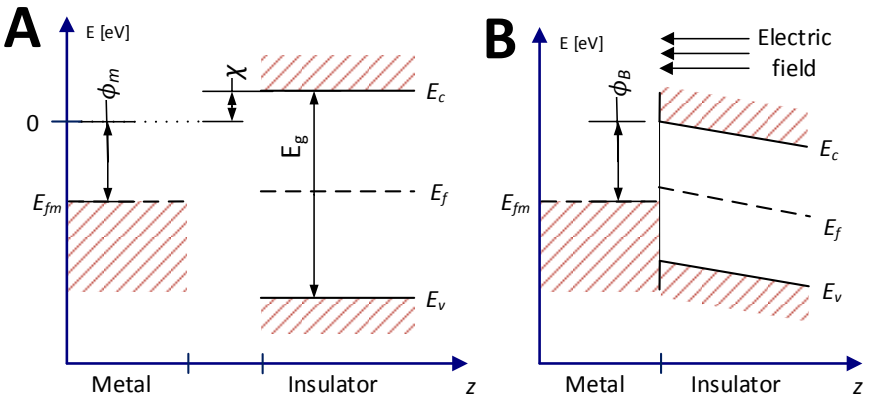

Figure 12. Ideal Schottky barrier before contact (A), and after contact (B) between an ideal metal and an ideal insulator. The result of including a background electric field is displayed in B.

Further derivation of the Schottky injection is based on its ideal barrier height as shown in Figure 12. The barrier height ϕ_B in eV, for charge injection, is thus defined as:

$$\phi_B = (\phi_m - \chi) \tag{10}$$

The electron affinity χ typically lies within 3-5 eV for ordinary semiconductors, while for all-crystalline polyethylene it is around -1 eV. Note that negative electron affinity adds to the total barrier height. Typical metal work functions ϕ_m vary between 4 and 6 eV. The estimated, ideal Schottky barriers for polyethylene are thereby of such magnitude that they predict infeasibly low injection currents. Injection barrier values used in simulations are generally in the range of 1-1.3 eV to match experimental observations, thus not matching the theoretical barrier values.

The Schottky injection current density can be derived with help of thermionic emission theory. The current density from the metal into the insulator is a function of electron concentration, flowing in the *z*-direction with sufficiently high velocity to overcome the barrier (without reflection). This defines v'_z, the minimum speed required for emission into the insulator, such that its kinetic energy $\frac{1}{2}m_e(v'_z)^2$ exceeds the height of the energy barrier, as illustrated in Figure 13.

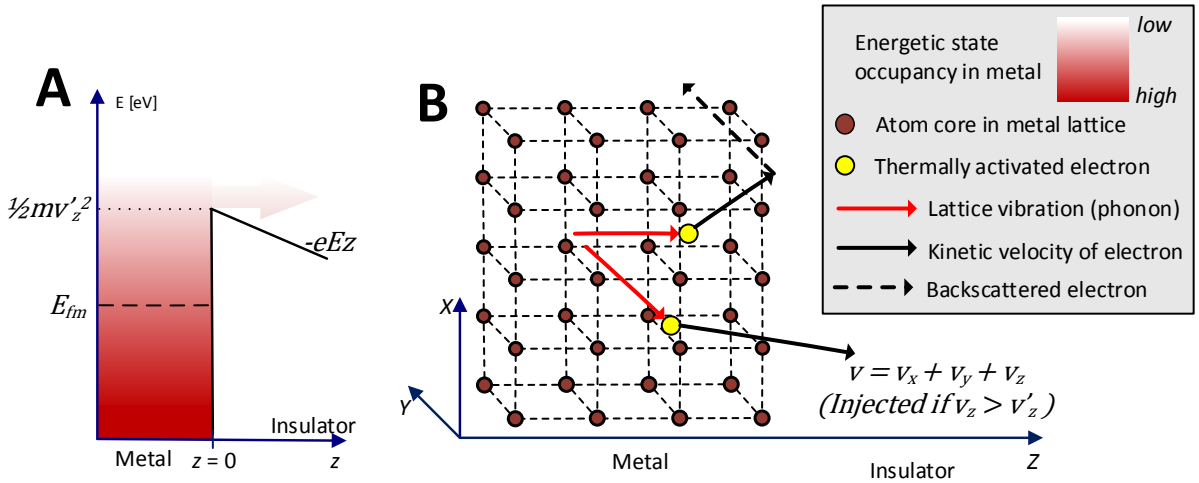

Figure 13. Energetic state occupancy and barrier height (A). Spatial illustration of phonon activation and subsequent injection or backscattering (B)

As observed in Figure 13, backscattering at the barrier is also accounted for through the introduction of a unitless reflection correction factor λ_R. This yields the current expression for Schottky injection as:

$$J_S = \lambda_R A_0 T^2 e^{\frac{-(\phi_B - \Delta\phi)}{k_B T}} \tag{11}$$

where ϕ_B is the barrier height in eV, and $\Delta\phi$ is the reduction of the potential barrier (equation (13)) in eV. A_0 is the Richardson's constant in $Am^{-2}K^{-2}$, which for the insulator-metal junction is given by:

$$A_0 = \frac{4\pi e m_e^* {k_B}^2}{h^3} \tag{12}$$

where m_e* is the effective mass, which can be simplified to the electron mass m_e with a value of $9.109 \cdot 10^{-31}$ kg and h is the Planck's constant with a value of $6.626 \cdot 10^{-34}$ Js. Expression (11) resembles the reverse-saturation current density for metal-semiconductor interfaces [33]. However, a field lowering effect arises in the Schottky barrier. An electron at distance z from the metal's surface will create a coulomb electric field towards the barrier. This is best described with an image charge at the other side of the barrier (at -z) creating a coulomb force acting on the electron. The image charge effect results in a lowering of the potential barrier expressed as:

$$\Delta\phi = \sqrt{\frac{e^3 E}{4\pi\varepsilon_o\varepsilon_r}} \tag{13}$$

For the reduction of the potential barrier $\Delta\phi$, in eV, in expression (13) to be valid, a barrier towards metal or material of sufficient high permittivity to create a symmetric image charge effect is needed. The true image charge effect is thus a function of both the electrode and the insulator permittivities [34], [49], [50], which is simplified in the derivation owing to the large permittivity discrepancy between insulators and metals (i.e. $\varepsilon_{electrode} >> \varepsilon_{insulator}$). For hole injection, the image charge effect is synonymous with electron injection, giving the same field dependency to the equation. By inserting equation (13) into (11) and assuming the expression to be equally valid for electron and hole injection, the current density through the metal-insulator interface is expressed as:

$$J_{S(e,h)} = \lambda_{R(e,h)} A_0 T^2 e^{\frac{-\phi_{B(e,h)}}{k_B T}} e^{\frac{e}{k_B T}\sqrt{\frac{eE}{4\pi\varepsilon_0\varepsilon_r}}} \tag{14}$$

where the unitless material-specific correction factor $\lambda_{R(e,h)}$ and the barrier height $\phi_{B(e,h)}$ in eV allow for determining the temperature and field dependent hole and electron injection current densities. Equation (14) thus defines the Schottky injection current density into the material, originating from phonon excitation (thermal activation) of free electrons in the metal which enter the conduction band (or the valence band for hole injection) of the insulator by overcoming the energetic barrier reduced by means of the image charge effect.

The one-dimensional calculation of the image charge effect neglects the impact of space charge effects in the injection process. Taylor and Lewis [51] suggested instead an activation process to account for space charge effects, which resulted in a different field dependency in the final equation. The limitations of the ideal Schottky barrier are thus frequently reported, being:

- The theoretical barrier height does not match experimental observations [27], [30], [37], [39], [40], [42], [44], [48], [52], [53].
- The theoretical value of Richardson's constant is reported to be too high [54].
- The image charge effect is inaccurate for high field strength and only valid for high permittivity electrodes [49], [50].
- It injects too much charge at low field strength [30], requiring unphysical modifications.
- It describes injection into the conduction band, whilst the transport level in a bipolar transport model typically describes states located below it.

Given these limitations, the impact of non-ideal barrier properties is further investigated in section 2.4

2.3.3.2 Fowler-Nordheim injection

Two types of tunneling can be applicable, being: direct tunneling and Fowler-Nordheim (FN) injection (or cold field emission). In direct tunneling, the charge carrier passes through the entire material or layer in question and is therefore only considered for extremely thin atomic devices. When encountering a potential barrier of non-infinite height, the wave equation (describing the probability density of the carrier) will exhibit exponential decay. For electrons, behaving both as particle and wave per its particle-wave duality principle, this yields a low but non-zero probability density a certain distance into the insulating material. If allowed states are encountered at the same energetic level (e.g. within a different material layer (direct tunneling), within a conduction band (FN-injection), or localized states) before the probability density effectively vanishes, they can be accessed by the numerous electrons attempting to penetrate the barrier.

For FN injection, the electron tunnels from the electrode into the conduction band of the insulator [55], [56]. This effect becomes significant if electric field strength is high enough and thus the barrier sufficiently thin. Electrons in the adjacent metal around and below its Fermi level (E_{fm}) are directly injected into the conduction band of the solid insulator without requiring thermal (phonon) activation. Their energy level thus remains constant during the process, thus making it a cold type of field emission, able to inject carriers also at extremely low temperatures. The electric field is assumed to be negligible inside the metal as it would be neutralized by any available free charges. Outside the electrode, the electric field is oriented perpendicular to the electrode surface [56]. By first utilizing a spatial expression of the potential barrier, along with the one-dimensional time-independent SE, the transmission coefficient of the barrier is estimated, which expresses the probability for a carrier to enter the conduction band. Thereby, the total current density is found by integrating this transmission coefficient multiplied with the number (density) of carriers arriving at the surface (with certain *z*-momentum). This derivation results in the injection current density (at 0 K and without image charge effect, hence the subscripts "*c*" for cold and "*n*" for no image charge effect) as originally derived by Fowler and Nordheim expressed as:

$$J_{FN,c,n(e,h)}(E) = \frac{e^3 E^2}{8\pi h \phi_{FN(e,h)}} e^{\left(-\frac{4}{3}\sqrt{\left(\frac{2m_e}{\hbar^2}\right)}\frac{\phi_{FN(e,h)}^{3/2}}{eE}\right)} \tag{15}$$

where $\phi_{FN(e,h)}$ is the barrier height in eV, E is the electric field in V/m, $\hbar$ is Planck's reduced constant with a value of $h/2\pi = 1.054 \cdot 10^{-34}$ Js and m_e is the electron mass in kg. Interestingly, equation (15) expresses a strong dependency on electric field strength, through its quadratic

pre-exponential term and the additional negative inverse exponential term. The pre-exponential term is stated to be difficult to notice in experiments. On experiments carried out with metallic tips in vacuum, the measured current density exceeded the values estimated with equation (15). This discrepancy was, to some degree, attributed to the electrode's roughness, but the lack of image charge effect contributed to this deviation [56]. Therefore, equation (15) can be expanded to account for the image charge effect or temperature, which is further addressed in section 5.2.2

It should be noted that, whilst the expression for FN injection is derived from the wave properties of electrons, the tunneling phenomenon is valid for both electrons and holes. Limitations however arise, like in Schottky injection, from the assumption of an ideal electrode-insulator barrier. Thereby, no localized states are assumed to be present along the tunneling path of the electron and the injected charges enter directly the conduction (or valence) band.

2.3.3.3 Hopping injection

A charge injection mechanism comprising of a subsequent hopping process through the boundary layer of the insulator is relevant for polyethylene [31], [57]. Contrarily to Schottky or FN injection, which neglect surface states, hopping injection relies on the surface state distribution, through which the electronic carrier may overcome the potential barrier by subsequent hops. Since no direct equation exists expressing the current density, a simplified expression has been developed within the present study, as described in section 5.2.3.

2.3.3.4 Charge extraction

Under normal conditions, electronic carriers are considered to exit the material with a drift velocity previously expressed in equation (4). In e.g. poorly degassed XLPE with a significant concentration of PDP, Ion-electron or ion-hole pairs can be thermally or electrically ionized. This may form an extraction barrier when ionic charge carriers are blocked at the electrode [35]. In the case of metallic electrodes, no vacant space exists in the atomic lattice and ionic carriers are thus prevented from entering. For organic electrode materials (i.e. the CB doped polymeric cable semiconductor), ionized molecules can be adsorbed, however, ionic drift seizes the instant the molecule enters the electrode. With time, a concentration gradient can thereby build up over the interface, which forces a diffusion process back into the insulation material. Thereby, a quasi-equilibrium builds up with a high concentration of ionized or non-ionized molecules adjacent to the electrode. This drift-diffusion equilibrium can thus act as an extraction barrier, as it hinders ionic carrier ejection from the material.

An extraction barrier magnitude of 0.8 eV was employed by Fukuma et al. [58] to investigate the impact of PDP in a bipolar charge model. Delpino et al. [59] also address an extraction barrier for PDP. This extraction barrier accumulated heterocharges of larger magnitude than estimated with Maxwell-Wagner-Sillars (MWS) interfacial polarization [59]. Extraction barriers are thus closely linked to the formation of heterocharges, which may, due to enhanced field strength in the weak interfacial region, cause premature breakdown. The image charge effect may counteract the extraction barrier formation to some degree [50], as it strengthens the escape rate of individual charge carriers near the electrode-insulator interface. The existence of interface dipoles [60] could also impact the extraction barrier magnitude, decoupling the electrode and insulator. Consequently, high chemical cleanliness is an important factor when studying electronic processes in the material.

2.4 Surface specific properties

Aspects that physically and electrically characterize a polymer surface, are to be addressed. Four different categories can be distinguished, being:

- **Surface states**, comprising surface-specific chain defects and other trap sites.
- **Impurities**, arising from surface-specific change in chemical composition.
- **Surface morphology**, being the polymer chains' structural arrangements towards the surface.
- **Surface roughness** or topography, defining the shape and local geometry of the material surface.
- **Surface free energy** (SFE), defined as the sum of intermolecular forces at the surface.

Given such surface parameters and certain inter-dependencies among them, the challenge lies in selecting at which geometrical scale (as shown in Figure 9) their electrical impact can be accurately elucidated. With regards to modelling, additional hardship arises when inter-dependencies exist between the surface parameters, such as the local state distribution's dependency on morphology. Accurately resolving such effects requires a multi-scale simulation approach making use of several different modelling techniques. Also, while some effects are resolvable within one-dimensional geometries, most local properties vary in three dimensions and need to be modelled accordingly. As these local properties scale injection and transport rates exponentially, a linear model would thereby not create the three-dimensional "least path of resistance" through the material.

Given such requirements, the emphasis has been placed on elucidating the effect of theorized surface states (section 2.4.1) and measurable three-dimensional surface topography (section 2.4.3) on the injection process, as these factors combined are identified as key parameters in governing the initiation of breakdown in physical interfaces [61]. Thereby, the impact of local structural disorder (section 2.4.2) and the surface free energy (section 2.4.4), are considered of secondary importance.

2.4.1 Surface states and impurities

Localized states or traps, being allowed energy levels within the band gap of the insulator which charge carriers may occupy, are key for determining its electrical properties. Some states arise when non-ideal bonds (i.e. bonds other than *C-C* or *C-H*) are present in the material, which locally facilitate the trapping of a charge carrier. Others originate from disruptions in crystalline structure or the presence of nano-voids. On the polymer surface, additional surface-specific chain defects and other trap sites arise, referred to as surface states, which from their different origins can be categorized as [62]:

- **Intrinsic surface states** such as dangling bonds, dependent on polymer chain termination type at the surface (positioned strictly at the surface).
- **Metal-induced states**, dependent on electrode material (positioned at and close to the surface).
- **Bulk extrinsic states**, such as physical and chemical defects, present in the same concentration at the surface as in the material bulk (with constant density from the surface into the bulk of the material).
- **Surface specific extrinsic states**, such as additional surface originating physical and chemical defects (with a certain density and depth distribution from the surface).

When manufacturing cable terminations and joints with the methods discussed in this work, intrinsic surface states are generally unavoidable, as they originate from atomic bond disruption introduced in the necessary surface preparation stage of the cable end. When cutting a polymeric surface, radicals (also referred to as loose or dangling bonds) may be created through chain scission (i.e. $R\text{-}CH_2\text{-}CH_2*$ where R denotes the polymer chain and * the radical). The radicals can react to form carbonyl groups ($\text{-}CH_2\text{-}CH{=}O$) in (atmospheric) oxygen presence, but also alkynes ($\text{-}CH{=}CH_2$) or other functional groups may be formed. While such intrinsic surface states are created and strictly defined at the surface, a relocation of the radical along the chain could also locate them further into the material bulk. Such created functional groups are also obtained in polymer ageing, where instead a randomly spread of chain scission (initiated through thermal, electric or other processes) yields extrinsic states within the material bulk. The bulk and surface specific extrinsic states thus classify states created in additional to the unavoidable (intrinsic) ones. Such surface and bulk states can thus originate from oxidation and material ageing, but also from chemical impurities (i.e. PDP, antioxidants, catalysts, etc.). Such chemical impurities could be present in different concentrations at the interface compared to the material bulk. The energetic levels of traps (respectively from conduction or valence band edges) have been thoroughly studied in different types of molecular simulation [63]–[65], with results being in the range of 0.04-1.7 eV. Such results are dependent on calculation method and the surrounding polymeric structure [34]. Collectively, all states with their respective densities will form the density of states (DOS) within the band gap of the material, which is superimposed onto the existing band structures. The abrupt ending of the polymer's structure at the interface could skew the energetic levels further. Thereby a specific surface-DOS arises, originating from the local structural impact and additional states created in the surface preparation process.

Furthermore, tailor engineering of the surface-DOS is achievable through surface fluorination and possibly other methods. Fluorination may introduce a desirable state distribution through the introduction of Fluor atoms in the surface layer [66]. However, the surface layer's permittivity could be affected [66] yielding an impact on the image charge effect in carrier injection events. The local density of low molecular weight chemical impurities can also be altered by the preparation process through local introduction or outgassing of such species. Such impurities have been shown to migrate into insulation material from e.g. PET press films [67], resulting in leakage currents with non-monotonic temperature dependencies. Moreover, significant thermal ageing in the surface region could create an undesirable surface-DOS through surface oxidation. If deep traps are introduced in high density, sub-bands can be developed [34]. Thereby, inter deep trap transport (hopping) can become significant, and it may also facilitate the injection process, both of which may reduce the surface's breakdown strength [35].

Modifications of the surface-DOS between different preparation types might be difficult to confirm in electrical measurement, as surface roughness might more strongly govern interfacial performance. Also, accurately accounting for specific states, is extremely challenging as it requires that such states can be measured and modelled at the molecular level with the presence of the interface. However, an alternative (hopping) injection equation was formulized in the present study, accounting for the non-ideal nature of the injection barrier, with its parameters reflecting the surface-DOS.

2.4.1.1 Surface states in the injection process

In this section, the impact of surface states on Schottky and FN injection is addressed. Figure 14 shows a possible impact of surface states on Schottky injection. The state density's

distribution towards the surface is of importance, illustrated with a very narrow spread in Figure 14A, and wider distribution in Figure 14B.

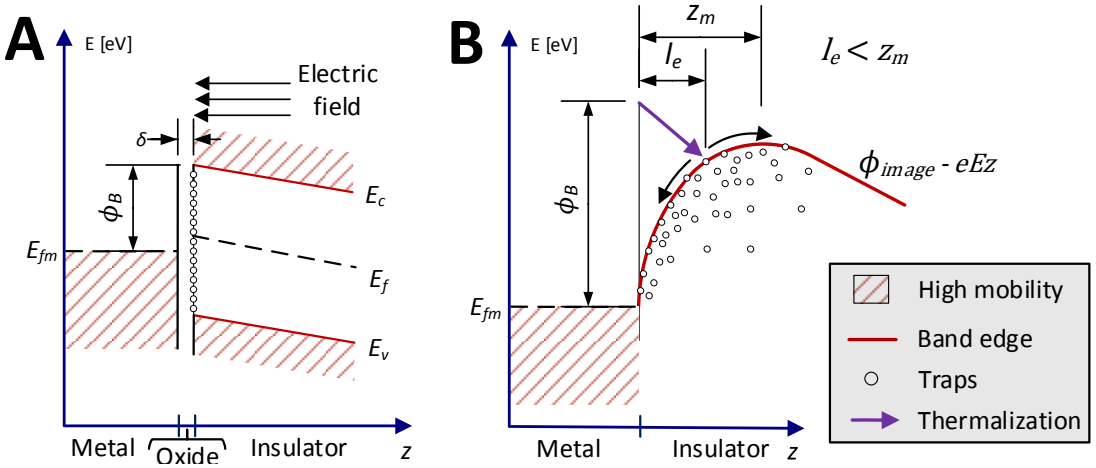

Figure 14. Schottky barrier with surface states and oxide/dipole layer of thickness δ (A) and impact of lattice collision and thermalization before reaching the potential maximum (B).

For certain semiconductors, an oxide or dipole layer with thickness δ measuring a few Ångström is usually assumed, separating surface states (originating from intrinsic surface states or metal induced states) from the electrode, as shown in Figure 14A. This separation causes the Fermi level to become "pinned" at the surface, eliminating the impact of the metal work function in such semiconductors [62]. This pinning effect was also modelled by Chen et al. [68], for metal – polyethylene interfaces, claiming that the interface dipole layer is responsible for the weak influence of metal work function on injected current density into polymers. Baldo and Forrest [60] also addressed the interface dipole effect, concluding it could lower the injection barrier as much as by 1 eV. Additionally, their approach regards the injection process as being dependent on local energetic disorder (morphology), governed by a hopping process out of interfacial molecular sites.

Another departure from the ideal Schottky barrier, considering scattering events in the injection process [69], [70], is shown in Figure 14B. Such events are probable when the electron's mean free path l_e (in the range of 1 nm in organic solids [69]) is shorter than the maximum barrier height position z_m. Thereby, scattering is likely to occur before the carrier reaches the conduction band, causing it to lose its speed (and thus energy) in the collision. This process is referred to as thermalization, as indicated by the arrow in Figure 14B. The thermalized electron must overcome the image charge potential, giving it certain probabilities for forward and backward diffusion. The impact of diffusion within the injection process will depend on electron mobility [71]. However, when surface states are introduced, they will be accessed by thermalized electrons, yielding a hopping process through the surface states in the image charge potential [72].

The dominating scenario for carrier injection is dependent on the impact of the image charge potential (and thus the electric field strength), and shape (depth) of the surface-DOS, thus governing whether a major energetic barrier exists in the bulk or not. Without a major energetic barrier to be initially overcome, a hopping process through the surface states could be dominating, as modelled by Taleb et al. [57] and Baldo et al. [60]. On the other hand, with a strong impact of the initial injection event, thermo-electrically stimulated processes in the electrode will likely dominate the injection process, as considered in the works of Arkhipov et al. [69], Blossey [70], Scott and Malliaras [72] and Conwell et al. [73]. The complex state

distribution towards the surface (created through intrinsic surface states, metal-induced states, bulk extrinsic states and surface-specific extrinsic states) must be known to derive a relevant expression of the injection current density. This region could span from 10 nm to some µm [57], while the maximal barrier position z_m (with relative permittivity of 2.3) is located at respectively 12.5, 4 and 1.2 nm for field levels of 1, 10 and 100 kV/mm. This makes predicting electrode-polyethylene barrier properties extremely challenging, as both lowering of the overall potential barrier, and a modification of its field dependency [74] could be relevant. For high electric field strength (exceeding 100 kV/mm), the trap dependent injection expression derived by Arkhipov et al. [69] predicts very similar current densities to the equation derived by Fowler and Nordheim [55], which shows the validity of using equation (41) for predicting high field behavior in the charge injection process.

2.4.1.2 Dominating charge injection mechanisms

Schottky and FN injection models could still have a certain degree of validity in that they constitute the rate-determining part of the injection process respectively at low and high electric field strength, as shown in Figure 15A, with most of the surface specific states located within a narrow region, spanning a few nanometers from the surface. However, at intermediate field strength and with surface-specific states located within a wider region beyond several tens of nanometers from the surface, subsequent inter-state hopping could be the dominating process, as illustrated in Figure 15B.

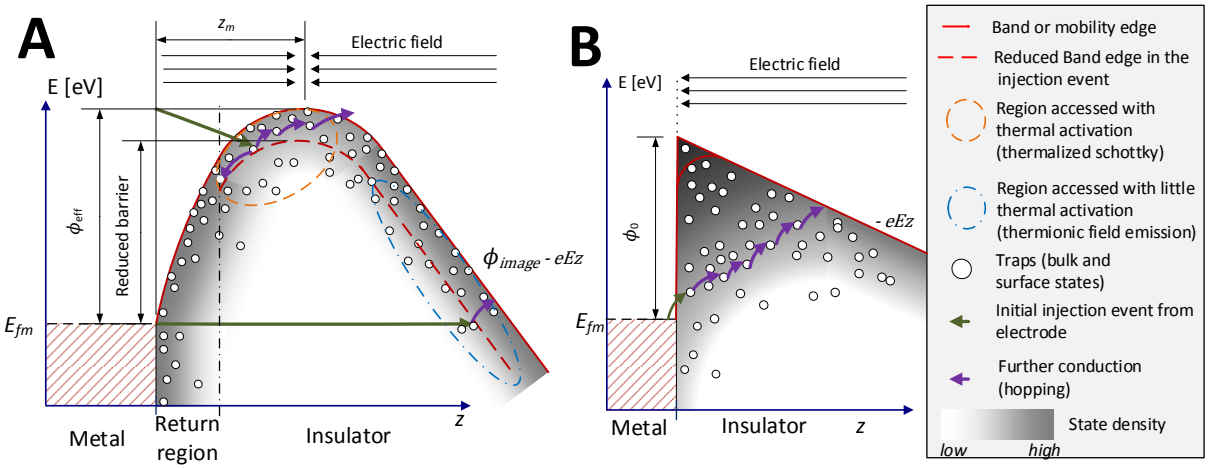

Figure 15. Lowered potential barrier due to the surface-DOS, when considering a major energetic barrier at the surface (A). Subsequent hopping through interfacial states (B).

As depicted in Figure 15, the dominating, rate-determining part in the injection process, depends on applied field strength and width of the surface specific DOS region, thus:

- At low (enough) field strength, not only intrinsic and metal-induced states but also a narrow region of surface-specific extrinsic states will be located within the indicated return region. Hereby, Schottky injection with reduced barrier height (from bulk extrinsic states) could dominate the injection process.
- At medium field strength and with a wider region of surface-specific extrinsic states, they will be positioned beyond z_m, so that an inter-state hopping process [57] dominates the injection process.
- At high field strength, FN injection can supply excess amounts of carriers to extrinsic bulk states, with weak thermal dependency.

Thus, three injection mechanisms are especially interesting to investigate further. Schottky and FN injection, respectively defined in equation (38) and (41), can be used with their theoretical barrier values (ϕ_B, ϕ_{FN}) lowered by ~0.7-0.9 eV owing to the state depth they access, and possibly some additional amount due to an interface dipole effect and impact of energetic disorder in the surface region [60]. For hopping injection, the barrier is overcome in subsequent hops, decoupling the theoretical barrier height value from its equation.

2.4.2 Surface morphology

The semi-crystalline material structure and the size distribution of lamellae, previously addressed in section 2.1.1, will be specific to the material sample and is impacted by its specific properties (e.g. chain configuration, crosslinking, etc.) and its processing (e.g. thermal history, processing method, etc.). Chain conformation, being highly entangled in amorphous regions or ordered in crystalline regions, can have a significant impact on dielectric properties. Different DOS and conduction properties have been derived for amorphous and lamellar crystalline phases [6]. This semi-crystalline structure will feature a localized impact on both the injection barrier height [24] and the local transport capabilities of the injected charges, as the free volume in the material will strongly affect the location of excess electrons [25]. Chain conformation variations can furthermore impact the conduction band edge's energetic level and introduce shallow traps close to the band edge [26]. In the amorphous phase, the conduction band edge can be around 1 eV lower than in crystalline polymer regions, which has a significant impact on local conduction processes. An amorphous/crystalline barrier can prevent significant electron transport within the crystalline phase of the material. The cross-links introduced in XLPE have been determined to affect the DOS weakly [26], thus similar characteristics between LDPE and XLPE are achievable with low PDP content (by thorough degassing) and similar morphologies (which may be unachievable due to the impact of cross-links on crystalline regions [12]).

Conclusively, electrons are favorably transferred through the material's free volume, while holes mainly transfer along the chains in the crystalline regions. This effect, along with the individual states in the material (with their levels skewed by surrounding polymer structure) forms the DOS in the bulk of the material. Additionally, the impact of the abrupt ending of the material, impacted by the surface preparation process, must be regarded as shown in Figure 16.

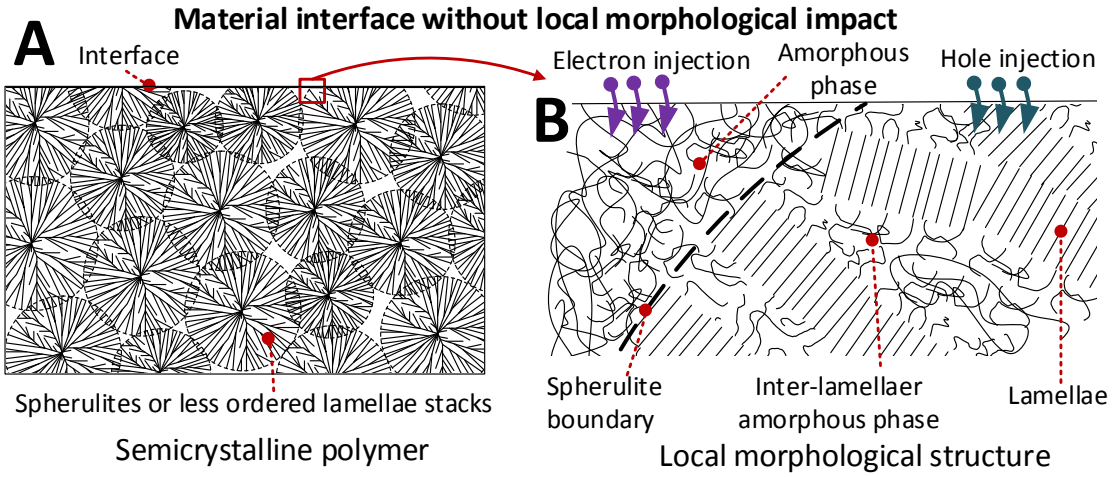

Figure 16. Surface crystalline structures when a neat polymer material is cut, assuming no impact from the cutting on the local morphology. With appearance in the mesoscale (A), and local appearance in the molecular scale (B). Electron injection is favorable into the amorphous phase while hole injection is more favorable into crystalline regions.

While the structural description in Figure 16 is true the moment the surface is created, it is likely to evolve over time to reduce the free energy in the system. Thus, processes such as chain reptation in the amorphous phase [11], could slowly re-arrange the position of surface states. Also, when remolding or applying surface heating, melting the crystalline phase, a faster re-arrangement occurs. However, the present crosslinks might hinder such re-arrangement to some degree. The intrinsic and extrinsic surface states in the near vicinity of the surface could thus migrate further into the bulk, making for a surface-DOS with a certain spatial dependency. This surface-DOS can evolve further over time after finalizing the surface's preparation, making it extremely difficult to predict with accuracy. The local morphology towards the interface can also be strongly affected when a surface epitaxial layer develops [26, 27]. It was shown to strongly impact charge injection, indicating that an accurate representation of mesoscopic polymer structure towards the interface, would aid in better describing the injection process. The surface region's morphology can thus be affected by the preparation method [24], which as indicated in Figure 16B could influence individually hole and electron injection processes.

Additionally, dissolved chemical residues as well as oxidation will be primarily localized in the amorphous phase. This results in a non-homogenous distribution of charge traps in the material. A representation of crystalline microstructure can be modelled by using the degree of crystallinity as a parameter that locally dictates injection, transport and further properties at certain spatial positions, as previously achieved for a mesoscopic two-dimensional domain by Guffond et al. [75], [76]. Also, the impact of PDP localized in the amorphous phase was addressed in this approach. Thereby, the same model was capable to match measurements on polymers with vastly different degrees of crystallinity.

Proper assessment and modelling of localized interfacial morphology is thus a requirement for accurately describing the impact of impurities and states on charge injection and transport in the bipolar charge transport model. Also, as charge transport and other effects in the model rely on average state separations in each resolved domain section (mesh cell), the structure illustrated in Figure 16B cannot be addressed. Resolving the structure in Figure 16A is achievable assuming a certain distribution of crystallinity among the spatial coordinates in two to three spatial dimensions, as addressed by Guffond et al. [75], [76]. However, this either forces control over the model's spatial meshing or implementation of a high-resolution mesh with mesh-dependent model parameters. Therefore, it cannot be accurately superimposed with irregular electrode geometry, where meshing is governed by the surface coordinates. The focus in this work therefore remains on surface roughness, considering the crystallinity to be uniformly distributed amongst the spatial coordinates in the simulations. The material's morphology is still accounted for by individually defining the rates and balancing parameter values for electrons and holes, indicated with their respective subscripts *(e,h)*.

2.4.3 Surface roughness

Surface roughness defines the geometrical shape of the interface, which can evoke a multitude of dielectric phenomena and have a strong impact on the interface's electrical performance. However, the geometrical magnitude and repetition rate of this topography is of importance, as it can range from near-atomic dimensions up to tens of micrometers. As illustrated in Figure 17, the three different geometric ranges; the atomic scale, the mesoscale and the macroscale [25] are thus of importance for surface roughness.

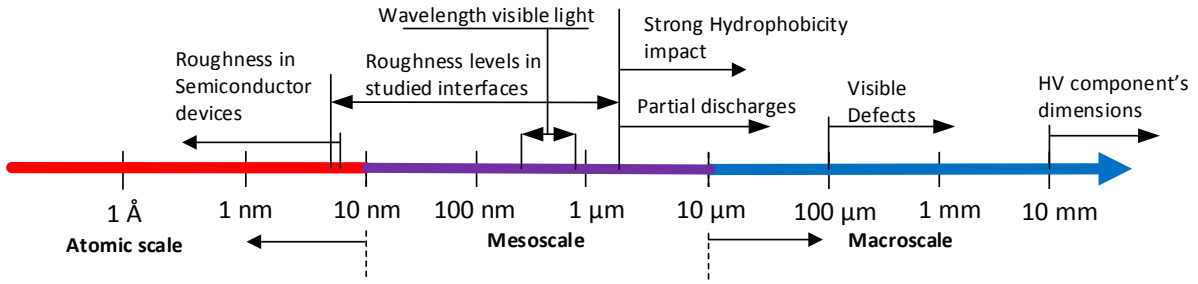

Figure 17. Logarithmic geometric scale of roughness in the studied surfaces and other applications, and certain roughness or geometry originating effects. Hydrophobicity is addressed in the next section.

As seen in Figure 17, the geometrical scale of roughness can determine the relevance of a certain phenomenon. The presence of partial discharges (PD) in the void areas created upon mating a rough surface is reported to act as main initiator of an electrical breakdown process in cable joints and terminations [23], [77], [78]. However, the inception voltage of such discharges is known to depend strongly on the void's sizes. The AC inception field can be estimated given known material parameters in the voids and the material bulk (e.g. relative permittivity of 1 and 2.3, respectively), and considering the well-defined Paschen's law for breakdown in air. For a normal gaseous spherical void, it is around 19 kV/mm for a 7 µm void, while for a 2 µm void the inception field strength is around 150 kV/mm [79]. Thereby, given that the roughness levels of the studied interface types are even lower, PD activities can be considered as irrelevant, as depicted in Figure 17.

A lot of the physiological understanding of charge dynamics in solid materials comes from research related to semiconductor devices [33], which later have been adapted to explain phenomena in HV devices. However, the levels of surface roughness in semiconductor devices, are most often far lower than for HV cable applications, in the atomic scale [80]. The impact of roughness is therefore generally less studied for semiconductor devices, probably in part because it is possible to create nearly atomically smooth surfaces on such devices. Such smoothness, however, hinges on intricate manufacturing (polishing) methods and is aided by the hardness of the base material. The impact of mesoscopic roughness levels on electrical properties in applications is therefore not covered within the scope of traditional semiconductor physics.

2.4.3.1 Surface roughness measurement

Relevant observation and measurement techniques also differ depending on the geometric size. For characterizing 3D surface topography, atomic force microscopy (AFM) is well suited all the way down to atomic levels of roughness [21], however, its high resolution comes at the cost of not being able to time-efficiently scan a larger mesoscopic surface region. Therefore, in the mesoscopic range relevant for the studied surface types, optical profilometry is typically better suited. In the macroscale, laser scanning techniques can be easily adopted and are frequently used. All three techniques are thus capable of acquiring surface coordinate planes, $Z(x,y)$, with different scan rates (m^2/s) and resolutions. From the acquired surface's coordinates, a variety of roughness parameters can be estimated. It is also possible to use such coordinates directly in calculations [81], [82], though requires some data processing to avoid artifacts. Without such techniques, a quick estimation of mesoscopic roughness levels can still be made by assessing the surface's gloss level. Given the wavelength of visible light shown in Figure 17, matte, opaque surfaces can indicate mesoscopic surface texture present, whereas a mirror-finish indicates no such texture being present.

2.4.3.2 Geometrical electric field distribution

Since the electric field is always oriented in the normal direction from the electrode interface, the incline of a local surface section (e.g. $\partial Z(x,y)/\partial x$) distort the local electric field. Thereby, roughness manifests itself as a local redistribution of the average bulk field at the insulator surface, locally enhancing or reducing the electric field strength due to the introduced micro-scale geometrical heterogeneities [83]–[85]. For Laplacian fields (e.g. solving Laplace's equation assuming spatially uniform material parameters in the domain) the distribution of field can be simplified using field enhancement factors (FEF), defined at the surface as:

$$FEF(x,y) = \frac{E_{local}(x,y)}{E_{applied}} \tag{16}$$

where $E_{local}(x,y)$ is the field strength in V/m at a local (x,y) coordinate positioned on the surface, and $E_{applied}$ is the applied macroscopic field to the interface in V/m when surface roughness is neglected. Thereby, when $FEF(x,y)$ is estimated for a certain surface type, it can be used to calculate the local field strengths for any applied voltage regardless of the insulator's conductive properties. Also, since the electric field is only redistributing itself along the surface, the mean value of $FEF(x,y)$ should be unity, such that the surface average of the local fields equals the globally applied electric field in equation (16). Such re-arrangement forms the FEF distribution, providing a statistical overview over local reduction ($FEF < 1$) and increase ($FEF > 1$) of the Laplacian electric field at the surface, as highlighted in Figure 18.

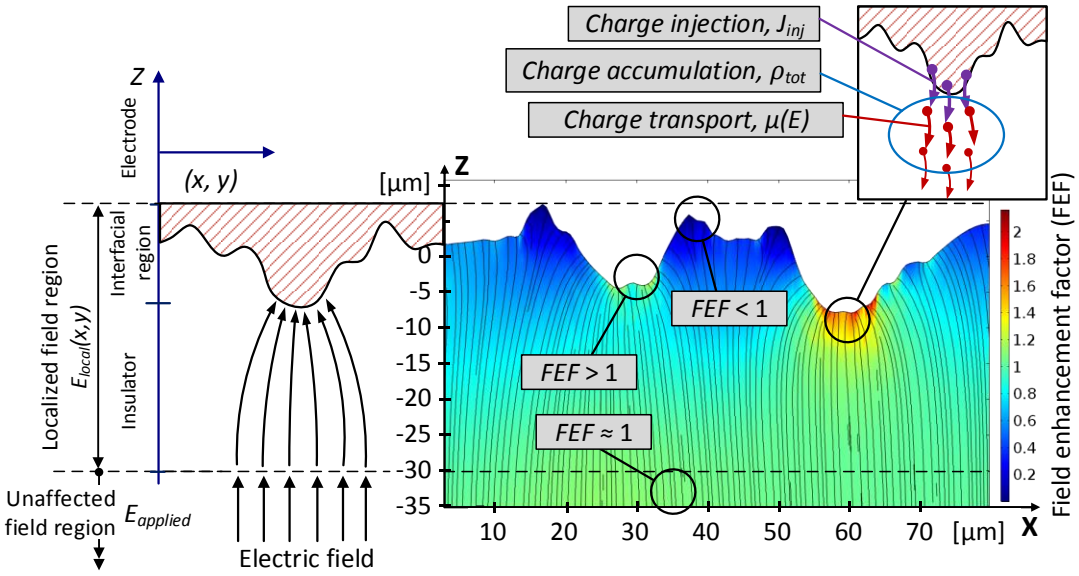

Figure 18. Local redistribution of electric field strength and orientation towards an irregular surface, obtained through Laplacian field simulation on an abraded surface. Further notations of local fields and conduction processes are made in the insets.

However, as indicated in Figure 18, several processes are occurring in the material bulk adjacent to the rough asperities, that give rise to spatially non-inform material conduction properties, owing to their dependency on electric field strength in the interfacial domain. Thereby, the accurate and straight-forward Laplacian field assessment needs to be re-evaluated. As field-dependent conduction mechanisms feature a weak or strong field dependency at respectively low or high field strengths, this dependency's magnitude governs the amount of charge density accumulated in the charge transport gradient. Thereby, the Poisson fields now yield a field-dependent FEF distribution (i.e. $FEF(x,y,E_{applied})$) which is governed by the material's specific conduction properties.

However, due to the conductivity's weak field dependency at low (enough) applied field strengths, simplification of such distributions to the Laplacian case will still be accurate (i.e. when $E_{applied}$ is low: $FEF(x,y,E_{applied}) \rightarrow FEF(x,y)$).

2.4.3.3 Charge transport and injection localization

The complexity thus arises when considering space charge-controlled fields, and assumptions are needed regarding which types of bipolar charge injection and transport mechanisms (indicated in Figure 18) must be accounted for in simulations. As such mechanisms require a large set of well-calibrated parameters for accurate results, it is beneficial to simplify charge transport in the interfacial domain. One approach is to make use of a Laplacian FEF distribution and to calculate the local and average charge injection currents. The average injection current (J_{avg}) can be adopted in a one-dimensional bipolar charge simulation [81], [82]. A more refined approach could, by making use of macroscopic bulk conductivity data, estimate a predefined Poisson FEF distribution. Again, charge injection is affected of which the average injection rate (J_{avg}) can be adopted in a one-dimensional bipolar charge simulation. Given spatially zero-dimensional data obtained with conductivity or surface potential decay measurements or one-dimensional measurement data obtained in pulsed-electro-acoustic measurements, the one-dimensional simulation approaches above need to be evaluated first over a wide range of applied electric field strength. Thereafter, a full simulation of the interfacial domain, accounting for all conduction effects in a two- or three-dimensional bipolar charge transport model, can be realized [86]. It is for this reason that such multi-dimensional simulations are only seldomly encountered in literature, with a few exceptions [75], [86].

While the assessment of local fields, the averaging of local injection currents and introduction of roughness dependent β-parameters (which scale the field dependency in the injection equation) in injection was already considered almost 100 years ago [54], today's computing power and finite element methods (FEM) allow for a more accurate assessment than what was possible at that time. The above-outlined approach was also adopted by Taleb et al. [81] in an artificial two-dimensional domain, showing a higher Schottky injection current density for a rough interface compared to a smooth interface. The same approach also estimated an enhanced FN injection rate for rough electrodes in the works of Novikov [82]. Additionally, Koeningsfeld et al. [87] showed through measurements that surface roughness had a significant impact on FN injection from a polycrystalline diamond surface. Tunneling into vacuum can be experimentally observable at electric field strengths as low as 100 kV/mm with already moderate levels of surface roughness [24]. A clear impact of surface roughness on the field dependency of FN injection into vacuum has thus been discovered [87], [88]. Furthermore, a strong correlation between roughness and breakdown strength has been identified for air-insulated systems [89].

2.4.4 Surface free energy

The surface free energy (SFE) describes the excess energy of a surface in relation to the material bulk. SFE thus arises from the sum of the intermolecular forces at the interface (e.g. van der Waals, hydrogen bonding and dipole-dipole interactions). Thereby, it quantifies the work (W) spent in bond disruption during the surface's preparation (e.g. cutting, abrasion). It correlates with the surface's work function [90], [91], but is most frequently used for predicting solid-liquid interactions. SFE is, however, not responsible for direct causation of most electrical phenomena in solid-solid interfaces, it instead being a surface parameter that is in correlation with certain parameters (e.g. work function, non-ideal bonds present, etc.). Therefore, while SFE assessments were carried out, it may not be possible to translate them into parameters that correlate with observed effects of charge carrier dynamics.

2.5 Ageing, degradation and breakdown mechanisms

As the electrical lifetime and failure prevention in the cable system is of utmost importance, relevant ageing, degradation and breakdown mechanisms must be addressed, as described in detail by Dissado and Fothergill [34]. By identifying levels of charge density, current density, field strength and recombination rates that might initiate such electrical mechanisms, their onset can be predicted from quantities estimated in simulation. Thereby, surface-induced breakdowns found at certain field strengths in experiments can be better explained.

Hot electrons will be encountered if the carrier's velocity exceeds levels required for impact ionization. Thus, drift velocity values defined with equation (4) could be used to anticipate ageing in the material. However, non-uniform spatial distributions of the DOS and other randomly distributed properties could make this anticipation challenging. Furthermore, a certain probability is involved in the relation between maximal velocity and drift velocity of hot carriers. Measurements of electroluminescence have detected radiation related to hot electrons upon transient voltage application [39], [40], [48], which disappeared upon stabilization. In polyethylene samples, field levels as low as 40 kV/mm and 80 kV/mm for voltage application and 50 kV/mm for grounding have shown such electroluminescence [39].

Space charge limited current (SCLC) identifies three distinct regions; the ohmic, the trap-limited and the trap free region. With increased carrier density, states are increasingly occupied and eventually, when all (deep) energetic states are filled, additionally added carriers may transport unrestrictedly. Thereby current density increases significantly giving rise to the trap free transport region. However, such distinct SCLC regions are practically unobservable, due to a spread in the trap's energy levels and the field-dependent effects in detrapping, transport and injection. For example, an extended SCLC model with a single trap level and Poole-Frenkel effect, yielded a field dependency in the carrier ratio, thus showing a modified transition [92].

Realistic SCLC thus predicts an increase in current density when the DOS is gradually filled upon increased carrier density, from the bottom up to the energy level Δf [53], [93], [94]. Such an increased current density also reflects higher mobility of the carriers, which could create an earlier onset of ionizing lattice collisions. The presence of local charge concentrations exceeding a certain trap concentration, in conjunction with certain field strength could thus be harmful to the material. The challenge is that such an ageing onset is localized in certain material regions, where either local field and/or charge quantities are higher (e.g. near the asperities in rough interfacial geometry), or where the local DOS is favorable for higher transport rates. Furthermore, a high charge density region could also trigger the propagation of a charge packet, created when the space charge cloud moves enhanced by its own electric field, charge density, and diffusion. The fluctuating external current density generated by such packets has been correlated to electroluminescence fluctuations at 150 kV/mm [39].

The high-energy electrons previously described can also trigger electron avalanches when additional carriers are generated through collision with trapped or bound electrons. Under high enough field strength, such generated carriers will also reach critical velocity, thus producing additional carriers ultimately generating an avalanche mechanism. While this mechanism is challenging to apply to the bipolar charge model, it postulates that an additional critical energy level sufficient for internal carrier generation rather than permanent bond disruption may exist.

At slow ageing rates, the previously addressed hot electron and recombination mechanisms may gradually age a specific material region (e.g. near a rough asperity), until the first void is formed

allowing for electrical tree growth to ensue [95]. In well degassed HVDC systems, the shielding of enhanced field regions through homocharge accumulation is key for increasing the tree initiation voltage. The disappearance of electroluminescence after stabilization could indicate homocharge shielding at the interface [39], [40], [48]. For single large defects, a wide material region is available below it for shielding [86]. However, in roughness asperities are repeated at short intervals, such that less area is available below the asperity for homocharge shielding. Such repetition either forces a stronger charge accumulation in the bulk or results in higher field strength at the asperities. It is this key difference that can deduce information about the underlying phenomenon given that respective breakdown strengths are known. Furthermore, a high charge density layer may discharge itself towards a grounded point or initiated tree, giving rise to Lichtenberg patterns consisting of additional discharge traces.

2.6 Cable system adaptations for measurement and simulation

The simulation and measurement results encountered in literature, have considered certain simplifications of the actual application. Thus, to accurately study certain behavioral effects of the HVDC cable or its accessories in measurement or simulation, certain adaptations are required as shown in Figure 19.

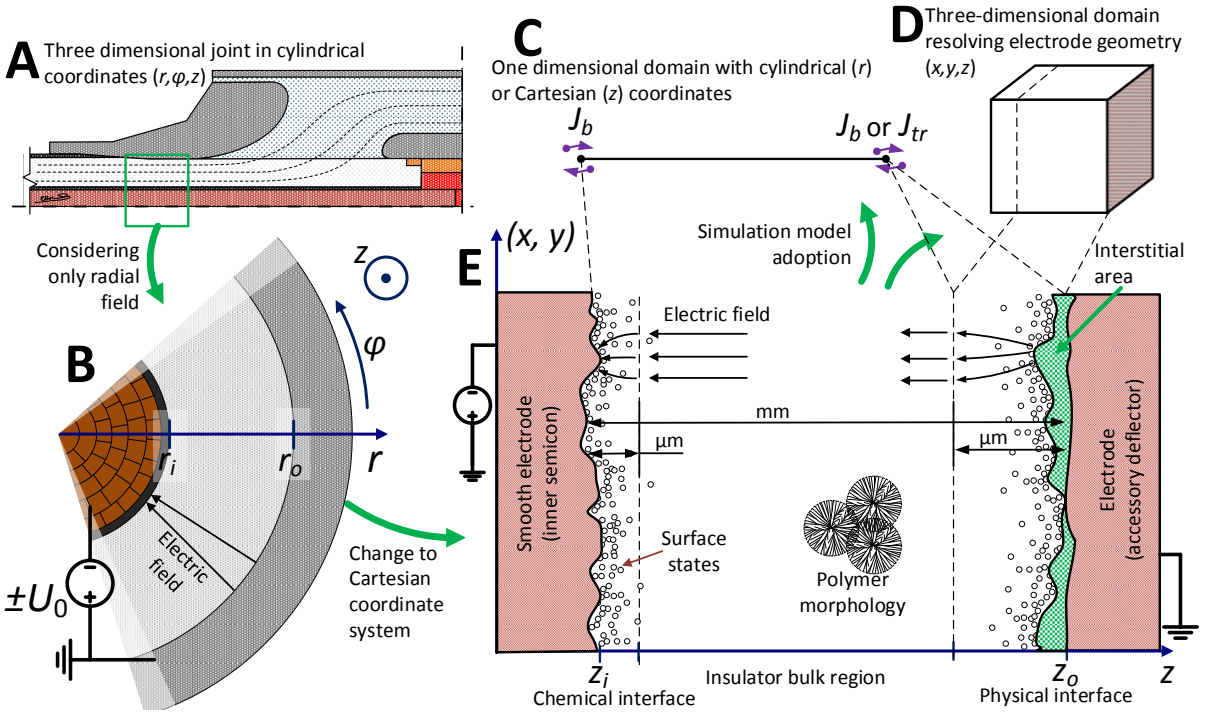

Figure 19. Adaptations and simplifications of the HV cable application (A) by: considering only the radial field (B), measurement adaptation to cable-peeling geometry (E) with smaller thickness (e.g. $(z_0 - z_i) << (r_0 - r_i)$). Simulations can be performed in a one-dimensional model (C) with boundary current densities J_b, or a local 3D interfacial model (D), or a combination of (C) and (D) linking the domains by boundary conditions (e.g. J_{tr} indicates exchange current between the two domains).

As shown in Figure 19, frequently used adaptations of the cylindrical (r,φ,z) HVDC cable system are:

- Cable calculations, neglecting parameter variations in φ- or z- orientations, thus only considering radial fields (Figure 19B), using the macroscopic conductivity σ in equation (55) and its field and temperature dependencies, with or without thermal gradients.

- Studying conduction on plate samples, or cable peelings cut out from the application (Figure 19E), represented in Cartesian coordinates (x,y,z). The radial divergence is thereby neglected. This simplification is common for leakage current measurements, deducing the conductivity σ, used in the cable calculation.
- Furthermore, changing the electrode types (Figure 19E) to sputtered insulator surfaces or metallic contact (with interstitial layers of oil, grease, etc.) is common, which can influence the injection process [81].
- Considering the interstitial area (Figure 19E) as part of the electrode assumes the injection barrier to exist in the insulator near the interface. MWS interfacial polarization is negligible when the field strength in the interstitial layer is low (e.g. $E_{layer} << E_{ins}$ valid in steady-state for $\sigma_{ins} \approx 10^{-15}$-$10^{-18}$ S/m << $\sigma_{oil} \approx 10^{-12}$ S/m).
- Neglecting the surface state distribution (Figure 19E), assuming the boundary current (J_b, equation (49)) to be represented by Schottky injection with a ~1.2 eV barrier. The state distribution can be included when using a hopping injection mechanism [31], [57].
- Considering the non-uniform distribution of crystallinity (Figure 19E), and its additional impact on state and impurity distributions, as uniformly distributed among simulation coordinates. This simplification is common as resolving it requires at least two dimensions to form the "least path of resistance" in the material [75].
- Neglecting PDP and other ionizable chemical species in conduction. While several one-dimensional simulations have included such impurities [44], [96], it brings additional complexity. Neglecting it and calibrating a model against thoroughly degassed XLPE or LDPE may therefore be preferable.
- Neglecting surface roughness (Figure 19E), thus the electrode's geometry influencing the electric field distribution in a microscale region, significantly smaller than the insulation thickness (which typically is 0.1-1 mm in plates/peelings and 10-30 mm in the cable application).

The above-listed adaptations are key for most bipolar charge transport models found in literature, which simulate space charge evolution in a Cartesian one-dimensional model (Figure 19C), or a cylindrical (cable) model [27]. Simulation of small two- or three-dimensional domains (Figure 19D) are encountered seldomly, resolving a needle tip [86], electrode geometry [81], [82], or morphology [75]. However, such simulations struggle to resolve the full cable insulation cross-section, as the spatial resolution (required for resolving the local effects) is many orders of magnitude smaller. Thus, if boundary current densities (J_{tr} in Figure 19C) and electrostatic potentials can be matched between a one and a multi-dimensional domain (e.g. linking the domains in Figure 19C with Figure 19D), it allows for resolving an effect (e.g. roughness, crystallinity, nanoparticles, etc.) with correct interface-bulk ratio. Furthermore, this could better anticipate the local quantities present that might trigger ageing, degradation and breakdown mechanisms previously outlined.

An all-encompassing representation of the HVDC cable accessory performing neither of the listed adaptations is thus impossible, given the multitude of possible effects and combinations thereof. Also, the many orders of spatial magnitude between the mesoscopic effects to be resolved and components macroscopic outer dimensions previously depicted in Figure 9 hinders this adoption. Therefore, the methodology is designed to represent only the dominating effect in the physical interface; surface roughness. Most of the other adaptations listed previously are thus applied.

Chapter 3

Experimental methodology

This chapter introduces the experimental procedures used in the thesis work, describing first the manufacturing method of the cable peeling samples. This is followed by the carried out physical and chemical characterizations performed on small cable peelings sections. They are made with different preparation methods and introduce identical surface characteristics to the surface within an industrialized cable accessory. It ends with a description of the performed electrical characterizations, being space charge measurements and DC breakdown tests. While space charge measurements were carried out on cable peelings, the DC breakdown tests were performed on both cable peelings and medium voltage (MV) sized DC cables.

3.1 Sample manufacturing

All samples were extracted from full-scale HVDC cables, with specific DC grade XLPE as insulation material [9]. The cable was priory degassed and screened for defects according to normal industrial procedures. Sample extraction commenced by taking a section (2-5 meters) of cable and exposing it layer by layer down to the outer semiconductor. Thereafter, the outer semiconductor was removed, exposing the insulation and was finally followed by various surface treatments. This final step is collectively referred to as surface preparation, and methods such as abrasion, cutting or remolding were employed within this work. The surface preparation step also included surface cleaning which eliminated most of the small particle contamination. These were all industrialized procedures, making them capable of on-site accessory installation, and no special adaptations were required to prepare the samples evaluated within the study. After preparing the insulation's surface, cable peelings were cut from the surface layer of the insulation using a specially designed rotational cutting tool, as shown in Figure 20.

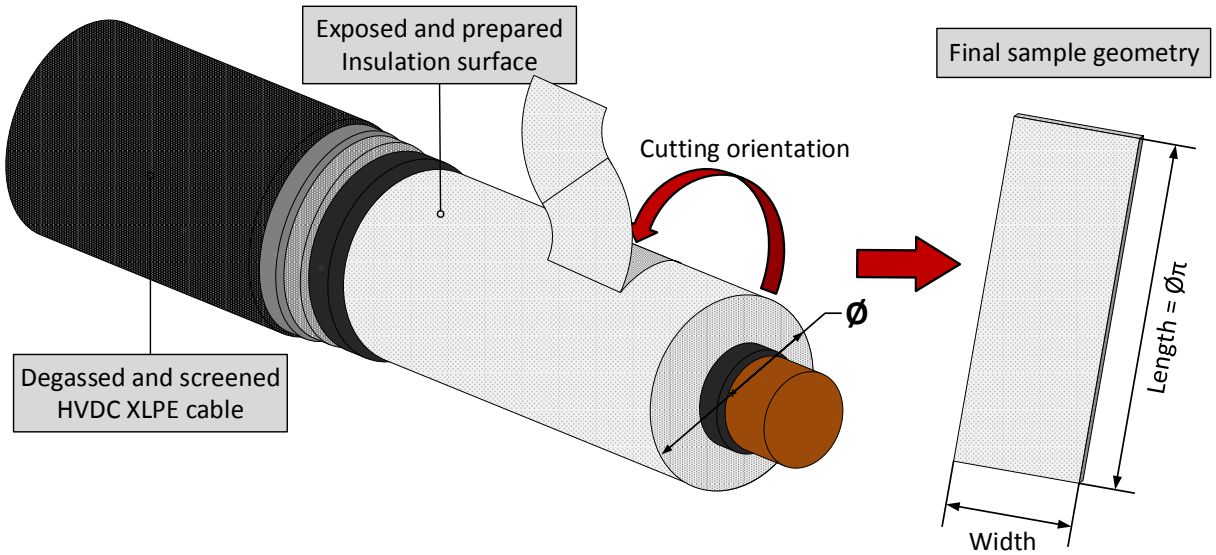

Figure 20. The manufacturing process of a cable peeling.

The cleaning procedure consisted of wiping the surface with 100 % polypropylene wipes and technical alcohol. It was performed with the utmost care not to scratch the surface during the

process. After manufacturing, the cable peelings were stored in an incubator at around 10 % RH, eliminating the influence of moisture on the measured properties and allowing additional outgassing of crosslinking by-products to occur.

The cable peelings were within the following dimensions:

- Width: 30-100 mm, depending on the selected knife's width.
- Length: around 300 mm, depending on cable circumference.
- Thickness: 100-1000 µm, depending on the selected radial knife position.

Since only the surface layer was extracted and the peeling tool required manual operation, coping with non-ideal cable dimensions such as ovality and lack of straightness where major challenges. Such deviations affected the thickness and its variation within each cable peeling. Due to such thickness variations, many electrical tests were adapted to make sure that this variation was accounted for. Accurate thickness measurements were always performed after electrical testing, as this assessment easily scratches and affects the surface structure of the sample.

The peeling process (shown in Figure 20) also introduces a new surface type, referred to as "backside" in this thesis. Its surface structure originates from the circumferential cut made by the cable peeling tool. The backside surface type is thus not made by a preparation method and it cannot be found and replicated in real accessories. Also, each cable peeling made has this surface type on its posterior (unless stated otherwise). In some cases, samples with backside surface types on both faces were utilized, referred to as backside samples. In such specific cases, the peeling tool was turned a few additional rotations, extracting such peelings from just below the surface. Dissado et al. [97] identified roughness variations and impact of sample orientation in similar peelings, however, no such discrepancies between the peeling's front and back faces were found in the present study. Therefore, the backside samples can be regarded as the reference, and are characterized by low roughness levels and low thickness variations.

While using cable peelings in electrical testing is not a novelty (others [97]–[100] have also made use of such samples), the present work stands out concerning the procedure for sample preparation. On one side, relatively small peelings can be made by microtomation [99]. This method benefits of accurate control over sample dimensions and thickness, with the drawback of not extracting it from a consistent circumferential layer in the cable. On the other side, larger peelings can be machined in a lathe. This method may, however, struggle to machine samples thinner than 1 mm. The present peeling method makes use of a dedicated manually operated tool with a wide blade, extracting the peeling in a single rotation. It suffers from neither of the limitations mentioned above. It is also capable of extracting the surface layer from the cable end (containing the priory made surface preparation), even with minor ovality present.

The DC breakdown tests performed on medium voltage cables utilized the same types of surface preparation. Minor changes were made to the preparation methods due to the cable's smaller diameter, but overall manufacturing methods and principles remained the same.

3.2 Physical and chemical surface characterization

3.2.1 SEM

For observations made in scanning electron microscopy (SEM), one minute of gold sputtering was applied to the sample surface, using an S150b Edwards sputter coater. The SEM observations were performed by detecting secondary electrons (SE) using an FEI/Philips electron microscope. The electron beam was energized with 3 kV and observations were made at various magnifications.

3.2.2 Optical profilometry

The surface's texture and topography with height variations in the range of 0.01-10 µm, was assessed on all surface types by means of optical profilometry. The surfaces were first sputter-coated with gold for 3 minutes to improve their reflective capability. Sputtering was necessary as the opaque white appearance of some surfaces needed to be enhanced, as optical profilometers have difficulty capturing light reflected off highly angled parts. Sputtering thus increased the fraction of valid data points (e.g. reducing points with not a number (*NaN)* values) obtained in the scan. Thereafter, a Wyko RST plus interferometer was used using white light interferometry. It projects interference fringes across the surface, which's shape projections allow for deducing the surface coordinates in a 612 by 459 µm domain. Each such coordinate corresponds to 3.2 μm^2 of surface area on the sample. The obtained data points, (a 3D plane with *x, y* and *z* coordinates) were post-processed, where any *NaN*-points were replaced with interpolated values. Furthermore, global profiles such as tilt or major sample curvatures where removed. This post-processing fitted and removed the coordinates of a 3rd polynomial plane from the data. The use of higher-order polynomial planes was also investigated but yielded no further improvement. An example of an extracted surface profile is shown in Figure 21.

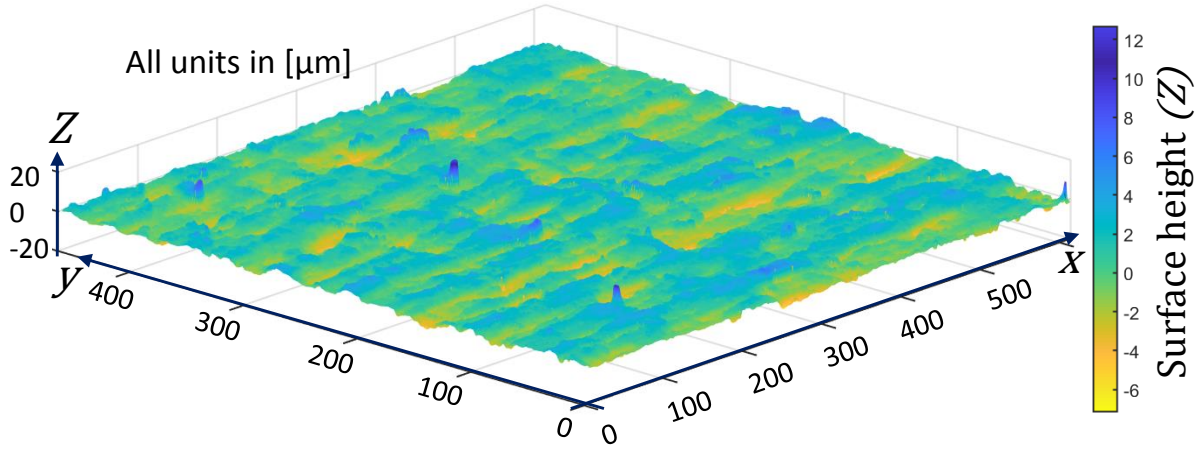

Figure 21. Example of an extracted surface profile, here shown for an abraded surface with (x,y,z) coordinates. The light-yellow regions in the colormap indicate the asperities.

The surface profiles shown in Figure 21 allowed for determining its three-dimensional roughness parameters, as defined in the next section. The characteristic or "global" parameters for each type of surface preparation were estimated from the average of 5 measurements. Representative smaller regions found within the measured surface profiles were also selected, their texture and surface parameters were compared to the global parameters, ensuring similar features. Such sections were after further data processing directly used in the different simulation approaches.

3.2.2.1 Surface roughness parameters

Features in the surface texture can be quantified using roughness parameters, which represent features in a certain measurement domain with a single parameter value, thus facilitating direct comparisons of certain surface types. The average roughness (or arithmetical mean height variation) of a certain 3D surface is quantified through *Sa*, expressed as:

$$Sa = \iint_a |Z(x,y)| dxdy \tag{17}$$

where *Z(x,y)* represents a matrix of 3D coordinates on the surface, with *Z* expressing the local distance from the mean plane in m. Another relevant parameter, the root mean square (RMS) roughness *Sq*, is expressed as:

$$Sq = \sqrt{\iint_a (Z(x,y))^2 dxdy} \tag{18}$$

Sa and *Sq* parameters, in m, are useful for comparing the height in the surface texture. However, two surface types having identical *Sa* and *Sq* parameter values can have vastly different textures, as the texture's spacing can be present with different widths. Therefore, a third parameter, the unitless RMS surface slope *Sdq*, is introduced as:

$$Sdq = \sqrt{\frac{1}{A}\int_0^{Lx}\int_0^{Ly} \left(\frac{\partial Z(x,y)}{\partial x}\right)^2 + \left(\frac{\partial Z(x,y)}{\partial y}\right)^2 dxdy} \tag{19}$$

where *A* is the area of the measurement domain in m^2, *Lx* and *Ly* are respectively the *x* and *y* length of the investigated domain in m. The *Sdq* parameter thus quantifies the steepness in the surface texture (i.e. with *Sdq* = 0 for a fully flat surface and *Sdq* = 1 for all gradient components at 45° incline) and is sensitive to both the amplitude and spacing in the surface texture. By using both *Sa* and *Sdq* parameters in surface type comparisons, a texture sensitive analysis is made covering most surface types. A wide range of additional surface parameters exists, including *Si* parameter, measuring the repetition rate of texture (as previously shown in Figure 9), and *Sdr* parameter which quantifies the developed interfacial area ratio. The latter represents the relative percentage increase of surface area calculated from the ratio between the "real" irregular surface area and the *x-y* domain size it spans.

3.2.3 HPLC measurements

High-performance liquid chromatography (HPLC) was performed on peelings and full sections of cable. In this method, polymer samples are dissolved into a mixture, which is subsequently pressurized, and forced through a column. In chromatography, different molecules exhibit different flow rates through the column, allowing for their timewise separation and individual identification at the column's end [11]. HPLC thereby allows for the identification of different chemical substances within the polymer (i.e. PDP, antioxidants, etc.). The used equipment was an HPLC system with a UV detector (Agilent 1260 HPLC). The polymer samples were taken at different radial positions in an HVDC cable with different surface preparations applied to it. Such measurements were also performed on cable peelings before and after storage in the incubator.

3.2.4 FTIR-ATR measurements

Fourier transform infrared spectroscopy with attenuated total reflection used as sampling technique (FTIR-ATR), was performed on cable peelings. The measurements were carried out with two different crystals, allowing for different penetration depths of the beam. The used crystals were Diamond (Dia) and Germanium (Ge) with respective penetration depths of 1.66 μm and 0.65 μm at 45° incident beam angle. The background spectrum was filtered out to reduce noise levels and avoid the impact of ambient changes during the measurement. Each sample was assessed with a minimum of three separate scans on each side.

3.2.5 Surface free energy measurement

The wettability of a surface is determined by its surface free energy (SFE), which impacts the contact angle θ, between a deposited droplet and the surface. Additionally, roughness has a certain impact in this relation, making the contact angle sensitive to the sample's base material, its surface states and its roughness. By depositing a liquid, a droplet is formed and pulled down onto the surface by overcoming the surface tension of the liquid. Thereby, SFE can be deduced from the known liquid's surface tension and the observed contact angle. Complete wettability is achieved when the liquid spreads across the surface as film, as SFE in this case exceeds the liquid's surface tension. A series of liquids can be applied in incremental surface tension levels, finding the surface tension that only just fully wets the surface, thus determining the SFE.

The SFE of the studied polymer surfaces was determined through sessile drop measurements with deionized water, obtaining the contact angles θ. From such contact angles, the SFE was calculated with the Neuman method [101], [102]. Such results were compared with a DYNE test set, finding the lowest possible surface tension fully wetting the surface ($\theta = 0$) in 2 mN/m increments [102]. Both methods required a surface roughness correction using Cassie Baxter's equation:

$$\cos\theta_m = (Sdr/100 + 1) f \cos\theta_Y + (f - 1) \tag{20}$$

where θ_m and θ_Y respectively are the measured (advancing) and the Young's (ideal, advancing) contact angles in radians, *Sdr* is the developed interfacial area ratio parameter in % and *f* is the fraction of the droplet in contact with the surface. The parameter *f* thus accounts for air pockets present underneath the droplets, which were only observed in the sessile drop measurements.

3.3 Electrical characterizations

3.3.1 Space charge measurements

The space charge distributions and their evolutions over time, within cable peelings having different surface types, were measured by means of the Pulsed-Electro-Acoustic (PEA) method. While the setup and main methodology were in place at Nexans Research Centre (NRC) in Lyon, previously developed by Guffond et al. [76], the signal processing and data visualization were refined within this work.

3.3.1.1 Measurement setup

In the experimental setup, shown in Figure 22, a pulse generator (G), isolated from high voltage potential through the decoupling capacitor (I), applies a defined voltage step (with high-

frequency content) over an energized sample. During the voltage pulse's propagation through the insulation layer, it induces a transient displacement of encountered space charges, due to a local Coulomb effect. Thereby, a local pressure wave is generated, with its amplitude proportional to the local charge density. Such generated pressure waves propagate at the speed of sound within the material and are measured below the sample by means of a piezoelectric sensor, indicated with (D). The sensor translates the pressure wave to a voltage signal through electrostriction.

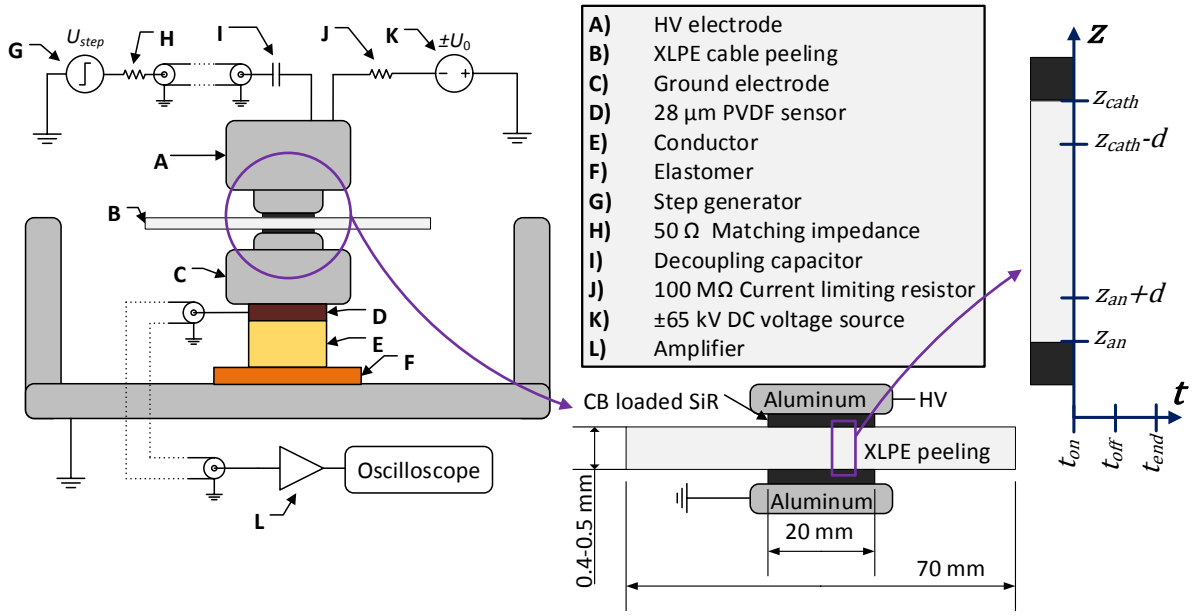

Figure 22. Illustration of the PEA setup, the electrode configurations and the coordinate systems and positions considered in post-processing.

The sample, being a cable peeling of ~500 µm thickness, was placed between to semi-conducting Silicone Rubber (SiR) electrodes. Such SiR electrodes were held in place by using a small amount of dielectric grease, which ensured both good electric and acoustic contact. Below the sample, the piezoelectric sensor and an absorber were located. The absorber, consisting of (E) and (F) in Figure 22, ensured that no acoustic waves were reflected backward into to sensor during the measurement acquisition window. The entire set-up was placed inside a climate chamber for uniform temperature control. The measurements were performed at three temperatures; 25 °C, 50 °C or 70 °C. All tests were performed on virgin samples, avoiding the impact of electrical history in the measurements. Six hours of polarization was applied, at +7.5 kV, ±15 kV, +22.5 kV or ±30 kV through the voltage source ((K) in Figure 22). After the polarization, the measurement acquisition system was reset, and thereafter 18 hours (overnight) or 66 hours (over-weekend) of depolarization was performed. Measurement signals were acquired at 60-second intervals during the polarization and at 300-second intervals during the depolarization stages.

3.3.1.2 Signal processing

From the (acoustic) voltage signal S_{meas}, the net space charge density S_{sc} can be deduced through the transfer function:

$$S_{sc} = S_{meas} - A(t)S_{meas}(t-\tau) \tag{21}$$

Here $A(t)$ and τ are the transfer function parameters and are identified through calibration. In calibration, a "charge free signal" was deduced by taking the signal just prior voltage shut down and subtract from it the signal just after the voltage was shut down (at the end of polarization). It is assumed that, during the few elapsed minutes required to turn off, safety ground and reset the setup, no change occurs in the space charge density within the sample. If this assumption holds true, the difference between the signal just post to the signal just prior should yield a flat curve with only induced peaks at the electrodes. During calibration, the $A(t)$ and τ parameters are thus modified until this signal difference is charge free, and a realistic value of the sound velocity is obtained. The calibration was repeated for each new measurement, however, in most cases, similar parameter values were found to be applicable.

Further data processing was developed, consisting of noise elimination. It was realized through a recursive spline interpolation filter, applied both in the thickness and time dimensions, creating the signal $\rho_{meas,or}$. The eliminated noise was also assessed such that no trends, and thus underlying information, existed in it. Other data processing methods involved estimating the peak-free signal $\rho_{meas,pl}$, by eliminating the induced signal peaks at the electrodes occurring during polarization. Two gaussian peaks were fitted to the previously mentioned charge free signal and were thereafter subtracted from the measurement data during polarization. During depolarization, no such treatment was performed, as it was deemed infeasible due to the injection of opposite charges at the electrodes. This processing method might also introduce some errors when strong image-charges also exists in the depolarization signal. The signal $\rho_{meas,pl}$ was mainly used to estimate net and mean charge densities in the sample, and to better compare the measurement results with the bipolar charge transport model. The time-dependent net charge density $\rho_{net}(t)$ was calculated as:

$$\rho_{net}(t) = \frac{1}{(z_{cath} - z_{an} - 2d)} \int_{z_{an}+d}^{z_{cath}-d} \rho_{meas}(z,t)\, dz \tag{22}$$

Where ρ_{meas} is the charge density in C/m^3 (with peakless signal, $\rho_{meas,pl}$ during polarization and original signal, $\rho_{meas,or}$ during depolarization). z_{an} and z_{cath} are respectively the anode and cathode positions in the signal, meters; and d is used to exclude a 75 µm section adjacent to the electrodes from the estimation. The mean charge density $\rho_{mean}(t)$ is expressed as:

$$\rho_{mean}(t) = \frac{1}{(z_{cath} - z_{an} - 2d)} \int_{z_{an}+d}^{z_{cath}-d} |\rho_{meas}(z,t)|\, dz \tag{23}$$

Since the PEA signal measures overlapping positive and negative charge as the net quantity at each position, there is no possibility to assess the total charge within the material at a given time. Also, the mean deviation ρ_{dev}, C/m^3; between a certain simulation and the measurement it attempted to describe was estimated by:

$$\rho_{dev} = \frac{1}{t_{end}(z_{cath} - z_{an} - 2d)} \int_{t_{on}}^{t_{end}} \int_{z_{an}+d}^{z_{cath}-d} |\rho_{sim}(z,t) - \rho_{meas}(z,t)|\, dz dt \tag{24}$$

Here $\rho_{sim}(z,t)$, C/m^3; was the local charge density simulated with the bipolar charge transport model and $\rho_{meas}(z,t)$, C/m^3; consisted of the peak-free measurement data, $\rho_{meas,pl}$ in polarization

and the ordinary charge density, $\rho_{meas,or}$ in depolarization. Modification of the integral limits t_{on} and t_{end} allowed for estimating the mean deviation in only the polarization, depolarization or the full measurement sequence. Integration over time was similarly applied to equations (22) and (23) for estimating net and mean charge densities from a certain period in the measurement.

3.3.2 DC breakdown tests

DC breakdown studies were performed on both MV-sized cable ends and on cable peelings. The MV-sized cable ends were chosen for their similar geometry and electrode configuration to a full-size cable application. Cable peeling tests, on the other hand, are more cost-efficient thus allow producing data with better statistical certainty.

3.3.2.1 DC breakdown on MV sized cables

The used MV sized cables were made in an extrusion line, with similar degassing, screening and sheathing processes as a full-scale HVDC cable. The major difference is that the cable's dimensions were significantly reduced, allowing for manual cable handling in the lab. As seen in Figure 23, the MV sized cable features a ~5 mm thick insulation layer made of the same DC grade XLPE as used in the full-scale cables [61]. Similar performance in DCBD fields can thus be expected for the MV-sized cable, although a minor scaling effect could exist given its smaller dimensions. The exposed and prepared cable ends, shown in Figure 23, were connected to a DC generator. The DC generator applied an automated continuous DC ramp at -1 kV/min until breakdown occurred in the sample.

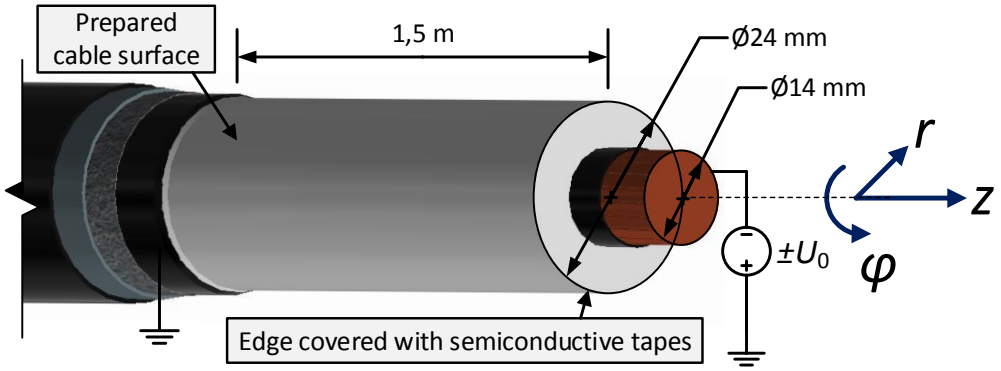

Figure 23. Geometry of MV-sized cable end (not to scale) for DC breakdown testing and its coordinates.

As neither any accessories nor any components were placed onto the cable surface, longitudinal field grading was ensured from the insulation's surface towards the ambient air. The test cell was dehumidified to reduce the risk of flashovers during testing. After testing, microscopic observations were used to determine the breakdown characteristics (failure mode) and to measure the sample thickness at the breakdown position. The latter was used to calculate the average electric breakdown field in the test.

3.3.2.2 DC breakdown on cable peelings

For performing breakdown tests on cable peelings under controlled conditions, a specialized test cell was developed and manufactured. The test cell is illustrated in Figure 24. The setup used a ±65 kV, 0.5 mA HCP FUG voltage source, with an external control system allowing for automated ramping of the applied DC voltage. The system also used a well-protected Keithley 6485 picoammeter which aimed to detect the leakage current during the test and prior to

breakdown. However, due to high background noise levels, and fast transient nature of the breakdown, the picoammeter mainly served as a triggering system for automated system shutdown.

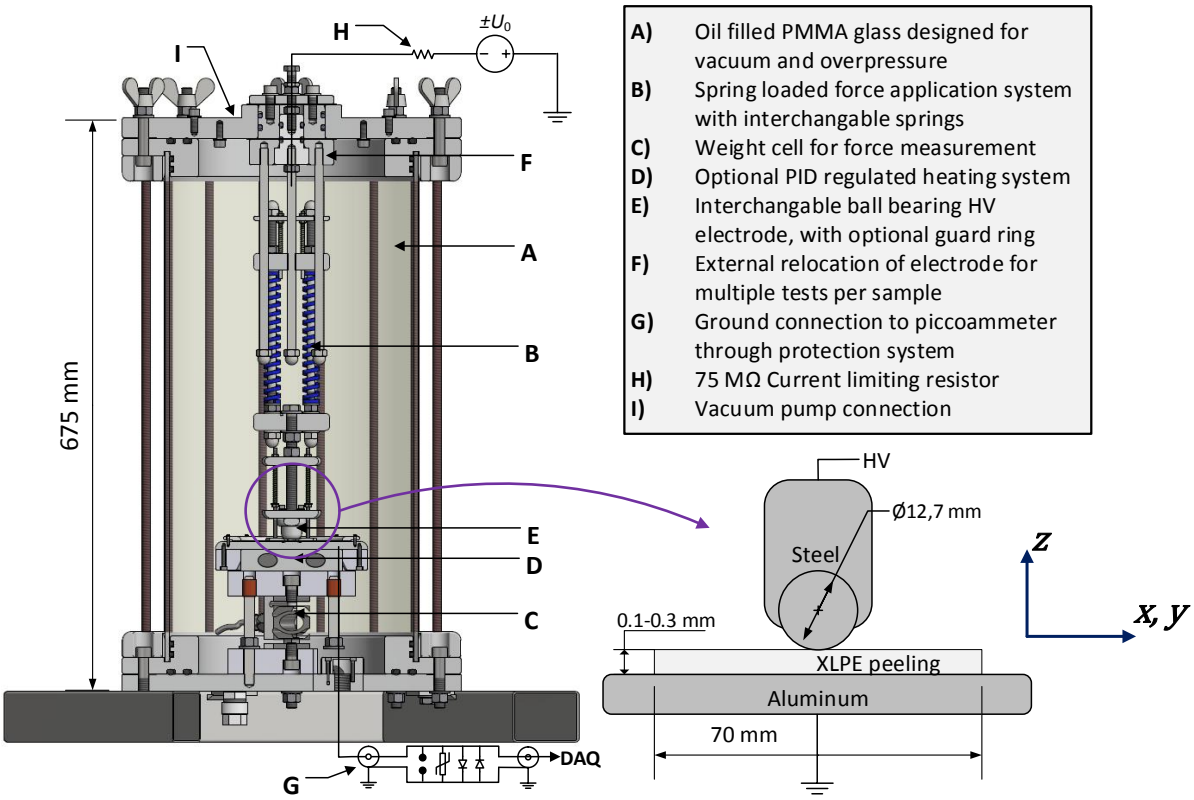

Figure 24. Design of the DCBD test cell and illustration of the used sphere-plane geometry.

The transparent PMMA cylinder was sealed with double O-rings and filled with mineral oil specifically suitable for DC voltage, having good moisture tolerance and breakdown strength exceeding 30 kV/mm. Each new sample was inserted from the top, after which a vacuum treatment was performed, effectively eliminating air pockets trapped between the sample and the ground plate, and elsewhere in the system. Only very low forces were applied from the spring-loaded top electrode, externally controlled by rotating a bolt on top of the cell, as the used ball bearing electrode has a small contact area with the sample. This small contact area easily creates high mechanical stress at the spherical electrode tip. The electrode imprint was consistently observed to be below 1.5 mm in diameter. The observed current, drawn from the voltage source, was below 1 μA for all tests, yielding a voltage drop below 75 V over the current limiting resistor. An automated ramping and breakdown detection system allowed for testing with low ramping voltages and long test durations, with remote supervision of the tests. The maximal output current from the voltage source was set low to limit the power dissipation during breakdown to below 300 μW (excluding capacitive discharge from the sample and cell itself). During each test, the applied voltage profile and the breakdown level were recorded. After testing, breakdown appearance, breakdown location (distance from the ball electrode) and the sample thickness at each breakdown location were assessed.

As shown in Figure 24, a sphere-plane geometry consisting of a steel bearing ball and an aluminum ground plane was used. Both electrodes had been polished to a high degree of smoothness (mirror finish). As the electrodes were submerged in oil, both the HV and the ground electrode featured a physical interface, having an interstitial layer of mineral oil in

between the metal and the material sample. In some tests the ground electrode side of the sample was gold sputtered for 6 minutes, to change the nature of this interface type.

3.3.2.3 Statistical treatment of breakdown data

The average breakdown field was obtained by dividing the breakdown voltage over the thickness at the sample position. The Weibull distribution, being an asymmetric extreme value distribution, is particularly applicable for breakdown tests [103]. The statistics in each test series were therefore investigated with the two-parameter Weibull distribution. It estimates the failure probability *P* at a given stress level *E*, kV/mm; given by equation (25).

$$P(E) = 1 - e^{-\left(\frac{E}{E_c}\right)^k} \tag{25}$$

Here, E_c is the characteristic breakdown stress in kV/mm (also commonly known as the scale parameter) and *k* is the unitless shape parameter of the distribution. The inverse power law (IPL) is also useful to consider, it calculates the time-to-failure *t*, as:

$$t = KE^{-n} \tag{26}$$

Here, *K* and *n* parameters are respectively the ageing factor in s·mm/kV and the unitless life-time exponent relating the applied field *E* to the time-to-failure *t* [34], [103]. Due to the IPL's exponential decay of lifetime with increased stress levels, higher breakdown levels may be achieved with faster voltage ramping rates. At high field strength, space charge effects within samples are known to significantly affect the applicability of the inverse power law [104]. Thus, while certain IPL parameters could be identified, because of the high field strengths used for their estimation, their exact implications remain subject to interpretation. Additionally, systematic thickness variations between different test series, affecting the rate at which the electric field increases (given a constant voltage ramp), may impact the results. For this reason, averaged breakdown fields against sample thickness were assessed in addition to the Weibull distribution. Lastly, the IPL also predicts a minor scaling effect between the cable peelings and the MV cable breakdown test, as the former is performed within hours, and the latter requires a full day of testing per sample.

Chapter 4

Experimental results

This chapter presents the obtained measurement results, beginning with the results of physical assessments, such as SEM and optical profilometry. Thereafter, chemical assessments, such as HPLC, FTIR-ATR, and SFE determination are presented. These are followed by a section highlighting the most important features observed in the electrical tests, comprising of the impact of orientation, polarity, field strength, and temperature in space charge measurements, followed by the DC breakdown results on MV sized cable ends and on cable peelings.

4.1 Physical and chemical surface characterization

4.1.1 SEM

Scanning Electron Microscopy (SEM) analysis was performed to investigate the surface texture and topography of the created surfaces. The results are shown in Figure 25 below.

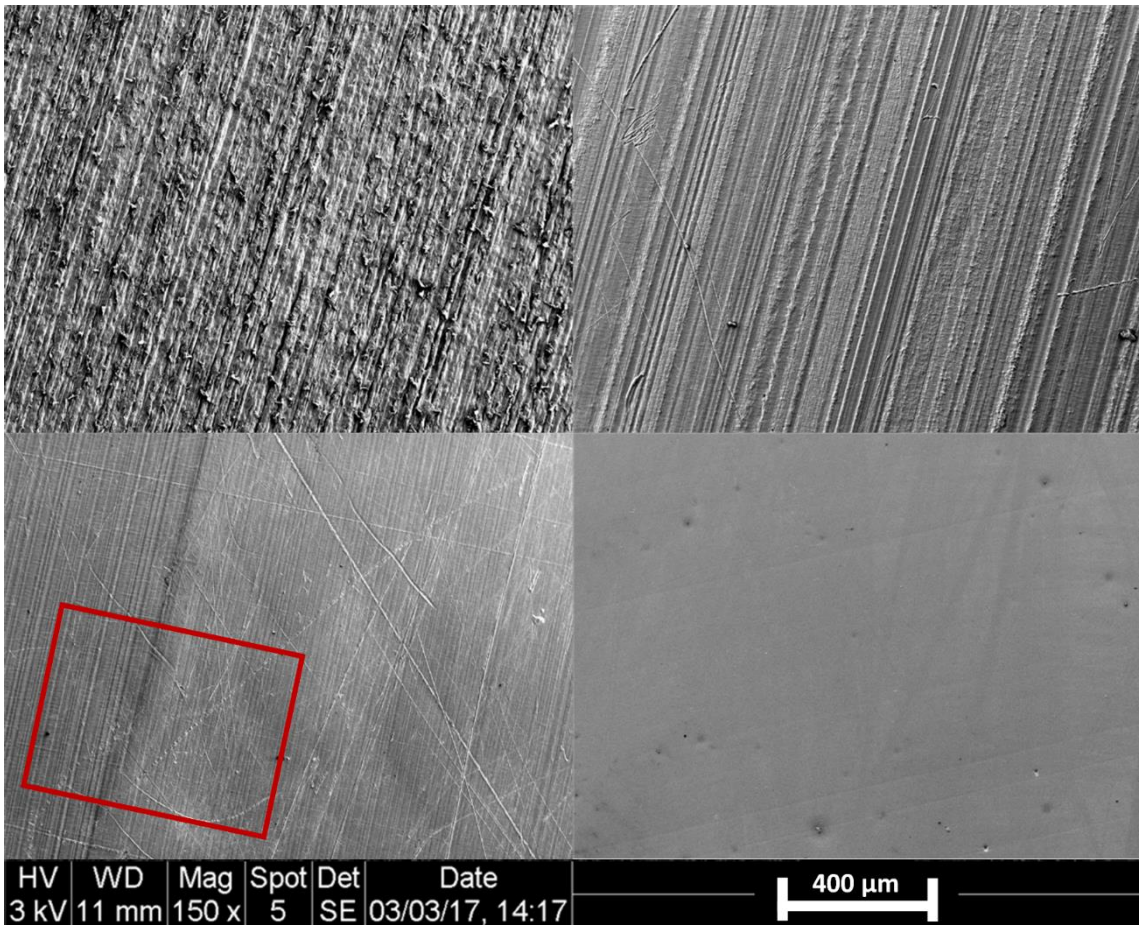

Figure 25. SEM of abraded (top left), backside (top right), cut (bottom left) and remolded (bottom right) surface types at 150 times magnification. The 612 by 459 µm domain size of optical profilometry is indicated in the red rectangle for perspective.

Minor scratches and non-embedded contaminants (dust etc.) are present on the surfaces, with most of them likely originating from sample handling and cleaning. As seen in Figure 25, distinguishing between scratches originating from sample handling and surface texture is achievable through checking their angular orientation. Randomly oriented scratches indicate the former, while parallel lines along or perpendicular to the preparation's orientation are features of the surface topography. Embedded contaminants, while being uncommon, were in certain cases observed on the abraded surface. Such contaminants originate from the abrasive substrate but can be limited if the last performed abrasion step (with highest grit number) is conducted for long enough time. Thereby only a few substrate particles from the latest abrasion step are embedded, which are of similar magnitude to the texture created. The vastly different surface textures, identified by their more regular patterns, are represented in the domain of optical profilometry indicated with the red rectangle in Figure 25. They can also be better observed at higher magnification as shown Figure 26.

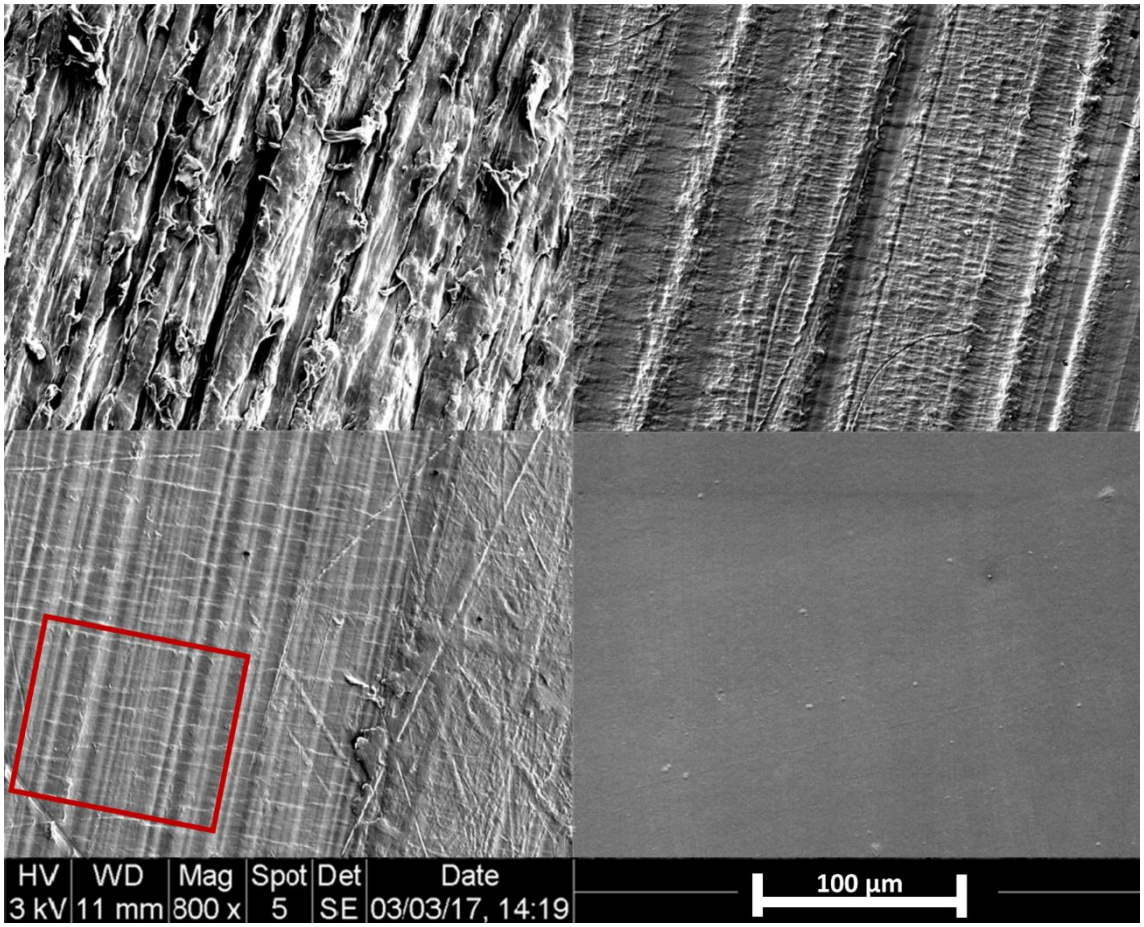

Figure 26. SEM of abraded (top left), backside (top right), cut (bottom left) and remolded (bottom right) surface types at 800 times magnification. The 83 by 96 µm domain size used in further simulations is indicated in the red rectangle for perspective.

As observed in Figure 26, the abraded surface texture shows scratches in the abrasion direction as well as small folded peaks, also reported by Hasheminezhad et al. [77]. Such scratches originate from the grains on the abrasion substrate, rubbing along the surface and pulling off polymeric particles. The peaks are likely originating from a yielding process, occurring when polymeric particles are pulled off from the surface. The backside and cut samples in Figure 26 show striations of different magnitude in the cutting direction. These striations likely originate from imperfections on the cutting knife's edge. Lines parallel to the orientation of the cutting

edge (near-horizontal lines Figure 26) are also observed, which could be caused by a fracture mode of material removal during the cutting operation. They do not resemble any severe knife chatter traces as such traces would generate a repeating profile with a higher degree of roughness. It is thus more likely related to the means of material removal in the cutting process. The remolded surface is very smooth as its texture is a replication of the polymeric contact film used in this preparation method. Some parallel lines where observable, which might originate from the manufacturing process of the film.

As mentioned, the 612 by 459 µm domain for optical profilometry captured the full characteristics of the surface, as seen in Figure 25. The 96 by 83 µm domain shown in Figure 26, indicates the domain size used in further calculations. However, its size is approaching the texture's repetition rate, *Si*. Thus, it has the smallest dimensions possible for resolving the roughest surfaces, given that each striation has similar dimensions. Furthermore, the resolution in the indicated domain is 50 by 50 data points. Thus, while the here visible height variations are resolved, further sub-micrometer level accuracy in *(x,y)* dimensions cannot be achieved with profilometry, owing to the wavelength of light previously indicated in Figure 17. The surface's height Z(*x,y)*, however, is resolved among the microlevel spaced coordinates with accuracy down to approximately 50 nm. The results of profilometry for the full and sectionalized domains are addressed in the next section.

4.1.2 Optical profilometry

Three-dimensional surface roughness parameters were estimated through equations (17)-(19), making use of the height distribution *Z(x,y)*, obtained by means of optical profilometry measurements. The results are shown for the *Sa* and *Sq* parameter in Figure 27 below.

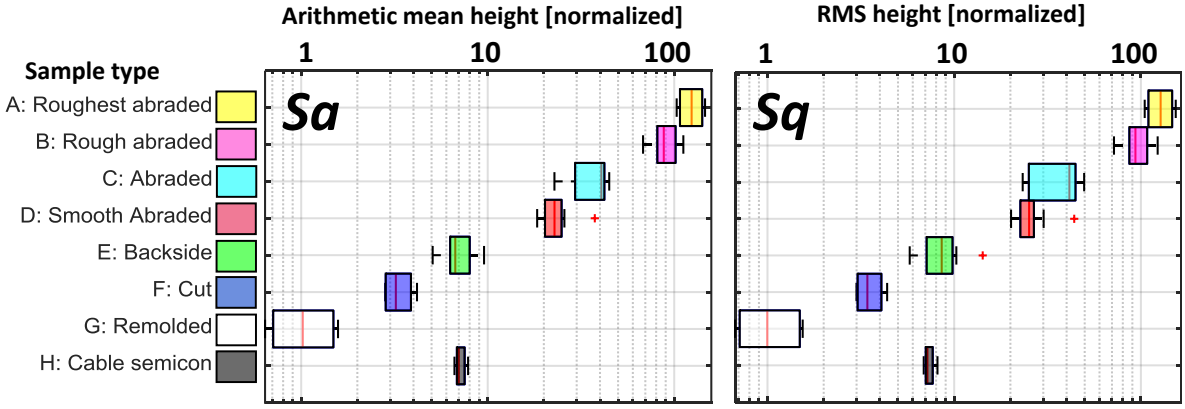

Figure 27. Height parameters Sa and Sq and for different surface types. Their results, in nm-µm range, have been normalized against the remolded surface. Each boxplot consists of five or more measurements, in some cases performed at different occasions during the project work.

As observed in Figure 27, *Sa* and *Sq* both show different, reproducible surface height variations spanning over two orders of magnitude. Incremental roughness levels are observed for each preparation type, starting from the remolded surface (G) and ending at the roughest abraded surface (A). The four different types of abrasion show a clearly discernible impact of the grit size used. The backside and cut surfaces show a significantly lower height variation, while the even lower remolded surface features were below the height resolution limit. Due to the reproducibility of results, individual roughness measurement of each batch or individual samples could be avoided. Also, for sake of comparison, ideal regions (i.e. no visible scratches) of the cable's outer semiconductor were analyzed. The semiconductor surface was found to

have similar roughness levels to the backside surface. While the cable's internal insulator-semiconductor interface is not assessed, it may exhibit very similar features to its outer surface [7], [105].

As surface type comparison by the height variations alone is insufficient, the texture's repetition rate and steepness amongst the surface coordinates can be assessed through the hybrid *Sdr* and *Sdq* parameters, shown in Figure 28.

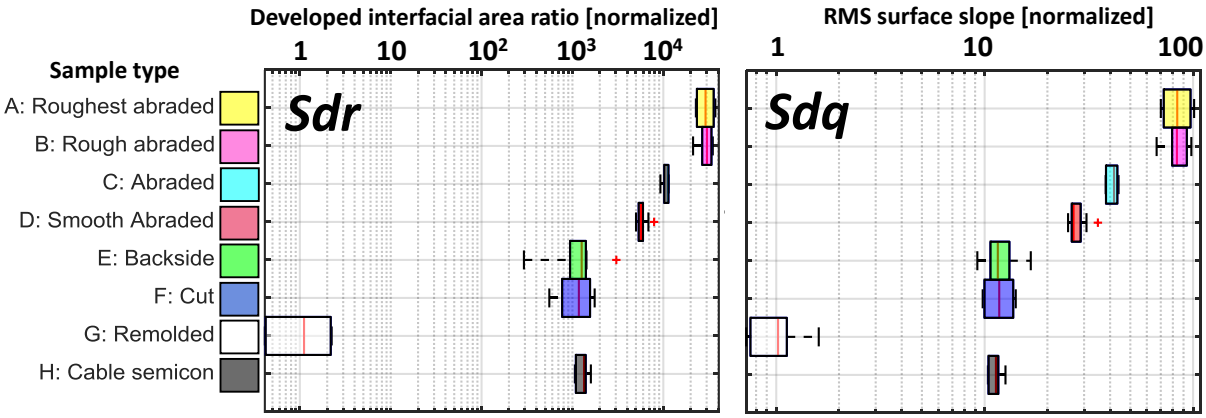

Figure 28. Hybrid parameters Sdr and Sdq for the investigated surface types. Their results, in % or degrees, have been normalized against the remolded surface, which featured ratio and slope respectively well below 1 % or 1 degree. The original values were significantly lower than indicated.

While again large variations amongst the preparation types are observed, the rough and roughest abraded surface types yield similar results. Furthermore, the cut surface yields similar results to the backside surface. These similarities prevent perfect correlation between *Sdq* and *Sa* parameters, which is indicative of textural effects creating different slope-height relations. The *Sdr* parameter was used further in roughness correction of SFE results in section 4.1.5. The *Sa* and *Sdq* parameters were used for surface type comparisons and for investigating possible correlations with electrical quantities. However, more accurate investigations can be made by omitting the averaging and instead displaying all surface coordinate values in histograms, as shown for the height *Z(x,y)* and derivative distributions (e.g. $\partial Z/\partial x$ joined with $\partial Z/\partial y$) in Figure 29.

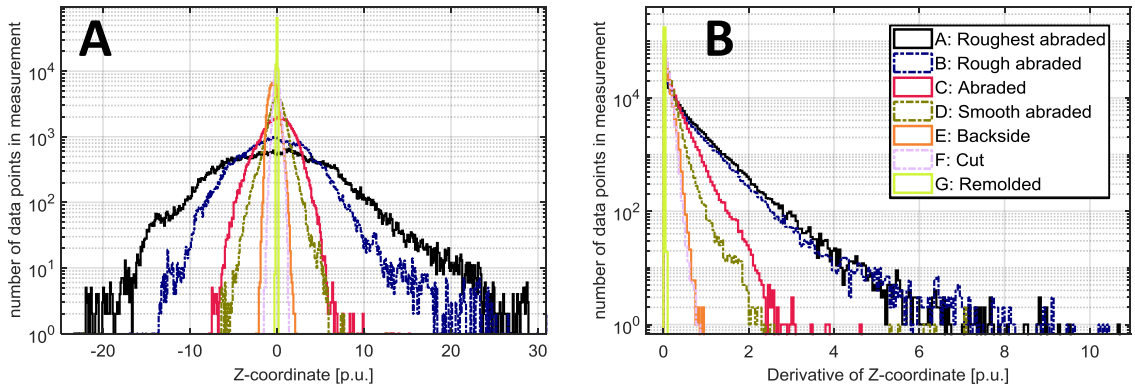

Figure 29. Histogram over the height population (A) and absolute values of the derivative population in both x and y orientations (B). Coordinates are normalized and represent the full domain of the profilometry measurement.

The height and derivative histograms shown in Figure 29 correlate with their respective *Sa* and *Sdq* parameter values in Figure 27 and Figure 28. Furthermore, owing to the similar shape between individual distributions, the *Sa* and *Sdq* parameters can be concluded to accurately represent their topographies, and only minor variation exists in the distribution tails. Furthermore, the impact of sectionalization and interpolation can be studied through the comparison of such histograms pre- and post-processing, with a typical post-processing result shown in Figure 30.

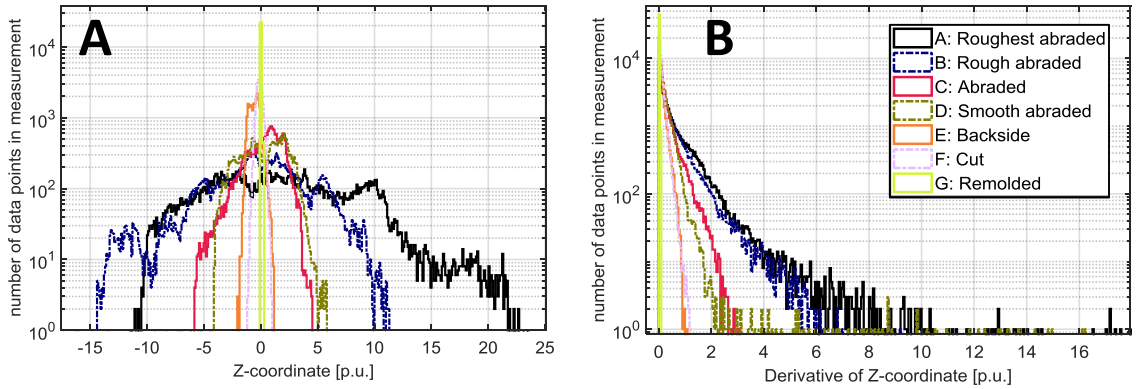

Figure 30. Histogram over the height population (A) and absolute values of the derivative population in both x and y orientations (B). Coordinates are normalized and represent a small section of the profilometry domain, with interpolation.

As observed from a comparison of Figure 30 with Figure 29, some modifications in coordinate distributions arise from the performed interpolation and sectionalization (described in section 5.6.1). The height distributions (A), alter from being a smooth near-gaussian spread to a slightly more disordered distribution. This alteration likely arises from sectionalization, as the smaller section better shows the degree of disorder present the local texture, which averages out over the full surface. The derivative distribution (B), however, does not show significant disorder introduction in the histogram. It instead shows an increase in the distribution tail, with a few increased values among the derivatives being developed. The increased tails are likely linked to interpolation which, for smoothening out the local profile at sharp points on the surface, introduces additional coordinate points with some of them having higher derivative values.

To better understand the implication of certain geometric features and reveal which surface parameters may best anticipate field enhancements, a mathematical representation of measured texture is relevant. Investigations performed with artificially generated textures showed that exponential noise best represented the tails in both height and derivative distributions towards high or low values. Thus, the texture could be regenerated from the previously obtained roughness parameters (i.e. *Sa*, *Sdq* and *Si*) as:

$$Z(x,y) = Sa \cdot 2\sqrt{2}\sin\left(\frac{2\pi}{Si}x\right) + Sdq \cdot exprnd(x,y)) \tag{27}$$

Where *Sa* is the arithmetical mean height parameter, thus governing the height of the sine wave. *Si* is the repetition rate of the texture, thus being the argument within the sine function. *Sdq*, being the RMS surface slope, dictating the amplitude of a specifically tuned exponential noise generator *exprnd* (e.g. with tuned amplitude, tuned interpolation in (*x*,*y*) coordinates and symmetry in -*z* and *z* orientations). Other noise types, such as generated with the Gaussian distribution used in [81], will also introduce field enhancement in simulation, but it matches

less with the distribution tails in Figure 29. Equation (27) yields surface coordinates shown in the histogram in Figure 31.

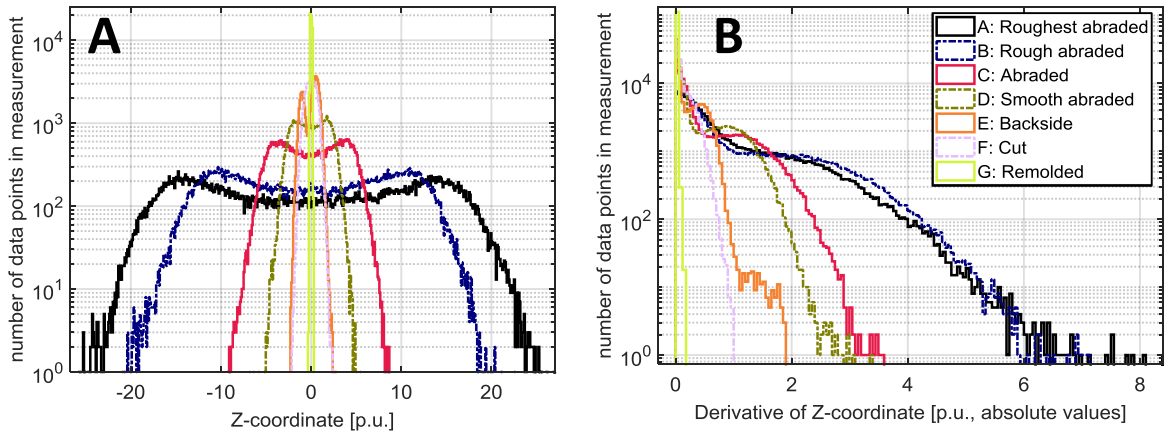

Figure 31. Histogram over the height population (A) and absolute values of the derivative population in both x and y orientations (B). Coordinates are normalized and represent artificially generated surface texture.

As seen in Figure 31, the sine function in equation (27) represents the height variation, while the exponential noise tunes in the tails in the histogram. When properly tuned, the artificial distributions in Figure 31 can match the real distributions in Figure 29. Using artificially generated texture with ridges tuned to the texture's striations, superimposed with exponential noise, represents the real texture better when domain size approaches the texture's repetition rate, *Si*. Also, its features, exponential noise and smooth striations, can be isolated and thus evaluated separately in field simulations.

4.1.3 HPLC measurements

The results of the HPLC measurement on differently prepared cable ends, are displayed against cable radius in Figure 32 below. Cable sections prepared with cutting, abrasion or remolding procedures were compared against a reference cable section, without outer semiconductor removal.

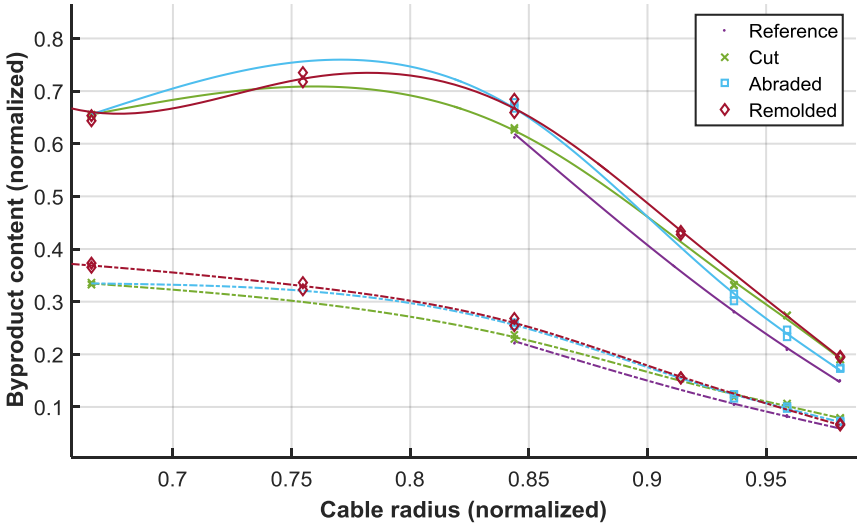

Figure 32. Byproduct content of cable sections with differently prepared surfaces. Quantities shown are for Cumyl-alcohol (solid curves) and Acetophenone (dashed curves).

In addition to the Cumyl-alcohol and Acetophenone concentrations shown in Figure 32, the concentration levels of Alfa-methyl styrene and Dicumyl-peroxide were below the detection limit. No significant impact on the byproduct distribution in the cable end was thus found depending on preparation method. Also, in the increased resolution towards the surface (shown to the right in Figure 32), no significant deviations where observed. Hence minimal impact of the preparation method on the radial byproduct distribution can be considered. The concentration levels of PDP in cable peelings after 3 months of storage in the incubator was investigated, as shown in Table 2 below.

Table 2. HPLC measurement on stored cable peeling before and after 3 months of sample storage

	Before peeling, in surface area	After storage	After storage
Thickness [µm]		700	400
Cumyl-alcohol [ppm]	585±4	180±7	138.5±3.5
Acetophenone [ppm]	198.5±2.5	43.5±4.5	26±1

The results in Table 2 indicate that additional outgassing of the byproducts during storage, with its rate depending on sample thickness. Besides the byproducts shown, concentrations of Alfa-methyl-styrene and Dicumyl-peroxide were again below the detection level. The low PDP concentration levels of the cable sections arise from cable degassing following normal industrial procedures (prior to manufacturing the cable peelings). Furthermore, most specimens used for DC breakdown were below 300 µm in thickness and stored for at least 2 months. Peelings used in space charge measurements were below 500 µm in thickness and stored for at least 3 months. Low PDP concentration levels can thus be expected in the peelings during electrical testing, such that electronic charge transport processes should be responsible for the observed phenomena.

4.1.4 FTIR-ATR measurements

The respective results of infrared spectroscopy of a cut, an abraded and a remolded sample, compared against the backside in these peelings, are shown in Figure 33.

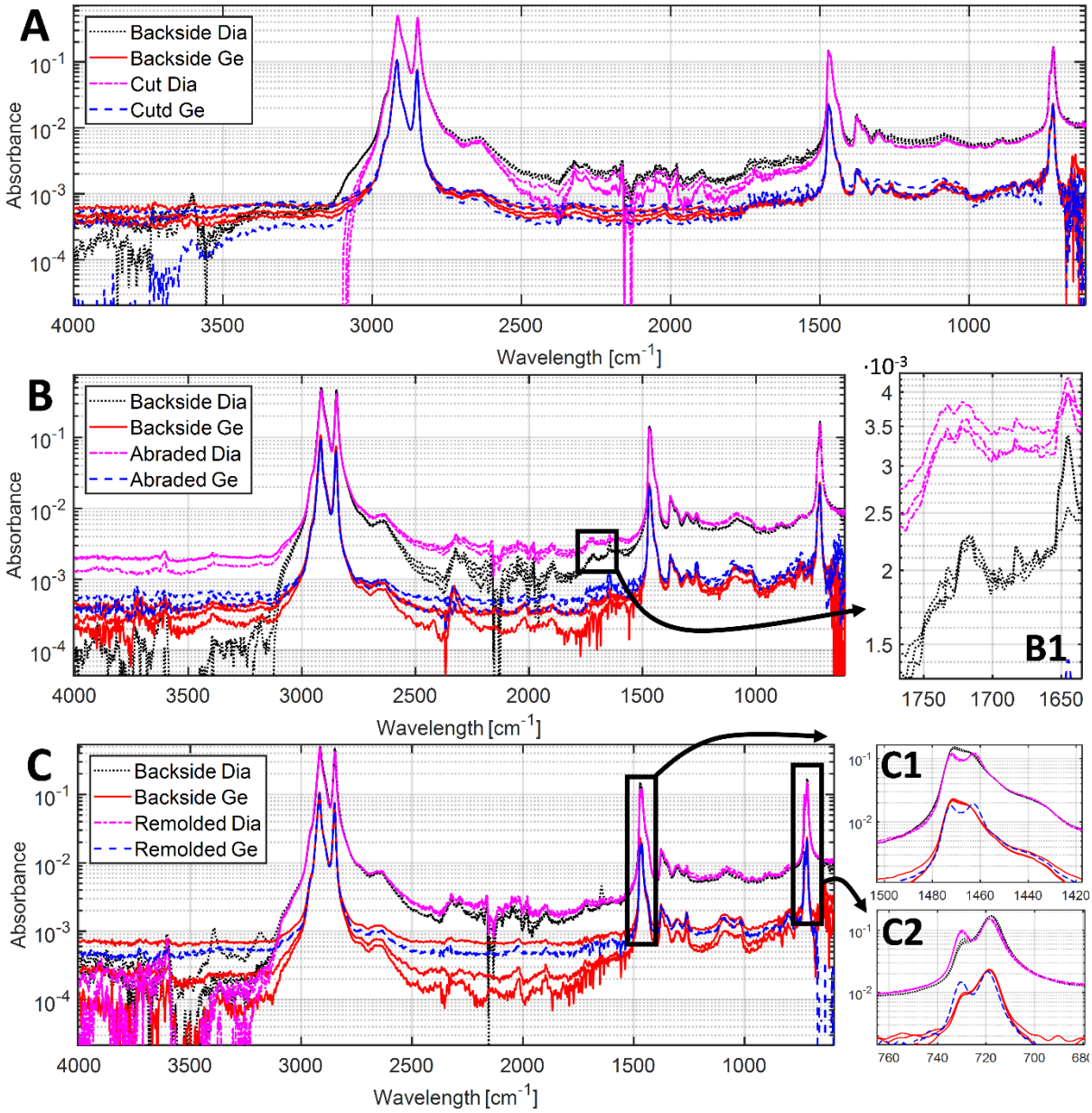

Figure 33. FTIR-ATR scans (three overlaid scans per measurement) of a cut (A), an abraded (B) and a remolded (C) sample and their backsides obtained with two different crystals as indicated. Magnification of the 1650-1750 cm^{-1} wavelengths (B1) indicates a small spectral change between the abraded and its backside. Magnification of the 1420-1400 cm^{-1} and 680-760 cm^{-1} wavelengths (C1 and C2) show a spectral change on the remolded surface.

The cut (Figure 33A) and backside surfaces (in all subfigures in Figure 33) show the typical spectrum for polyethylene, without noticeable spectral changes. These spectra indicate chemically unaltered surfaces, without significant introduction of oxidation, foreign species (bonds) and morphological alterations. Furthermore, for the abraded surface (Figure 33B) the overall spectra are also unaffected. However, closer investigation (Figure 33B1) reveals a small broadening of the double peak at 1733-1755 cm^{-1}. This broadening could be indicative of a marginal increase of *C=O* bonds (carbonyl groups) on the surface of the abraded sample. This oxidation process could be related to some heat development on the surface during the preparation, or the additional surface area introduced. The overall ATR spectrum of the remolded surface (Figure 33C) shows no signs of foreign species (bonds) introduction. However, spectral changes are observed at 720-730 cm^{-1} and 1460-1470 cm^{-1} (respectively,

Figure 33 C2 and C1). The development of such double-peaks shows a modification of the *C-H* stretch vibration, and the splitting of these two bands could be attributed to the regularity of the backbone structure [13]. This morphological change indicates an increase in the degree of crystallinity. Such double-peak development is observed identically with both germanium and diamond crystals. Based on the similarity in the curves in Figure 33 C2 and C1, it seems that the effect spans at least a micrometer thick layer from the sample surface. As the peeling's thickness was ~500 µm, and its backside surface remains unchanged, the morphological impact seems to be limited to the micron-level.

4.1.5 Surface Free energy

Based on the methodology described in section 3.2.5, the SFE results were obtained separately by sessile drop and DYNE tests, with results shown in Table 3.

Table 3. Mean values of SFE in [mN/m] from the Neumann method and sessile drop measurements, or tests with DYNE liquids. Both are shown with and without roughness correction according to Cassie-Baxter's formula. Adopted from [101], [102].

[mN/m]	Abraded	Backside	Cut	Remolded	Backside	Backside Oxidized
SFE, sessile drop	20.0±4.9	24.5±1.8	24.9±1.5	27.1±1.6	25.1±2.4	30.8±1.8
Roughness corrected SFE, sessile drop	20.8±4.4	24.6±1.8	24.9±1.4	27.1±1.6	25.1±2.3	30.8±1.8
SFE, DYNE test	36	29	27	27	29	32
Roughness corrected SFE, DYNE test	32.5	28.5	26.7	27	28.5	31.3

While the 2 mN/m increments in the DYNE liquids and large standard deviations in the sessile drop measurements make it difficult to determine the source of discrepancy between the two methods, they yield comparable results for backside, cut and remolded sample types, in the range of 25-29 mN/m. Also, a backside surface subjected to strong oxidation through heat gun application, showed that surface states introduced were detectable with both methods. One underlying issue is observable in the roughness correction (e.g. through *Sdr*), which shall increase the sessile drop SFE and decrease the DYNE test results. After the correction, some discrepancy remains, especially for the abraded surface. While this issue could indicate underestimated contact areas *f*, being estimated at 75% for the abraded surface which is close to a superhydrophobic state (Lotus leaf effect). However, since such air pockets do not exist in the DYNE test, some discrepancies must come from elsewhere. As higher *Sdr* parameters would have made for a better roughness correction, underestimated *Sdr* parameters may be a viable cause. Such underestimation is a known problem, since profilometry may interpolate a few steep, and thus unmeasurable, surface coordinates. Furthermore, directional effects (such as the texture's striations) which may also contribute to reduced wettability, which is not accounted for in the non-directional roughness correction in equation (20).

Conclusively, the SFE indicates the present polar and dispersive forces and can thus relate to the surface states, originating from work (*W*) involved in molecular bond disruption and formation. As different preparation methods feature slightly different means of material removal, a slight modification of the surface DOS for certain surface types is plausible. However, given the stronger impact of surface roughness, and low accuracy of SFE results, individual modification of a specific surface type's surface DOS and thus its injection parameters based on these results cannot be justified.

4.2 Electrical characterizations

4.2.1 Space charge measurements

4.2.1.1 Impact of orientation and polarity

Charge accumulation was first investigated for abraded and backside surface types with results shown in Figure 34. The electric field was increased in a stepwise manner, with short depolarization sections of at least 30 minutes in between.

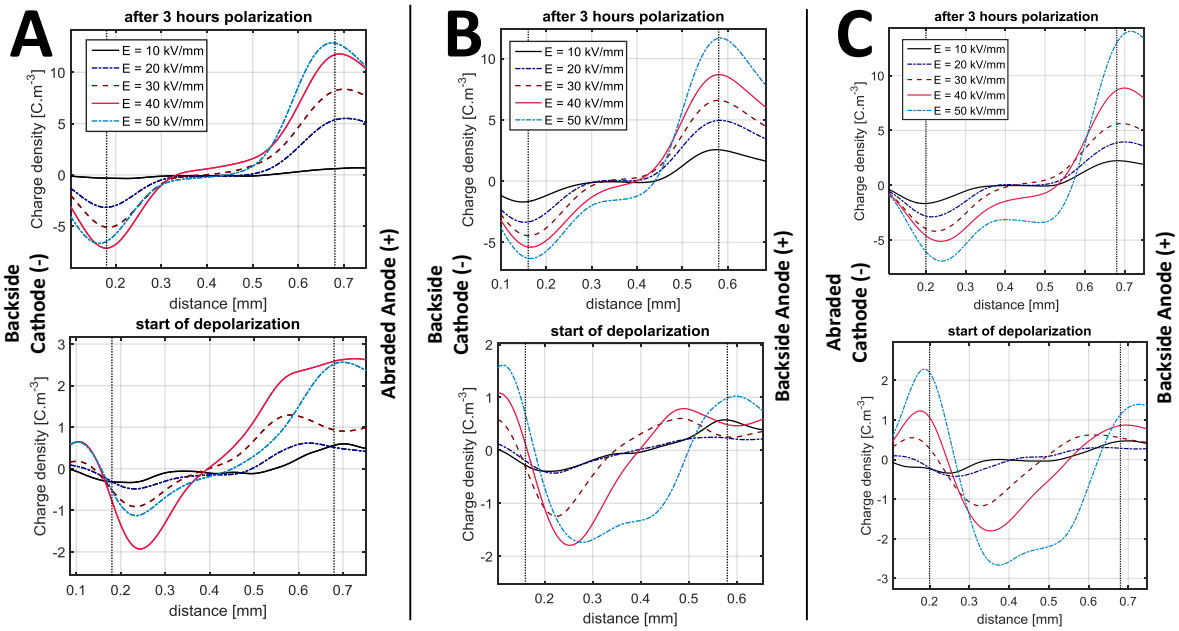

Figure 34. Initial PEA measurements at increased positive stress at 30 °C. Top graphs show results during poling and bottom ones show depolarization sequences. Electrode types are indicated with a rough anode (A), smooth anode and cathode (B), and a rough cathode (C).

The measurements performed during polarization and depolarization stages, consistently indicated negligible charge injection at 10 and 20 kV/mm. At 30 kV/mm homocharge accumulation commenced and slowly propagated into the bulk. Homocharge density was the highest at abraded surfaces as compared to backside, regardless of sample orientation (polarity). This effect was even more pronounced at 40 kV/mm. A reference sample with two smooth surfaces (Figure 34B) showed a more balanced concentration of positive and negative homocharges at their respective electrodes, with slight domination of negative charge. At 50 kV/mm, negative charge accumulation dominated, even for the reference sample. Lowest negative charge density was found with a rough anode (Figure 34A), and the highest for a rough cathode (Figure 34C). As such results indicate a strong impact of surface roughness on charge injection, a more systematic approach was adopted, making use of virgin samples for each stress level. Thereby, accurate model calibration could be realized without residual charges skewing the developing charge density.

Using identical abraded peelings, only modifying polarity and sample orientation, yielded four different PEA measurement conditions displayed in Figure 35. Charge exceeding 5 C/m^3 is placed out of the colormap's range, as it corresponds to electrode charges during polarization.

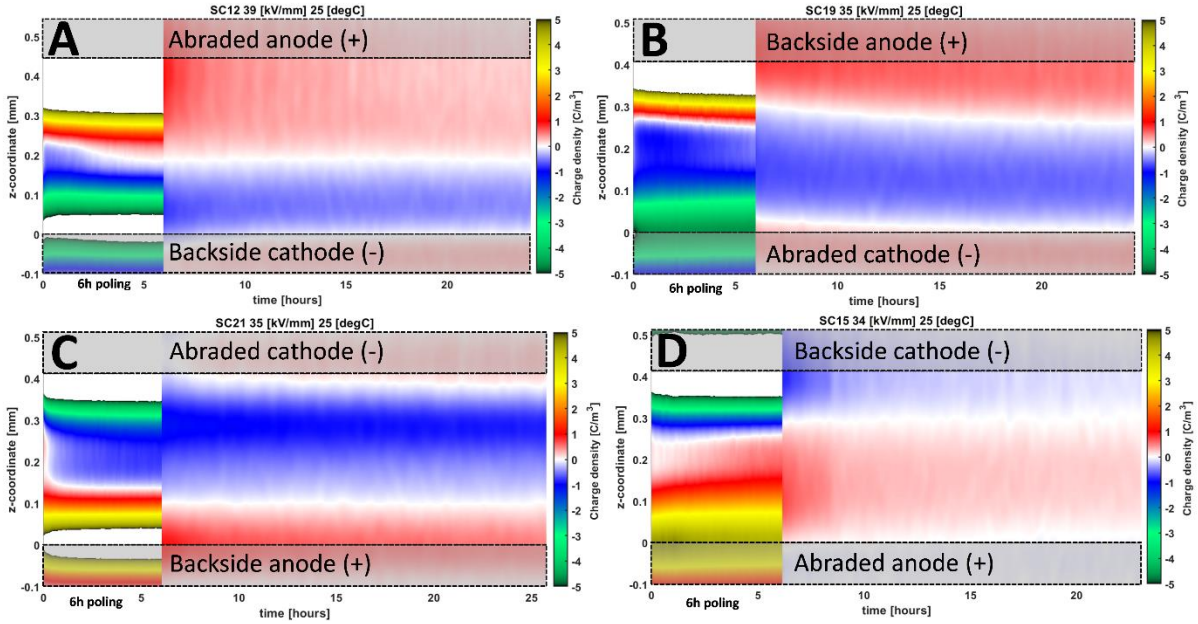

Figure 35. PEA measurements showing impact of polarity and sample orientation. 15 kV of positive or negative poling voltage was used at 25 °C. The electrode types are indicated in the figures. In each figure, SC-# indicates a sample identification number, followed by the mean field strength during poling (poling voltage divided by sample thickness) and temperature. Data positioned at 0 C/m^3 or larger than ± 5 C/m^3 have been colored white in the colormap.

At medium field strengths (34–39 kV/mm) the abraded surface injected consistently more charge than backside surface, regardless of the polarity. This increased accumulation could be related to enhanced charge injection with increased roughness levels. Comparison of Figure 35A and Figure 35D, as well as Figure 35B with Figure 35C, should yield similar charge distributions as both orientation and polarity are reversed. This anticipated behavior holds true, although some deviation arises possibly related to the thickness variations. Also, fast charge buildup is noticed during polarization which stabilizes over time after its establishment. Furthermore, a slow charge decay is observed during depolarization. Negative charge carriers seemingly exhibit lower injection and transport (detrapping and/or hopping transport) barriers than positive carriers. This effect can be attributed to the material's semi-crystalline structure since the crystalline and amorphous phases are known to respectively favor hole and electron transport [26], [76].

4.2.1.2 Impact of poling field strength

Measurements carried out on samples with different degrees of surface roughness, at different poling voltages, allowed determining the injection current density increase with electric field strength. The results are shown in Figure 36 for rough abraded, abraded, and backside anodes, while all cathodes featured a backside surface type. Note that peakless signals ($\rho_{mean,pl}$) are displayed in the polarization sequence (e.g. electrode's charges were removed as described in section 3.3.1.2), allowing for a better comparison.

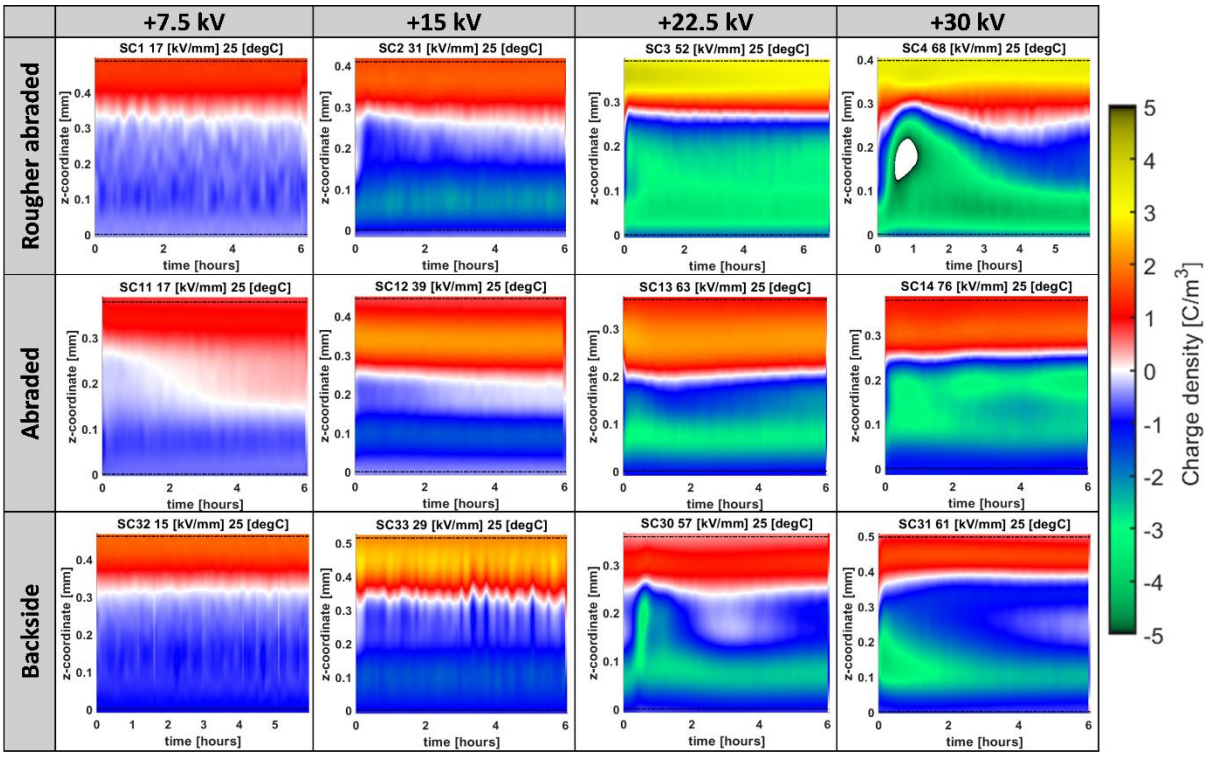

Figure 36. PEA measurements at 25 °C and different poling voltages, polarization sequence only. All samples feature the listed surface type as anode (top) and a backside cathode (bottom). Charges at the electrodes were removed through gaussian peak removal. Data at 0 C/m^3 or larger than ±5 C/m^3 appear in white.

The charge densities observed in Figure 36 increase with poling field, and negative charge dominates at high field strength, thus similar to the high field behavior in Figure 34. Minor thickness deviations between samples resulted in variation of mean poling field, as indicated above each sub-figure in Figure 36. While charge density increases more for the rougher surface types, the positive charge injected from such anodes does not exceed the negative charge density from the smooth cathode. This negative charge domination can be related to the morphology of the polymer favoring injection and transport of electrons. Thus, when higher positive charge density is injected from rough anodes, it increases the field strength at the cathode and, therefore, an increase in both positive and negative charge density is observed. The net and mean charge densities calculated with equations (22) and (23) are displayed against the poling field in Figure 37. Additional measurements, not shown in Figure 36, are also included in Figure 37.

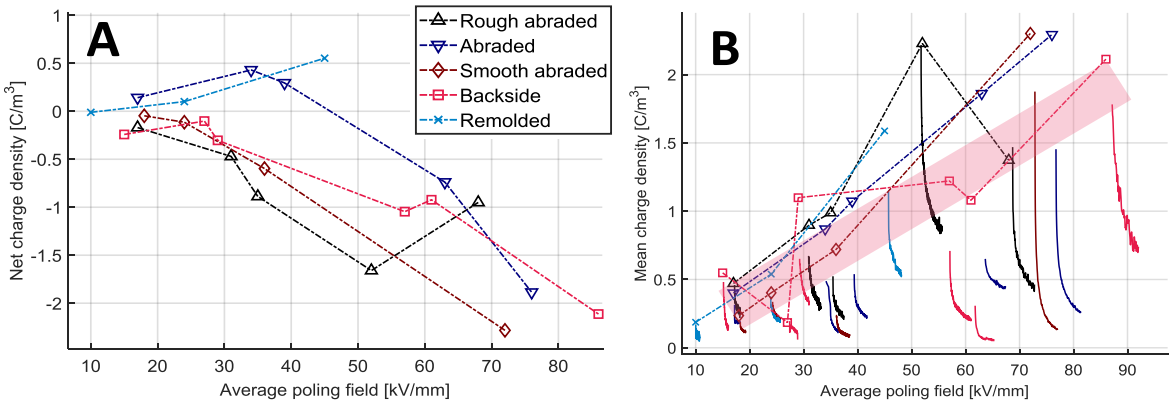

Figure 37. Impact of mean poling field at 25 °C on net charge density (A) and mean charge density (B). Indicated surface types are used as positive anode, while the cathode is a backside surface in all experiments. Markers indicate the value at the end of the polarization. Solid lines in (B) show the mean charge density against time during depolarization. Dashed lines indicate trendlines. The shaded region in (B) indicates the backside surfaces' trend, regarded as reference.

The net charge density in Figure 37A decreases with the poling electric field for most samples, which likely is related to their morphology [26], [76]. Above 45 kV/mm, charge density in smooth, remolded samples deviated from the anticipated low charge accumulation (predicted with low injection rates). Such deviation could arise from either higher thickness (700 µm) of this specific sample or its manufacturing method. The remolding process could affect the surface layer's crystalline structure, thereby locally affecting injection and transport barriers. The depolarization curves (solid lines in Figure 37B) show, especially at high electric field strength, the disappearance of some charges between the polarization's end (markers) and the depolarization's start (solid lines). Note that ~5 minutes elapsed in between such measurements, required for grounding and resetting the system. For rough abraded, abraded, and smooth abraded surfaces, higher mean charge densities compared to backside surfaces, are observed in Figure 37B. This effect, related to charge injection, may indicate the presence of its electric field thresholds E_{th}, at approximately 30, 36, and 44 kV/mm, respectively, for rough abraded, abraded, and smooth abraded. Such injection effects will be addressed with simulation presented in section 6.3.

High field strength behavior was evaluated further, in both polarization and depolarization sequences, with Figure 38 showing typical measurement results.

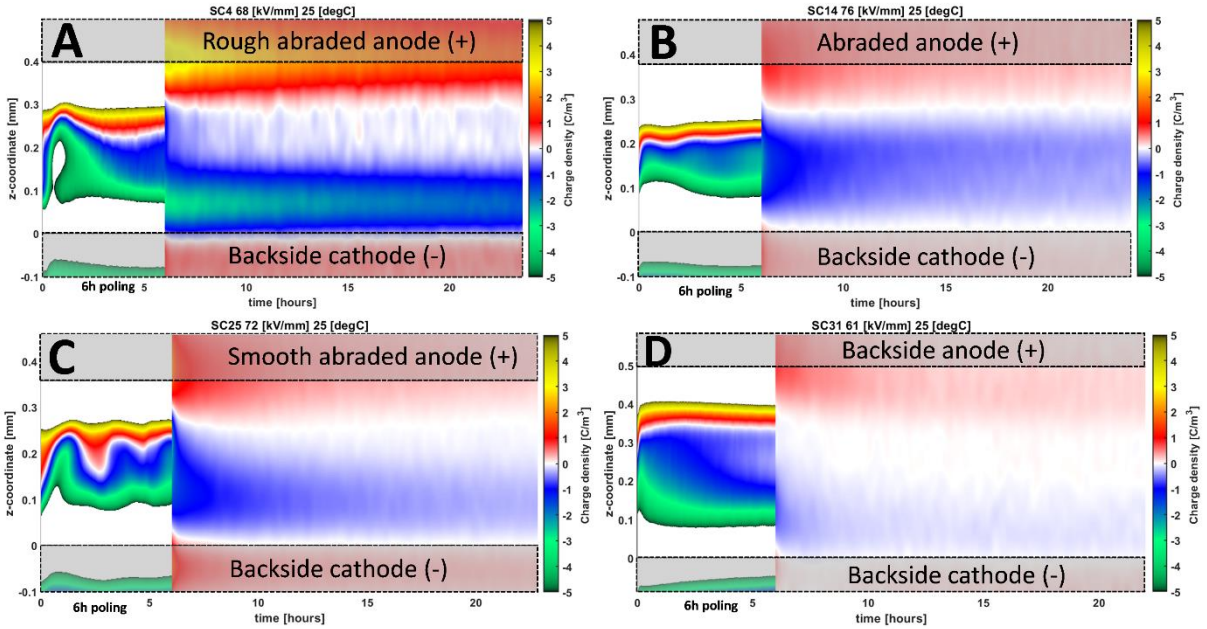

Figure 38. PEA measurements at high electric fields (61–76 kV/mm), at 25 °C and using +30 kV poling voltage, showing space charge packet-like behavior and fast initial depolarization. With a rough abraded sample (A), an abraded sample (B), a smooth abraded sample (C) and a backside sample (D). Data at 0 C/m^3 or larger than ±5 C/m^3 appear in white.

The charge packet-like evolution observed in Figure 38, at high field strength, may originate from a strong field dependency in the injection rate, or a tunneling onset [106]. This mechanism provides a sudden large quantity of injected charge when the electrode's electric field strength is transiently increased. Such packets can propagate and cause field enhancement upon arrival at the opposite electrode, triggering a new charge packet. While the results observed in Figure 38 cannot indisputably reveal the nature of the injection type, it indicates a strong field dependency in charge injection for such surface types. Additionally, charge decay during depolarization is observed to initially proceed at a fast pace, but after 3–4 hours it slows down significantly. Considering a different ratio between mobile charges (trapped in shallow and inter-level states) over deeply trapped charge, referred to as the mobile charge ratio, explains such depolarization effects. A strong poling field yields a high mobile charge ratio, causing a fast-initial charge decay, while, after some hours (during the low fields in depolarization) mostly deeply trapped charge remains. Poling at medium (observed in Figure 35) or low fields could yield a lower mobile charge ratio, therefore not giving rise to the fast-initial charge decay. This observed decay nature demonstrates that trapping and detrapping mechanisms exhibit a field dependency, increasing the mobile charge ratio with poling field strength. Finally, the high positive charge densities appearing at rough anodes are also visible in the depolarization sequence.

4.2.1.3 Impact of temperature

Figure 39 shows a typical impact of temperature on charge accumulation at 50 °C and 70 °C for abraded (A, B) or backside (C, D) anodes, both with backside cathodes.

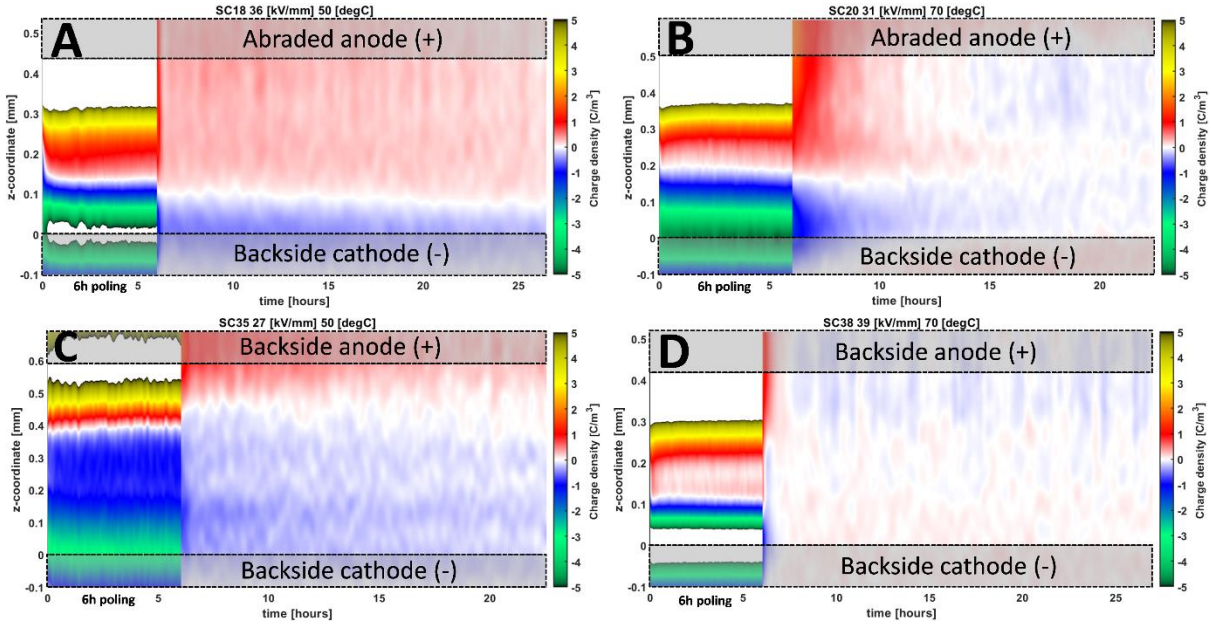

Figure 39. PEA measurements performed at 50 °C (A and C) and 70 °C (B and D) with +15 kV of poling voltage. Top figures (A and B) show measurements with abraded anode, while bottom figures (C and D) feature a backside anode. Data at 0 C/m^3 or larger than ±5 C/m^3 appear in white.

The mean charge density, accumulating during polarization, was weakly affected by temperature, which was consistently observed in all the performed measurements. Furthermore, during the depolarization, the decay rate increases with temperature, which is also observed regardless of electrode type. Thermally activated detrapping explains such increased decay rates, yielding an increased mobile to trapped charge ratio. However, an increase in opposite charge injection may also occur when the electric field orientation at the anode or cathode becomes reversed during depolarization (created by the residual charge density). The decay rate near the anode seen in Figure 39B is faster than in the bulk of the material, which may be attributed to such an injection mechanism.

4.2.2 DC breakdown tests

4.2.2.1 MV-sized cables

The results of DC breakdown tests on MV cable ends, with 2-parameter Weibull distributions estimated through equation (25), are shown in Figure 40.

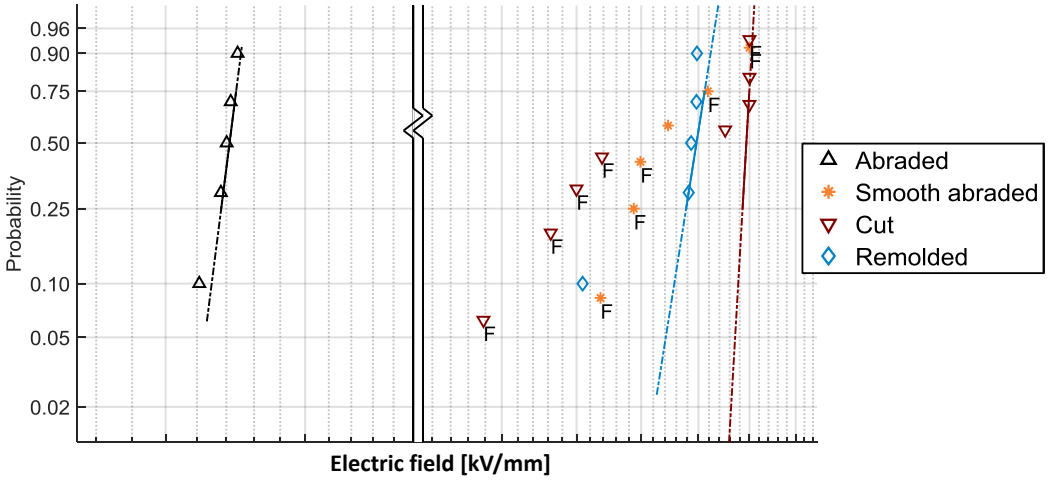

Figure 40. Weibull probability plot of DC breakdown test on MV sized cable ends. Flashovers are indicated with "F" and are right-censored in the analyses. Mean field strength is estimated from breakdown voltage divided by sample thickness at the breakdown position.

The shape parameters *k*, of the distributions shown in Figure 40 are low for the remolded, abraded and cut surface type, indicating a repeatable breakdown phenomenon. However, on smooth abraded and cut surface types, many flashovers occurred which made for a more challenging assessment. Using the flashovers as right-censored data can still anticipate a breakdown strength exceeding the flashover values. Thus, the abraded surface triggered breakdowns at low electric field strength, at levels above known onset field values for significant charge injection into DC cables [107]. The cut surface, on the other hand, exhibited significantly higher breakdown strength, near the limit of the test cage. Thereby, a strong correlation between surface smoothness and breakdown strength was observed. Furthermore, the limited data of smooth abraded surfaces indicated a reduction of breakdown strength compared to the cut surface, which again showed the correlation with surface roughness. The remolded surface, however, breaks this correlation as its practically non-observable roughness level should have made for even higher breakdown strength. Thus, other effects could influence its breakdown strength. In addition to the breakdown strength correlation, also an impact on the shape of breakdown and degradation channels was observed, shown in Figure 41.

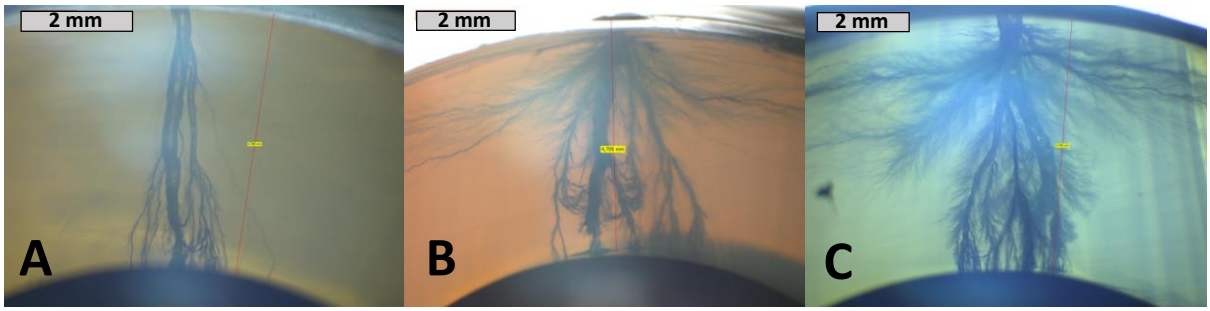

Figure 41. Breakdown channels in cable ends with abraded (A), remolded (B) and cut (C) surfaces. Different coloration of the material bulk originates from the used light source.

For all surface types shown in Figure 41, inward branching degradation channels are observed. Widened full breakdown channels are also observed, with the degradation channels on some occasions bending inwards towards the main channel. This observation is indicative of tree propagation occurring prior to the feedback and streamer development in the main breakdown channel. While the abraded surface (Figure 41A) only shows such features, the remolded and cut surfaces show here additional discharge traces, propagating mainly at a certain layer depth

in both tangential (z) and axial (φ) orientations. Thus, when such discharge traces were observed from above, a star-like shape centered on the main channel was seen, as shown in Figure 42.

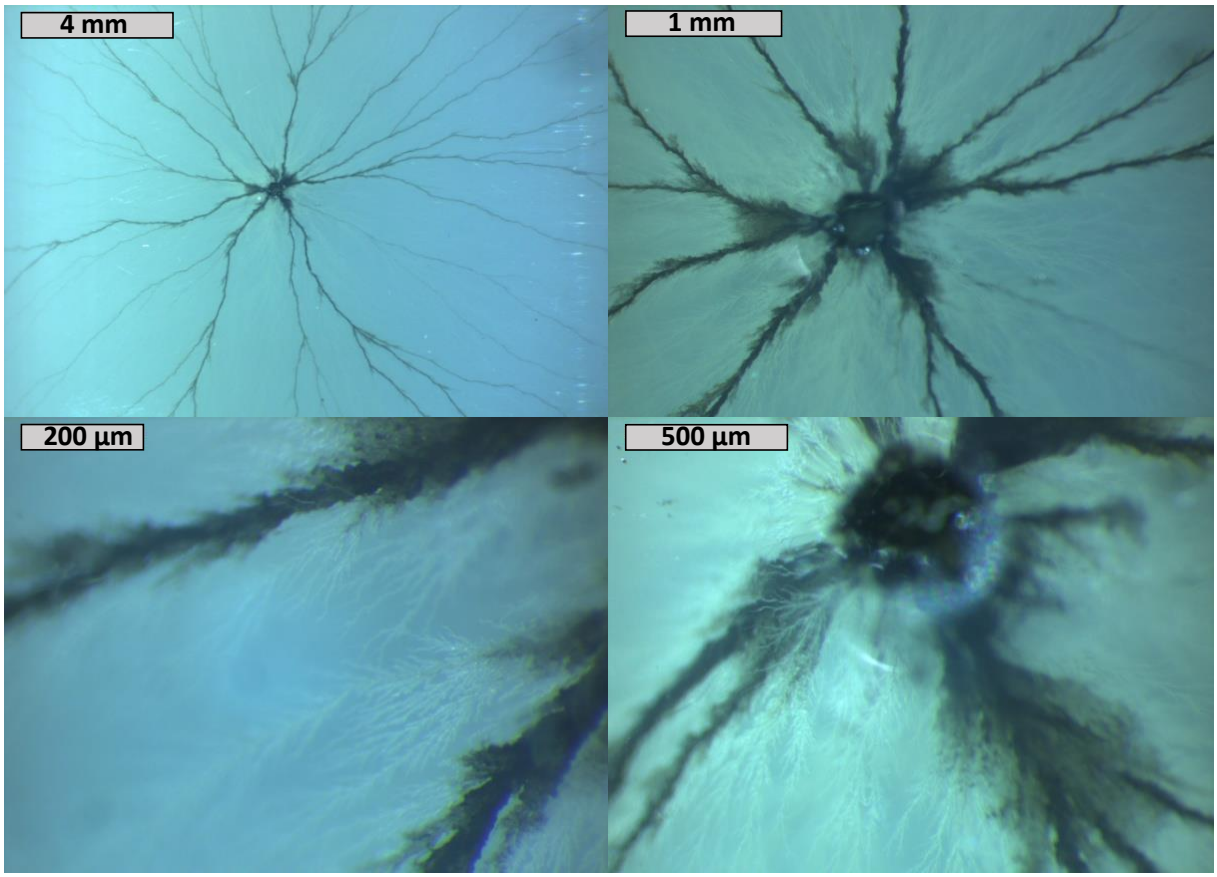

Figure 42. Breakdown channels viewed from above for a breakdown in a remolded cable end at different magnifications.

The star-shaped pattern is composed of larger channels with black carbonized deposits and branching from them a high density of small discharge traces (white, lacking such deposits). The channels lacking carbonized deposits are invisible in Figure 41, because of light scattering in the thicker specimen bulk. Such star-shaped breakdown channels are indicative of a highly stressed material, with a driving force for propagation within a cylindrical shell towards the main channel. As orientation (tangential (z) and axial (φ)) is unaligned with the electric field's orientation (r), accumulation of significant space-charge density towards the outer surface is indicated. Upon breakdown initiation, this charge cloud creates high local field strength towards the main channel, discharging the region in a stepwise manner.

The breakdown location was additionally affected, occurring at different distances from the outer semiconductor shield break. For the abraded surface breakdown occurred repeatedly within a few mm from the SC break, while this distance was significantly increased and showed greater spread for the other surface types.

4.2.2.2 Cable peelings

Initial tests making use of a guard ring consistently resulted in flash-overs at around -45 kV independent of surface type. This voltage corresponded to a tangential field strength of around 4.5 kV/mm, far below the breakdown strength of the oil. While reduced breakdown strength along interfaces was expected, such low strength was not anticipated. After removal of the

guard ring, flashovers occurred infrequently, and the voltage limit of -60 kV could be reached. Also, neither flashovers nor impact on breakdown strength was observed from priory made breakdowns or sample edges when located beyond 20-30 mm from the test area. Due to such robustness, multiple DCBD tests could be performed in different regions on the same peeling.

The results of DC breakdown tests are shown in Figure 43, where the peeling surface type facing the ground electrode was altered.

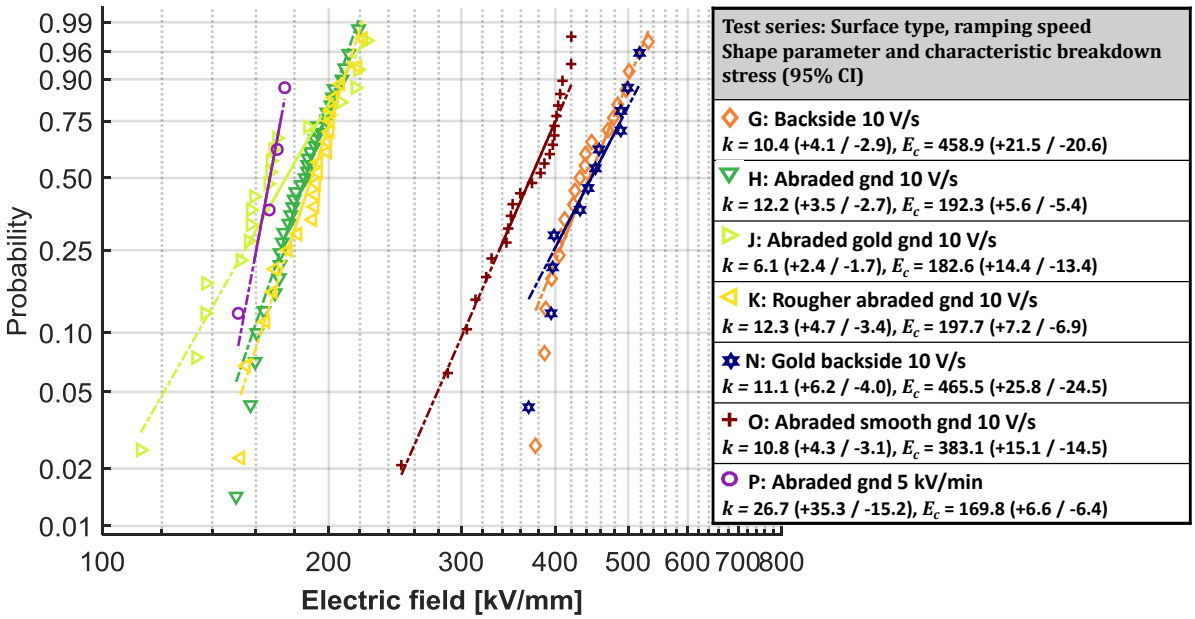

Figure 43. Weibull probability plot of the DC breakdown tests performed on cable peelings at room temperature,10 V/s ramping speed and negative polarity. Any flashovers or withstands are excluded from the statistics. Shape (k) and characteristic breakdown stress (E_c) parameters are indicated with their 95% confidence intervals in the legend.

Due to the narrow confidence intervals of the estimated Weibull parameters, these results can be estimated with a higher statistical certainty, as compared to the results on MV cable tests. Also, a scaling effect is recognized from significantly higher breakdown strength in peelings compared to the MV cable tests. Geometric scaling is known to affect space charge properties, due to different bulk to surface ratios between the two sample types. However, correlation between surface roughness and characteristic breakdown stress (E_c) is again observable, with here a few additional test series added. The additional gold sputtered backside and abraded surface types (series N and J in Figure 43) indicated that such a surface treatment did not improve breakdown strength against their non-sputtered counterparts (series G and H). These similarities indicated that the interstitial oil layer between the sample and ground electrode had neglectable impact on the results. Furthermore, series P was performed elsewhere on thicker specimens, investigating the influence of sample thickness, and will be addressed later in this section.

Before elucidating the impact of roughness in the preparation types (series G, H, K, and O), their breakdown characteristics at higher voltage ramping speed are addressed, shown in Figure 44.

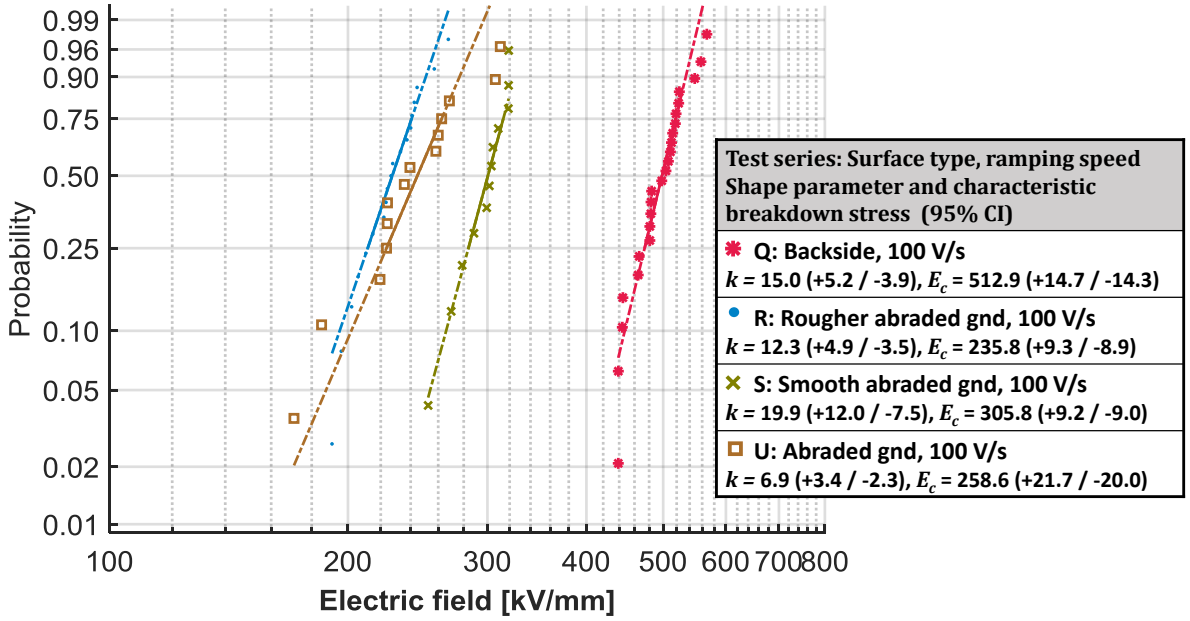

Figure 44. Weibull probability plot of the DC breakdown tests performed on cable peelings at room temperature, 100 V/s ramping speed and negative polarity. Any flashovers or withstands are excluded from the statistics. Shape (k) and characteristic breakdown stress (E_c) parameters are indicated with their 95% confidence interval in the legend.

As observed in Figure 44, the characteristic breakdown stress (E_c) increased with faster ramping speed for all surface types, except for smooth abraded (series S). Therefore, a re-assessment of its roughness level was made post-measurement, to better understand the discrepancy's origin. The impact of surface roughness, quantified by its *Sdq* parameter, on breakdown strength is better visualized in Figure 45.

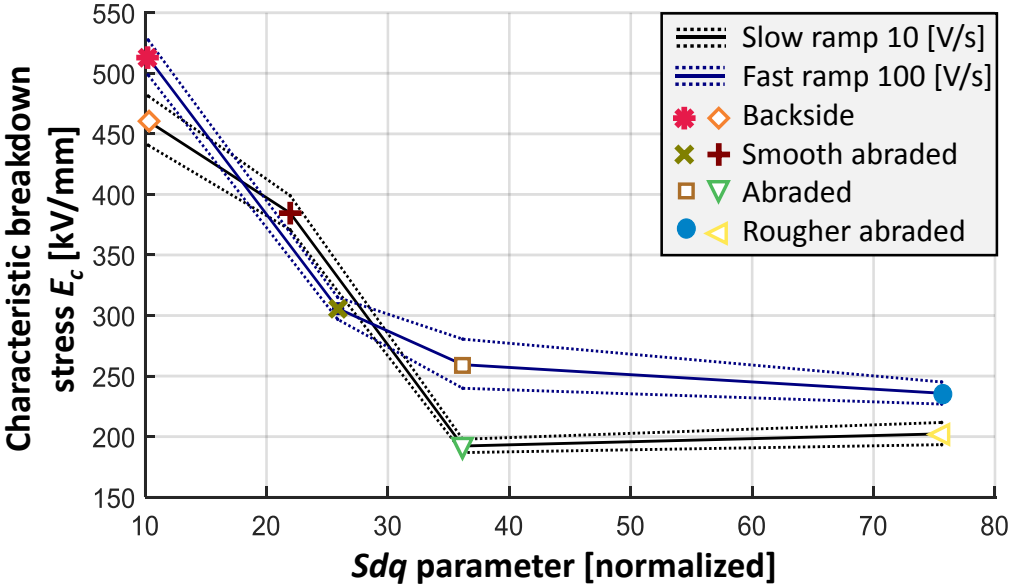

Figure 45. Breakdown strength against the (normalized) roughness parameter Sdq. Dotted lines indicate the 95% confidence interval of Ec. The roughness of smooth abraded surface was re-assessed after the breakdown test, shifting the 100 V/s x-value from 22 to 25.

As observed in Figure 45, backside samples (series G and Q) yielded high breakdown strengths of comparable magnitude to plate tests on this material [108]. Only a marginal reduction of

intrinsic breakdown strength (i.e. strength of an infinity smooth surface) is expected due to their low but finite smoothness level. Furthermore, the results show the inverse correlation between roughness and breakdown strength, which seemingly levels out at higher roughness levels yielding no further reduction of breakdown strength. The results with different ramping speeds indicate an exponential life-time relationship. Given the stress-failure time relationship expressed with the IPL in equation (26), and making use of the inverse of the ramping fields (expressed as t/E instead of t, thus changing the IPL exponent from $-n$ to $-(n+1)$), a life-time exponent of $n \approx 14$ was estimated. This exponent level matched the increased breakdown strength for both the backside samples (series G and Q, Figure 43 and Figure 44) and for the abraded samples (series P, H and U). The exponent also matched values of polyethylene found in literature [104], [109]. Most surface types showed weak impact of sample thickness on breakdown strength, especially when the IPL was accounted for. Abraded surfaces (series P, H and U), were tested with thickness ranging from 100 to 500 µm revealing only marginal decrease of breakdown strength at increased sample thickness. This low impact of the bulk-interface ratio could indicate a breakdown phenomenon strongly governed by the interface. Such trends can be compared with maximal field and charge quantities in the interfacial domain estimated through simulation in sections 6.1 and 6.4.

4.3 Electrical result interpretation

The experimental results allow for a series of observations to be made. The DC breakdown tests showed an inverse correlation between surface roughness and the characteristic breakdown stress (Ec). The internal charge evolution during the experiment remains unknown, making it challenging to predict the origin of effects beyond the observed correlation without a simulation approach. The space charge measurements, on the other hand, provide information about the internal charge evolution, for which homocharge accumulation was observed to increase with the roughness level of the electrode. This correlation is symptomatic of increased charge injection originating from the rough interfacial geometry. However, the exact quantities of charge density and field strength at the electrodes remain hidden in the measurement signal. Furthermore, the measured levels of local charge densities and field strengths are well below the levels explored in the DC breakdown tests.

Conclusively, the measured levels of space charge density and breakdown strength showed correlation with the level of surface roughness. However, before the causation of such behavior can be determined, the involved charge transport mechanisms must be elucidated. Since charge transport involves a multitude of complex carrier-matrix and other interactions, their contribution to the internal charge evolution must be assessed. It is for this reason a bipolar charge transport modelling approach is required before any further interpretation of the observed measurement results can be made. The performed simulations are described in chapters 5 and 6, allowing for the development of the theoretical framework in section 7.3.

Chapter 5

Simulation background and methodology

This section summarizes bipolar transport and injection mechanisms unique to the present study, and their implementations. As the experiments (e.g. the polarization and depolarization stages in the space charge measurements) featured a strong diversity in the applied electric field strengths, assessments of the operating field dependent transport mechanisms were paramount. Furthermore, such mechanism models were purposely developed to account for significant mesoscopic variations of local field strengths in rough interfacial geometry.

The simulation approach begins with a description of the material's DOS and its discretization required for formulating the carrier-matrix interactions. Thereafter, described are principle features of field-dependent charge transport, detrapping, trapping and recombination effects which constitute the base for the herewith developed model. Furthermore, modifications of charge injection mechanisms and the formulation of a hopping injection mechanism, including the impact of surface roughness on the average charge injection current density are described. Transport and injection mechanisms are thereafter summarized, following a review on their impact on current densities, field strength and charge density in the material. Also, their effect on local ageing mechanisms is addressed. Lastly, the practical realizations of different modelling approaches are described.

5.1 The state density and its discretization

As shown earlier in Figure 10 C, the adopted DOS description is similar for holes and electrons, with gaussian distribution functions representing deep traps and exponential depth extensions of the conduction and valence band edges for shallow traps. These states and their depth-density relations (or traps if their energy is measured from the conduction/valence band edge) are also shown in Figure 46 A and B. It is useful to introduce different classifications based on their energetic levels. Four discrete levels for both electrons and holes are distinguished, i.e. deep states, inter-level states, shallow states and hot carrier states (the states for band transport). From this description, a mobility gap approach with a single deep trap level has frequently been used in literature to describe bulk conduction in polymers [27], [30], [37], [39], [40], [42], [44], [48], [52], [53]. It represents a favorable simplification, as depicted in Figure 46 C and D.

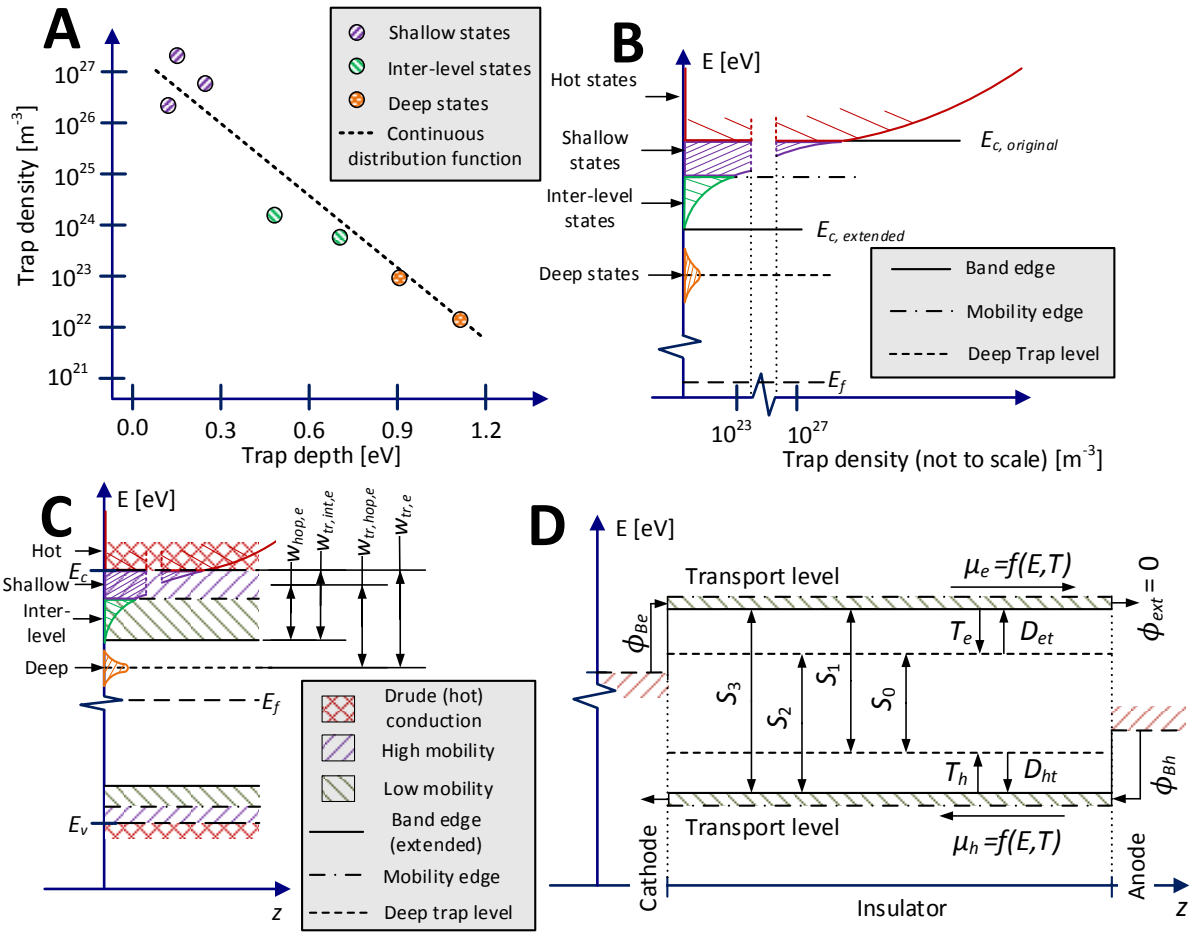

Figure 46. Trap density-depth relations and classifications in polyethylene (A), adapted from [35] *and* [53]. *Extension of the density-trap depth relations for electrons in relation to the conduction band edge (B). Simplified band gap description with band gap extension (C), only showing the electron states. Effective mobility approach used in calculations (D). Energetic levels are not to scale.*

Hot states refer to the states in the valence or conduction band. However, only on rare occasions will charge carriers be at the energetic level of the conduction or valence bands (where a near-infinite state density exists), as significant energy is required for their excitation. Such "hot" carriers are therefore considered to only exist after the onset of polymer ageing, resulting in ionizing collisions with the polymer lattice after being accelerated by the local electric field.

Shallow states/traps represent physical defect and conformational discrepancies in the material [35], [63]. They feature energetic depths in the range of 0.05-0.3 eV and are present in densities in the range of 10^{26}-10^{27} m^{-3} [35], [110]. Thereby, each nm^3 of material contains 0.1 to 1 state, yielding a mean separation between them of about 1-2 nm. Due to their high density, transport through shallow traps is the main mode of spatial charge movement in the material. Resting times within these states are so short that inter-state conduction amongst them cannot be directly used in calculation. Therefore, the shallow trap level is not represented in the charge transport models, as shown in Figure 46 D. Instead, their presence is accounted for indirectly within the parametrization of charge transport equations. The respective state densities, $N^0_{shallow(e,h)}$ express the most frequently occurring shallow states at the upper level in the exponential distribution.

Inter-level states feature energetic levels in the range of 0.5-0.7 eV and originate from the lower tail of the exponential distribution. Their density is in the range of 10^{23}-10^{24} m^{-3} [53],

corresponding to ~10-20 nm of average spacing between the isolated inter-level states. While shallow and inter-level states originate from the same exponential distribution depicted in Figure 46 B, the sake of separating them into two classes is because charge transport rates are governed by the energetic level of the inter-level states in the lower end of the exponential distribution. However, such states are most likely surrounded by states from the upper end of the exponential distribution. Thereby, charge transport is likely to be limited by a hopping process between the inter-level states through the surrounding shallow states. The respective state densities $N^0_{int(e,h)}$ express, in the transport equations, the rate-limiting states from the lower tail of the exponential distribution.

Deep states, representing physio-chemical defects in the material [35], [63], can capture charge carriers for prolonged periods. Their energetic depths can be in the range of 0.9-2 eV and their density in range of 10^{20}-10^{21} m^{-3} (i.e. a state density of 16-160 Cm^{-3}) [35], [53]. This density corresponds to far higher spacing, in the range of ~100-200 nm, between individual deep states, compared to the other states. Because of their low density, inter-deep trap conduction without interaction of inter-level states is highly improbable. Therefore, before further transport can ensue, the carriers captured in deep states require a detrapping process, with energetic barrier $w_{tr(e,h)}$ (indicated for the electron case as $w_{tr,e}$, in Figure 46 C). The respective state densities, $N^0_{deep(e,h)}$ express single levels of deep states. While additional, deeper energy levels can also be considered, such energy levels are likely to be present in even lower density.

5.1.1 Modified hopping transport description

Since both shallow and inter-level states are contributing to the hopping rate, the hopping mode through such states is depicted in Figure 47.

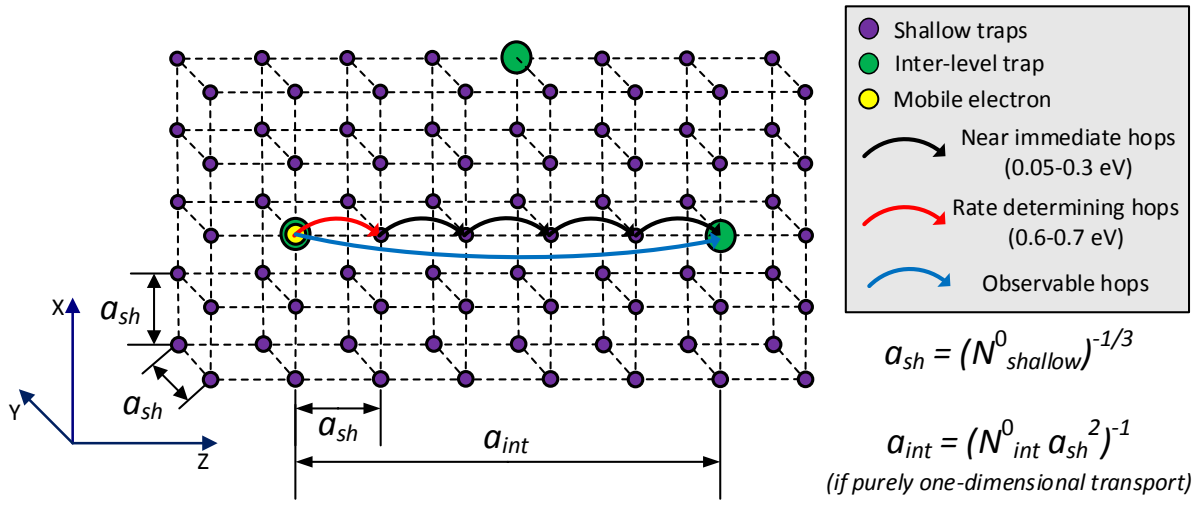

Figure 47. Schematic representation of hopping carrier transport through a cubic lattice of shallow states. Inter-level states can be assumed as isolated in the lattice, owing to significantly higher shallow state density in relation to the inter-level state density ($N^0_{int} << N^0_{shallow}$).

As seen in Figure 47, the largest encountered energy barrier (disregarding deep states) arises from the isolated inter-level states. Thereby, hopping from such states in the lower tail of their distribution will be the rate-determining step in the charge transport. Thereby, the hopping rate is determined by the spacing to the neighboring shallow traps (or, the shallow state spacing) and the energetic depth between the inter-level trap and its surrounding shallow states. However, due to the fast transfer through the shallow states, the net observable hop length will

be defined by the distance between inter-level states, as the carrier will seemingly move from one inter-level state to the next one. Based on this description, the carrier's mobility in $m^2/(V \cdot s)$ can be expressed as:

$$\mu_{(e,h)}(E,T) = \frac{2va_{int(e,h)}}{E} e^{-\frac{w_{hop(e,h)}}{k_B T}} \sinh\left(\frac{eEa_{sh(e,h)}}{2k_B T}\right) \tag{28}$$

where e is the elementary charge measuring $1.602 \cdot 10^{-19}$ C, k_B is the Boltzmann's constant, T is the temperature in K and E is the electric field strength in V/m. v is the attempt-to-jump/escape frequency (defined as $v = k_B T/h \approx 6.2 \cdot 10^{12}$ s^{-1} at 25 °C), and $w_{hop(e,h)}$ is the average encountered energy barrier for hopping in eV. $a_{sh(e,h)}$ and $a_{int(e,h)}$ are, respectively, the average spacing between shallow and inter-level traps in meters.

5.1.2 Detrapping mechanisms

To express the detrapping mechanism over a wide range of electric field strengths, it can be separated into superimposed low and high field mechanisms expressed as:

$$D_{(e,h)t} = D_{0(e,h)t} + D_{(e,h)t}(E) \tag{29}$$

where the first term $D_{0(e,h)t}$ expresses the process at low fields in s^{-1}, and the second term $D_{(e,h)t}(E)$ represents a hopping detrapping mechanism in s^{-1}. To express an electric field-dependent detrapping rate, activating deeply trapped electronic carriers, the neighboring states surrounding the deep trap must be accounted for. A mechanism analogous to the previously outlined hopping transport can be adopted, now describing a thermally activated tunneling process from the deep trap to its neighboring states. As the states present in highest density are shallow states from the upper level of their exponential distribution, such states are the most probable neighbors. The deep trap can therefore be assumed to share a cubic lattice with surrounding shallow trap states separated by $a_{sh(e,h)}$. As the hopping mobility defines how swiftly a carrier moves when pulled by an electric field, the activation rate can thus be deduced from expression (28) yielding thereby the detrapping rate as:

$$D_{(e,h)t}(E) = 2ve^{-\frac{w_{tr,hop(e,h)}}{k_B T}} \sinh\left(\frac{eEa_{sh(e,h)}}{2k_B T}\right) \tag{30}$$

where $a_{sh(e,h)}$ is the mean spacing in m and $w_{tr,hop(e,h)}$ is the mean energetic barrier in eV, both of which measure between the deep trap and its surrounding shallow traps. When electric field approaches zero, the field-dependent detrapping rate in equation (30) approaches zero as well. Therefore, a low field expression for detrapping becomes:

$$D_{0(e,h)t} = ve^{-\frac{w_{tr(e,h)}}{k_B T}} \tag{31}$$

where $w_{tr(e,h)}$ now measures the energy from the deep state up to the conduction/valence band edge. At low electric field strength, thermal activation up to the band edge with subsequent transfer to the nearest shallow trap is thus more probable (gives a higher rate) than a thermally activated tunneling process to the nearest shallow trap. After activation from the deep trap to a neighboring shallow trap, the electronic carrier is likely to move further, so that it appears in an inter-level trap in its vicinity as $N^0_{int} >> N^0_{deep}$.

5.1.3 Poole Frenkel effect performance

The field dependencies of detrapping rates of PF effects (equations (7) and (8)) and the hopping detrapping mechanism (equation (30)) are illustrated in Figure 48.

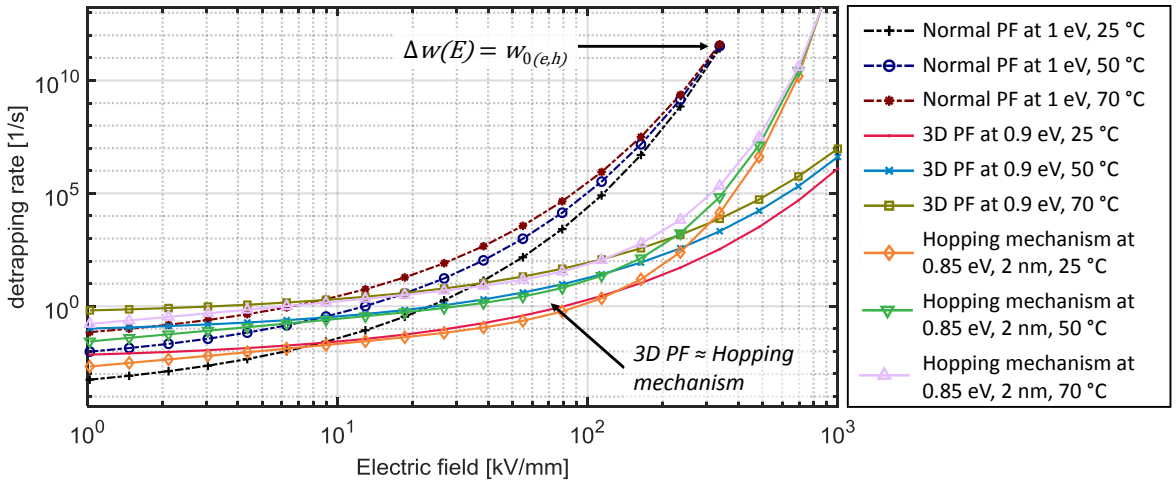

Figure 48. Detrapping rates and their field and temperature dependencies. Three types, a normal (one-dimensional) PF effect, a 3D PF effect, and a hopping detrapping mechanism are shown.

It is observed that the one-dimensional PF effect expressed by equation (6) is characterized by such a high field dependency that it exceeds 1 eV barrier at ~350 kV/mm ($\Delta w(E) > w_{0(e,h)}$). It therefore poorly describes charge transport in clean materials at high field strengths. The 3D PF effect expressed by equation (8) shows, on the other hand, a lower field dependency. It yields a similar dependency as the hopping detrapping mechanism at field strengths 10-100 kV/mm.

When PF effect was used in simulations of ultra-clean XLPE peelings [111], it exhibited a too strong field dependency, forcing the use of high barrier height, ultimately resulting in underrepresented detrapping rates during the depolarization. On the other hand, given the similar field dependencies in the three-dimensional PF effect (used by Liu et al. [47]), and the hopping mechanism, both can yield similar results. However, as the PF effect relies on a coulomb field interaction between the carrier and the trap site, the deep trap state has electrostatic potential making it a donor or acceptor state. As the energy required for activating such donors or acceptors in polyethylene is still large, they do not contribute to doping of the material at room temperature, as is the case for semiconductors [34]. Such states should thereby exist in neutral form, releasing charge carriers (ionization) only upon significant energetic activation. Thereby, the underlying question on internal carrier generation remains, which is generally not observed in space charge measurements on clean polyethylene [84]. Therefore, the use of PF effect is limited to cases when high content of water or other ionizable impurities exist in the material. An additional issue is that PF effect activates electronic carriers up to the conduction (or valence) band levels, which requires a high energy activation and disregards the impact of any neighboring (shallow) states. It is therefore more appropriate, for clean HVDC cable insulation material, to instead use the hopping detrapping mechanism which considers deep traps as neutral by nature [35].

5.1.4 Charge trapping mechanisms

To describe the effective trapping rate $T_{(e,h)}$ over a wide range of electric field strength, a superposition of low and high field mechanisms is required:

$$T_{(e,h)} = \left(B_{0(e,h)} + B_{(e,h)}(E)\right)\left(1 - \frac{n_{(e,h)t}}{N^0_{deep(e,h)}}\right) \tag{32}$$

where $B_{0(e,h)}$ and $B_{(e,h)}(E)$ are respectively the (core) trapping rates at low and high fields in s^{-1}, and $N^0_{deep(e,h)}$ is the density of deep traps in m^{-3}. The expression in brackets $(1-n_{(e,h)t}/N^0_{deep(e,h)})$ defines the percentage of deep traps not occupied by trapped charge carriers $n_{(e,h)t}$. Thereby, it ensures that any mobile carrier encountering an occupied state is not trapped by it. To define trapping rates, the dominating mechanism at which mobile electronic carriers move in the material must be considered. At low fields, charge movement is presumably dominated by a thermally activated random walk process through shallow traps, as shown in Figure 49. At high fields, charge movement is dominated by hopping aligned with the orientation of electric field.

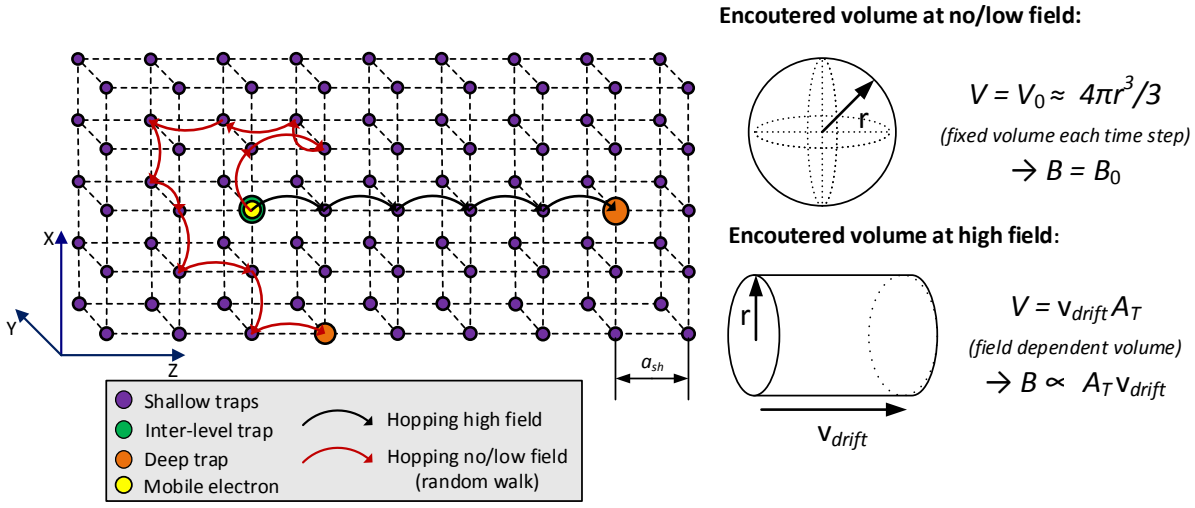

Figure 49. Schematic representation of trapping (and detrapping) concepts. For sake of simplicity, shallow, inter-level and deep traps are assumed to be placed in a shared cubic lattice. Lattice spacing is thereby dependent on shallow trap density only as $N^0_{deep} << N^0_{int} << N^0_{shallow}$. Two deep traps are shown within the shallow trap lattice for illustration purposes. Volumes encountered by the mobile carrier at each time step are shown at low and high fields, from which the number of encountered traps, and thereby trapping rates, can be deduced.

The amount of encountered deep traps can be deduced by considering space (volume) around the hopping carrier through shallow and inter-level states. These are schematically represented in Figure 49 by the sphere and cylinder, respectively depicting probable directions of the random movement at low fields and directional movement at high fields. Based on such assumptions, the following expression for the field-dependent trapping rate, as used by N. Liu et al. [47], is introduced:

$$B_{(e,h)}(E) = P_{T(e,h)} N^0_{deep(e,h)} A_{T(e,h)} \left|\vec{v}_{d(e,h)}\right| \tag{33}$$

where $P_{T(e,h)}$ is a unitless trapping probability, $A_{T(e,h)}$ is the circular trapping area in m^2 (or capture cross-section [47]) and $\mathbf{v}_{d(e,h)}$ is the drift velocity in m/s. The trapping rate at low field strength $B_{0(e,h)}$, used in equation (32) can be introduced assuming that carriers are thermally excited from inter-level states, after which they move in a random direction to meet a deep trap. This description yields the trapping rate:

$$B_{0(e,h)} = \frac{N^0_{deep(e,h)}}{N^0_{int(e,h)}} ve^{-\frac{w_{tr,int(e,h)}}{k_B T}} \quad (34)$$

where the ratio between deep trap density $N^0_{deep(e,h)}$ and inter-level state density $N^0_{int(e,h)}$ is used as it expresses the probability to encounter a deep trap. The energetic barrier $w_{tr,int(e,h)}$ in eV is the depth of the inter-level state in relation to the conduction/valence band edge. This barrier is larger than $w_{hop(e,h)}$, which measures from the inter-level state to the nearest adjacent shallow trap.

Only extreme cases are well defined; at high fields where charge transport is aligned with the electric field's orientation, and at low fields where it is mostly 3D oriented (due to random carrier motion with very small component aligned with electric field). Therefore, the distance a_{int}, traveled by a charge carrier until the next inter-level state is encountered, is within the bounds:

$$1/\sqrt[3]{N^0_{int}} \leq a_{int} \leq 1/N^0_{int} {a_{sh}}^2 \quad (35)$$

where N^0_{int} is the inter-level state density in m^{-3}. Hence, the inter-level state spacing a_{int} should fall within the limits set by equation (35), and no direct relation exists between it and its state density.

5.1.5 Langevin recombination

To define recombination rates, the charge carrier drift velocity $\mathbf{v}_{d(e,h)}$ is again considered in conjunction with the local coulomb forces acting between the carriers of opposite charge. The combination of these effects, yields the so-called Langevin recombination rate, as used by e.g. Daomin et al. [112] and Le Roy et al. [27]. In Langevin recombination, charge carriers hop towards oppositely charged ones if located close enough in the lattice. Between each hop, a short but finite time is spent in a shallow or inter-level state, causing the energy (velocity) of the carrier to be instantly dissipated to the surrounding lattice. Since there is no stored energy causing the charged particle to "fly past" the opposite charge carrier, the capture cross-section should be solely related to the local electric field around the carriers. At low electric fields, this carrier motion yields fixed recombination rates, while at high electric fields, a field dependency is introduced through the superposition of the carriers' coulomb fields with the background electric field [111]. Thereby, the capture cross-section, m^2; is expressed as:

$$A_R = \frac{e}{\varepsilon_0 \varepsilon_r E} \quad (36)$$

For recombination between two mobile charge carriers, one of them is considered stationary (in an inter-level state) as the hops made by the other carrier (through the shallow traps) proceed at a much faster rate. The event of both carriers being simultaneously excited from their respective inter-level state and approaching each other through the shallow trap lattice is thus improbable. Equation (36) is therefore considered valid for both mobile–mobile and mobile–trapped carrier interactions, at high electric field strength. A mobile charge carrier is likely to exhibit an increased probability of hopping towards an opposite charge carrier, given that their separation is low enough. This scenario is further exemplified in Figure 50, where a mobile electron hopping towards a trapped hole is shown.

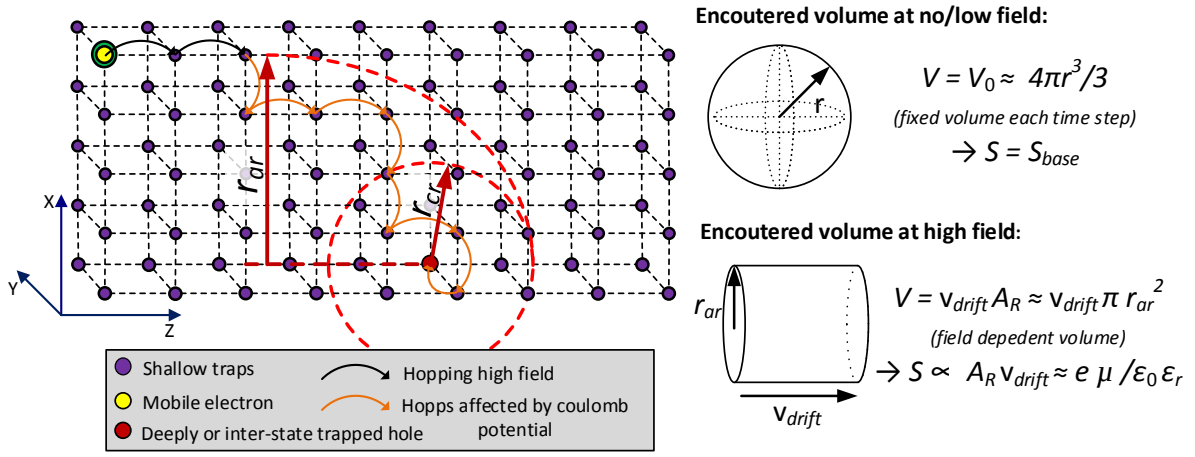

Figure 50. Charge recombination scheme (mobile electron–trapped hole) assuming again the charge movement patterns to be random at low field strength and aligned with field orientation at high field strength. The effect of local coulomb interaction between the participating charge carriers is added through the critical radius r_{cr} and recombination radius r_{ar}. Shallow traps are assumed to be uniformly spread in a cubic lattice.

The patterns shown in Figure 50 indicate spherical interaction regions around the mobile carrier hopping through shallow and inter-level trap sites. Whenever an opposite charge carrier exists within the sphere, the mobile carrier is pulled in towards it by electrostatic forces and the probability for the recombination increases. At low fields, this spherical volume yields base level recombination rates $S_{(0\text{-}3),base}$, whereas, at high field strengths, the effect of the field-controlled drift of the charge carriers needs to be considered. Therefore, the following expressions are suggested for the recombination rates:

$$\begin{cases} S_0 = S_{0,base} \\ S_1(E) = S_{1,base} + P_R A_R |\vec{v}_{de}| = S_{1,base} + P_R \dfrac{e\mu_e(E,T)}{\varepsilon_0 \varepsilon_r} \\ S_2(E) = S_{2,base} + P_R A_R |\vec{v}_{dh}| = S_{2,base} + P_R \dfrac{e\mu_h(E,T)}{\varepsilon_0 \varepsilon_r} \\ S_3(E) = S_{3,base} + P_R A_R |\vec{v}_{de} + \vec{v}_{dh}| = S_{3,base} + P_R \dfrac{e(\mu_e(E,T) + \mu_h(E,T))}{\varepsilon_0 \varepsilon_r} \end{cases} \quad (37)$$

where for trapped hole-trapped electron recombination S_0, it only exhibits a base level $S_{0,base}$, and no velocity dependency as both carriers are stationary. S_1, S_2 and S_3 define recombination rates for trapped hole–mobile electron, mobile hole–trapped electron and mobile electron–mobile hole recombination, with respective base level rates $S_{1,base}$, $S_{2,base}$ and $S_{3,base}$, in m^3/s. P_R is the unitless recombination probability, A_R is the capture cross-section in m^2 defined by equation (36), $\mathbf{v}_{de}$ and $\mathbf{v}_{dh}$ are the respective drift velocities of mobile electrons and holes in m/s. The recombination rate at high field is derived based on the assumption of the cylindrical shape of the interaction region covered at each time step. Note that the multiplication of capture cross-section (equation (36)) with drift velocity (equation (4)) cancels out E^{-1} with E, yielding the term $e\mu_{(e,h)}/\varepsilon$ in the recombination rates. Equation (36) thus exhibits a direct dependency on carrier mobilities, and recombination rates will thereby exhibit a field and temperature dependency inherited from the mobility expression.

5.2 Charge injection mechanisms and roughness simulation

This section describes adaptations made to Schottky and FN injection models for improving their performance in the simulations. The modifications made to Schottky injection do not represent physical behavior but are required to reduce injection currents at low field strength (during depolarization). For FN injections, physical effects such as temperature and the image charge effects are accounted for by adopting modifications provided in literature [56]. Thereafter, a hopping injection equation is formulated. The chapter ends by describing the relationship between local (J_{local}) and average (J_{avg}) injection current densities, the latter of which may account for rough interfacial geometry in 1D simulation.

5.2.1 Adaptations of Schottky model

An underlying issue with Schottky injection is its low field injection rate. To better describe low injection current densities observed at low field strength in experiments [30], the exponential field terms in equation (14) can be reduced with a factor, f_s:

$$J_{S(e,h)} = \lambda_{R(e,h)} A_0 T^2 e^{\frac{-\phi_{B(e,h)}}{k_B T}} (e^{\frac{e}{k_B T}\sqrt{\frac{eE}{4\pi\varepsilon_0\varepsilon_r}}} - f_s) \tag{38}$$

where the unitless term f_s, is used as either zero or one [27], [30], [37], [39], [40], [42], [44], [48], [52], [53]. Using $f_s = 0$ results in the unmodified Schottky equation. When it is equal to one, charge injection is reduced below 1–2 kV/mm and no charge is injected at zero field strength. This modification ($f_s = 1$) was among others used by Le Roy et al. [27].

Another method to further reduce the injection rate below a certain (ohmic) field threshold $E_{ohm,th}$, is realized by introducing a (unitless) smooth Heaviside step function:

$$f_{step}(E) = \frac{1}{2}(1 + \frac{2}{\pi}\tan^{-1}(S_{pr}(E - E_{ohm,th}))) \tag{39}$$

where $E_{ohm,th}$ is an ohmic threshold field, possibly in the range of 1–5 kV/mm [113], and S_{pr} is a spread parameter used to widen the transition and tune the base level below $E_{ohm,th}$. To gain more accurate injection rates at low and medium field strengths, equation (39) is multiplied with equation (38).

5.2.2 Temperature and image charge effects in Fowler-Nordheim injection

It is relevant to also derive an FN expression accounting for the image charge effect, which as depicted in Figure 51B could somewhat reduce the thickness of the tunneling barrier. As illustrated in Figure 51C, the FN injection expression can also be expanded to account for temperature, affecting the state occupancy in the adjacent electrode.

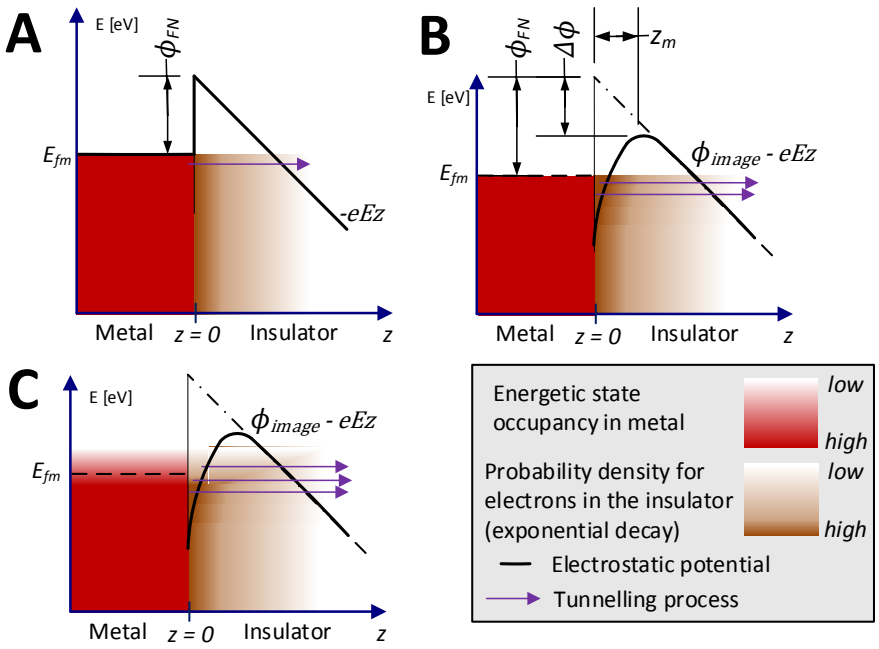

Figure 51. Fowler-Nordheim emission and probability density for the electron. Derived with triangular potential shape at 0 K (A). Impact of image-charge field lowering effect at 0 K (B). Simultaneous impact of temperature and image charge effect (C).

In an approach made by Good and Muller [56], the field lowering effect was introduced, yielding FN current density at 0 K (hence the subscript "*c*" for cold):

$$J_{FN,c(e,h)}(E) = \frac{1}{t\,(\Delta\phi/\phi_{FN(e,h)})^2}\frac{e^3E^2}{8\pi h\phi_{FN(e,h)}}e^{\left(-\frac{4}{3}\sqrt{\left(\frac{2m_e}{\hbar^2}\right)}\frac{\phi_{FN(e,h)}^{3/2}}{eE}v\left(\frac{\Delta\phi}{\phi_{FN(e,h)}}\right)\right)} \qquad (40)$$

Two unitless functions $t(\Delta\phi/\phi_{FN(e,h)})$ and $v(\Delta\phi/\phi_{FN(e,h)})$ were introduced, being dependent on barrier height $\phi_{FN(e,h)}$ and the field lowering effect $\Delta\phi$ described in equation (13). These functions vary between 0 and 1.2, depending on the effective barrier height $(\Delta\phi/\phi_{FN(e,h)})$ as shown in Figure 52.

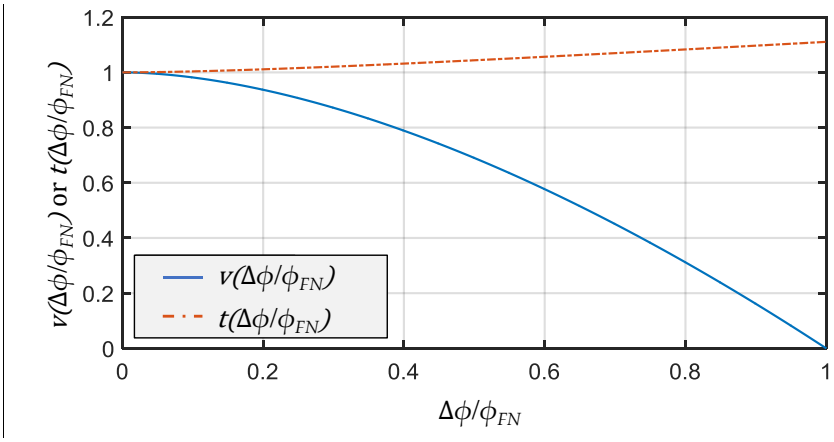

Figure 52. Plots of the unitless functions v and t which are used for including the image charge effect in equation (40). The functions are described in [56].

Whilst it is recognized that the pre-exponential term *t*, only weakly impacts the total current density, a strong impact arises from the term *v*, introduced in the exponential. This modification allows the expression to better match measurement results, making the impact of surface roughness separable from the impact of image charges. Good and Muller [56] also derived an expression for the temperature dependency in FN injection, by extending the integration limits and modifying the momentum density expression. This phonon excitation affects the Fermi-Dirac distribution function in the metal, and for some electrons, now at higher thermodynamic energy, the encountered barrier becomes slightly thinner, as depicted in Figure 51C. The following expression for thermionic field emission is achieved:

$$J_{FN}(E,T) = J_{FN,c}(E) A_T \frac{f_T(E)T}{\sin(f_T(E)T)} \tag{41}$$

where A_T is a constant equal to $2.77 \cdot 10^4$, $J_{FN,c}(E)$ is the cold current density at 0 K as expressed in equation (40) and $f_T(E)$ is a field dependent function expressed as:

$$f_T(E) = t\left(\frac{\Delta\phi}{\phi_{FN(e,h)}}\right)\frac{\sqrt{\phi_{FN(e,h)}}}{E} \tag{42}$$

where the function $t(\Delta\phi/\phi_{FN(e,h)})$, as earlier shown in Figure 52, is field-dependent through the barrier height $\Delta\phi$. As J_{FN} (equation (41)) now includes both the (weak) impact of temperature and the image charge effect, it allows for a more accurate estimation of the injected current density. Thereby, the impact of surface roughness on FN injection can be described separately.

5.2.3 Formulation of hopping injection

In this section, an equation is derived to represent the hopping process through the surface-DOS, as shown in Figure 15B. While it is accurately modelled by Taleb et al. [31], [57], a drawback is brought by the use of spatially dependent parameters for the surface-DOS region in the model. Given this spatial dependency, different approaches (i.e. combinations of trap depth versus distance from the surface) are feasible in the model, all attempting to describe a practically unknown DOS in the surface region. Simplifying such an approach to a single equation, as here presented and shown in Figure 53, is thus favorable for sake of simpler implementation and calibration against the measurement (especially in rough interfacial geometry) as well as a better adoption if changes in material or interface nature arise.

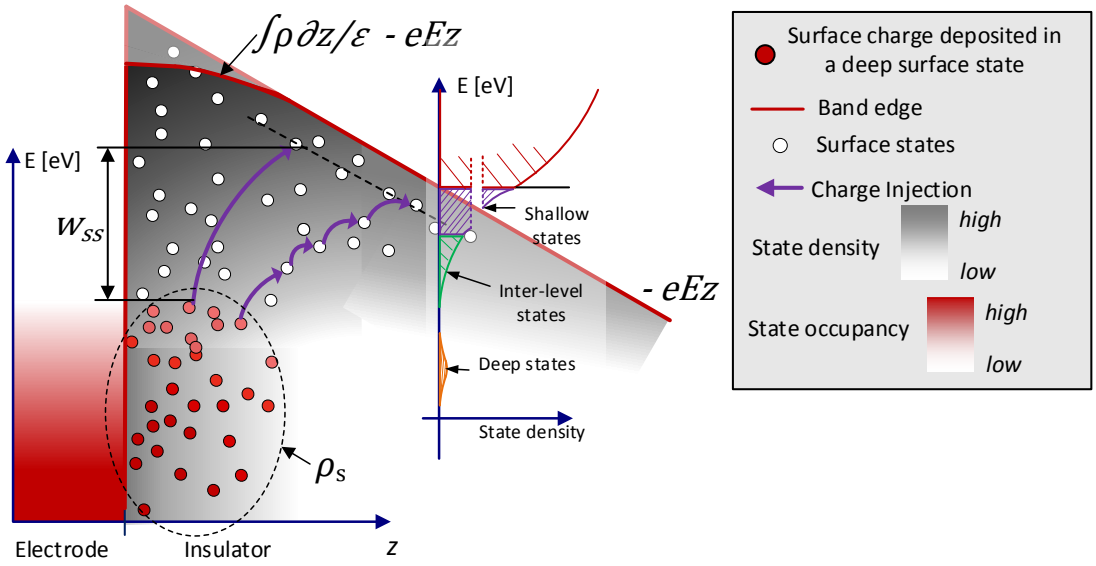

Figure 53. Injection as a hopping process originating from charge deposited in surface states. The surface charge density ρ_s, is assumed to be deposited in deep surface states, which attempt a hopping process including a single, or multiple hops for accessing states in the exponential extension of the conduction band edge.

As the surface charge density ρ_s, C/m^2; is deposited in a region with certain depth, this charge can be assumed to ultimately access states in the exponential tail from the conduction band edge (shallow or inter-level states). The hopping attempt rate can thus be deduced by removing the parameter a_{int} from the (hopping mobility dependent) drift velocity expression in equation (4). Thereby the hopping injection equation can be expressed as:

$$J_{H(e,h)} = 2v\rho_s e^{-\frac{w_{ss(e,h)}}{k_B T}} \sinh\left(\frac{e a_{ss(e,h)} E}{2k_B T}\right) \tag{43}$$

where w_{ss} is either the energetic difference in eV, between the trapped surface charges and the accessed states or represents an average value from the numerous hops made through the surface-DOS. a_{ss} is the mean spacing between trapped surface charges and accessed states, or the mean spacing between states in the subsequent hops. While the barrier and spacing parameters arise from a hopping attempt rate in the unknown surface-DOS, the main challenge is here (and in the approach of Taleb et al. [31], [57]) the definition of the surface charge density ρ_s present at the material boundary. However, by utilizing Gauss law and assuming the electric field strength within the electrode and the boundary to be low (e.g. $E_{electrode} << E_{insulator}$), the surface charge density can be approximated to:

$$\rho_s = \varepsilon_0 \varepsilon_r E \tag{44}$$

As the position and the energetic level of charges positioned in the surface-DOS at the material boundary is not well-defined, the results and parameters of equation (43) must be considered representing an average flux through the surface-DOS. This representation contrasts with the ideal metal-insulator contact considered in Schottky and FN injection, where a well-defined DOS and Fermi-level is present in the metal. The accurate prediction of ideal barrier performance, as in a semiconductor is thus unattainable. Since the hopping injection mechanism represented by equation (43) does not involve such ideal conditions nor the image charge effect, its validity can be extended to less defined injection barriers, for example as when an interstitial

layer of dielectric oil or grease is present between the electrode and insulator in the physical joint interface.

Furthermore, the field dependency in equation (43) (e.g. $E \cdot \sinh(E)$) can be evaluated and compared with the modified Schottky expression (e.g. with $f_s = 1$ yielding $e^{\sqrt{E}}$-1 in equation (38)). The hopping injection mechanism can closely match the Schottky model, except for their dependencies at low fields, where hopping injection predicts lower rates. Conclusively, the introduced modifications in Schottky emission (e.g. $f_s = 1$ and f_{step}), which arose from empirical attempts to match experimental data, are not required for the hopping injection mechanism. The hopping injection mechanism also allows for different field dependencies between electron and hole injection through its parameter $a_{ss(e,h)}$.

Certain limitations also arise when simplifying the approach made by Taleb et al. [31], [57] into a single equation. Effects beside injection, such as a homocharge accumulation in the states that gradually increase in their energy level away from the surface and its response to the arrival of opposite charge carriers at the surface, are lost in the simplification. As shown in Figure 53, the charge density in the surface-DOS makes for a local impact on electric field through $\int \rho dz/\varepsilon$. When it is simplified to a surface charge density ρ_s, assumed to be placed at the boundary layer, no local field and/or recombination impact from opposite charge carriers is accounted for. While such effects could play a certain role in e.g. charge packet formation, the simplification is necessary for modelling the effect of surface roughness. Modelling a spatially varying surface-DOS from an electrode with geometric variations, forms such complexity that cannot yield reproducible nor accurate results. Therefore, the impact of surface roughness described in the next section relies on different charge injection types expressed through equations lacking quantities whose evolutions are to be resolved in the model.

5.2.4 One-dimensional impact of surface roughness

As strong field dependencies exist in the Schottky, FN and hopping injection mechanisms, the injected current density is sensitive to the local electric field at each coordinate point (x,y) on a rough surface. As addressed in section 2.4.3.2, local fields can be expressed with the aid of field enhancement factors $FEF(x,y)$, locally scaling the applied field strength present in the bulk of the material. As illustrated in Figure 54, such field enhancements may locally intensify or reduce charge injection from their respective regions on the surface [81], [82].

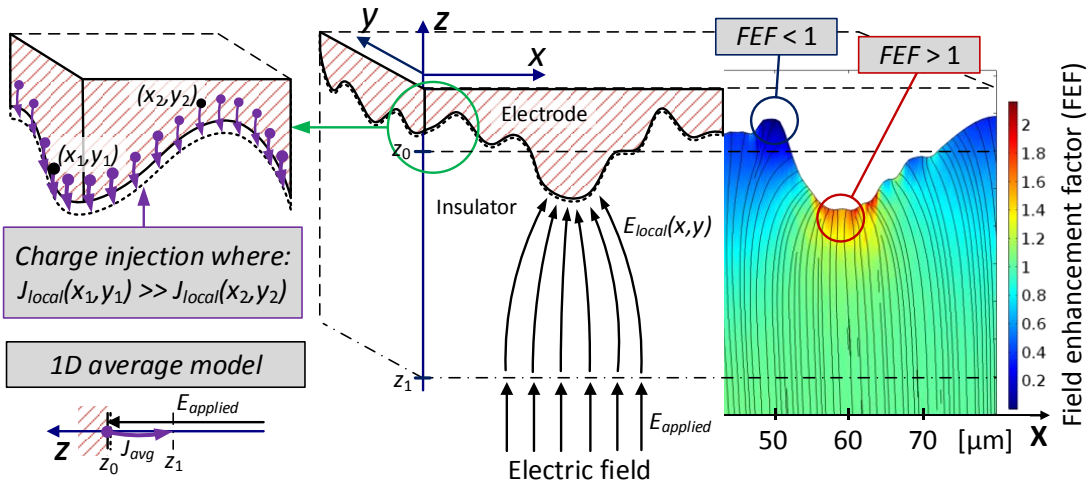

Figure 54. Local impact of surface roughness on electric field and charge injection intensity, yielding an average injection flux J_{avg}, from the surface.

As seen in Figure 54, because of the strong non-linear field-dependencies in the injection equations, the increase in current density from the surface area fractions with *FEF*>1 exceeds the reduction in current density from the surface area fractions with *FEF*<1. Thereby the average amount of current injected from the entire surface increases as soon as the applied field strength causes the local field quantities to enter the non-linear regimes in the injection expressions. Thus, by first calculating the local current density $J_{local}(E_{local}(x,y))$ at each coordinate point on the surface with the local fields previously defined in equation (16), it is possible to derive the average injection current densityas a function of applied field strength [81] by:

$$J_{avg}(E_{applied}) = \iint_A J_{local}\big(FEF(x,y) \cdot E_{applied}\big)dA \tag{45}$$

where integration is performed over the entire area *A*, of the investigated domain in m^2. *FEF(x,y)* are the local, unitless field enhancement factors of the surface displayed in Figure 54. It is assumed that the local current density vector J_{local}, is dominated by the directional component (e.g. J_z) coinciding with that of the average field (i.e., the field produced by ideally smooth electrodes). Some errors are introduced as the local current density directions, being normal to the surface, are disregarded at each point on the irregular surface. The resulting average current density J_{avg} is thereby a field-dependent scalar measure of the charge entering the material at each time step. The averaging in equation (45) can be applied to any (one-dimensional) injection mechanism, such as the expressions for Schottky (equations (14) and (38)), Fowler-Nordheim (equations (15), (40) and (41)) and hopping (equation (43)) injection mechanisms.

From the average current density J_{avg}, roughness dependent injection equations can be derived that make use of a β-parameter with some additional modifications. Given the strong non-linearity in injection equations, and how the average current density is estimated in equation (45), weak impact on injection rate is expected at low field strength, whereas at high field strength, the required β-parameter is expected to be in strong correlation with the maximum FEF values present on the irregular surface. Also, as derived equations are to be used and interpreted as directional quantities (i.e. $\vec{J}(E) = J_{avg}(E)\hat{n}$), this assumes that there is no significant difference between the average charge injected into the non-ideal microscopic interface geometry and the observable macroscopic flux, oriented normal to the electrode in the measurement.

It is also possible to consider the superposition of relevant injection mechanisms (i.e. Schottky, FN and hopping) [86]. This superposition will effectively express a current density fully dominated by one single mechanism at a certain field strength, given the logarithmic field dependencies present. Thereby, Schottky or hopping injection will dominate at low-medium field strength, and at above certain onset field Fowler-Nordheim injection will ensue. Also, since the here outlined approach [81], [82] relies on Laplacian field distributions, the β-parameters will be overestimated at high field strength, as locally accumulated space charges will allow for better shielding of the maximal FEF:s in the distribution. However, when the interface geometry is resolved in three dimensions, none of the modifications outlined in this section are required, as the original injection equations can be readily adopted for the flux oriented normal to the irregular local electrode geometry.

5.3 Summary of charge transport and injection mechanisms

The mechanisms outlined in the previous sections are summarized in Table 4 and visualized in Figure 55. It is shown that each mechanism exhibits a strong but differently expressed field dependency, which makes for challenging behavioral predictions, especially in the strongly divergent fields near irregular surface geometry.

*Table 4. Summary of relevant charge injection and transport effects and their field dependencies, where γ is an arbitrary constant. *PF-effect is generally inapplicable for electronic carrier transport.*

Describes	Effect	Field dependency	Origin of expression	Section
Charge transport	Hopping mobility	$\mu(E) \propto \frac{1}{E}\sinh(\gamma E)$	Probability density of electron	5.1.1
	Diffusion	$D \propto \mu(E)$	Hopping mobility	2.3.2.4
	Poole-Frenkel effect*	$D_{t,PF}(E) \propto e^{\gamma\sqrt{E}}$	Coulomb field interaction	2.3.2.2
	Detrapping	$D_t(E) \propto \sinh(\gamma E)$	Hopping rate to adjacent shallow states	5.1.2
	Trapping	$T(E) \propto E \cdot \mu(E)$	Drift velocity of carriers	5.1.4
Recomb-ination	Langevin recombination	$S(E) \propto \mu(E)$	Coulomb field interaction and drift velocity	5.1.5
Charge injection, $J_{inj(e,h)}$	Schottky injection	$J_S(E) \propto e^{\gamma\sqrt{E}}$	Coulomb field interaction (image charge effect)	2.3.3.1
	FN injection	$J_{FN,c,n}(E) \propto E^2 e^{\gamma E^{-1}}$	Probability density of electron	2.3.3.2
	Hopping injection	$J_H(E) \propto E\sinh(\gamma E)$	Hopping rate through surface states	5.2.3
Charge extraction	Drift out from the material	$\mu(E) \propto \frac{1}{E}\sinh(\gamma E)$	Probability density of electron	2.3.3.4

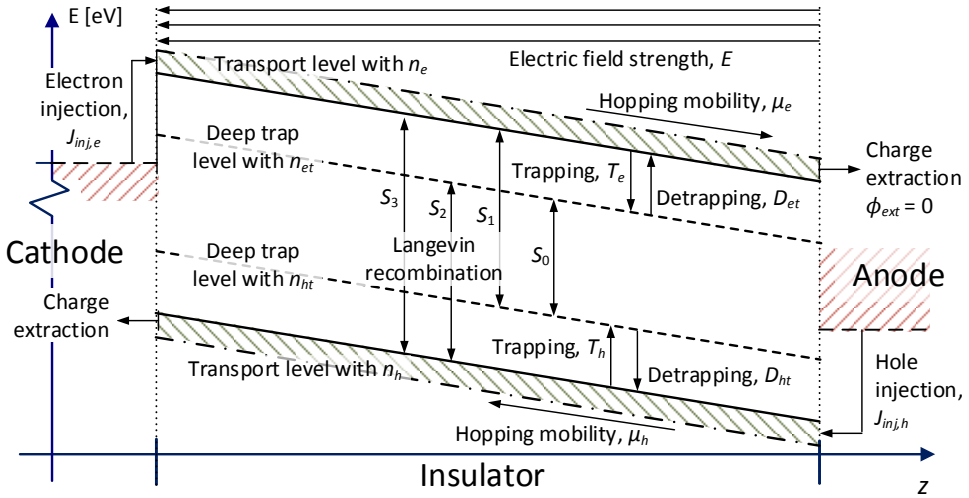

Figure 55. Band gap model, highlighting transport phenomena listed in Table 4. Energetic levels are not to scale.

Figure 55 elucidates the factors that can be accounted for in a bipolar charge transport model. The impact of a uniformly distributed degree of crystallinity is additionally accounted for in the balance between electron and hole injection and transport. Also, the impact of surface states is accounted for within the injection laws. The parameters and equations used for charge carrier transport and injection respectively reflect the DOS in the bulk and surface regions. It must be

emphasized that its distribution has been greatly simplified through the selection of three discrete energy levels (e.g. the depths and densities of shallow, inter-level and deep states). Other bipolar charge transport modelling approaches [53], [93], [94] make use of an exponential energetic distribution in favor of the here used discrete levels. This modelling approach can provide a more accurate DOS representation, as the dept-density relation is resolved continuously. In such a model, charge carriers fill the distribution from the bottom up to the upper filled energy level Δf. Additionally, as hopping carriers originate from Δf, increased charge density yields increased mobility in the material. While the bipolar model used in this work lacks the possibility to represent this effect, a reduced trapping rate to deep states with increased trapped charge density is still accounted for in equation (32). Additionally, the recombination rates used in the discretized approach are not accounted for in the continuously resolved model [53], [93], [94].

Furthermore, the charge density at the surface will be closely related to the balance between injection and transport in the system. This balance can in extreme cases be injection-limited or bulk-limited [60], [69]. For a sufficiently low injection barrier, the externally measured current density will no longer be governed by the interface, but rather by bulk space charge effects. For bulk-limited systems, sample thickness thereby correlates with external current density, which is not the case for injection-limited cases.

5.4 Charge and field calculation

In this section, equations for current density, charge density and electric field strength estimation are introduced, which allow for estimating the impact of the effects shown in Table 4 and Figure 55. The (one dimensional) drift current density in the insulation can be estimated from the mobile carrier densities and mobilities as:

$$\vec{J}_{drift} = e(n_e\,\mu_e + n_h\,\mu_h)\vec{E} \tag{46}$$

where n_e and n_h respectively are the mobile carrier densities for electrons and holes in m^{-3}. μ_e and μ_h are the mobilities for electrons and holes in $m^2/(V{\cdot}s)$, which can be assigned through equation (1) or equation (28). Furthermore, the diffusion current density for electronic carriers is defined as:

$$\vec{J}_{diff} = e(D_e\,\nabla n_e - D_h \nabla n_h\,) \tag{47}$$

where D_e and D_h are respectively the diffusion coefficients in m^2/s for electrons and holes defined in equation (9). Also, the mobile carrier gradients equate to $\nabla n_{(e,h)} = \partial n_{(e,h)}/\partial z$ when the simulation domain consists of one dimension. Also, the displacement current density (neglecting polarization current density) can be expressed as:

$$\vec{J}_{disp} = \varepsilon_o \varepsilon_r \frac{d\vec{E}}{dt} \tag{48}$$

Thus, the local current density in the material bulk will be a superposition of equations (46), (47) and (48). Furthermore, for electrons and holes respective injection and extraction current densities exist at the material boundaries, yielding a total of four flux types dependent on the local field orientation. Thus, the boundary injection/extraction current density, oriented normal to the surface, can be defined for electrons and holes as:

$$J_{b(e,h)}(E) = \begin{cases} \left(\vec{E} \cdot \hat{n} \leq 0\right) \rightarrow J_{inj,e} \\ \left(\vec{E} \cdot \hat{n} > 0\right) \rightarrow -en_e\mu_e E \\ \left(\vec{E} \cdot \hat{n} \geq 0\right) \rightarrow J_{inj,h} \\ \left(\vec{E} \cdot \hat{n} < 0\right) \rightarrow -en_h\mu_h E \end{cases} \quad (49)$$

where $\hat{n}$ denotes the normal vector of the surface. Thereby, a hole and an electron flux will simultaneously exist at the boundary, injecting one of the carrier types while extracting the other through a drift current. The injection current density in the boundary can be considered as a superposition of injection mechanisms as:

$$J_{inj(e,h)} = J_{S(e,h)} + J_{FN(e,h)} + J_{H(e,h)} \quad (50)$$

with the respective injection current densities $J_{S(e,h)}$, $J_{FN(e,h)}$and $J_{H(e,h)}$ being defined by Schottky (equation (14) or (38)), Fowler-Nordheim (equation (15), (40) or (41)) and hopping (equation (43)) injection, with or without roughness accounted for. In practice, given the strong and logarithmic field, temperature and parameter dependencies present, one single injection mechanism will always dominate at a given temperature or field. Furthermore, the hopping injection mechanism can be considered a replacement for Schottky injection.

Additionally, trapping $T_{(e,h)}$ and detrapping $D_{(e,h)t}$ yield exchange rates between the carrier densities n_e and n_{et}, or n_h and n_{ht} throughout the material. Also, recombination rates $S_{0\text{-}3}$, yield symmetric removal of carriers. The currents and exchange rates ultimately give rise to the dynamic evolution of the total (net) charge density, C/m^3, defined at each point in the material as:

$$\rho_{tot} = e(n_h + n_{ht} - n_e - n_{et}) \quad (51)$$

The charge density in the material will scale the local potential through Poisson's equation:

$$\nabla^2 V = -\frac{\rho_{tot}}{\varepsilon_o \varepsilon_r} \quad (52)$$

where V is the electrostatic potential in Volts and ρ_{tot} is the charge density. Furthermore, the electric field strength is estimated as:

$$\vec{E} = -\nabla \mathrm{V} \quad (53)$$

Thus, given the field dependencies existing in the transport phenomena listed in Table 4 that govern the evolution of carrier densities and impact the electric field distribution, a non-linear solver is required as described in section 5.6.3.

For large, complex geometries, certain assumptions allow for reduced computation cost by not describing the complex local carrier evolution. Poisson's equation allows for a straightforward calculation of electrostatic potential in absence of internal charge density (e.g. $\rho_{tot} = 0$), which is normally considered for AC applications. This simplification of equation (52) yields Laplace's equation. It is, on the other hand, seldomly applicable for DC cable systems as a gradient in σ/ε exists that results in space charge accumulation. However, macroscopic field

estimations can still be simplified by neglecting the diffusion current, individual transport parameters (arising from morphology and DOS) for positive and negative carriers, charge injection and by making use of the material conductivity σ, S/m, expressed as:

$$\sigma = e(n_e\,\mu_e + n_h\,\mu_h) \tag{54}$$

Thus, when a single conductivity parameter is used in equation (46), defining ohm's law, a simplified calculation approach is adopted. However, the material's conductivity is for insulators frequently observed to depend strongly on temperature and field strength. It can therefore be expanded to exhibit such dependencies through Klein's conductivity expression:

$$\sigma(E,T) = \sigma_0 e^{\alpha T} e^{\beta E} \tag{55}$$

Here σ_0 is the base-level conductivity in S/m, α is the temperature parameter in 1/°C (or sometimes 1/K) and β is a field parameter in mm/kV. Thus, it can be regarded that the multitude of field and temperature dependencies for bipolar electronic (and ionic) carrier transport have been averaged into a single material-specific parameter. While this simplification of bipolar charge transport facilitates macroscopic field assessments, when it is applied to mesoscopic simulations the generated results may be less accurate. Macroscopic expressions for space charge and electric field strength are generally in good agreement with experimental results up to the onset of significant space charge injection [19], [113]. Above this onset, in the range of 5-30 kV/mm, the adoption of a single conductivity parameter fails to accurately account for the underlying non-linear mechanisms, and the ohmic condition becomes invalid. The wide range of onset fields is because the underlying mechanisms depend strongly on numerous factors, such as interfacial nature, temperature [114], material types and many other parameters.

5.5 Ageing prediction in the model

Rates of charge recombination can be monitored in the bipolar charge transport model. As the energetic difference between the two carrier types is high (e.g. ~5 eV for n_{et}-n_{ht} and ~8 eV n_e-n_h), all four rates, $S_{0\text{-}3}$ can be considered generating ionizing radiation. Such radiation can be observed through electroluminescence investigations and is considered harmful to the material. It may thus be correlated with the recombination rates of the model when two opposite charge fronts meet each other [39], [40], [48]. This recombination can trigger electrical ageing through chain scission uniformly spread throughout the material or in regions of field enhancement where carrier density and Langevin rates are high.

Hot electrons are encountered when the carrier velocity exceeds that required for impact ionization. Both band conduction, according to the Drude model, and hopping transport with defined energetic barriers can help to predict drift velocities in the material and compare them with the critical velocity required for impact ionization. This comparison yields the following limit for drift velocity:

$$\mathrm{V_{d,crit}} \geq \sqrt{E_{bond}/2m_e} \tag{56}$$

where E_{bond} indicates the polymer bond strengths, being 3.8 eV for *C-C* and 4.5 eV for *C-H* bonds [34]. The onset of electrical ageing through ionizing collisions can thus be determined for assumed band and hopping mobilities as shown in Figure 56.

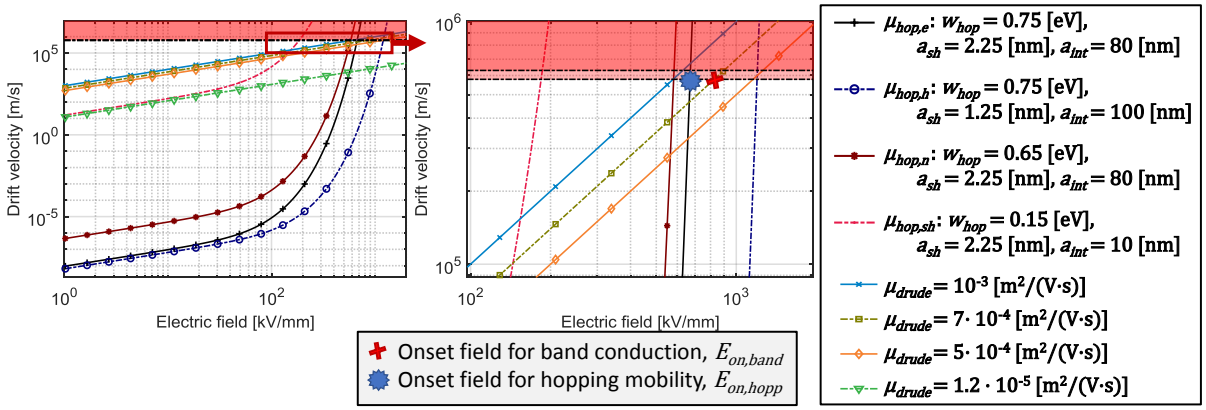

Figure 56. Drift velocities for band (Drude) and hopping transport in comparison to the critical drift velocities for C-C and C-H ionization (red regions) at 25°C and with $\nu = 6.2 \cdot 10^{12}$ s^{-1}. Multiple parameter combinations are considered as indicated in the legend. Onset fields are indicated when critical drift velocity is exceeded.

While the (lower) limit for band conduction mobility can be estimated at $1.2 \cdot 10^{-5}$ $m^2/(V \cdot s)$, it can be as high as 10^{-3} $m^2/(V \cdot s)$ [34]. The latter predicts a hot electron onset, $E_{on,band}$ of ~580 kV/mm. As shown in Figure 56, the considered hopping mobilities with shallow trap separation a_{sh} of 1.25 nm or 2.25 nm and 0.75 eV barriers yield the onsets, $E_{on,hopp}$ at 1200 kV/mm and 670 kV/mm. For the latter, a 0.1 eV decrease of the hopping barrier to 0.65 eV can reduce the onset value $E_{on,hopp}$ down to ~580 kV/mm. Thus, as n_e or n_h approach the respective levels of $N^0_{int(e,h)}$ a reduction of the hopping onset $E_{on,hopp}$ is expected, until it is as low as $E_{on,band}$. Note that deep states are considered separately in the transport model such that $n_{(e,h)t}$ does not contribute to an increase in mobility. While mobility increasing with inter-state trap filling is not accounted for in the two-level transport model, it is accounted for in the continuously resolved bipolar model [53], [93], [94].

Carrier transport below the mobility edge is considered non-harmful, whereas above it band-like conduction arises [26]. As seen in Figure 56, hopping with a 0.15 eV barrier (e.g. transport through shallow states alone, with also lower a_{int}) predicts mobilities exceeding the Drude level already below 150 kV/mm. However, when it approaches Drude mobility, it is likely to be capped there, as non-ionizing lattice collisions will govern the maximal speed in the material. Thus, hot carriers can be encountered in the material first when Drude conduction exceeds the critical velocity. Conclusively, in between the onset fields $E_{on,band}$ and $E_{on,hopp}$ only band conduction is ionizing, but as the majority carriers will be occupying the lowest energy states, such ionizing collisions will be few. However, when field is increased above $E_{on,hopp}$ all carrier transport is ionizing. Also, significant amount of charge density is required before $E_{on,hopp}$ is reduced significantly, due to a presence of high density of inter-level states $N^0_{int(e,h)}$.

The here listed mobility and onset field values are only ideal case estimates, and actual values can differ due to the non-uniform spatial distribution of DOS within the band gap and in the conduction band. Furthermore, certain probability is involved in the relation between the maximal and drift velocity of hot carriers, which here is simplified to a factor of two. The indicated onset field levels in Figure 56, exceed the through electroluminescence measurement determined onset fields [39], [40], [48], which indicates the strong impact of the random polymer nature, random transport processes and possibly the interface. The rate of ageing can still be slow for infrequent ionizing collisions at such field strengths far below $E_{on,band}$, whereas above $E_{on,hopp}$ certainly imminent failure is predicted. The latter predicted intrinsic level can be below other intrinsic breakdown criteria (e.g. von Hippel model or internal field emission).

Furthermore, the predicted onset fields, being dependent on the hopping mobility's parameters, may define the maximum level of field dependency in charge transport (e.g. a shallow state separation a_{sh} above 2.5 nm may predict breakdown strength lower than experimental results).

5.6 Simulation methodology

As the goal was to predict the phenomena occurring within rough interfacial geometry, allowing for better interpretation of the performed electrical characterizations, multiple simulation approaches were necessary. These approaches are visualized in the flowchart in Figure 57.

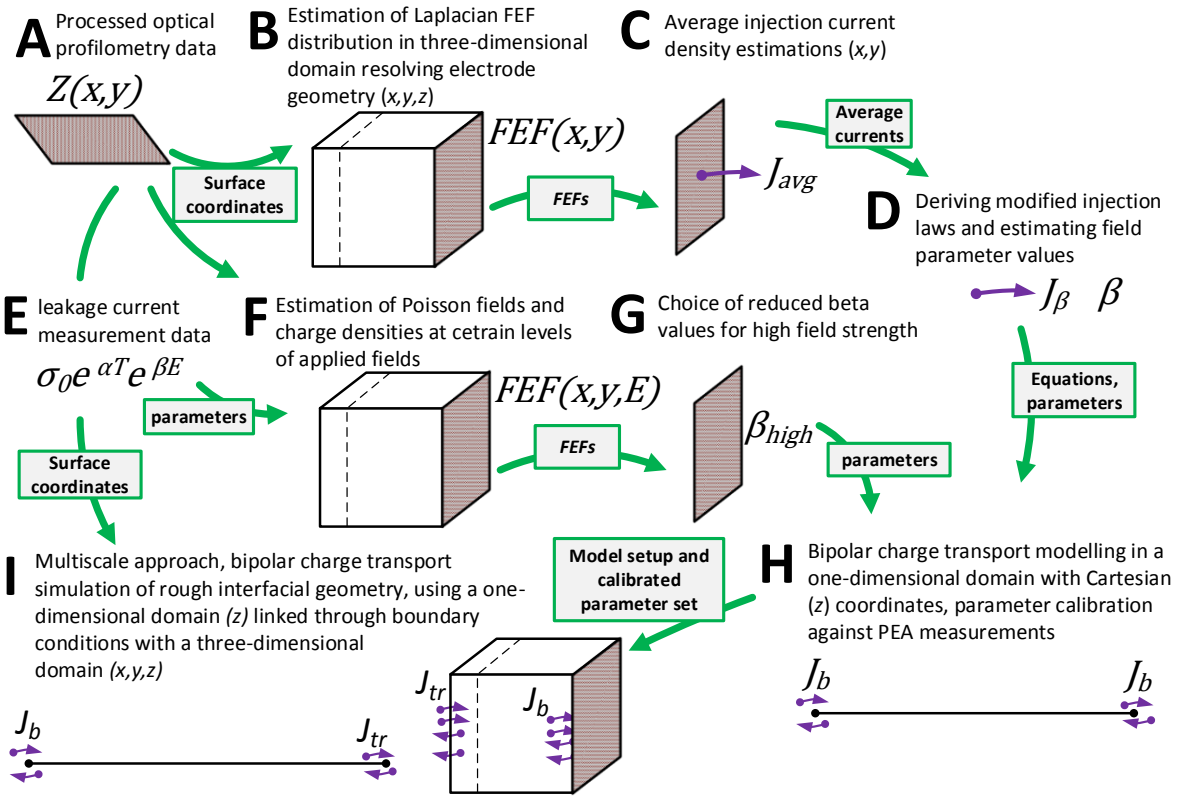

Figure 57. Flowchart outlining the performed simulation steps and approaches used in the thesis work. Additionally, the data transfer between the steps is indicated in green boxes.

The flowchart in Figure 57 categorized the steps and the transferred data between them. Steps A, B, E, F, and G comprise different approaches to quantify the surface field distributions and are presented in sections 5.6.1 and 6.1. Steps C and D aim to derive the injection characteristics for differently prepared surface types and are described in sections 5.6.2 and 6.2. Step H describes the one-dimensional simulation and calibration of the model parameters against space charge measurements described in sections 5.6.3 and 6.3. Step I shows the ultimate adoption of a multi-scale approach, relying on accurate input parameters, described in sections 5.6.4 and 6.4.

5.6.1 Surface field distributions

To use the surface coordinates *(x,y,z)* obtained through optical profilometry (sections 3.2.2 and 4.1.2) in the Finite Element Method (FEM) simulations, further processing was required (step A in Figure 57). Such processing consisted of sectionalization and interpolation, the former process was required for reducing memory requirements whereas the latter was required for accurate meshing of the surface geometry in FEM. A selected region in the roughness

measurement, confirmed to reproduce a consistent height distribution *Z(x,y)*, was sectionalized to a 50 by 50 coordinate point region. Furthermore, a recursive spline interpolation filter was used to generate additional meshing points in between the coordinates, ultimately creating a 150 by 150 coordinate point surface which could be imported to the FEM software COMSOL Multiphysics® [115]. This method was preferred over further refining the surface mesh within the software, as it allowed for better control over the input data and prevented sharp corners on the electrode geometry. This processed surface (an example is shown in Figure 58) was at the limit of the calculation server's physical memory capability.

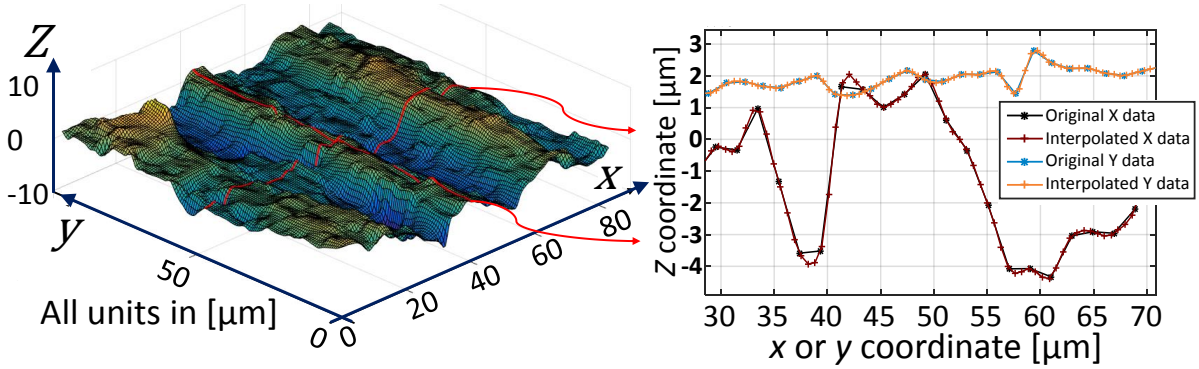

Figure 58. Coordinates of an interpolated section of the abraded surface (left). The indicated x and y data before and after interpolation (right).

As seen in Figure 58, in this way, the 83 by 96 µm surface section can be readily adopted in the simulation, with each interpolated coordinate point corresponding to 0.35 µm^2.

Simulations of Laplacian fields were performed in the FEM software (step B in Figure 57), in a cubic simulation domain using the surface section as one of its sides. The *z*-length of the domain was extended to 100 µm. The domain's surface section face was assigned to a ground boundary condition, while its opposite face was assigned to electric potential U_0. By solving for equations (52) and (53) with $\rho_{tot} = 0$, field enhancement factors *FEF(x,y)* were deduced in the surface coordinates with equation (16) and were exported as a matrix. Such factors were additionally visualized in histograms for better comparisons of different surface types with surface parameters (*Sa*, *Sq*, *Sdq*, etc.). The Laplacian FEF distribution was also utilized in further calculation work.

Simulations of Poisson fields (step F in Figure 57) were performed identically to Laplacian field simulations, but with ρ_{tot} being resolved in equations (52) and (53), which required information about the material's conductivity since its gradient gives rise to charge accumulation in the material. The conductivity's parameters were adopted from the results of measurements performed elsewhere for identical insulation material and were employed by using equation (55) accounting for field and temperature dependencies. This simulation generated a space charge distribution $\rho(x,y)$ amongst the surface coordinates. Additionally, a FEF distribution was generated, being dependent on the applied field strength (e.g. $FEF(x,y,E_{applied})$). The FEF distribution allowed for a crude estimate of field parameters at high field strength, β_{high}. Beyond this parameter and visualization, the generated data were not used further, as the use of a macroscopic conductivity expression in mesoscopic surface geometry is considered an extreme simplification. While it was possible to observe the impact of conductivity gradients in the strongly divergent surface field region, such results remain a subject of interpretation.

Lastly, surfaces with artificially generated coordinates dominated by exponential noise or smooth waves were investigated. Once again, they utilized the steps considered in Laplacian field simulation and allowed for better understanding of the impact of certain surface features on the FEF distribution.

5.6.2 Roughness enhanced charge injection

Average injection current densities J_{avg} (step C in Figure 57), were estimated separately for each injection mechanism considered. For calculating them, equation (45) was first adopted for estimating the average flux from all surface coordinate points. At each point, the local current densities $J_{local(x,y)}$ were estimated from the local field strength, using the Laplacian field distribution $FEF(x,y)$ from the previous calculations and $E_{applied}$ as input parameters. The latter parameter was swept over field strength levels to derive the dependency of the current density against applied field strength. The averaging in equation (45) was specifically applied to the injection current density expressions derived assuming Schottky (J_S, equation (14)), Fowler-Nordheim (J_{FN}, equation (41)) and hopping (J_H, equation (43)) mechanisms. While the exact values of their input parameters remained unknown until the bipolar charge transport model was calibrated, approximate levels were selected.

As equation (45) estimates the result of a specific set of input parameters, it was desired to derive a new set of injection equations that can account for the roughness impact directly (step D in Figure 57). Thereby there is no need to re-estimate the average injection rates each time a certain injection parameter requires adjustment. To derive such new equations (e.g. for hopping injection) the original equation is split into a field-dependent part, and a section of proportional scaling, thus yielding:

$$J_{H(e,h)} = 2v\varepsilon_0\varepsilon_r e^{-\frac{w_{ss(e,h)}}{k_B T}} \cdot E \sinh\left(\frac{e a_{ss(e,h)} E}{2k_B T}\right) = J_0 \cdot f(E) \tag{57}$$

As the first term J_0, which includes quantities determining the base level and the temperature dependency, can be brought out from the integration in equation (45), its parameters can be readily adopted in the new roughness dependent expression. In the field-dependent term, a certain surface-specific field parameter β can be adopted to maintain the correct injections at high field strength. By assuming that the field strength E in the original expression is to be replaced with $FEF \cdot E$ in equation (45), this yields βE in the new expression. However, also additional modifications are required to maintain the correct injection rates at low field strength. The new roughness dependent equation can therefore be written as:

$$J_\beta = J_0 \cdot \big(f(E) + B \cdot f(\beta E)\big) \tag{58}$$

where β is a dimensionless, surface-type-specific field parameter; J_0 and $f(E)$ are respectively the proportional and field-dependent part of the original injection expression. The scaling parameter B originates from the surface fraction in the FEF distribution that is positioned at the level of the field parameter β. Thereby, equation (58) expresses a superposition of low and high field effects, where the latter is dominated by the strongly increased injection current from the rough asperities. The development of such modified injection equations has been a part of the present study and is further described in section 6.2. The approach outlined above can be applied to other injection mechanisms such as Schottky injection. However, in the case of Fowler-Nordheim injection expression, the field-dependent term is rather complex especially when image charge effect and temperature are accounted for in equation (41). Since the functions *t*

and v in equation (40) are functions of $\Delta\phi$ they introduce additional field dependencies. The product $FEF \cdot E$ was therefore used in their estimation at each coordinate, before estimating the average current density in equation (45). Because of their complexity, the approach for roughness correction described in equation (58) could not be adopted for FN injection, instead, a simplified equation (e.g. $J_\beta = J_0 \cdot f(\beta E)$) introducing a β-parameter was derived [54].

The impact of the field distributions on the injection intensity was assessed using the modified injection expressions, skipping a high number of iterations. It has been found that the field parameters β are in strong correlation with the surface's maximal field enhancements FEF_{max}. Thereby, two sets of field parameters β and β_{high}, for use at low and high applied field strengths respectively, were deduced from the Laplacian and the Poisson FEF distributions. This approach simplifies the field parameter $\beta(E)$, which is gradually decreasing with field strength, into two discrete levels at low and high field respectively. Thus, it corrects shortcomings in the Laplacian field assumptions. Nevertheless, a more accurate adoption is realized in the multiscale approach described in section 5.6.4 which more accurately accounts for trapping, detrapping, and transport being affected by strong field variations found in the interfacial region. Furthermore, the derived equations and their surface specific field parameter values (β and β_{high}) were ultimately used in the bipolar charge transport model described in the next section, where the field strength-current density relationships were verified.

5.6.3 Bipolar space charge transport simulation

The physical processes outlined in section 5.4 are incorporated in a charge transport model, which accounts for the drift of charged species in the electric field (equation (46)), their diffusion (equation (47)), trapping (equation (32)) and detrapping (equation (29)) as well as for recombination between charge carriers (equation (37)). Assuming that the electric charges in the material are transported by mobile electrons and holes, the incremental change in their densities n_e and n_h with time can be expressed as:

$$\begin{cases} \dfrac{\partial n_e}{\partial t} - \nabla \cdot \left(n_e \, \mu_e \vec{E} + D_e \, \nabla n_e \right) = -S_1 n_e n_{ht} - S_3 n_e n_h - T_e n_e + D_{et} n_{et} \\ \dfrac{\partial n_h}{\partial t} + \nabla \cdot \left(n_h \, \mu_h \vec{E} - D_h \, \nabla n_h \right) = -S_2 n_h n_{et} - S_3 n_e n_h - T_h n_h + D_{ht} n_{ht} \end{cases} \tag{59}$$

where ∇ in one dimension corresponds to $\partial/\partial z$ for the transport along the z-coordinates and $\mu_{(e,h)}$, $m^2/(V \cdot s)$; $D_{(e,h)}$, m^2/s; $T_{(e,h)}$, s^{-1}; $D_{(e,h)t}$, s^{-1}; and $S_{(1\text{-}3)}$, m^3/s respectively refer to the aforementioned mobility, diffusion, trapping, detrapping and recombination rates. For trapped electrons and holes (respective densities n_{et} and n_{ht}), the incremental change in carrier density with time is defined as:

$$\begin{cases} \dfrac{\partial n_{et}}{\partial t} = -S_2 n_h n_{et} - S_0 n_{et} n_{ht} + T_e n_e - D_{et} n_{et} \\ \dfrac{\partial n_{ht}}{\partial t} = -S_1 n_e n_{ht} - S_0 n_{et} n_{ht} + T_h n_h - D_{ht} n_{ht} \end{cases} \tag{60}$$

Between equation (59) and (60) rates of trapping and detrapping are equal, but with opposite sign, thus establishing an exchange of carrier density between the two energy levels. Also, the charge recombination terms feature equal charge carrier loss rates for the two types of participating species.

The equations and parameters were implemented in a one-dimensional model in COMSOL Multiphysics® [115]. Three coupled sets of predefined physics interfaces were used: two sets of Transport of Diluted Species (TDS) for implementing the continuity equations for mobile and trapped carriers (equations (59) and (60)) and Electrostatics (ES) interface for solving Poisson's equation (52) and the electric field in equation (53) with ρ_{tot} from equation (51). Note that the latter module also accounts for the displacement current described by equation (48). Charge injection and extraction were implemented on the boundaries of the computation domain (representing the electrodes) by implementing equation (49), such that carriers were either injected or ejected depending on the field's orientation at the electrodes.

The computational mesh featured the largest size in the center, of approximately 1 μm, and was gradually refined towards the electrodes where the mesh size was around 10 nm. The direct parallel solver PARIDISO was used along with the Backward Differentiation Formula (BDF) in the time-stepping algorithm, which was further stabilized by ensuring Jacobian matrix updates on each time step to enhance the convergence rate. While an optimization algorithm [116] was considered, a different methodology was employed. As manual control over equations and the parameter space was preferred, calibrations were performed manually, starting with the non-field dependent versions of the transport, trapping, detrapping and recombination rates summarized in section 5.3 and gradually employing the field dependencies as the need arose for describing the polarization-depolarization sequence of the space charge measurements. This process was significantly facilitated by using a MATLAB Livelink interface [117], which allowed for automated multi-parametric sweeps, while also facilitating calibrating against multiple measurement conditions (thickness, biasing voltage's magnitude and polarity, temperature, electrode type) at once. This automated approach allowed for gradually improving the simulation results for a set of samples by comparing them with the measured results through equation (24), ultimately finding the best set of equations and parameters for matching the space charge measurements.

First the Schottky and Fowler–Nordheim injection mechanisms were evaluated, by using them in the boundary current equation (49). In total around 3245 simulations were required in the first step, which calibrated the model against measurements on the samples with abraded and backside electrode types at 25°C. Thereafter, 666 additional simulations further calibrated the parameter space for the additional surface types at room temperature, and lastly, 1382 simulations further calibrated the model for results at elevated temperatures. Thereafter, the hopping injection mechanism was evaluated, by replacing Schottky injection in the boundary current equation (49). While the injection current's superposition in equation (50) was maintained, it was in practice achieved by increasing the Schottky barrier height to 3 eV. After its implementation, calibration began from the values in [57], gradually adjusting $w_{ss(e,h)}$ and $a_{ss(e,h)}$ while maintaining the bulk conduction parameters. After 212 simulations, the optimal parameter values were found, achieving the lowest charge deviation against all 45 space charge measurements (with their behavior presented in section 4.2.2). This calibration process ultimately yielded the results presented in section 6.3.

5.6.4 Multi-scale simulation approach

The multi-scale simulation approach (Step I in Figure 57), made use of a small mesoscopic 3D domain to resolve the surface topography on its boundary, and it was linked to the 1D domain of the bipolar charge transport model described in section 5.6.3. The 3D domain was constructed using the same charge transport setup, with the splitting of mobility into (x,y,z) constituents being

the only modification. This was necessary due to its use in the directional drift current in equation (59). The boundary flux in equation (49) is used for the insulation-electrode boundaries, using only hopping injection for sake of simplicity. The roughness corrected equation is used in the 1D domain (equation (65)) and the original expression used in the 3D domain (equation (43)). The boundary flux $J_{tr(e,h)}$ in between the two domains was also modified as follows:

$$J_{tr,3D(e,h)} = \begin{cases} \left(\vec{E}\cdot\hat{n}_{3D}<0\right)\rightarrow J_{tr,1D,e} \\ \left(\vec{E}\cdot\hat{n}_{3D}>0\right)\rightarrow -en_e\mu_e E \\ \left(\vec{E}\cdot\hat{n}_{3D}>0\right)\rightarrow J_{tr,1D,h} \\ \left(\vec{E}\cdot\hat{n}_{3D}<0\right)\rightarrow -en_h\mu_h E \end{cases}, J_{tr,1D(e,h)} = \begin{cases} \left(\vec{E}\cdot\hat{n}_{1D}<0\right)\rightarrow \overline{J_{tr,3D,e}} \\ \left(\vec{E}\cdot\hat{n}_{1D}>0\right)\rightarrow -en_e\mu_e E \\ \left(\vec{E}\cdot\hat{n}_{1D}>0\right)\rightarrow \overline{J_{tr,3D,h}} \\ \left(\vec{E}\cdot\hat{n}_{1D}<0\right)\rightarrow -en_h\mu_h E \end{cases} \quad (61)$$

Here, $\hat{n}_{3D}$ and $\hat{n}_{1D}$ are respectively the boundary's inward-oriented normal vectors in the 3D and 1D domain. The injection current density is thus replaced with the extraction current density from the neighboring domain, requiring also estimation of the arithmetical mean value in the 3D domain ($\overline{J_{tr,3D(e,h)}}$). Additionally, the boundaries' electrostatic potentials are matched by using a floating potential condition in the 3D domain and implementing its magnitude in the 1D boundary ($V_{1D}=V_f$), while overriding the boundary condition's displacement field magnitude in the 3D domain with the 1D domain's magnitude (i.e. $\left|\vec{D}_{3D}\right| = \left|\vec{D}_{1D}\right|$). Setup adjustments were required to improve the solver's stability. An initial charge density, ρ_{init} of 0.25 C/m^3, was adopted for all four carrier types (n_e, n_h, n_{etr} and n_{htr}) preventing negative carrier quantities in case of poor wavefront resolution. Furthermore, the 3D domain's (x,y,z) dimensions were reduced to improve mesh quality as listed in Table 5, with their resulting degrees of freedom being capped close to the limit of computational performance.

*Table 5. Performed multi-scale simulations, 3D domain dimensions and mesh quality. *Reduced ramping rate at 100 V/s used for better stability, with 6 hours polarization and 6 hours depolarization simulated. †Mesh quality growth allowed towards surface irregularities. ‡Simulations were stopped at 100 kV/mm due to short time-steps made by the solver.*

Simulation case	**Applied field profile**	***(x,y,z)* dimensions**	**Mesh max/min†**
PEA sample SC11	17 kV/mm followed by 0 kV/mm*	57.8 × 24.9 × 50 µm	1.5 µm / 2 nm
PEA sample SC12	39 kV/mm followed by 0 kV/mm*	28.9 × 24.9 × 50 µm	1 µm / 2 nm
DCBD simulations	Ramp to E_c value (section 4.2.2)‡	28.9 × 11.6 × 50 µm	0.75 µm / 2 nm

The results of the multi-scale simulations are summarized in section 6.4.

Chapter 6

Simulation and calculation results

This chapter presents the simulation results, which develop a framework, relating measured surface topography in section 4.1.2 with the observed behavior in the electrical measurements introduced in section 4.2. It begins with a review of surface field distributions, which by resolving the mesoscopic surface topography estimated the Laplacian and subsequently the Poisson field distributions in a 3D domain. In the following section, these field distributions allowed for estimating the average injection current densities J_{avg}, which were matched by a set of derived roughness enhanced charge injection equations. Thereafter, these equations are implemented in the bipolar charge transport model which is calibrated against space charge measurement results presented in section 4.2.1. First, the final parameter set obtained from the calibration is outlined, after which typical results are shown. Thereafter, the limitations in the model's behavior are summarized, finishing by listing deviations in charge densities between the measurements and the model. Lastly, a multi-scale simulation approach is adopted for better estimating local charge and field quantities in the irregular surface domain.

6.1 Surface field distributions

6.1.1 Laplacian field distributions

Making use of the largest possible domain size and resolution, the results of Laplacian field simulation (i.e. assuming $\rho_{tot} = 0$ in equation (52)) are shown in Figure 59 and Figure 60. The surface's spatially resolved field enhancement factors (i.e. *FEF(x,y)*) show a strong impact on the texture. Two results are shown per surface type, from different domain locations in the same profilometry measurement region.

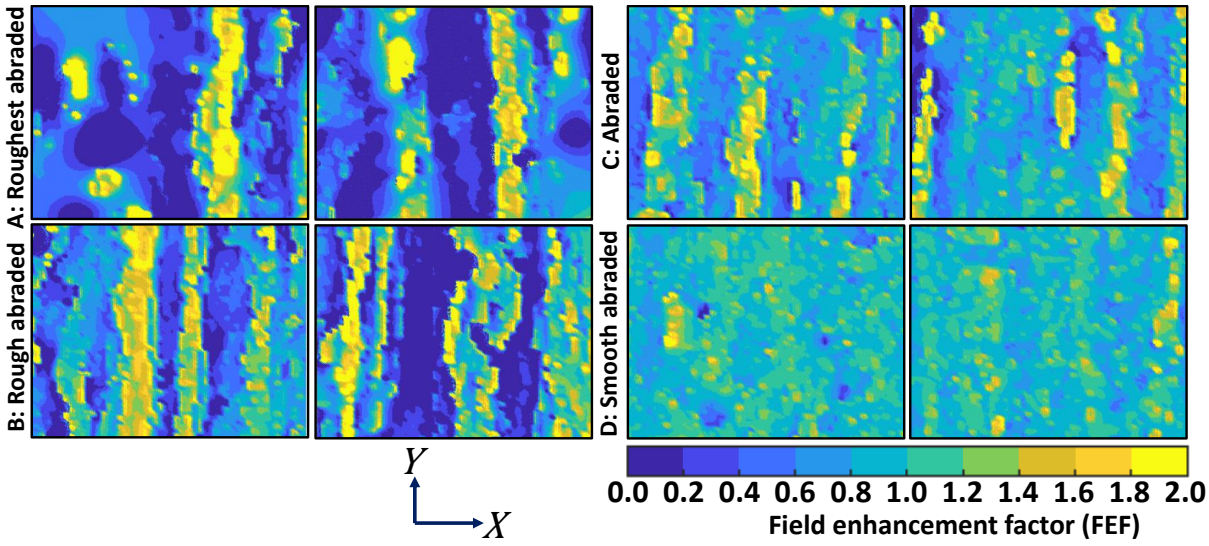

Figure 59. Surface field distribution in the 83 by 96 µm domains for the abraded surfaces. Values extending significantly beyond the colormap's limits exist.

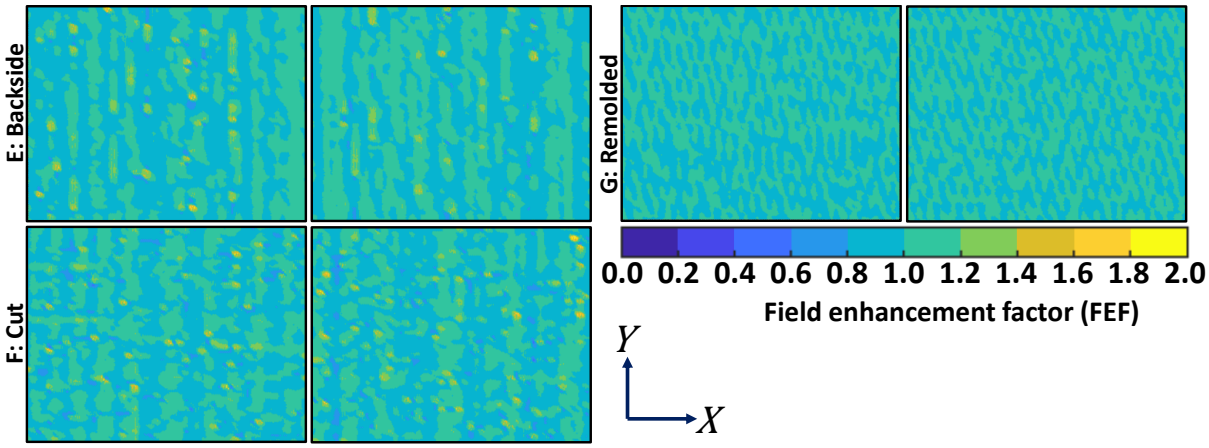

Figure 60. Surface field distribution in the 83 by 96 µm domains for the smoother surfaces. No values extend beyond the colormap's limits exist.

As shown in Figure 59 and Figure 60, the anticipated enhancement of electric field strength occurs at the topography's valleys (i.e. $FEF > 1$), while it is reduced at the topography's hills (i.e. $FEF < 1$). Thus, the electric field is re-arranging itself towards the surface, yielding an average FEF value for the entire domain equal to unity. With each coordinate point corresponding to 0.35 µm^2, such resolution allows for observing a surface texture representation, comparable to SEM observations in Figure 26. However, the remolded surface's field distribution shown in Figure 60 originates from the interferometry pattern in optical profilometry. Due to its low roughness, below the profilometry's height resolution limit, it represents an ideal surface with regards to the FEF distribution. The other surfaces show that increased roughness level forces a stronger field re-arrangement, where regions of large field enhancement are surrounded by regions of strong field reduction. Also, the texture in the roughest surfaces lacks a perfect repetition (e.g. as represented in the sine wave in equation (27)) and shows some discrepancy between the two sections in Figure 59. Therefore, a fourfold repetition of the FEF simulation at different surface positions was required. The results of these simulations were merged into the same dataset and shown in the histogram in Figure 61.

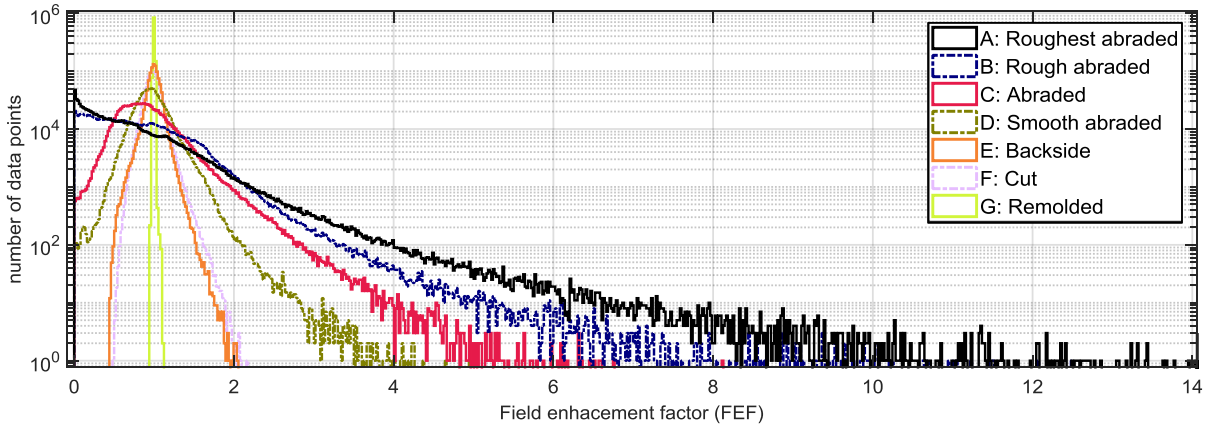

Figure 61. Histogram of the FEF population, established from measured surface texture for each surface type. The FEF values represent a merged dataset from four separate simulations.

Figure 61 facilitates a statistical review of the local field strengths, allowing for a better comparison between the surface types and their different roughness levels. The histogram's ordinate corresponds to the number of data points and thus the surface fraction, which is positioned at a certain FEF value. The histogram reveals a similar FEF distribution shape as found by Novikov [82]. The majority of the field's re-arrangement over the surface (as shown

in Figure 59 and Figure 60) manifests itself as a Weibull distribution, as expressed in equation (25), but with scale parameter equal to one. The narrow spread of FEF values for the remolded surface indicates a large shape parameter ($k >> 1$), and the increased roughness levels contribute to a decrease in the shape parameter k. The decreasing k parameter develops a distribution tail, consisting of a low surface fraction with high FEF values, which is particularly pronounced for the rougher surface types. As such distribution tails also existed in the surface height $Z(x,y)$ and surface derivative $\partial Z/\partial x$ histograms in Figure 29, the FEF tail can be compared against roughness parameters to investigate its origin. The FEF tail, estimated as the root mean square value of the 100 highest FEF values in the distribution, is therefore displayed against the *Sa* and *Sdq* parameter of each surface type in Figure 62. Artificial texture types generated through equation (27), with either the noise or the ridges represented, subsequently subjected to the same interpolation, sectionalization and subsequent field simulation, are added to the comparison.

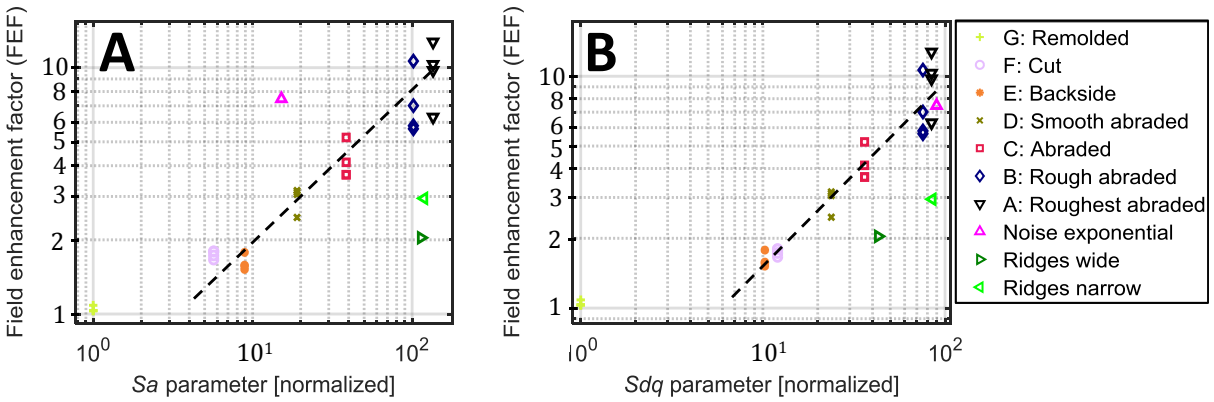

Figure 62. Root mean square of the 100 highest FEF values (FEF tail position) estimated without the merged dataset, displayed in a double logarithmic plot against the Sa parameter (A) and the Sdq parameter (B). Three artificially generated texture types are added, being exponential noise, and ridges with different spacing, controlled with the Si parameter in equation (27).

Figure 62 shows a strong correlation between the FEF tail and both *Sa* and *Sdq* parameters for the real surface types. However, as inter-correlation also exists between these roughness parameters, the underlying cause of this correlation is unclear. While the artificially generated surfaces break the correlation against the *Sa* parameter, only ridges that lack the exponential noise in equation (27) break the correlation with the *Sdq* parameter. The histograms of such artificial surfaces revealed that exponential noise featured a Weibull distribution whilst the smooth ridges did not. It is thus indicated that the *Sdq* parameter anticipates the maximal field enhancement well for the surface types studied in this work, due to their Weibull distributions in Figure 61. A majority of their Laplacian FEF distributions could arise from the disorder present in them, while the repeated striations make for a lesser widening in the distribution to which this Weibull distribution is superimposed.

Whilst the *Sdq* parameters, and thus the local surface derivatives (i.e. $\partial Z/\partial x$), are in strong correlation with the maximal field enhancement on the surface, they are not responsible for direct causation of the FEF distribution. The correlation is also strengthened by exclusion of sharp surface points, through the recursive spline interpolation filtering. The correlation can be broken by specific texture types or local features not adhering to equation (27). As situations, where high derivatives (or sharp points) are consistently shielded by smoother surrounding texture, cannot be easily distinguished amongst surface coordinate distributions, there is no reliable replacement for performing field simulations. This conclusion emphasizes that

exploiting measured topography is a requirement for accurate simulations, whilst the adoption of artificially generated texture may neglect certain irregular features.

6.1.2 Poisson field distributions

Simulations including localized charge accumulation ($\rho_{tot} \neq 0$) in equation (52) and making use of field-dependent conductivity through equation (55), provided estimations for the field enhancement factors $FEF(x,y,E_{applied})$. An example of the results yielding localized charge accumulation and field distributions is shown for single surface sections in Figure 63 for 30 kV/mm of the applied field strength.

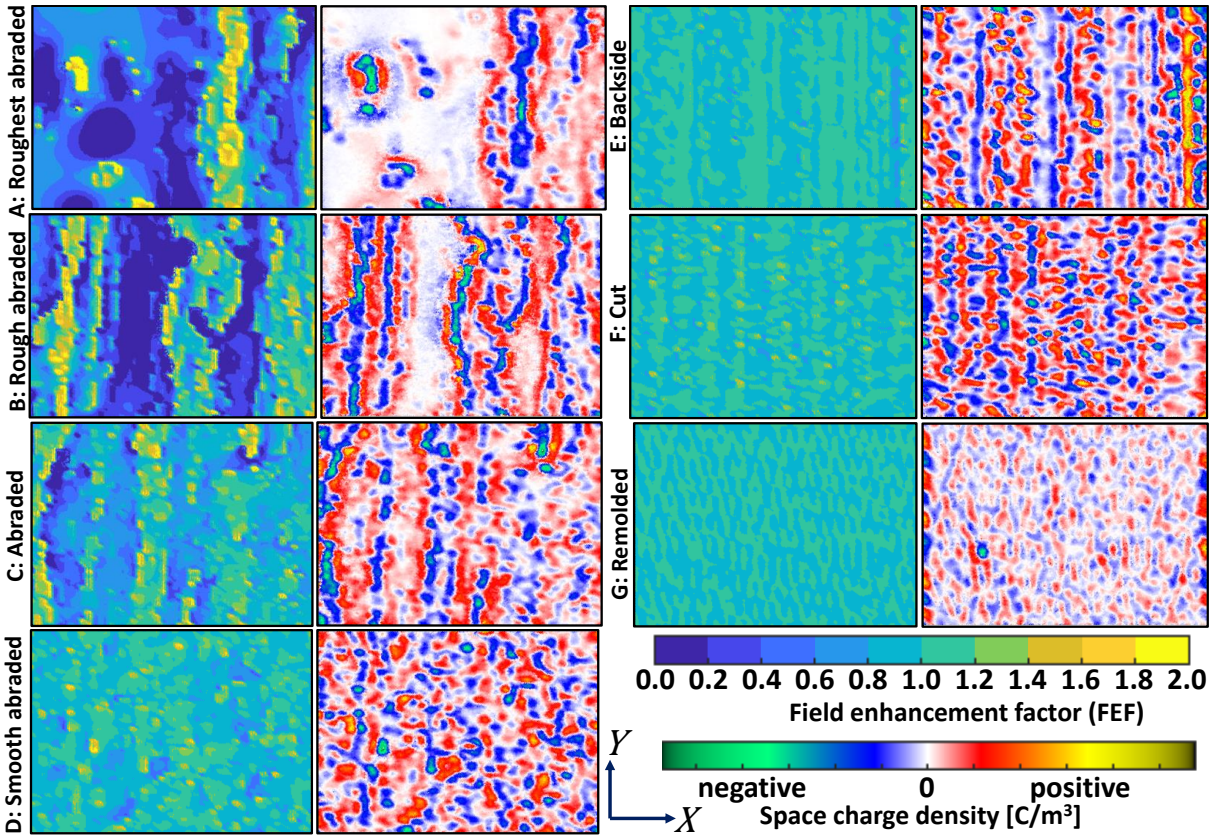

Figure 63. Localized charge accumulation (right figures) and field distributions (left figures) in the 83 by 96 µm domains for the studied surface types. Values extending significantly beyond the FEF colormap's limits exist, while individual colormap limits are applied to the charge accumulation figures. The polarity of the surface is negative, thus homocharge appears in blue and heterocharge in red.

Both positive and negative charges are observed in Figure 63 (note that the electrode is at negative polarity) with homocharges accumulating at regions of field enhancement and heterocharges accumulating at regions with reduced field strength. As the origin of the charges is not specified in the simulation, their accumulation merely arises from the model's steady-state condition with locally strong conductivity gradients (shaped by the field dependency of the conductivity in equation (55)). It is also observed that surface topography, being visible in both the FEF and the charge density distributions, is the driving force for the localization of such quantities. For better comparisons of FEF and charge densities, the surface's histograms can again be assessed as shown in Figure 64.

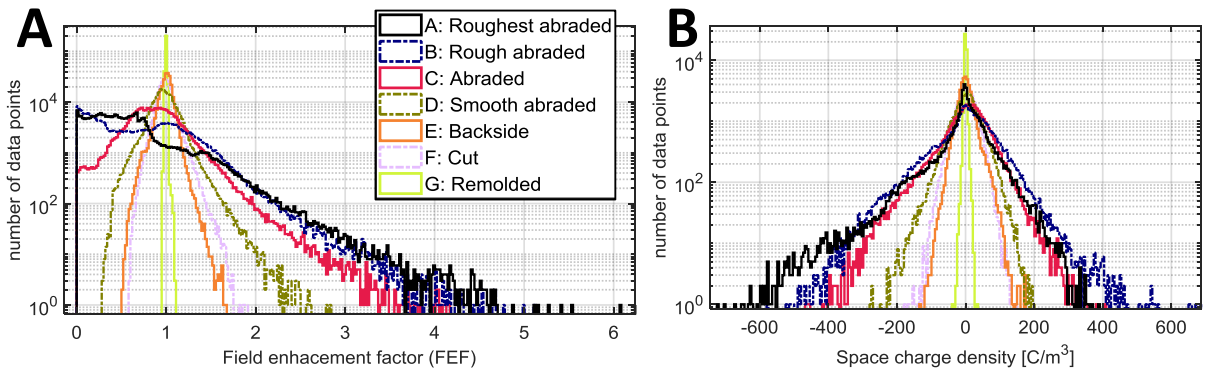

Figure 64. Histogram of the FEF population (A) and charge density variation (B), established from the measured surface texture in a single surface section for each surface type.

The FEF populations in Figure 64A feature significantly narrowed Weibull distributions compared to their Laplacian counterparts shown in Figure 61, caused by shielding of the local field enhancements by the field induced by the charge density ρ_{tot}. At the spatial positions with low field strength, the FEF values are increased due to positive heterocharges in these regions. Respectively, at the positions with high field strength, the space charge lowered the Laplacian field strength due to the negative homocharge accumulation. The accumulated charge densities in Figure 64B significantly exceed quantities normally found in one-dimensional measurements and simulations, arising from high local electric field gradients ($\partial E_z/\partial z$), which force decades of conductivity change within few micrometers. The distribution tails corresponding to high FEF values (Figure 64A), being significantly lowered through homocharge shielding, are of similar magnitude for roughest, rough and normally abraded surfaces. For such abraded surfaces, their charge distribution tails towards high negative charge densities (Figure 64B), do not differ distinctly. This observed similarity is related to local geometry, where the rougher abraded samples exhibit a larger region available for field re-distribution driven by the charge accumulation. Therefore, they (roughest and rough abraded) do not require higher charge density for reducing Laplacian field strength further, compared to their smoother counterpart (abraded). The homocharge and field distribution tails, estimated with a Poisson field strength of 30 kV/mm, are thus in correlation with the observed flattening of characteristic breakdown stress E_c towards higher roughness values (see results of the DCBD tests in Figure 45). Even though applied field strength in the simulations is well below the applied field in the breakdown experiments, the trends calculated under 30 kV/mm can be considered to prevail at higher field strength. Further narrowing in the distribution $FEF(x,y,E_{applied})$, with increasing applied field strength is expected for all surface types, as shown in Figure 65 for an abraded surface.

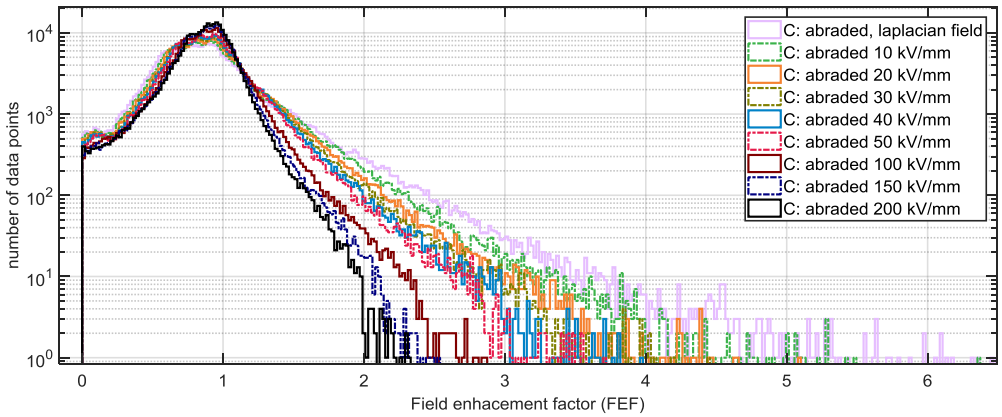

Figure 65. Histogram of the FEF population, established from measured surface texture for the abraded surface at different levels of applied field strength.

The narrowing of the distribution with increasing applied field strength is demonstrated in Figure 65. By comparing it to the case with Laplacian field, it is seen that the effects become more and more pronounced at higher field strengths. This behavior arises from the exponential term in the conductivity equation (55) and the fact that the FEFs bring about a local increase or reduction in the conductivity. Therefore, the variations are stronger at high applied field strength due to the steepness of the exponential curve. Also, the FEF distribution never fully disappears at high field strength and the strongest impact is noticed in the distribution tail.

As mentioned earlier, as the origin of space charges is unresolved in the presented simulations, the observed charge distributions originate from locally strong conductivity gradients. When considering bipolar charge transport, the homocharges can be expected to be readily injected from the adjacent electrode, while heterocharges may appear only when the injected charges cross a significant part of the sample while drifting in the field (if dissociation or ionization of chemical impurities in the bulk is negligible). Therefore, heterocharge accumulation is likely to be significantly slower compared to that obtained from the conductivity-based model. Also, heterocharges, traveling along the field's local orientation would be directed towards the enhanced field regions, and thus reach the reduced field regions to a lesser degree. Strong homocharge accumulation is thus expected from the bipolar charge transport model, while it is uncertain whether the heterocharges may accumulate at all. Furthermore, the simplification in equation (54) assumes symmetric carrier density and transport rates with regards to polarity, which may result in further inaccuracy. Also, the parameters in equation (55), obtained from leakage current measurements, are valid up to ~70 kV/mm. Beyond this limit, the exponential field dependency is not necessarily accurate. These uncertainties may give rise to overestimated space charge densities, and thus underestimated field enhancement factors. Conclusively, whilst FEF and charge distributions in this section suffer from inaccurate quantities, they allow for better anticipation of effects true to the interface's local behavior.

6.2 Roughness enhanced charge injection

6.2.1 Roughness enhanced Schottky injection

The average current density J_{avg} calculated by using equation (14) describing Schottky injection is shown in Figure 66B. One can observe two distinct field regions brought about by the FEF distribution. The low field region originates from the injection equation being linear at low field strength. Thereby, the FEF distribution yields a locally, linearly increased and decreased injection current. As the average of the FEF distribution equates to 1, the original expression is maintained at low field strength. At high field strength, the injection equation is highly non-linear. At this stage, the highest FEF values in the distribution will produce the majority of the injection current, and thus, govern its field dependency (e.g. $\beta \approx FEF_{max}$).

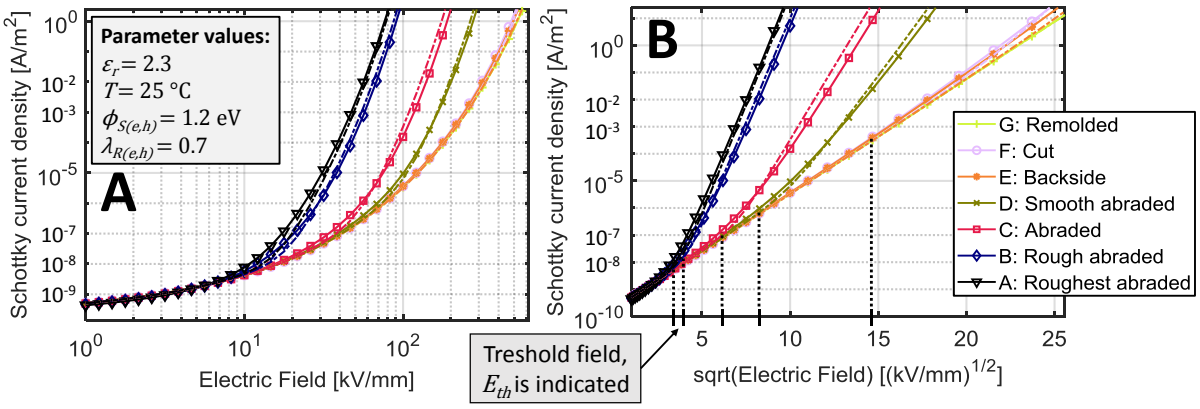

Figure 66. Calculated injection characteristics (solid lines with markers) using the Laplacian FEF distributions, fitted with curves using equation (64) (dash-dotted lines). Schottky currents are shown in a double logarithmic plot (A) and a Schottky plot (B). Used parameters are indicated in the legend.

This behavior could be matched by superimposing the original current density with a field enhanced current density (dash-dotted lines in Figure 68), the latter having a unitless field parameter β_S and a barrier height reduction $\Delta\phi_s$ in Volts [84], [118]:

$$J_{S,\beta(e,h)} = \lambda_{R(e,h)} A_0 T^2 e^{-\frac{\phi_{B(e,h)}}{k_B T}} \cdot \left(e^{\frac{e}{k_B T}\sqrt{\frac{eE}{4\pi\varepsilon_0\varepsilon_r}}} + e^{\frac{e}{k_B T}\left(\sqrt{\frac{e\beta_S E}{4\pi\varepsilon_0\varepsilon_r}} - \Delta\phi_s\right)}\right) \tag{62}$$

By comparing equation (62) with equation (58), the pre-parenthesis part can be seen as being of proportional scaling (thus J_o) but the field dependency in equation (62) is expressed differently (e.g. it doesn't adhere to the form $f(E)+Bf(\beta E)$). However, as an identical barrier height reduction (e.g. $\Delta\phi_s$ = 0.27) performed well for all surface types, the B parameter can be estimated by bringing it out from the exponent as:

$$e^{\frac{-\Delta\phi_s e}{k_B T}} \approx B_s = \frac{A_{tail}}{A_{tot}} = \sum_{1}^{N_{tot}} \left(\begin{cases} 1 & if\ (FEF \approx \beta_s) \\ 0 & if\ \neg(FEF \approx \beta_s) \end{cases}\right) \Big/ N_{tot} \tag{63}$$

Here B_s is the unitless scaling factor, A_{tail} is the surface area of the tail in the FEF distribution in m^2, A_{tot} is the total measurement area in m^2. Owing to identical (x,y) spacing between surface coordinates, the areal fraction can be estimated from the number of coordinates positioned at around β_S, divided by the total number of coordinates N_{tot}. The estimated value of $\Delta\phi_s$, yielding the parameter B_s in equation (63), was found to be accurate within the temperature range relevant to the experiments. Calibrations performed at extreme temperatures (e.g. T = 50 K), showed that expressing it independently on temperature yielded more accurate results. Furthermore, in separate estimations with abnormal FEF distributions, B_s was found to correlate strongly with the surface fraction within the FEF distribution tail. Combining equation (62) with equation (63) yields a re-formulated expression as:

$$J_{S,\beta(e,h)} = \lambda_{R(e,h)} A_0 T^2 e^{-\frac{\phi_{B(e,h)}}{k_B T}} \left(e^{\frac{e}{k_B T}\sqrt{\frac{eE}{4\pi\varepsilon_0\varepsilon_r}}} + B_s e^{\frac{e}{k_B T}\sqrt{\frac{e\beta_S E}{4\pi\varepsilon_0\varepsilon_r}}}\right) \tag{64}$$

Equation (64) adheres to the general form of roughness enhanced injection current $J_o(f(E)+Bf(\beta E))$. Furthermore, the low field reduction factor f_s, introduced in equation (38), does not affect the field dependency strongly, and can thus be readily added to equation (64).

6.2.2 Roughness enhanced hopping injection

For hopping injection, using equation (57) results in the following expression:

$$J_{H,\beta(e,h)} = 2v\varepsilon_0\varepsilon_r e^{-\frac{w_{ss(e,h)}}{k_B T}} E\left(\sinh\left(\frac{ea_{ss(e,h)}E}{2k_B T}\right) + B_H\beta_H \sinh\left(\frac{ea_{ss(e,h)}\beta_H E}{2k_B T}\right)\right) \quad (65)$$

where β_H and B_H are respectively unitless field and scaling parameters. The modified equation adheres to the form $J_o(f(E)+Bf(\beta E))$ in equation (58). The factor B_H again equates to the surface fraction positioned at around β_H in the tail of the FEF distribution. The current density estimated with equation (65) is compared with the average current density J_{avg} arising from the FEF distribution in Figure 67.

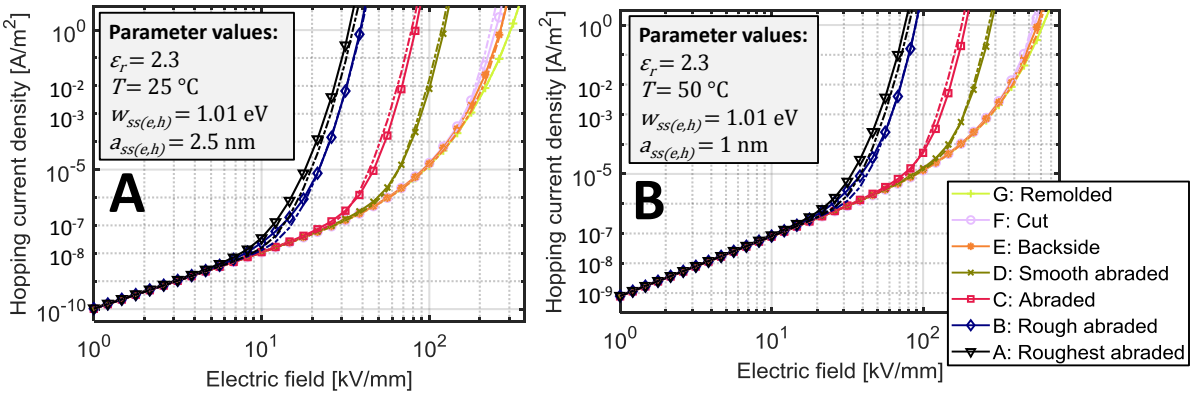

Figure 67. Calculated hopping injection characteristics (solid lines with markers) using Laplacian FEF distributions, fitted with curves obtained using equation (65) (dash-dotted lines). Used parameters are indicated in the figure, with strong field dependency (A) or weak field dependency (B).

As observed in Figure 67, equation (65) predicts earlier onset of the roughness enhanced injection for some of the surface types. This arises from the two extremes, low and high field strength, that are assumed in it. Realistically, the injection current exhibits a gradual transition, with B_H gradually decreasing and β_H gradually increasing upon crossing the field threshold. At high field strength, equation (65) predicts rates that match the average current density J_{avg} rather accurately.

6.2.3 Roughness enhanced Fowler-Nordheim injection

The temperature-dependent Fowler-Nordheim (FN) injection current density J_{FN} (equation (41)) was first evaluated at temperatures and in the field range relevant to the experiments (e.g. at 10-400 kV/mm, 10^{-17}-10^{-7} A/m^2 and 300-370 K), yielding an increase in average tunneling current J_{avg} caused by the FEF distribution as shown in Figure 68.

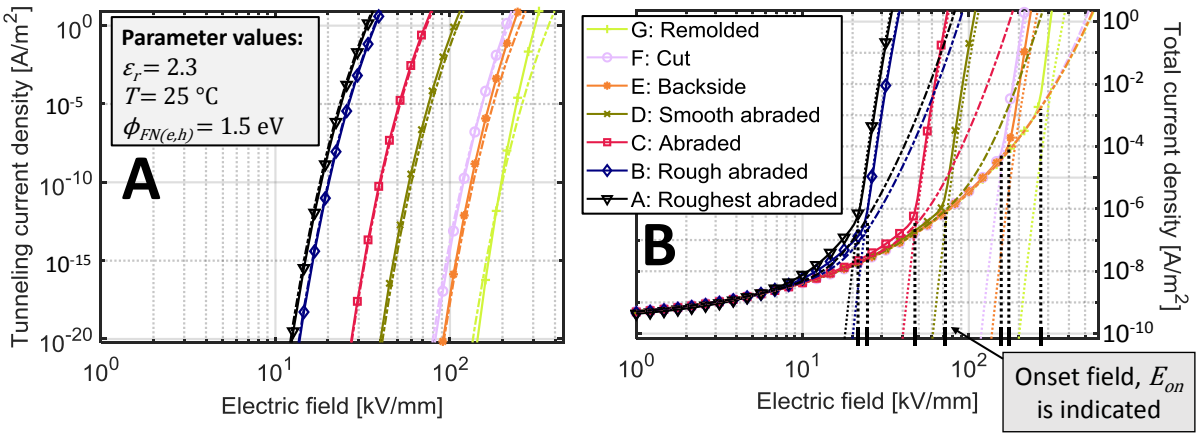

Figure 68. FN injection displayed in a double logarithmic plot (A). The total current (B) corresponds to the sum of the Schottky (from Figure 66) and Fowler-Nordheim injection current densities. Fitting curves are from equation (66) (dash-dotted lines). Used parameters are indicated.

To reduce the complexity, the average current was matched with the cold (0 K) current density $J_{FN,c,n}$ obtained from equation (15) (the results are shown with dash-dotted lines in Figure 68A), through the introduction of the unitless field parameter β_{FN}:

$$J_{FN,\beta(e,h)} = \frac{e^3(\beta_{FN}E)^2}{8\pi h\phi_{FN(e,h)}} e^{\left(-\frac{4}{3}\sqrt{\left(\frac{2m}{\hbar^2}\right)}\frac{\phi_{FN(e,h)}{}^{3/2}}{e\beta_{FN}E}\right)} \tag{66}$$

The cold current density $J_{FN,c,n}$, of an ideal surface yielded around 5 decades lower current density compared to its temperature-dependent counterpart J_{FN} (e.g. $J_{FN,c,n} \approx 10^{-5} \cdot J_{FN}$). However, this discrepancy is compensated by the lack of a scaling parameter B_{FN} in equation (66), which was found to exhibit approximately this value. Furthermore, the lack of image charge effect in equation (66) was compensated by increasing the field parameter β_{FN} for an ideal surface by 30 % (i.e. from 1 to 1.3). As the impact of the temperature and image charge effects is weak within the relevant range (due to the strong tunneling onset), only minor inaccuracy is introduced in this simplification. Equation (66) thereby adheres to the form $J_\beta = J_0 \cdot f(\beta E)$, and a superposition with the low field limit is not required because of its strong onset at the field strength E_{on}. Thereby, the average tunneling current density J_{avg} is seemingly only shifted along the abscissas towards lower field values. The summed current densities shown in Figure 68B reveal a threshold effect, corresponding to the onset field E_{on} of FN injection. Above E_{on}, bulk-limited charge transport arises, through the high field dependency in the injection current.

6.2.4 Surface specific parameters for charge injection

Investigations with arbitrarily chosen barrier heights $\phi_{(e,h)}$ (1.5 eV and 2 eV) and different temperatures (25 °C and 50 °C) in Schottky and FN injection expressions, estimated their impact on the average current density J_{avg} through equation (45) for the different surface types [111], [118]. For Schottky injection, it yielded the expected shifts along the ordinate, while for FN injection a shift along the abscissa was noticed and was matched by the roughness enhanced equations (64) and (66). For hopping injection, modification of its barrier height, $w_{ss(e,h)}$ still yielded a shift along the ordinate, but temperature, T and interfacial state spacing, $a_{ss(e,h)}$ modified its field dependency. This dependency was represented in equation (65).

The field and scaling parameters β and B are related to the Weibull FEF distribution and strongly correlate with the distribution's tail. However, as equations (64) and (65) only account for the extreme cases, low and high field strength respectively, a more realistic representation would be to omit the superposition and make use of field-dependent parameters, e.g. $\beta(E)$ and $B(E)$, respectively increasing from 1 to β and reducing from 1 to B. However, such a representation would introduce additional strong sensitivity to the FEF distribution's shape. Furthermore, the parameters' field dependencies (e.g. $\beta(E)$ and $B(E)$) are further affected by the locally distributed charge density at the surface, as anticipated by Poisson field simulations in section 6.1.2. Thus, at high field strength, owing to the FEF tail's shift along the abscissa, field parameters are expected to be significantly reduced. This reduction is an intricate balance of the FEF distribution's shape, the field dependency in the injection expression, and the local charge transport effects occurring in the interfacial domain. Due to such complexity, which renders any proposed field-dependent parameters inaccurate, extreme cases were again adopted. Thus, at low field strength, identical field parameters were used in all injection types, (i.e. $\beta_S = \beta_H = \beta_{FN}$). This is represented by the dash-dotted curves in Figure 66, Figure 67 and Figure 68. At high field strength exceeding 40 kV/mm in the experiment, reduced field parameters β_{high} were unanimously adopted in the injection expressions. Furthermore, for the sake of simplicity, the scaling parameters B were considered identical between the surface types. The parameter set representing the surface-type-specific parameters is shown in Table 6.

*Table 6. Roughness parameters, field enhancement, and estimated field (β) and scaling (B) parameters for the different surface types. A=roughest abraded, B=rough abraded, C=abraded, D=smooth abraded, E=backside, F=cut, G=remolded. *normalized against the remolded surface. **RMS of the 100 highest FEF values, corresponding to the tail in the histogram. †Parameters that best fitted the charge injection behavior, as shown in the previous figures (dash-dotted lines). For rough abraded a lower value was later used in the simulations, displayed within the parenthesis. ‡reduced field parameters estimated from Poisson fields, used in bipolar charge transport model above 40 kV/mm.*

Surface type	**A**	**B**	**C**	**D**	**E**	**F**	**G**
Roughness, *Sa* *	135.3	101.8	38.6	19.0	8.9	5.7	1
Roughness, *Sdq* *	84.3	75.6	36.2	23.7	10.3	12.0	1
Field enhancement, FEF_{max} **	10.0	7.5	4.2	3.0	1.6	1.7	1.1
Field parameter, β_S, β_{FN} and β_H †	14.5	13 (8)	6.5	4.3	1.9	2.2	1.3
Reduced field parameter, β_{high} ‡	6.5	6	4.2	2.8	1.5	1.8	1.3
Scaling parameter, B_s †	$2.718 \cdot 10^{-5}$						
Scaling parameter, B_H †	$2 \cdot 10^{-4}$						

The maximal field enhancement and field parameters β are shown to best correlate with the roughness' *Sdq* parameter due to the texture's disorder as described in section 6.1.1. However, the field parameters β are shown to be consistently higher than the value of FEF_{max}. This indicates that the surface fraction at high field strength corresponded to less than 100 data points. As the scaling parameters B represented approximately 25 data points in the merged dataset shown in Figure 61, the RMS of the FEF values in this fraction was in better agreement with the field parameters. This low surface fraction indicates how strong the estimated localization (represented by the scaling parameters B) of injection current density is. This localization also has a strong impact on the onset of FN injection as shown in Figure 68B. While such strong onset currents can be locally viable, its one-dimensional representation may be overestimated. Furthermore, the reduced field parameters β_{high} from Poisson field assumptions (section 6.1.2) would lessen the degree of localization, however, for sake of simplification, this behavior was not accounted for.

Conclusively, for Schottky, hopping and FN injection currents, their roughness enhanced equations (64), (65) and (66) account for the local field distribution in the irregular surface geometry. Their strong non-linearity leads to most of the charge being supplied from a small surface fraction, at which the divergent interface field is most enhanced. They can be introduced into a one-dimensional bipolar charge model, allowing for calibration of their injection barrier heights (i.e. $\phi_{B(e,h)}$, $\phi_{FN(e,h)}$, and $w_{ss(e,h)}$) as well as other parameters (i.e. T, $\lambda_{R(e,h)}$ and $a_{ss(e,h)}$) against measurement results. They allow for altering such parameters without forcing the time-consuming process of calculating local currents and averaging them into J_{avg} (equation (45)).

6.3 Bipolar charge transport modelling

6.3.1 Estimated conduction parameters

The final parameter set for bulk conduction, found after ~5500 simulations and providing the best results (lowest deviations from measurement data), is listed in Table 7.

*Table 7. Conduction parameters and their values used in the model. *Ranges of bulk conduction parameters found in literature* [27], [37], [39], [40], [42], [44], [48], [52], [53], [76]. *†Equations where the parameters are used.*

Description	Para-meter	Min*	Max*	Value	Unit	Eq.†
Deduced quantities. ‡Estimated from other parameters at E = 0 and T = 25 °C.						
Base level mobility *e* ‡	$\mu_{0,e}$	$8\cdot10^{-17}$	$1.2\cdot10^{-13}$	$6.3\cdot10^{-15}$	$m^2/(V\cdot s)$	(2)
Base level mobility *h* ‡	$\mu_{0,h}$	$4\cdot10^{-16}$	$2\cdot10^{-13}$	$9.5\cdot10^{-15}$	$m^2/(V\cdot s)$	
Base level trapping rate *e* ‡	$B_{0,e}$	$1\cdot10^{-3}$	0.1	$3.2\cdot10^{-4}$	s^{-1}	-
Base level trapping rate *h* ‡	$B_{0,h}$	$2\cdot10^{-3}$	0.2	$1.7\cdot10^{-3}$	s^{-1}	-
State densities. **Deduced from trap separation, $a_{sh(e,h)}^{-3}$.						
Shallow trap density *e* **	$N^0_{shallow,e}$	-	-	$8.78\cdot10^{25}$	m^{-3}	-
Shallow trap density *h* **	$N^0_{shallow,h}$	-	-	$5.12\cdot10^{26}$	m^{-3}	-
Inter-level trap dens. *e* and *h*	$N^0_{int(e,h)}$	-	-	$1\cdot10^{23}$	m^{-3}	(34)
Deep trap density *e*	$N^0_{deep,e}$	100/e	200/e	40/e	m^{-3}	(32), (33) and (34)
Deep trap density *h*	$N^0_{deep,h}$	100/e	200/e	95/e	m^{-3}	
State separations. ††Parameter obeys the limits defined in equation (35)						
Shallow trap spacing *e*	$a_{sh,e}$	0.71	5.12	2.25	nm	(28) and (30)
Shallow trap spacing *h*	$a_{sh,h}$	0.71	6.23	1.25	nm	
Inter-level trap spacing *e* ††	$a_{int,e}$	-	-	80	nm	(28)
Inter-level trap spacing *h* ††	$a_{int,h}$	-	-	100	nm	
Energetic barriers. With 0.05 eV and 0.03 eV discrepancy between thermal and hopping activation, equating to the shallow trap depth.						
Hopping barrier *e*	$w_{hop,e}$	0.608	1	0.76	eV	(28)
Hopping barrier *h*	$w_{hop,h}$	0.532	0.83	0.74	eV	
Inter-level state depth *e*	$w_{tr,int,e}$	0.608	1	0.81	eV	(34)
Inter-level state depth *h*	$w_{tr,int,h}$	0.532	0.83	0.79	eV	
Detrapping barrier *e* and *h*	$w_{tr(e,h)}$	0.9	1.05	1.03	eV	(31)
Hop-detrap barrier *e* and *h*	$w_{tr,hop(e,h)}$	-	-	1.00	eV	(30)
Recombination parameters. ‡Total recombination rates $S_{1\text{-}3}$ are higher owing to Langevin recombination						
Trapped h and trapped e	$S_{0,base}$	0	$4\cdot10^{-3}$	$1\cdot10^{-3}$	$m^3/(C\cdot s)$	(37)
Trapped h and mobile e ‡	$S_{1,base}$	0	$4\cdot10^{-3}$	$1\cdot10^{-3}$	$m^3/(C\cdot s)$	
Mobile h and trapped e ‡	$S_{2,base}$	0	$4\cdot10^{-3}$	$1\cdot10^{-3}$	$m^3/(C\cdot s)$	
Mobile h and mobile e ‡	$S_{3,base}$	0	0	$1\cdot10^{-3}$	$m^3/(C\cdot s)$	

Description	Para-meter	Min*	Max*	Value	Unit	Eq.†
Miscellaneous parameters.						
Trapping cross-section	$A_{T(e,h)}$	-	-	$a_{sh(e,h)}^2$	nm^2	(33)
Trapping probability	P_T	-	-	100	%	(33)
Recombination probability	P_R	-	-	100	%	(37)
Relative permittivity	ε_r			2.3	none	

Given that the majority of bulk conduction parameters (shown in Table 7) originate from respective barrier heights and densities of shallow, inter-level and deep states, they can be considered to represent the material's density of states (DOS). The DOS (together with injection parameters described in the next section) yields near-symmetric charge accumulation at low field strength, while at higher poling voltages (stronger applied fields), electron transport and injection are favored. This asymmetry was observed in the space charge measurements described in section 4.2.1 and was therefore used as an aiming point for parameter selection. Further parameter calibration showed that such asymmetry produced the best results (i.e. the lowest deviations from measurement data), further visualized in the mobility's field dependency expressed in equation (28) as shown in Figure 69.

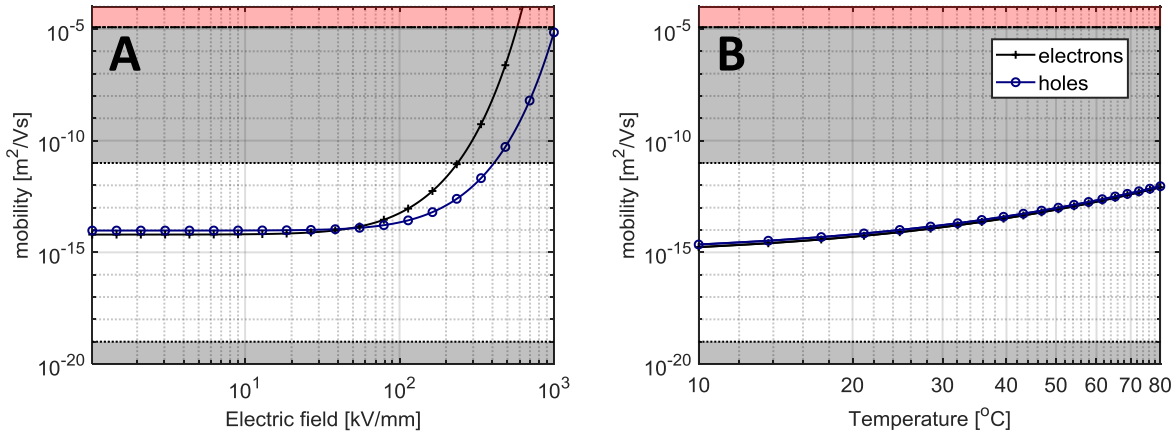

Figure 69. Apparent mobilities as a function of field strength at 25 °C (A) and temperature at 30 kV/mm (B). Used parameter values are indicated in Table 7. Grey areas indicate regions where the base level mobility is out of realistic range. The red area indicates the limit for band theory [34].

As observed in Figure 69, electron and hole mobilities remain similar at low field strength and against temperature, due to similar hopping barrier heights and inter-level state spacing ($w_{hop(e,h)}$ and $a_{int(e,h)}$ shown in Table 7). The asymmetry arises at high field strength due to the higher shallow state spacing ($a_{sh(e,h)}$) for electrons. The detrapping rate from equation (29) and the trapping rate without the state occupancy expression (i.e. $B_{0(e,h)t}+B_{(e,h)t}(E)$) from equation (32) are displayed in Figure 70A against field strength. Furthermore, the recombination rates ($S_{0\text{-}3}$) expressed by equation (37) are displayed against field strength in Figure 70B.

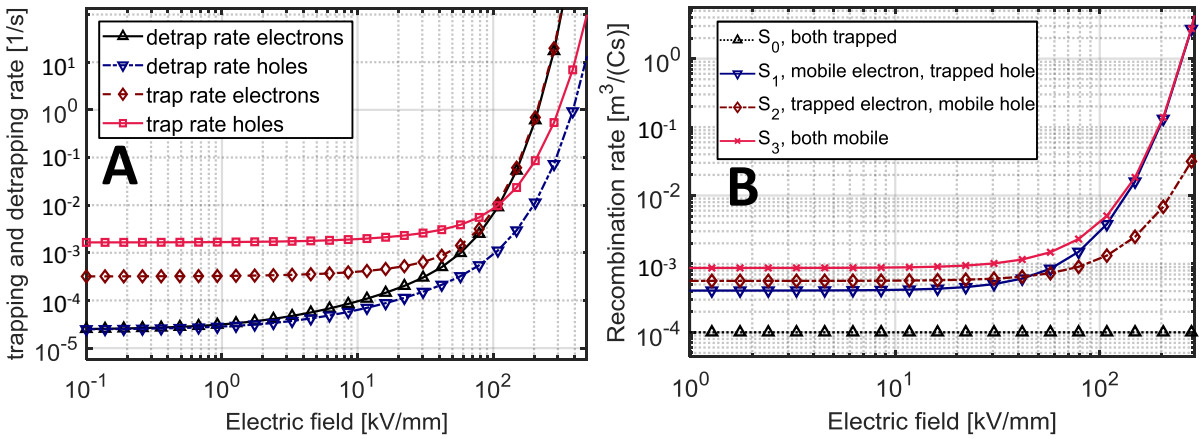

Figure 70. Trapping and detrapping rates as a function of applied field at 25 °C (A). Field dependent recombination rates at 25 °C (B). Trapping and recombination field (and temperature) dependencies originate from the mobility expressions, parameter values are indicated in Table 7.

The trapping and detrapping processes (the rates are shown in Figure 70A) allow for reduced residence time in deep traps at high field strength. This trapping behavior yields a higher fraction of mobile charge carriers (over their trapped counterpart). At low field strength, the trapping and detrapping rate discrepancy is larger, allowing for the slow depolarization observed in the space charge measurements. In order to reduce the parameter space, equations (33) and (37) were further simplified by assuming trapping and recombination probabilities operating at 100%. In addition, the capture cross-section was assumed to be of equal size as the two-dimensional cubic lattice spacing of shallow states. Even if the actual capture cross-section could differ from the trap lattice spacing [119], the deep trap density ($N^0_{deep(e,h)}$), capture cross-section ($A_{T(e,h)}$) and trapping probability (P_T) are all unknown parameters. Thereby, only one of them is required ($N^0_{deep(e,h)}$) for yielding accurate trapping rates, and their field and temperature dependencies are inherited from the mobility expression. The assumption of a trap depth dependent (and thus reduced) capture cross-section [119], requires higher deep trap densities for compensation. For this reason, the deep trap densities listed in Table 7 may be underestimated.

For recombination rates displayed in Figure 70B, a low base level trapped–trapped carrier recombination rate ($S_{0,base}$) is assumed. This process requires either two trap sites located in close vicinity, or one of the carrier's detrapping and subsequently finding the other one before encountering an inter-level state. By this definition, both such cases make their recombination improbable. Additionally, recombination between mobile electrons and mobile holes (S_3), which is normally considered to be low or zero, can here be assumed to obey the Langevin recombination theory [112]. Additionally, when the base level rates ($S_{1\text{-}3,base}$) are below the Langevin recombination rates, the amount of process altering parameters is reduced, allowing for easier calibration (e.g. base level rates not requiring fine-tuning, and recombination following the hopping mobility). This approach differs from the frequently used description, which makes use of only the base level recombination rate with a value of $4 \cdot 10^{-3}$ m^3/s for all rates, except for mobile-mobile carrier recombination [30], [39], [40], [48], [52]. Finally, in addition to the discussed field dependencies of the recombination rates, their temperature dependency also exists, originating from the mobilities displayed in Figure 69B. The field-dependent trapping, detrapping and recombination rates were key for establishing a measurement representative charge evolution during polarization with subsequent depolarization. Such an evolution is displayed in Figure 71 for a typical simulation, for individual carrier densities n_e, n_{et}, n_h and n_{ht}.

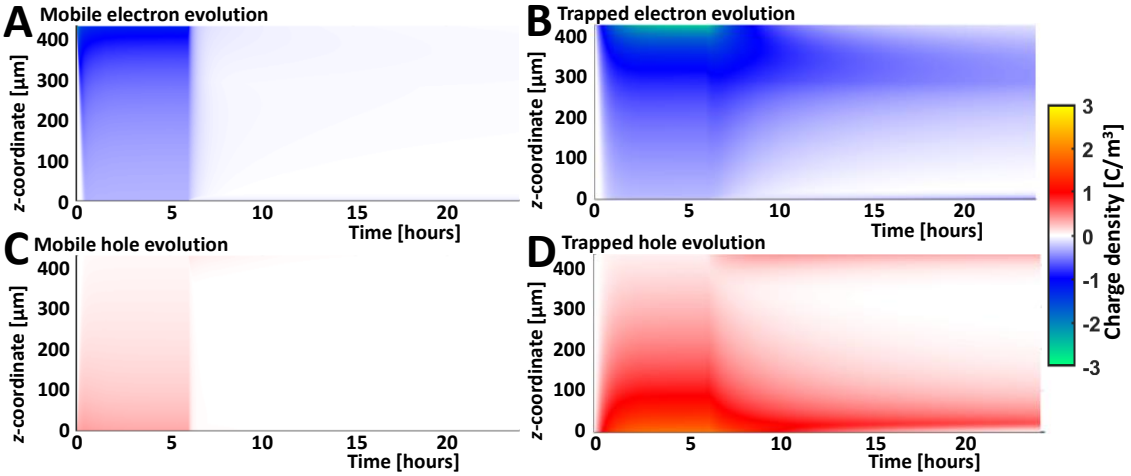

Figure 71. The evolution of individual carrier densities n_e (A), n_{et} (B), n_h (C) and n_{ht} (D). The results are shown for the case of 6 hours of polarization and 18 hours of depolarization, for abraded sample SC-21 subjected to −15 kV biasing voltage at 25 °C.

As observed in Figure 71, while more mobile charge carriers exist during polarization, they are subsequently trapped, or recombine during depolarization. The field-dependent rates shown in Figure 70 were crucial for establishing this carrier evolution. Thereby, the evolution of net charge density in the measurement was better represented, demonstrating a high initial decay at the onset of depolarization, which gradually decreases with time shown in the decay curves, displayed by solid lines in Figure 37B.

6.3.2 Injection types and parameters

The final parameter set charge injection, found after ~5500 simulations and providing the best results (lowest deviations from measurement data), is listed in Table 8.

*Table 8. Injection parameters and their values used in the model. *Ranges of injection parameters found in literature* [27], [37], [39], [40], [42], [44], [48], [52], [53], [76]. *†Equations where the parameters are used.*

Description	Parameter	Min*	Max*	Value	Unit	Eq.†
Schottky injection. **Parameters for reducing injection rate at low field strength. ‡Parameter values are lower due to the correction factors.						
Injection barrier *e*	$\phi_{B,e}$	1.1	1.27	0.905‡	eV	(64)
Injection barrier *h*	$\phi_{B,h}$	1.1	1.27	1.148‡	eV	(64)
Correction factor *e*	$\lambda_{R,e}$	1	1	$4.1 \cdot 10^{-5}$	none	(64)
Correction factor *h*	$\lambda_{R,h}$	1	1	0.1	none	(64)
Ohmic threshold **	$E_{ohm,th}$	-	-	5	kV/mm	(39)
Spread parameter **	S_{pr}	-	-	0.6	mm/kV	(39)
Reduction factor **	f_s	0	1	1	none	(38)
Fowler-Nordheim injection. ††A 0.5 eV barrier was used for charge packet investigations.						
Injection barrier *e*	$\phi_{FN,e}$	-	-	2, (0.5)††	eV	(66)
Injection barrier *h*	$\phi_{FN,h}$	-	-	2	eV	(66)
Hopping injection. ‡‡Field dependent quantity at 10 kV/mm in C/m^3 [57].						
Surface state spacing *e*	$a_{ss,e}$	4.3	5.8	3.3	nm	(65)
Surface state spacing *h*	$a_{ss,h}$	4.5	9.9	1.6	nm	(65)
Hopping barrier *e*	$w_{ss,e}$	-	-	1.01	eV	(65)
Hopping barrier *h*	$w_{ss,h}$	-	-	1.01	eV	(65)
Surface charge density	ρ_s	-70‡‡	-	$\varepsilon_0\varepsilon_r E$	C/m^2	

The charge injection parameters listed in Table 8 were used in conjunction with the surface-specific parameters listed in Table 6. The three individual injection types were assumed in superposition through equation (50), accounting for injection in the electrode's injection-extraction current density relationship in equation (49). However, hopping and Schottky injection were assessed separately by eliminating one of them with high barrier height values.

The FN electron injection was incorporated in the model by setting its barrier height $\phi_{FN,e}$ in equation (66) to 0.5 eV. This low barrier allowed for representing the charge packets observed in the experimental results at high field strength (Figure 38). FN injection created the packet-like shape, observed in the initial transient space charge pattern. However, along with the transient, too high charge density was observed subsequently during the rest of the polarization stage. Therefore, the FN injection barrier was finally set to 2 eV, preventing the appearance of this effect in the simulations. Furthermore, its roughness enhanced expression was deemed unusable in a one-dimensional domain, as the charge packet phenomenon was not observed at lower field strength for rougher cathodes. This observation indicates that packet formation, while originating from a strong onset current density, has such current capped above a certain level [106]. It could be capped by either the phenomenon itself, or localized charge accumulation suppressing the tunneling current at the asperity or inherently.

For Schottky injection, a higher injection rate was assigned for electrons (through $\lambda_{R,e}$ and $\phi_{B,e}$) compared to holes (through $\lambda_{R,e}$ and $\phi_{B,e}$), reflecting the experimental features. It provided the conditions for the dominating negative charge accumulation within the material, as observed in the measured space charge patterns in section 4.2.1. Moreover, injection barrier heights at room temperature exhibited values similar to those found in the referenced literature. However, at elevated temperatures, the injection rates needed some reduction, which was realized by simultaneous adjustment of $\lambda_{R(e,h)}$ and $\phi_{B(e,h)}$. This adjustment allowed for decreasing the injection barrier while maintaining the injection rate at room temperature. The values of the parameters f_s, S_{pr} and $E_{ohm,th}$ were tuned yielding unaffected injection above 5 kV/mm, while reducing injection below this ohmic field threshold. This threshold limited the injection of opposite charge carriers during the depolarization stage, which was driven by the reversed orientation of the field resulting from the residual carriers.

For hopping injection, the dominant negative charge accumulation observed in the experiments at high field strength was again adopted. However, because of the capability of tuning its field dependency (through $a_{ss(e,h)}$), a higher electron surface state spacing reflected this injection asymmetry better. Also, it allowed for symmetric barrier heights, $w_{ss(e,h)}$ listed in Table 8. Neither introduction of ohmic field thresholds (equation (39)), nor a reduction with factors f_s, were required since the hopping injection expression readily approaches zero at low field strengths. Thereby, its expression matched better with the instances where opposite charge carriers were observed in the measurements during the depolarization stage. The performance of Schottky and hopping injection is presented in the following sections.

6.3.3 Sample specific observations

To quantify the origin of local deviations between the model and the measurement signals, one-dimensional space charge distributions, obtained with Schottky injection, are shown in Figure 72 for several instants.

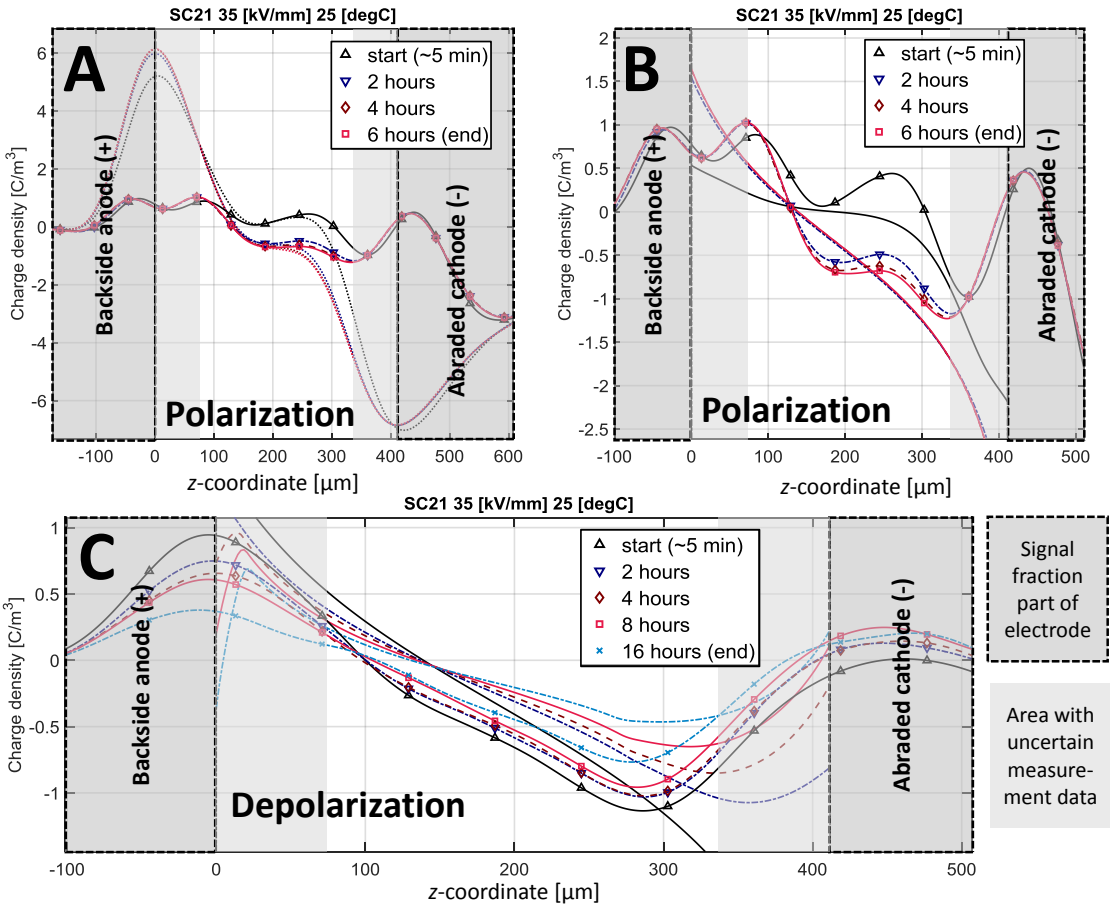

Figure 72. Results for abraded sample SC-21, subjected to -15 kV biasing voltage at 25 °C Line plots show the measurement data before and after Gaussian peak removal (A). Line plots comparing net charge density in the model (with Schottky injection) and measurement during polarization (B) and depolarization (C). The lines with markers indicate measurements whereas the lines without markers indicate model results. Dotted lines indicate the original signal with induced electrode charges during polarization.

The measurements began at ~5 minutes after applying or removing the biasing voltage at the beginning of polarization or depolarization sequences, respectively. This time was required to change the voltage and to reset and start the acquisition system. In Figure 72, the region (~75 µm) closest to the electrodes indicated in light gray, must be regarded as less accurate, as this signal region was originally occupied by induced electrode charges. It was therefore excluded in the estimation of the model deviations ρ_{dev} and mean charge density ρ_{mean} (respectively with equation (24) and equation (23)). During polarization, such electrode charges (dotted lines in Figure 72A) were removed, but as they made up a large portion of the measurement data, the underlying space charge signal was still difficult to deduce accurately. During depolarization, image charges were not removed as it was too difficult to ascertain which signal fraction originated from image charges, and which fraction originated from opposite carrier injection. The mean charge deviations ρ_{dev} were 0.29 and 0.28 C/m^3 during polarization and depolarization, respectively, that can be compared with the measured mean charge density, being 0.75 and 0.18 C/m^3. While the higher relative deviation in the depolarization stage seems to be related to insufficient negative carrier penetration, it instead originates from the measurement and its calibration. During polarization, the positive-negative signal transition is located at ~130 µm while in depolarization it occurs at ~100 µm. The non-ideal nature of the original and subsequently calibrated measurement signals thus generates some of the mean charge deviation (ρ_{dev}).

The model results obtained with Schottky or hopping injection are compared with measured data for a rough abraded or a smooth (backside) anode in Figure 73 at low field strength.

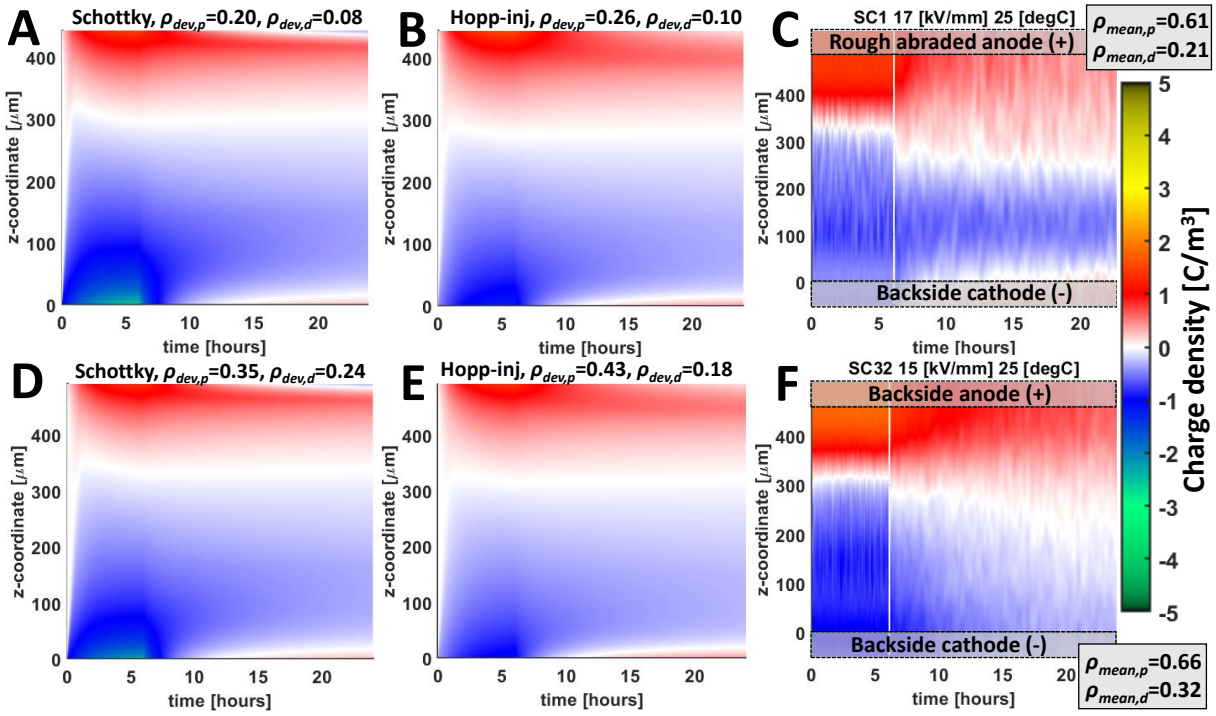

Figure 73. Colormap of net space charge density obtained in simulation with Schottky injection (A), hopping injection (B) and measurement (C) for rough abraded sample SC-1. Also, with Schottky injection (D), hopping injection (E) and measurement (F) for backside sample SC-32. Both samples were subjected to 7.5 kV biasing voltage at 25 °C. Mean deviation in C/m^3 for the polarization and depolarization ($\rho_{dev,p}$ and $\rho_{dev,d}$, respectively) is indicated above each model subfigure, comparable to mean charge densities in C/m^3 for each measurement ($\rho_{mean,p}$ and $\rho_{mean,d}$, respectively).

As observed in Figure 73, Schottky and hopping injection yielded similar results, being comparable to the observed experimental charge evolution. Furthermore, at low field strength, no difference in positive carrier density is observed between a rough and a smooth anode, which is also represented in the roughness enhanced charge injection expressions. Estimation of the mean charge deviation ρ_{dev} and the measurement's mean charge density ρ_{mean} (respectively with equation (24) and equation (23)), are indicated in the sub-figures separately for polarization (time < 6 hours) and depolarization (6 hours < time < 24 hours) sequences. Such quantities also indicate an agreement of the local charge densities obtained in the model and the measurements.

Results of the simulations with Schottky or hopping injection are compared with the measurement data for a rough abraded anode or an abraded cathode in Figure 74 at medium field strength. Again, the simulation results with both roughness enhanced Schottky and hopping injection are in good agreement with the measurement results. Furthermore, the initial (immediately after applying the electric field) transients in carrier densities match well, indicating that carriers' mobilities are within the correct order of magnitude. Furthermore, increased charge density is observed adjacent to the rough electrodes, being marginally higher for hopping injection compared to Schottky injection because of its stronger field dependency. Also, hopping injection provided marginally better opposite charge injection rates, observed close to the anode and cathodes during depolarization (thus at low field strength). However, the low field reduction of Schottky injection below 5 kV/mm may have been insufficient.

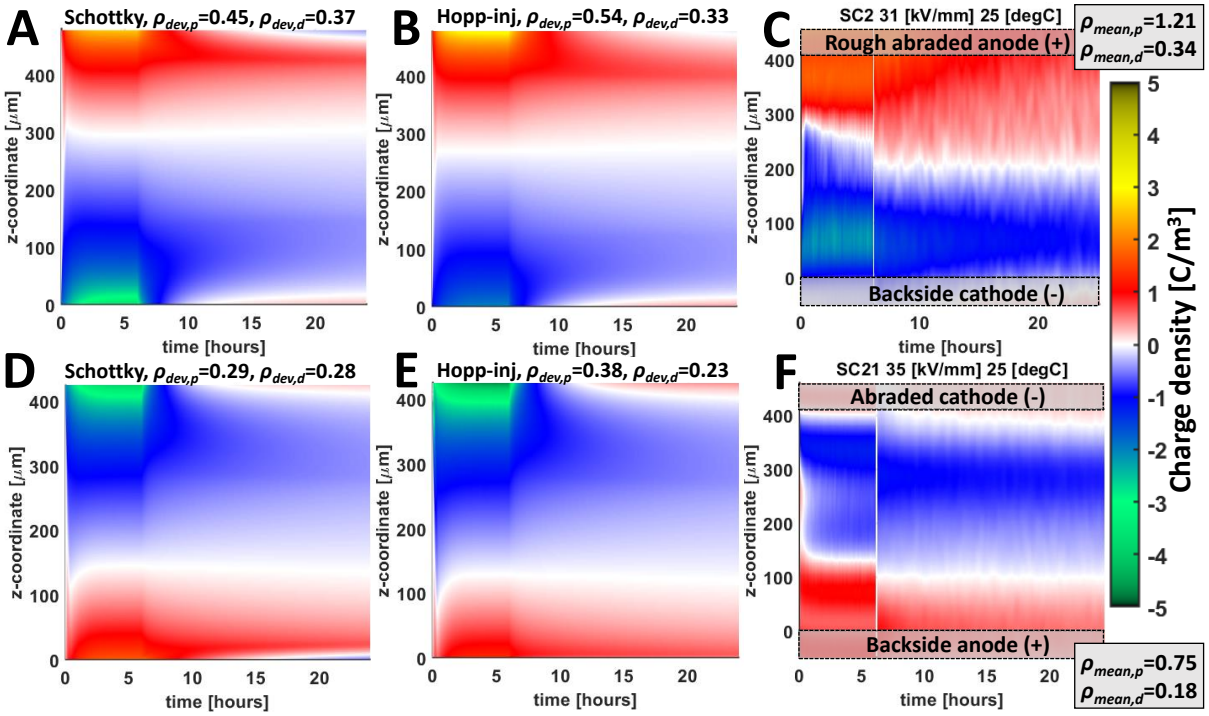

Figure 74. Colormap of net space charge density obtained in simulation with Schottky injection (A), hopping injection (B) and measurement (C) for rough abraded sample SC-2, subjected to +15 kV biasing voltage at 25 °C. Simulation Schottky injection (D), hopping injection (E) and measurement (F) for abraded sample SC-21, subjected to −15 kV biasing voltage at 25 °C. Mean deviation in C/m^3 for the polarization and depolarization ($\rho_{dev,p}$ and $\rho_{dev,d}$, respectively) is indicated above each model subfigure, comparable to mean charge densities in C/m^3 for each measurement ($\rho_{mean,p}$ and $\rho_{mean,d}$, respectively).

For both samples in Figure 74, their polarization sequences show the best relative agreement (i.e. by comparing ρ_{dev}/ρ_{mean}), while their depolarization sequences agree less with the measurement. For rough samples specifically, the model exhibited higher decay rates, as seen when comparing carrier density after the first hours of depolarization. This was also observed in local displacement currents in the simulations and measurement (through equation (48)), which during depolarization dominated over conduction and diffusion currents, shown in Figure 75.

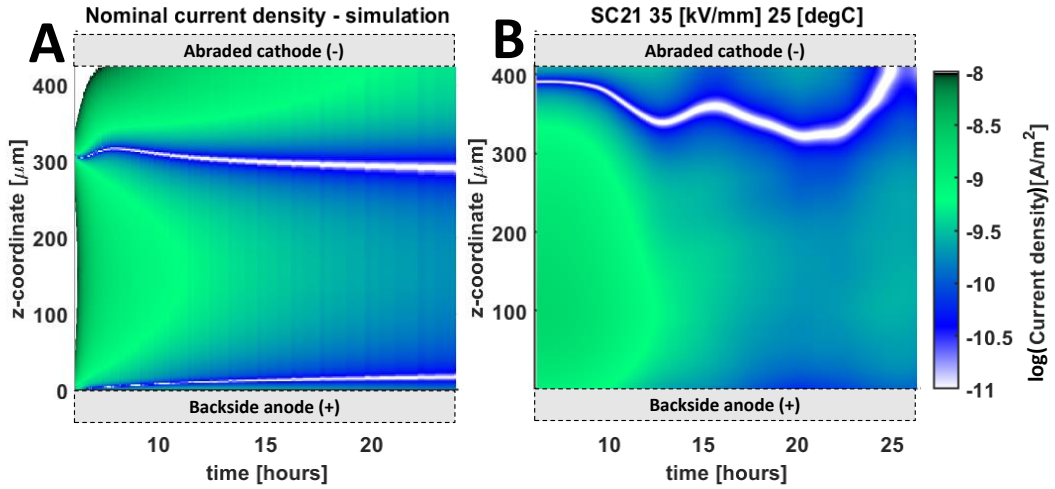

Figure 75. Logarithm of the displacement current in model (A) and estimated from space charge measurement (B), during depolarization. Displayed for sample SC-21 subjected to -15 kV poling at 25 °C. The white regions with low current density originate from positions with low electric field strength.

As observed in Figure 75, a similar evolution of the current density is observed between the respective depolarization stages in simulation and measurement, albeit the model features higher decay during the first hour. After approximately 12 hours (6 hours of depolarization), the decay rate slows down to below 10^{-9} A/m^2 in both the simulation and the experiment.

6.3.4 Limitations of the model

The performed comparison of the measured and computed space charge patterns indicated several phenomena affecting the agreement between the model and experimental results. One such phenomenon was the formation of charge packets in the material. As observed in the measured charge distributions presented in Figure 76 (C, F and I), surface roughness has a significant impact on positive charge accumulation adjacent to the anode.

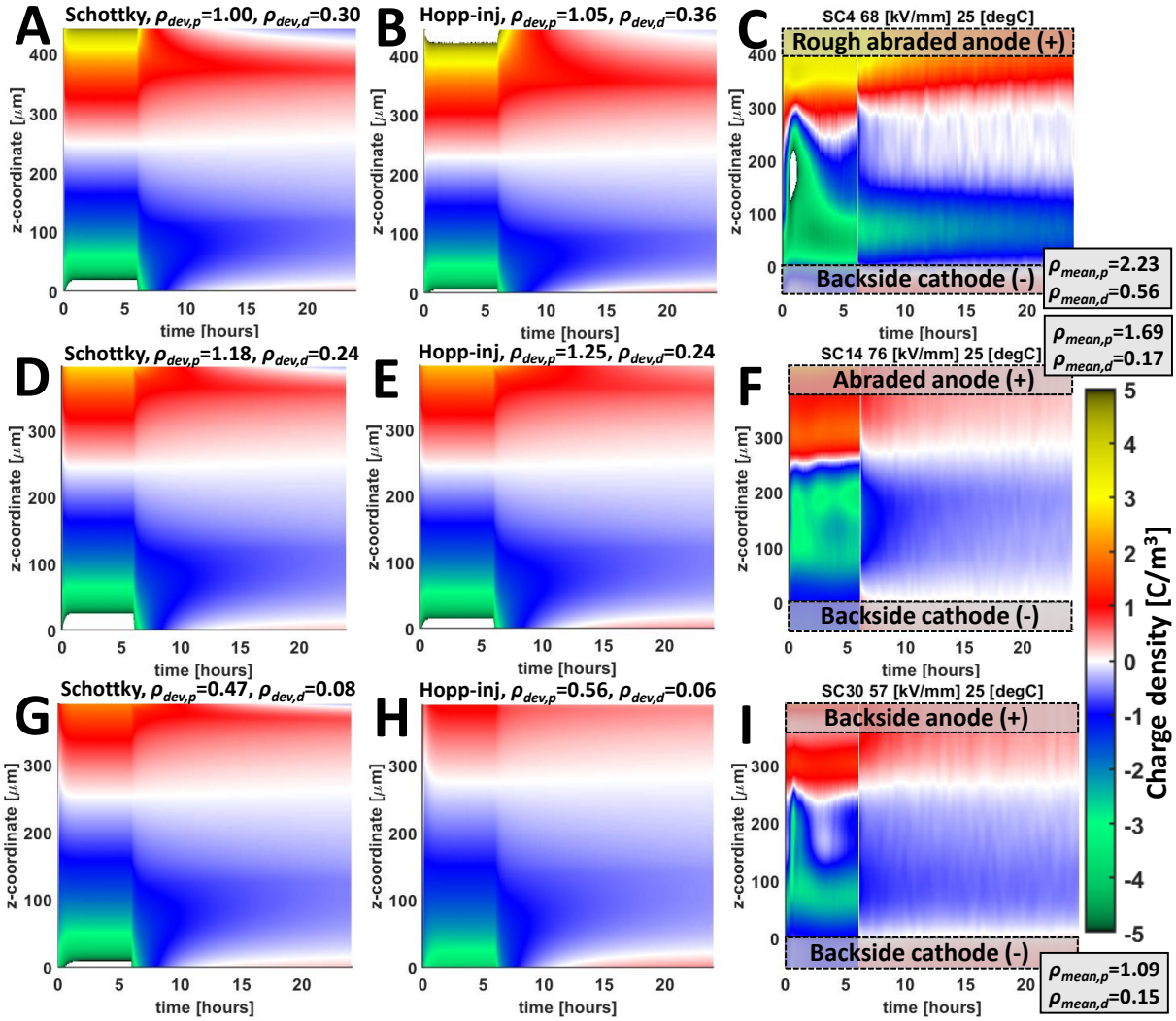

Figure 76. Colormap of net charge density in simulations with Schottky injection (A, D and G), hopping injection (B, E and H) and measurements (C, F and I) for the rough abraded sample SC-4 (A, B and C), abraded sample SC-14 (D, E and F) and backside sample SC-30 (G, H and I). All samples were subjected to + 30 kV biasing at 25 °C. Negative charge packets are observed in measurements (C, F and I), represented with the green peaks during the first hours of polarization. Mean deviation in C/m^3 for the polarization and depolarization ($\rho_{dev,p}$ and $\rho_{dev,d}$, respectively) is indicated above each model subfigure, comparable to mean charge densities in C/m^3 for each measurement ($\rho_{mean,p}$ and $\rho_{mean,d}$, respectively).

Roughness enhanced Schottky and hopping injection from the anodes in Figure 76 (A, B, D, E, G and H), yielded a higher positive charge density at rougher anodes, thus agreeing with the experimental observation. Also, hopping injection exhibits a higher field dependency over Schottky injection, yielding stronger variation in homocharge density against the anode's roughness level. However, discrepancies appeared at the cathode during the transients and subsequent negative charge accumulation. In the measurements, negative charge packets are observed, being more pronounced in rougher samples. In the simulation, only a marginal increase in negative charge accumulation is observed, and the charge packet is not represented. This lacking charge packet representation resulted in larger relative deviations between the model and the measurement.

Another experimental observation was a slow transient, where the internal charge density gradually changed its polarity, as shown in Figure 77C for an abraded sample. This recorded transient was not reproduced in the simulations (Figure 77A and B), as it stabilizes within ~ 2 hours of polarization. Such slow transients were observed with abraded or smooth abraded surfaces subjected to low-medium field strength (< 39 kV/mm) and, when pronounced, they increased deviations between the model and the experiment. Given their systematic appearance, they may be a feature of such electrode types. For Schottky injection in sample SC-11 (Figure 77A), it was the only case where the polarization sequence's deviation exceeded the measured mean charge density (i.e. $\rho_{dev,p} > \rho_{mean,p}$).

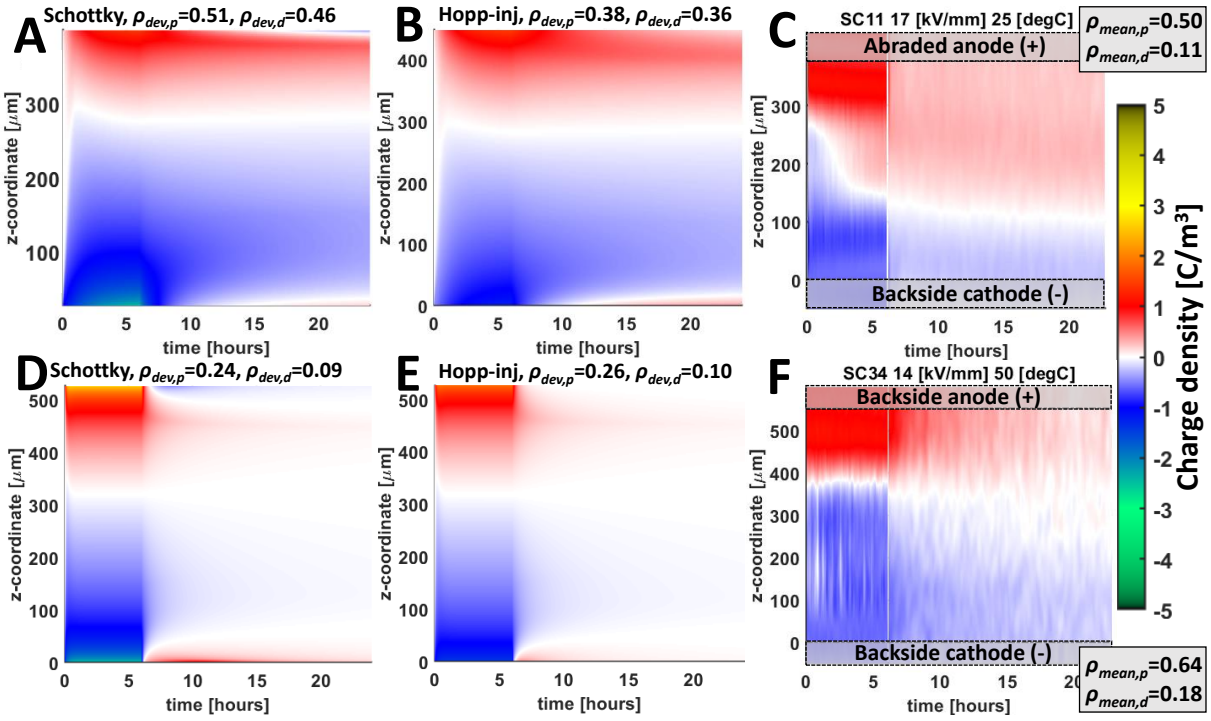

Figure 77. Colormap of net charge density in simulation (A and B) and measurement (C) for abraded sample SC-11, subjected to + 7.5 kV biasing at 25 °C. Simulation (D and E) and measurement (F) for sample SC-34 subjected to + 7.5 kV biasing at 50 °C. Mean deviation in C/m³ for the polarization and depolarization ($\rho_{dev,p}$ and $\rho_{dev,d}$, respectively) is indicated, comparable to mean charge density in C/m³ for each measurement ($\rho_{mean,p}$ and $\rho_{mean,d}$, respectively).

Furthermore, the measurement-model agreement at elevated temperatures can be commented on using the example of the data in Figure 77 (D, E and F) for a backside sample at 50 °C. At elevated temperatures, the decay rate obtained in the simulation is higher than in the experiment. However, this deviation does not yield a large relative deviation in the charge density.

Additionally, Schottky injection yields too high concentrations of opposite charge during depolarization (D) despite of having limited this effect through its ohmic field threshold (equation (39)) and its reduction factor f_s. For hopping injection, the injection rate at low field strength gives a better match with experimental data.

6.3.5 Overall model performance

For an efficient evaluation of the model performance and comparison with the space charge measurements, individual quantities were estimated for each sample. The mean deviation ρ_{dev} and measurement's mean charge density ρ_{mean} were calculated through equations (24) and (23), respectively. The results are shown in Table 9 for different measurement series, arranged by sample type, observation, or temperature in different columns.

*Table 9. Deviation for different measurement sections and injection types. Average for the measurement series where; B=rough abraded, C=abraded, D=smooth abraded, E=backside, G=remolded. *Average for all 45 performed measurements. †Average for ideal measurements, lacking charge packets and slow transients described in section 6.3.4. ‡Average sorted by temperature. **Estimated from a full sequence with polarization and depolarization weighted equally.*

Quantity	**Sequence**	**Unit**	**B**	**C**	**D**	**E**	**G**	**Aa***	**Ai†**	**25‡**	**50‡**	**70‡**
ρ_{dev}, Schottky	poling	C/m^3	0.70	0.63	0.44	0.58	0.45	0.58	0.43	0.57	0.61	0.60
injection, $J_{S,\beta}$	depoling	C/m^3	0.35	0.28	0.23	0.20	0.22	0.27	0.19	0.30	0.20	0.08
ρ_{dev}, hopping	poling	C/m^3	0.70	0.64	0.41	0.63	0.47	0.59	0.46	0.57	0.61	0.70
injection, $J_{H,\beta}$	depoling	C/m^3	0.37	0.24	0.20	0.17	0.20	0.24	0.17	0.28	0.20	0.08
ρ_{mean}, PEA	poling	C/m^3	1.37	1.11	0.87	1.33	0.85	1.15	0.96	1.06	1.20	1.62
measurement	depoling	C/m^3	0.31	0.16	0.13	0.20	0.23	0.20	0.19	0.23	0.15	0.11
ρ_{dev}/ρ_{mean}, $J_{S,\beta}$	both **	%	63	72	67	51	62	63	54	67	60	39
ρ_{dev}/ρ_{mean}, $J_{H,\beta}$	both **	%	64	69	61	52	62	61	55	66	60	45
Sample amount per test series			10	10	8	12	5	45	23	33	6	6

As seen in Table 9, a deviation ρ_{dev} lower than the measurement's mean charge density ρ_{mean} was achieved globally (column Aa) in polarization, yielding around 60% relative deviation (ρ_{dev}/ρ_{mean}). Also, roughness enhanced Schottky and hopping injection ($J_{S,\beta(e,h)}$ and $J_{H,\beta(e,h)}$) yielded similar deviations in charge density, and both injection expressions matched the carrier evolution at increasing roughness levels (columns B-G) and elevated temperatures (columns 25-70). Note any trend with increasing roughness level is difficult to note in Table 9, as the measurement series include different poling field strengths (10-80 kV/mm), polarities, sample orientations, temperatures or thickness variations in the peelings. When screening the samples based on observed charge packets and slow transients (column Ai), the relative deviation decreased by 10%. While some deviations could also arise from the measurements and their calibration, screening and selective censoring based on a specific sample's deviation was not adopted. Out of 47 screened measurements, only 2 samples were initially removed based on high noise to signal ratios. Further deviations can also arise from gaussian signal broadening in the measurement data, which was not accounted for in the model data.

While low deviation ρ_{dev} was achieved in depolarization, relative deviation ρ_{dev}/ρ_{mean} was larger for this sequence, resulting from its low charge density which makes artifacts more pronounced. While both deviations and the mean charge densities decreased with temperature in depolarization, the relative deviation remained similar. However, it was observed that since the calibrated parameter set (and specifically the deep trap depths and densities) was specifically tuned for best describing the initial stages of the depolarization sequence, it thus yielded decay rates marginally exceeding the measurement data. The underlying issue could be related to

representing the DOS on discrete energetic levels. As a deep state distribution could exist in the range of 0.9–2 eV [35], [53], the deeper states thus remain unresolved. Their impact could improve the carrier evolution during depolarization since they contribute less to the overall charge distribution (due to their lower density) and more to the decay rate (due to their increased depth and thus long carrier residence times). Simulations performed with two deep trap levels showed that a second deep trap level, with a density of ~(1-2) C/m^3 and depth of ~1.2 eV could be added with minimal impact on the deviations in Table 9, reducing the decay rates in later stages of depolarization. However, such results are not described further for the sake of reducing complexity (such simulation introduces 2 additional source equations, 5 additional recombination types, etc.).

In summary, the parameter set used in the simulations provided good agreement with the measurements. While a more accurate solution may exist in the parameter space, the model results provide strong evidence for the roughness enhanced injection mechanisms and provides a better understanding of the material's conduction properties.

6.4 Multi-scale simulation approach

The multi-scale simulations used hopping injection and methodology described in section 5.6.4 and parameter values listed in Table 7 and Table 8. The charge evolution in the multi-scale simulation's 3D domain (A, and C) and its 1D domain (B and D) are shown in Figure 78.

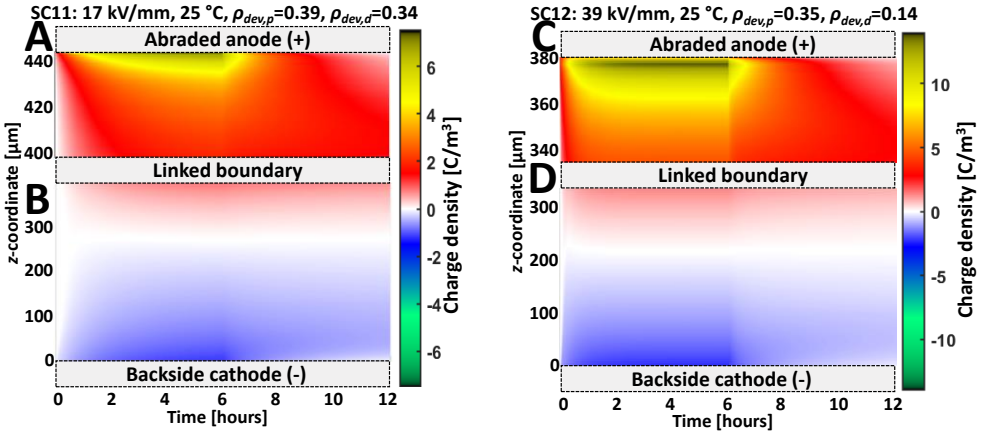

Figure 78. Multi-scale simulations with 6 hours polarization followed by 6 hours depolarization with respective deviations to measurement $\rho_{dev,p}$ and $\rho_{dev,d}$, listed above the figures. The insets show the charge evolution in the 3D domain towards the surface's maximal field enhancement (A and C) and evolution in the linked 1D domain (B and D).

As observed in Figure 78, the charge evolution in multi-scale simulation is comparable to the 1D simulation results shown earlier in Figure 77B, with both cases yielding similar deviation to the measurement results. Some minor differences arise related to the multi-scale model's higher surface mesh resolution, smaller surface section, and slower voltage ramping rate. Nevertheless, the similar charge evolutions indicate that the injected carrier flux through the boundary region was well represented with the derived roughness enhanced charge injection equations in section 6.2. Also, the linked boundary conditions operated successfully, and the averaging in equation (61) explains the observable discrepancy in charge density between the 3D and 1D domains in Figure 78, as the heterogenous charge distribution extends beyond 50 µm. The two simulations respectively reveal a maximum charge density of +7.29 C/m^3 and +13.3 C/m^3, found at 0.5 µm and 3.0 µm from the surface. The charge density and FEF quantities at the surface are shown in Figure 79.

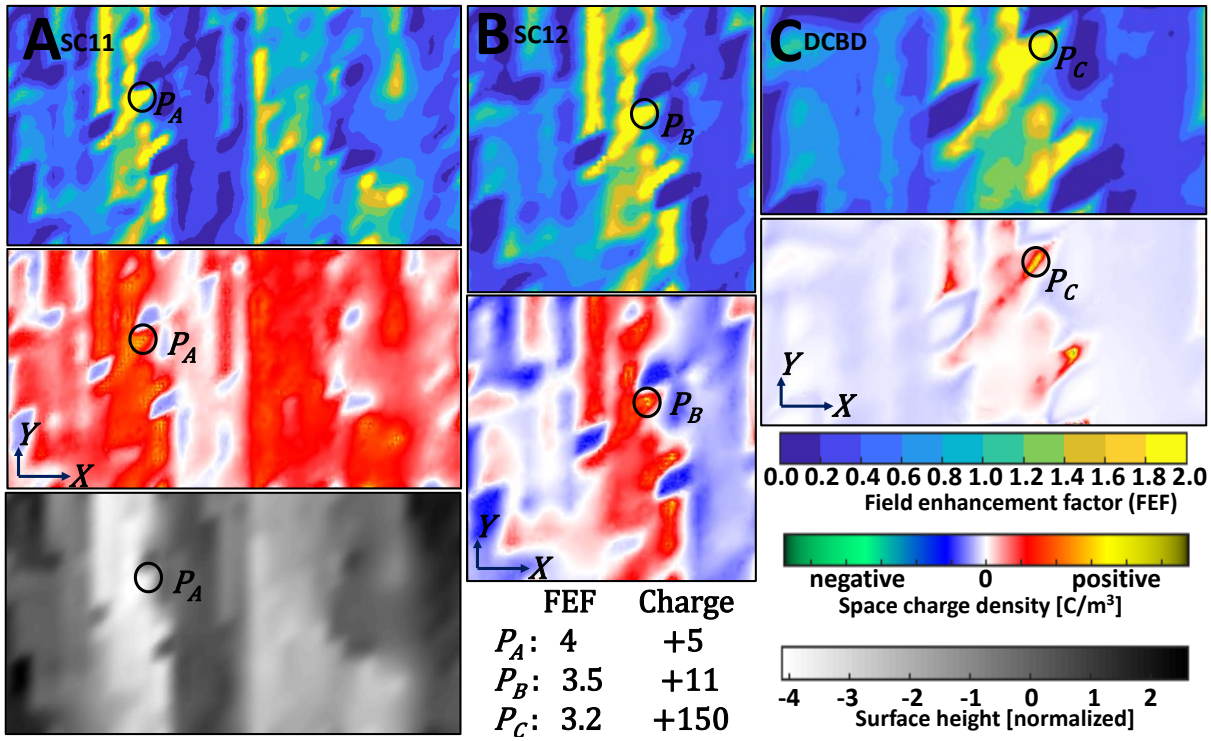

Figure 79. Charge density, FEF quantities and surface height Z(x,y) for the abraded surface, after 6 hours of polarization, biased at 17 kV/mm (A) and 39 kV/mm (B) or at 100 kV/mm in the DCBD test with 100 V/s ramp (C). Values extending beyond the FEF colormap's limits exist. The space charge colormap's limits are individual, with homocharge appearing in red and heterocharge in blue.

The surface charge distribution shown in Figure 79 reveals net domination of homocharges, ergo, the average FEF value no longer equates to unity (i.e. $avg(FEF(x,y)) \neq 1$). Heterocharged regions arise, at low field strength, they originate from the high initial carrier density used in simulation, while at higher field strengths heterocharges cross the sample and accumulate in the low FEF regions. Compared to the Poisson field calculations results in Figure 63, carrier densities at the surface are significantly lower in the multi-scale simulation, however, maximum charge quantities still coincide with locations of maximum field enhancement. Despite the now lower charge densities, a significant degree of shielding is achieved in multi-scale simulations due to the charge distribution penetrating deeper into the material bulk, with the highest charge density located a few µm below the surface. The charge density and field orientation, in an *x-z* plane in the center of the 3D domain, reveal this effect better as shown in Figure 80.

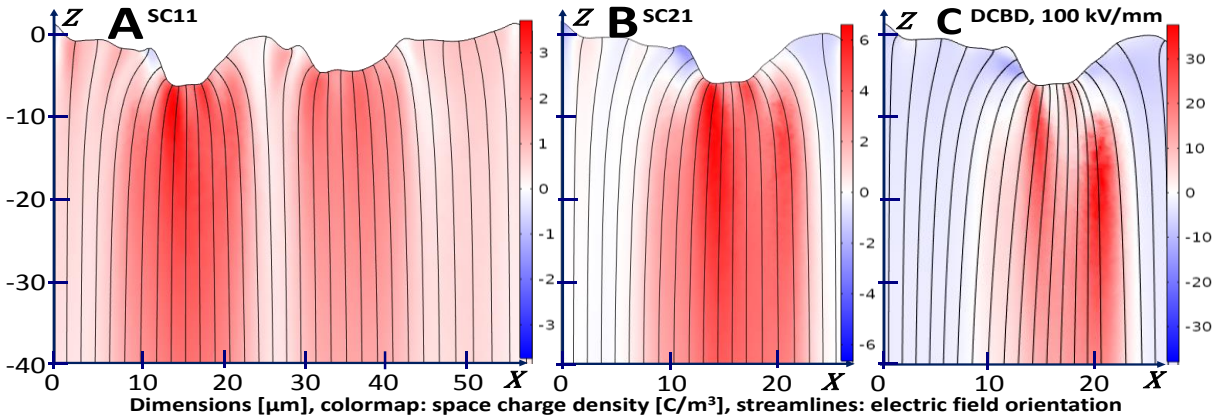

Figure 80. Charge density (colormap) and field orientation (streamlines) in an x-z plane in the center of the 3D simulation domain after 6 hours polarization for an abraded surface biased at 17 kV/mm (A) and at 39 kV/mm (B), and in a DCBD test with 100 V/s ramp at 100 kV/mm (C).

The charge evolution in Figure 80 forms a waterfall-like appearance, with charge injection supplying a high flux of carriers in the enhanced field region. Locally, carriers exhibit a swift transport through the enhanced field region and settle down beyond it where the field enhancement seizes. Thus, the homocharge intensity grows to its maximum a few µm below the surface, beyond which it decreases to a certain level. The heterogenous charge distribution penetrates deep into the material, beyond the 50 µm thick 3D domain. Several multi-scale simulations replicating DCBD test conditions were performed, with results listed in Table 10.

*Table 10. Maximum local quantities found at an asperity in different multi-scale simulations where; TRR = total recombination rate, CD = current density, ChDs = charge density at the surface, ChDb = charge density in the bulk (a few µm from the surface) and FEF = field enhancement factor. *Adjacent surface section. †Characteristic breakdown stress E_c from the MV-sized BD test. ‡Replicated conditions from MV-sized BD test, in Cartesian coordinates.*

Anode (+) type		**Ramp**	**Field**	**Thickness**	**TRR**	**CD**	**ChDs**	**ChDb**	**FEF**
Unit		V/s	kV/mm	µm	A/m^3	A/m^2	C/m^3	C/m^3	N/A
A1	Abraded	-100	25	150	$2.5\cdot10^{-3}$	$56\cdot10^{-6}$	+1.7	+2.7	4.2
A2			50		0.01	$52\cdot10^{-6}$	+12	+27.3	4
A3			100		0.5	$21\cdot10^{-6}$	+150	+1100	3.2
B1	Abraded	-10	100	150	0.3	$1.3\cdot10^{-6}$	+140	+1050	3.2
B2	Abraded*				0.15	$2.7\cdot10^{-6}$	+100	+850	3.8
C1	Abraded	-10	E_c†	350	$0.1\cdot10^{-3}$	$2.3\cdot10^{-6}$	+6.2	+7.5	4.3
C2			100		0.2	$1\cdot10^{-6}$	+150	+900	3.2
D	Abraded‡	-16.7	E_c†	4500	$2.8\cdot10^{-4}$	$0.1\cdot10^{-6}$	+6	+8.3	3.1
E	Smooth abraded	-10	100	100	0.1	$4.5\cdot10^{-6}$	+15	+50	2.2
F	Backside	-10	100	110	0.15	$3.7\cdot10^{-6}$	+8	+16.5	1.9

While applied field strengths beyond 100 kV/mm could not be simulated with the available computational performance, trends in maximum local quantities listed in Table 10 allow for anticipation of breakdown behavior. The maximum FEF decreases (from the Laplacian case where $FEFmax \approx 5$ in the surface section) with the applied field strength's level, explained by the increasing homocharge density (observed in rows A1, A2 and A3). Some quantity variance was observed in an adjacent surface section (rows B1 and B2), caused by the highly limited domain size no longer encompassing the full statistics of the surface height distribution $Z(x,y)$.

Neither ramping rate (rows A3 and B1) nor sample thickness (rows B1 and C2) were observed to impact the homocharge density and field strength in the surface domain significantly, likely because the steady-state homocharge distribution is reached rapidly at high field strength and it is weakly impacted by the rate of opposite carrier arrival. The lower characteristic breakdown stress E_c level of the MV-sized cable test could be reached in the simulations. It was revealed that the further increased bulk width in this cable test (row C1 and D) resulted in significantly less heterocharge and better shielding in the bulk beyond the interfacial domain, reducing the maximum FEF quantity while featuring a similar homocharge region around the surface asperity.

The maximum FEF and charge quantities thus correlate with surface roughness, and inversely with breakdown strength. While the total sum of recombination rates (TRR) increased with field strength, it did not correlate with surface roughness and its rate also gradually reduced towards the asperity due to the strong homocharge shielding present. Furthermore, current density increased marginally in the enhanced field region, however, no inverse correlation with the surface's breakdown strength was observed.

Chapter 7

Discussion

This chapter commences with a review of bulk conduction phenomena, followed by a discussion on charge injection. Thereafter, surface topography and its impact on measurements performed in the present work is addressed. Finally, alternative mechanisms governing interfacial performance are reviewed.

7.1 Bulk conduction

The accuracy of the bipolar charge transport model is strongly affected by the adopted assumptions on the physical processes involved. At the core of this is the discretization of the material's DOS through classifying it into three different state types within the band gap; shallow, inter-level and deep states. Their depth-density relations are represented by the parameters used in the model (listed in Table 7), which have provided the best match between the simulations and the experimental data. Their numerical values, and thus the corresponding DOS, can be considered a feature specific to the used insulation material. The found densities and energy levels of the discretely classified states are shown in Figure 81.

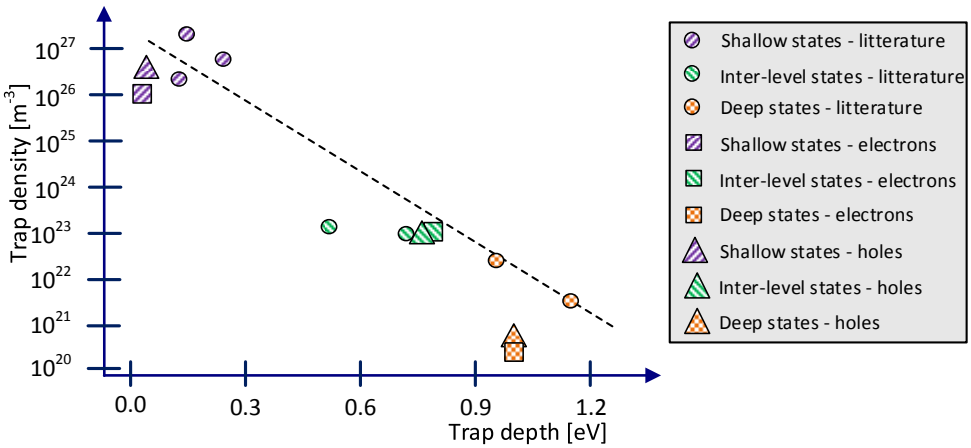

Figure 81. The state distribution adapted from [35] *and* [53] *(circles) and the density–depth relationships for electrons (squares) and holes (triangles) estimated from the calibrated parameters.*

As seen in Figure 81, some of the in calibration found discrete values match well the continuous state distribution described in [53] and represent the most impactful levels of the continuous distributions. For shallow states, the most probable state adjacent to an inter-level or deep state are the states from the upper level of the distribution with a depth of 0.03–0.05 eV. For the inter-level states, the lower end of the distribution is represented by its single levels of 0.79–0.81 eV, as such states could be rate-determining for hopping conduction and trapping mechanisms in the model. For deep states, an upper energetic level of 1.03 eV is used, since among the deep trap distribution such states govern the model's initial decay rate, being present with the highest density. Their density is anyhow lower compared to the values of the continuous distribution and values of the discretized approach in reference literature [27], [37], [39], [40], [42], [44], [48], [52], [53], [76]. This discrepancy could be related to the assumption of a shared lattice amongst states, yielding identical capture parameters between deep and shallow states, thus defining the capture cross-section as $A_T = a_{sh}^2$. An assumption of a lower

capture cross-section for states deeper in the distribution [119], could have estimated similar trap densities to what is proposed in the literature. However, this work additionally addresses charge evolution during depolarization, field-dependent trapping and detrapping and makes use of ultra-clean DC-grade XLPE [9] in the measurements. Such factors could make the found results incomparable to the references listed above.

The assumption of a shallow trap lattice, through which charge carriers make swift, energy dissipating hops and encounter inter-level and deep traps as isolated states in the lattice, is key for explaining the field dependencies exhibited in transport and detrapping. Moreover, trapping and recombination processes are affected by the lattice assumption via their dependency on drift velocity. While shallow states' occupancies are assumed as a uniformly distributed simple cubic lattice, significantly more disorder can be expected. Thereby, relating specific states in the found DOS to actual individual densities of known physio-chemical defects within XLPE (as estimated through molecular simulation [63]–[65]), remains unsurmountable due to the sheer complexity that such disorder introduces. While the disorder itself may introduce certain states, density related parameters (e.g. the spacings a_{sh}, a_{int} and trapping cross-section A_T) could also be locally distorted. Realistically, such disorder makes for a mesoscopic impact, featuring amorphous and crystalline regions with different local DOS and thus conduction parameters. Any additional morphological change in the material can impact the estimated global DOS shown in Figure 81 that best represents the disordered material. Therefore, the derived conduction parameters are specific for the used insulation material, the cable manufacturing methods and the cable peeling extraction method. While studies on press-molded LDPE plates often show a higher fraction of positive charge accumulation [37], [53], a distribution dominated by negative carriers at high field strength was observed in the space charge measurements. While the cross-links in DC grade XLPE affect the DOS weakly [26], spherulite growth may be reduced or even inhibited [12]. Furthermore, the material's processing affects the internal semi-crystalline structure, which for the used cable peelings originated from the extruded HVDC cable that subsequently was degassed, and these factors could create the favorable conditions for electron injection and transport in them.

During model calibration, different detrapping mechanisms were investigated: Poole–Frenkel (PF) effect, 3D PF effect [46], [47] and hopping-assisted release of charge carriers from traps. Given the PF effect's inability to achieve reasonable agreement with the experimental data, the 3D PF effect would have performed better due to its weaker field dependency [46], [47]. In the end, however, a hopping-assisted detrapping mechanism was formulated, which considered deep traps to be neutral by nature [35]. As this mechanism was formulated in the present work, it remains to be evaluated amongst peers in different simulations before it can be considered a consistent explanation.

7.2 Charge injection

Negative charge packets were observed at high field strength (shown in Figure 38 and Figure 76), which could neither be accurately reproduced with Schottky, hopping nor FN injection types. Furthermore, the packet was present with both smooth and rough electrodes, but it was not observed when a homocharge was present prior to applying the biasing voltage (during trials with stepwise field application described in the beginning of section 4.2.1.1). Its appearance in time (at 24 minutes in Figure 76I) also coincides with opposite charges reaching the electrode, thus implying an opposite charge dependent injection phenomenon. Schottky, hopping and FN injection, being derived for an isolated electron and yielding a field-dependency governed by probability density or image charge effect, do not account for such

opposite carrier interactions. However, looking into the hopping injection model with a resolved surface-DOS from Taleb et al. [57], which inspired the hopping current density expression, $J_{H(e,h)}$, formulated in the present study; some opposite carrier interaction effects can be found. The surface states, being energetically favorable for both carrier types, were shown to have an impact on the charge extraction rate, as opposite carriers were trapped in such states before their extraction. As opposite carrier extraction was delayed, a high density of opposite carriers arose in the surface region, which in turn increased the homocharge density. Since mobility was formulated with a carrier density dependency, with the highest occupied states in the distribution present at energetic depth Δf, this dependency reduced the energetic barrier and thus generated an opposite carrier dependent injection rate. In the present study, the resolved surface-DOS was simplified, yielding the surface charge density, ρ_s for which a carrier density independent hopping probability was assumed. In essence, by accounting for the evolution of negative and positive carriers within ρ_s, thus decoupling it from the injection equation, and reformulating the hopping expression could contribute to a better explanation of the charge packets.

Slow transients were also observed in measurements, specifically for the abraded and smooth abraded surface types (Figure 77C) at medium field strength. Given their systematic appearance, they may be caused by opposite charge carriers interacting with the localized charge distribution in the rough interfacial domain. However, the multi-scale simulations accounted for this effect, revealing no slow transient behavior (even in a simulation with 200 µm z-domain length). Thus, their appearance may require a charge injection process dependent on the local charge density, as previously described for charge packet formation. However, without any convincing evidence supporting their origin, it cannot be concluded if the slow transients are related to the injection process or if they are a measurement artifact.

The Schottky and hopping injection models with their calibrated parameters, listed in Table 8, are displayed against field strength and temperature in Figure 82.

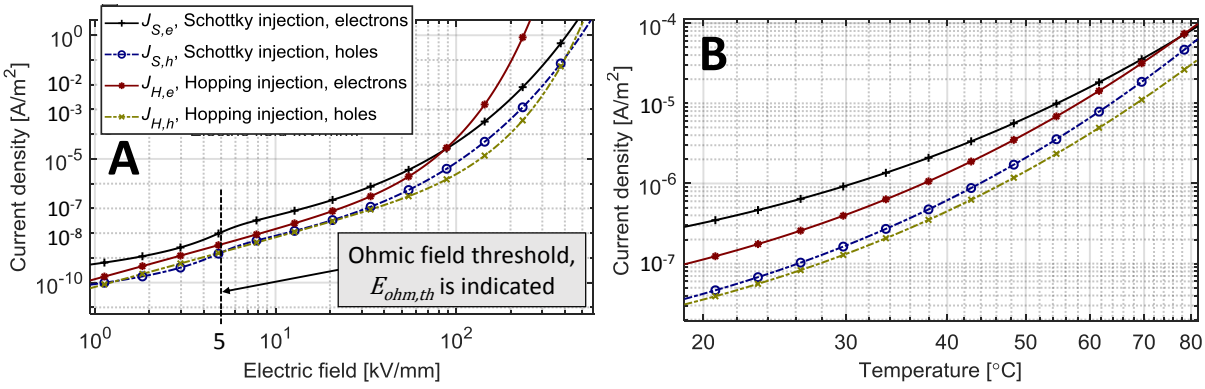

Figure 82. Schottky and hopping injections mechanisms, with calibrated parameters listed in Table 8, displayed against field strength (A) and temperature (B).

As observed in Figure 82, Schottky and hopping injection models matched closely within the ranges of field strengths and temperatures relevant to the experiments. Furthermore, at low field strength (during depolarization) a reduction of Schottky injection current was forced through the ohmic field threshold (equation (39)) and its f_s parameter (equation (38)). Neither of those modifications is true to its underlying physical description. Furthermore, an unphysically low barrier height $\phi_{B(e,h)}$ was required, in the range of 1.1-1.2 eV without its reflection parameter, $\lambda_{R(e,h)}$, accounted for. Also, its field dependency hinges on an electrode permittivity exceeding

the insulation's permittivity (i.e. $\varepsilon_{electrode} >> \varepsilon_{insulator}$), which was certainly not valid for the physical interfaces with an interstitial layer of dielectric grease or oil (which also yielded similar DCBD results to a gold sputtered interface in Figure 43). Given all such shortcomings, the hopping expression formulated in the present study seems to be a suitable alternative, as it suffers from neither of the limitations and matches the measured low current density at low field strength. It remains to be evaluated further in different conditions before it can be considered a consistent description of carrier injection into disordered insulators. Though, given the common adoption of Schottky injection in literature [27], [37], [39], [40], [42], [44], [48], [52], [53], [76], the weak impact of metal work function [60], [81] and matching injection current densities of Schottky and hopping injection in Figure 82, the hopping injection equation seems a viable alternative.

The values of hopping injection parameters, i.e. $a_{ss(e,h)}$ between 1.6 and 3.3 nm and $w_{ss(e,h)}$ at 1.01 eV, can represent the rate-limiting part in the injection process through the surface-DOS. In the results obtained with a resolved surface-DOS by Taleb et al. [57], at a few hundred nanometers from the electrode, a barrier arises with high and low charge density on either side of it. This observation confirms the presence of a rate-limiting barrier section, with its position depending on the model parameters, here represented by equation (43). The surface state density (derived from the surface state spacing $a_{ss(e,h)}$), can be lower compared to the bulk shallow state density, as the injection process can be accessing lower states in the distribution. Furthermore, while the formulation of the surface charge density, ρ_s may be inaccurate, its effect is relatively weakly affecting the current density.

7.3 Impact of surface topography

Limiting the degree of surface roughness was found paramount for reducing undesirable features in the HVDC cable application, such as localized field enhancements, increased charge accumulation, reduced breakdown strength, etc. To study its effects thoroughly, a series of different cable preparations were specifically selected to allow for varying the roughness levels. By also utilizing the measured surface topographies in simulations, the complex effects manifested in the measurements could be better explained. The literature review, measurements and simulations allowed to construct a theoretical framework visualized in Figure 83.

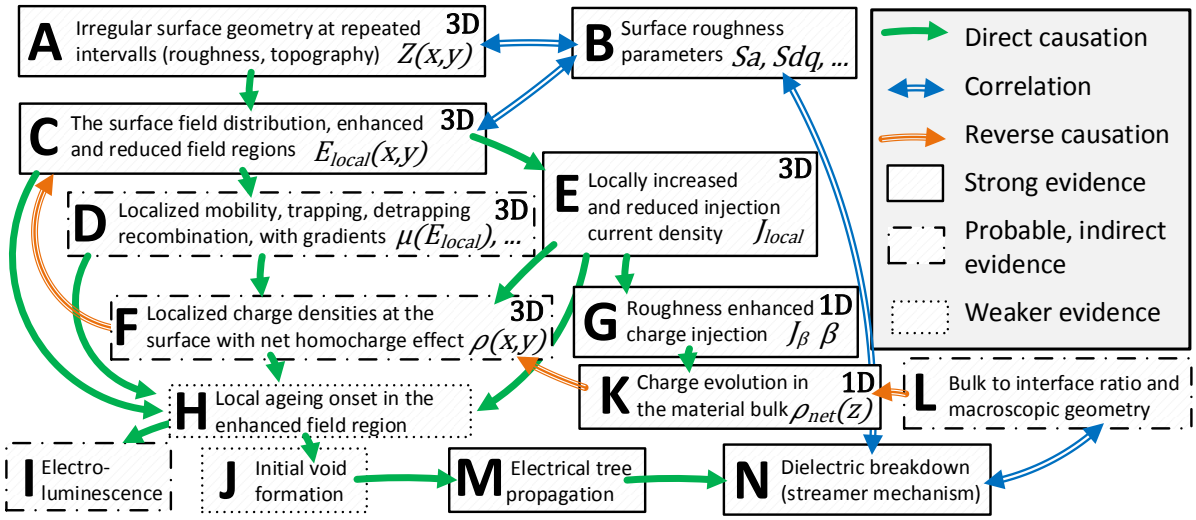

Figure 83. Theoretical framework linking surface topography with the electrical performance of the interface. Evident strength categorization implies that certain effects remained for practical reasons unresolved by the used measurement techniques.

As observed in Figure 83, the framework is complex, and many effects contribute to the electrical performance of the interface. Going through such causes sequentially, many of these effects can be confirmed by the results of the present work (i.e. effects A, B, C, E, G, K, M and N). The most challenging effects to prove with certainty remain the localized ageing type and subsequent void formation triggering the growth of an electric tree (i.e. H and J). Several factors could be involved in such localized ageing, being the local quantities of field strength, charge density, interfacial and bulk current density, recombination, (i.e. C, D, E and F) which together age the region around the rough asperity. While the initial multi-scale simulations of the rough interfacial domain (section 6.4) could not identify such quantities with accuracy, they still provided some indications towards the most likely occurring ageing mechanism. Furthermore, electroluminescence measurements could also aid the causation analysis by determination of the ageing mechanism's onset and rate, but this factor remains unexplored within the context of roughness investigations. Additionally, the bulk to interface ratio (L) impacts the charge evolution in the material (K). It in turn affects the charge distribution at the surface (F), and thus the field distribution at the surface (C). While this backward reaching line of reverse causes makes for a more challenging prediction, it can be exploited to better understand the effects taking place at the surface. The developed 1D model allowed for better understanding and calibration of the complex conduction phenomenon. It remains to be explored how such effects relate to electric breakdown and lifetime characteristics in 3D geometry. The multi-scale simulation approach, making use of the same continuity equations (59) and (60) and parameter space in 3D geometry (i.e. simulating effects A, C, D and F), has the potential to fully elucidate such behavior, with the initial simulations providing some insight into the localized charge evolution.

Strong evidence exists for the electric field distribution being caused by the irregular surface geometry, both of which correlate well with surface roughness parameters (i.e. A, B and C in Figure 83). Furthermore, the observation of roughness enhanced charge injection in both PEA and surface potential decay (SPD) measurements [83], also confirms the presence of locally increased and reduced injection currents (i.e. E and G). The performed tests on MV DC cables provided evidence of electrical tree formation prior to streamer initiation (i.e. M and N). The tests on cable peelings could neither confirm the presence of electrical trees nor reveal the position of the breakdown channel in the surface texture. However, the systematically observed correlation between breakdown strength and the *Sdq* parameter (Figure 45), indicates that a sequence of causes exists, linking the surface geometry with the observed breakdown strengths. While a *third-cause fallacy* being involved in the observed breakdown phenomenon cannot be fully excluded, the framework defined in Figure 83 provides the series of events that seem most probable. The individual contributions of electrical measurements to this framework are addressed in the following.

7.3.1 Effects revealed by multi-scale simulations

The multi-scale simulations make for a more accurate local behavioral prediction than the conductivity gradient simulations. However, the latter provides a better statistical overview by enabling the replication of a larger surface region. The charge evolution in the surface domain, governed by gradients in charge injection, mobility, trapping, detrapping and recombination (effects D in Figure 83) consistently reached a maximum homocharge intensity just beyond the enhanced field region. This may seem to depend on the field-dependent trapping/detrapping balance (Figure 70), causing an increased mobile carrier ratio in the enhanced field region. However, the effect persists even when the entire deep trap density $N^0_{deep(e,h)}$ is filled, showing

its strong dependency on the gradient in carrier mobility. Thus, the field and mobility gradients at asperities gave rise to homocharge enhancement, which away from the surface first grew to its maximum level and thereafter exponentially decreased. Furthermore, as observed in Figure 79, the charge density distribution at the electrodes comprised of charge carriers of both polarities, with heterocharges accumulating at the reduced field regions. Thus, the charge distribution started as heterogenous at the surface (i.e. effect F in Figure 83), and as the homocharged region penetrated deeply, it took several tens of µm before it began to form a homogenous distribution within the material bulk. Already at 17 kV/mm, the homocharge region was observed to penetrate ~25 µm and ~150 µm for the backside and abraded surfaces respectively.

The multi-scale simulations (with results in Table 10) provided further insight into the understanding of possible ageing mechanisms responsible for starting the degradation and subsequent breakdown of the material (i.e. effect H in Figure 83). Because the injected homocharge front penetrates deeply, it shields the asperities from opposite charges arriving at the surface, consequently reducing recombination rates and making this an implausible ageing source. The simulated local current density, on the other hand, increases locally in the enhanced field region but sees no correlation with the breakdown strength. Localized material damage through electron avalanches or hot electrons are thus the most probable mechanisms operating in the enhanced field region. The onset of electron avalanches can result in severe ageing, while hot electrons, on the other hand, may age the enhanced field region at a slower rate. Thereby, avalanches may not give rise to the IPL behavior observed in the breakdown tests, as the multiscale simulation indicated that ramping speed had a negligible impact on local quantities. The more gradual ageing by hot electrons produces IPL behavior, as the exposure time above its onset decreases with increased ramping rates.

7.3.2 Space charge measurements

The space charge measurements provided an assessment of the internal charge evolution. There are, however, three aspects that remain unresolved in such measurements; the actual charge density at the surface, its variation in (x,y) coordinates perpendicular to the measured signal, and its constituent carrier types. Thus, the model calibration relied on matching the one-dimensional net charge density in the material bulk, while the actual quantities at the electrode remained unknown. From the measurement and model's coordinated behavior, a series of observations can be made that reveal the processes taking place in the irregular interfacial domain. The appearance of electric field thresholds (e.g. E_{th}, Figure 66) was confirmed through the unaffected charge distributions at low field strength, and the increase of surface roughness dependent homocharge at high field strength, as shown in Figure 76. This observation confirms increased charge injection from the irregular surface. Amongst the measurement data, this observation provided the strongest evidence for the theoretical framework. Furthermore, the Laplacian field parameter set (β in Table 6) provided too high charge injection rates at high field strength, requiring a reduced field parameter set (β_{high}). This observation implies that localized shielding by homocharge is occurring at asperities, supported by simulation results shown in Figure 63 and Figure 79. However, the exact values of the reduced field parameter set (β_{high} in Table 6), being based on the results of the conductivity gradient simulation, may feature some inaccuracy as the true relations between surface type, local field strengths and carrier densities may differ. While the multi-scale simulations may replicate such relations better, it lacks the full statistics of the surface height distribution $Z(x,y)$ making it challenging to predict field $\beta(E)$ and scaling parameters $B(E)$ with such simulations.

7.3.3 Surface potential decay measurements

Earlier work showed that SPD measurements, performed on cable peelings with identical characteristics as in the present study [102], revealed little impact when the roughness level of the electrode facing corona charging was varied. However, when the roughness level of the ground electrode was altered a strong impact of surface roughness was observed. The results exhibited decay rates increasing with roughness level, along with a threshold field effect [83], [102]. As only the ground electrode was involved, the arising effects should be related to charge injection from the ground electrode [112], [120], [121]. The revealed threshold fields, above which opposite charge injection from the ground electrode increased, corresponding to the threshold fields calculated for 1D injection currents J_{avg} (section 6.2), thus confirming this effect (i.e. effect G in Figure 83).

7.3.4 Cable peeling breakdown tests

The DC breakdown tests on cable peelings performed at different ramping rates revealed a breakdown stress-time relationship following the IPL equation (26), from which the life-time exponent (n = 14) was deduced. It exceeds the conservative value used in standards that define type and pre-qualification test voltages in HVDC cable systems (i.e. n = 10). While the accuracy in the estimation of the IPL exponent may remain questionable due to its derivation at high field strengths [104], the insulation lifetime with a higher exponent can be predicted. Given the successfully performed qualifications at 320 kV [4], 400 kV, and 525 kV [6], the higher exponent (i.e. n = 14 instead of n = 10) anticipates a 450 years long lifetime of such HVDC cable systems. While remaining only an indication, large system margins are certainly predicted.

The DC breakdown tests on cable peelings identified a surface-type related breakdown strength, which, when displayed against the surface's *Sdq* parameter, confirmed a correlation between these quantities (*c.f.* Figure 45). By making use of the multi-scale simulation results (with results in Table 10), the local field strength that culminated in the breakdown may be estimated. For the backside, smooth abraded and abraded surfaces, assuming their respective maximum FEF quantities to be around ~1.4, ~1.7, and ~3.2 (extrapolated to their characteristic breakdown stress E_c), the respective local breakdown field strengths are anticipated to be approximately ~642 kV/mm, ~651 kV/mm and ~615 kV/mm. Also, for the rough and roughest abraded surfaces, the conductivity gradient simulations (Figure 64) showed that the local maximal quantities may be comparable to that for the abraded surface. Conclusively, the local onset field strengths triggering ageing, degradation and subsequent breakdown in the enhanced field region are anticipated to be ~600 - 700 kV/mm and may thus exhibit similar values regardless of the surface type. Such similarity relates the observed roughness - breakdown strength correlation in the cable peeling tests to a series of sequential causes (i.e. effects A, C, D, F, and H in Figure 83). It must be noted that further complexities may exist, such as increased charge density increasing the upper filled trap level Δf, increasing the local mobility and thereby the ageing rate, or the local morphological disorder which could superimpose to the observed localized quantities.

The absent impact of sample thickness on breakdown strength for 100 – 350 µm thick abraded peelings, especially when IPL behavior was accounted for, could indicate a surface-limited ageing process. The multi-scale simulations showed that such thickness variation impacted the total carrier flux through the sample, affecting the heterocharge density in the reduced field regions. However, the developed homocharge density and field enhancement level at the asperities were only weakly impacted (as observed in rows B1 and C2 in Table 10) because

they are dominated by the local injection-transport balance. The multi-scale simulation results thus foresee a weak impact of sample thickness on breakdown strength, which was also observed in the DCBD tests.

7.3.5 MV cable breakdown tests

The breakdown voltage levels in the MV-sized cable test showed a strong correlation with the roughness level for the cut, abraded and smooth abraded surfaces. The characteristic breakdown stress (E_c) levels were significantly lower as compared to the values obtained in the cable peeling tests. One reason for this discrepancy can be related to the slower ramping rate in the MV-cable test, thus predicting lower breakdown stress according to the IPL. However, interpolation from characteristic breakdown stress (E_c) for abraded peelings, using the life-time exponent n = 14, yields breakdown strength of the MV-sized cable at ~150 kV/mm, still in far excess of the test results. Instead, the significantly higher bulk to interface ratio in the MV cable explains this discrepancy. At the same time, the multi-scale simulations (with results in Table 10) revealed that the homocharge density remained similar between the thickness levels in the peelings and the MV cable, while the heterocharge density was reduced with the thickness. This yielded more of the positive net charge density $\rho_{net}(z)$ over a wider surface region, reducing field strength over the entire surface while increasing it in the material bulk. Since this behavior contradicts the observed scaling effect, the existence of a *third cause fallacy* is implied as it must originate from another factor. One could for example be the influence of cylindrical sample geometry (not accounted for in the multi-scale simulation) that may affect the charge evolution.

The additional discharge channels observed at high field strength in the cylindrical (z,φ) layer (Figure 41), are presumably caused by a space charge related mechanism. This layer may feature high charge density, although its polarity remains unknown. It certainly shows that internal carrier densities can contribute strongly to the chain of causation leading up to the breakdown events. As longitudinal field strength (Ez) was in the range of 0.05-0.3 kV/mm, whereas radial electric field strength (Er) was approximately 300 times higher, the lengthwise position of the breakdown location is most likely determined by the charge distribution within the insulation layer.

7.4 Additional factors contributing to interface performance

While non-roughness related parameters, such as polymer microstructure and content of chemical species were characterized, their potential impact in electrical measurements on cable peelings was concealed by the stronger impact of surface roughness. However, as they may skew the results, their eventual influence on interfacial performance should be addressed. Notably, the results obtained for remolded samples clearly indicate a possibility of non-roughness related phenomena.

7.4.1 Impact of ionized species

While the theoretical framework is based on bipolar charge transport dominated by electronic carriers, which seems to be suitable for the well-outgassed cable peelings, the presence of ionic carriers cannot be fully neglected in MV sized cables and full-size cable accessories. For the peelings, given their inherently low PDP quantities, strong variation related to sample storage time is unlikely. Also, heterocharge formation which would have been an indication of ionic carrier conduction was not observed. For the DCBD tests on MV cables, however, the internal

charge distribution remains unknown. Considering internal carrier generation and ionization of PDP, the surface's heterogeneous charge distribution (Figure 63) is likely to be impacted. With increased PDP concentration, the rate of opposite carrier arrival at the surface may increase. While the heterocharges observed in Figure 63 accumulate at reduced field regions, their appearance can be considered less harmful. However, arrival and generation of opposite carriers at constant rates in enhanced field regions could lessen the degree of homocharge shielding, thus increasing field strength at the asperities. As this effect may closely be linked to local breakdown initiation, the material's PDP concentration level may skew the results and superimpose them with the geometric (i.e. bulk to interface ratio) scaling effect. It may explain the variations in breakdown field levels in the tests on peelings and MV cables. Given the complex nature of such charge carrier interactions, it remains to be further evaluated before any solid conclusions can be drawn.

7.4.2 Impact of surface morphology

Any surface treatment involving exposure of the polymer surface to heat may alter its crystalline microstructure. For the remolding procedure, some indications of an increased degree of backbone regularity were observed in the FTIR analyses shown in Figure 33. An increased barrier for electron injection, and a reduced barrier for hole injection, due to a reduced amorphous fraction, can thus be postulated. However, in the space charge measurements, the original barrier heights fit well at low field strength. At medium field strength, a marginally higher homocharge density was observed at the anode in the measurement compared to the simulation, as shown in Figure 84.

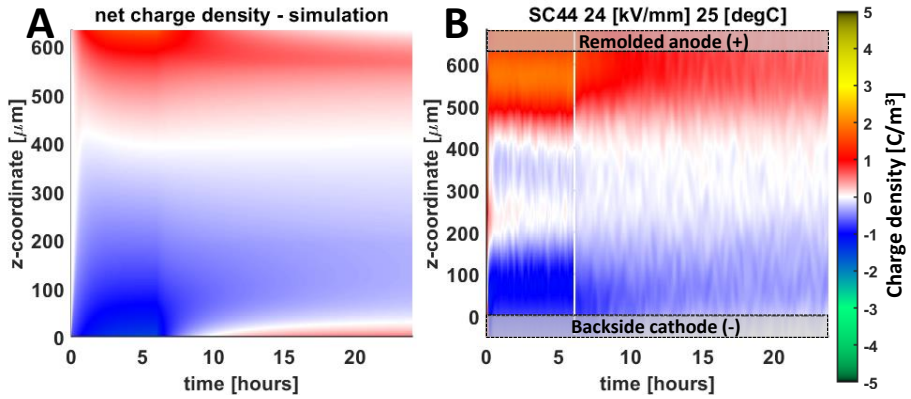

Figure 84. Space charge measurement (B) and simulation with hopping injection (A) for a remolded anode at +15 kV biasing at 25°C.

The impact of modified surface morphology may provide a marginal impact on positive charge carrier injection. It could be more complex than a modification of the barrier's height, as a modification of the surface DOS is possible. Furthermore, traps originating from polymer chain scission initially positioned at the surface, may, during the remolding process, be pushed into the material bulk with unknown effects. An impact of the remolding was also found in the breakdown strength test on MV cables, as shown in Figure 40, where the remolded surface yielded lower breakdown strength compared to the cut surface. While this reduced breakdown strength and increased homocharge density might be related to its modified surface morphology, further studies and space charge measurements are required before any incontrovertible proof can be presented. The remolded surface could not be included in the cable peeling DCBD tests due to the inability to prepare consistently thin and homogenous peelings.

7.4.3 Modification of the surface DOS

While the results of FTIR analyses presented in Figure 33 indicate an increase in carbonyl group formation on the abraded surface, the SFE results shown in Table 3 are less conclusive, due to inaccuracies brought by the difficult roughness correction. As cutting and abrasion feature different means of material removal, they both may have different surface DOS. While such an impact was not included in simulations (e.g. through abraded surface-specific injection $w_{ss(e,h)}$ and $a_{ss(e,h)}$ parameters), it was neither required for achieving good agreement with the measured space charge evolution. This observation implies that any impact arising from a weak modification of the abraded surface's DOS remains subjacent to surface roughness's impact on charge injection.

Conclusively, variations in surface DOS arising from oxidation, surface morphology, or the material removal method are superimposed to the effect of surface roughness. While such features, when present in moderate amounts, remain subjacent compared to the roughness effects, the superposition could be exploited in future experiments. By studying measurable surface DOS alterations in tailored surface geometries, different local geometric effects could allow forming a better understanding of the relation between the surface DOS and charge injection.

Chapter 8

Conclusions

The presented results demonstrate that control over micro-scale topography is paramount for HVDC cable accessory interfaces. While the theoretical framework, describing the consequences of irregular surface geometry, encompasses a multitude of complex mechanisms and their interactions, the greatest difficulty arises from the challenge of the scale. Surface roughness may span a mesoscopic space neither suitable in atomic nor macroscopic simulations. Nevertheless, stepwise performed simulations at different geometric scales allowed to sequentially deduce their impact on electric field strength, space charge density and charge injection such that coherent evidence could be obtained. As the electrical measurements revealed the symptoms of events taking place at the surface, reproducing such symptoms in simulation provided experimental validation of interfacial phenomena.

By carrying out surface preparation on cable ends with conditions matching real accessory installation, and reproducing such preparations by means of cable peelings, surface properties identical to the application were introduced in the small-scale measurements. Among assessed surface parameters, surface roughness was determined to be at the core of governing the electrical performance of the interface. The roughness' *Sa* and *Sdq* parameters, respectively relating to the surface geometry's height ($Z(x,y)$) and derivatives ($\partial Z/\partial x$ and $\partial Z/\partial y$), were found to best represent the disordered surface types and their values spanned over two orders of magnitude. The surface's irregular geometry was shown to introduce a localized redistribution of the electric field, from which regions with reduced or enhanced field strength arose. Furthermore, the *Sdq* parameter was revealed to be in close correlation with the surface's maximal electric field enhancement. Furthermore, the established field distributions of different surface types proved to be sensitive to localized charge accumulation, densities of which depend on bulk conduction properties.

The surface field distributions were incorporated in the equations of different charge injection mechanisms, allowing to estimate the average current density entering the material. Such average currents facilitated the formulation of roughness enhanced charge injection equations, respectively for Schottky, Fowler-Nordheim and the proposed hopping injection mechanisms, which could readily be adopted in the simulation work.

Space charge measurements revealed the behavior of material bulk conduction, exhibiting both field, temperature and polarity dependent effects. Furthermore, the density of injected homocharge increased with the roughness level of the cable peeling surface at high field strength. For explaining such behavior, the introduction of a bipolar charge transport model was required that included the actions of the previously formulated roughness enhanced charge injection, hopping transport, drift velocity dependent trapping, hopping-assisted detrapping and Langevin carrier recombination. Realized through a high number of model iterations, compared with the results of 45 different PEA measurements, a parameter set best representing the semi-crystalline material was defined. This parameter set describes the material's DOS, discretized into three state classifications, being shallow, inter-level and deep states within the band bap of XLPE. Furthermore, amongst the evaluated charge injection mechanisms, hopping injection was shown to provide the best performance and the best physical description. Thereby, the

hopping injection mechanism provides a realistic view of why high carrier injection rates are commonly observed in polymeric insulation, which traditionally has forced the use of unrealistically low Schottky barrier heights. The developed within this work roughness assisted hopping injection equation, can readily be adopted by researchers to account for non-ideal interfacial geometries.

Surface potential decay measurements showed the symptoms of opposite charge injection from the ground electrode. As the decay rate increased with the roughness level of this electrode and exhibited a threshold effect, such measurements provided additional evidence of the roughness enhanced charge injection mechanism.

A multi-scale, bipolar charge transport simulation approach revealed the highly dynamic interactions between charge carriers and the material in the irregular surface domain. These simulations elucidated the possible driving mechanisms responsible for the observed correlation between surface roughness and breakdown strength. High local quantities of field strength and charge density are the culprits of such reduced performance, causing localized ageing in the highly stressed regions. The local ageing adhered to a hot electron mechanism, which may cause localized damage over time and ultimately culminates in electrical tree formation and a subsequent streamer discharge.

Conclusively, surface topography, being a readily measurable surface feature, should either be avoided or exploited. Its exploitation should, however, remain in the lab where its strong impact on charge injection may allow forming a better understanding of a material's conductive properties. On the other hand, its avoidance is essential for ensuring the long-term reliability of cable accessories. The theoretical framework presented allows for defining certain acceptance criteria, crucial for controlling roughness during on-site installation works. However, as roughness is just one out of several undesired surface features, trade-offs arise as experienced in this study, as exemplified by the behavior of remolded surfaces. The atomic-level smoothness achieved in small semiconductor devices is unfortunately not adoptable (yet) in the high voltage industry. Nevertheless, despite having a controlled amount of surface roughness present, the DCBD results on smoother surfaces did anticipate significant margins in the life-time of the HVDC cable system. Such surfaces could allow for reliable system operation for many years to come. This longevity is an efficient way to provide intra-generational justice, supporting the renewable energy transition with high security of supply.

Chapter 9

Future Work

A few elements remain untouched, such as studying the impact of polarity and temperature in SPD measurements and breakdown tests. Also, conductivity measurements were not performed, but given the strong homocharge accumulation the measurable symptoms of roughness may be located just after bias application, superimposed on the polarization currents. However, the greatest potential lays within the exploitation of mesoscopic geometries in simulation and measurement. It must be stressed that surface roughness is one amongst few features that can be measured and introduced in a model with accuracy. The additional factors contributing to surface performance, listed in section 7.4, may thus be deeper studied if controlled surface geometry is introduced without affecting such parameters. Thereby, differently tailored geometries could allow for studying such factors with an accurately assessable feature present. This approach is particularly important given the poorly understood DOS and surface-DOS which introduce an unknown material response to experimental conditions (e.g. field strength, temperature, etc.). The greatest barriers, hindering exploitation and mastery of mesoscopic effects, are their representation in multi-scale simulations and more advanced electrical measurement techniques capable of providing local mesoscopic resolution.

The one-dimensional bipolar charge transport model was purposely designed and calibrated for a wide range of applied field strength. Thereby, its parameters and expressions could be readily adopted in a 3D assessment of irregular surface geometry. However, serious challenges arose especially from the requirement of high mesh resolution and short time steps, both yielding long simulation times. Such challenges were partially overcome through a multi-scale approach, in which a small, multi-dimensional domain with high resolution resolved the mesoscopic effect, being linked with a one-dimensional domain representing the component's macroscale dimensions. By linking the boundary conditions, the small domain was supplied with the correct fluxes of charge carriers. This approach determined localized field and charge distributions at the irregular surface accuracy, relating them to breakdown and the lifetime in XLPE. However, computational performance was still insufficient for resolving the full statistics of the surface height distribution $Z(x,y)$ or for reaching the characteristic breakdown stress (E_c) in the simulations. Thereby, future studies where increased computational performance is made available may elucidate the local origins of ageing, degradation and breakdown mechanisms in disordered materials with disordered electrodes.

Other poorly understood mesoscopic heterogeneities, being morphology [75], microscopically phase-separated polymer blends, nanofillers, organic contaminants [122], will remain inadequately understood until their localized effects are resolved in the mesoscale. The multi-scale approach touched upon in the present study can resolve their geometries while maintaining the apparatus's representation. Also, other clever alternatives, such as adopting fractional dimensional space commonly considered in disordered semiconductors [123], can be envisioned. It is mesoscopic simulation that may begin unraveling the arising complexities, moving their interpretation from being assumptions to their physical representations.

References

[1] BP, “Statistical Review of World Energy | Energy economics | Home,” 2019. https://www.bp.com/en/global/corporate/energy-economics/statistical-review-of-world-energy.html (accessed Nov. 19, 2019).

[2] Tomorrow, “Electricity Map | Live CO2 emissions of electricity consumption.” https://www.electricitymap.org/map (accessed Mar. 13, 2020).

[3] entso-e, “Project Sheet.” https://tyndp.entsoe.eu/tyndp2018/projects/ (accessed Nov. 04, 2019).

[4] D. Steinbrink and L. Hartman, “Nexans supplies 320 kV cables for ‘DolWin6’ offshore DC link to TenneT - Nexans,” *Nexans newsroom*, 2017. http://www.nexans.com/newsroom (accessed Aug. 01, 2017).

[5] Nexans, “Cross-Linked Polyethylene (XLPE) Cables - Nexans.” http://www.nexans.no/eservice/Norway-en/navigate_342597/Cross_Linked_Polyethylene_XLPE_Cables.html (accessed Jun. 09, 2017).

[6] J. Rothfeld, “Nexans successfully qualifies a 525 kV HVDC underground cable system to German TSO standards,” 2018. https://www.nexans.com/newsroom (accessed Dec. 03, 2018).

[7] P. Morshuis, “Interfaces: To be avoided or to be treasured? What do we think we know?,” in *2013 IEEE International Conference on Solid Dielectrics (ICSD)*, Jun. 2013, pp. 1–9, doi: 10.1109/ICSD.2013.6619726.

[8] T. Worzyk, *Submarine Power Cables*. Berlin, Heidelberg: Springer Berlin Heidelberg, 2009.

[9] A. C. Ulf Nilsson, Annika Smedberg, “Polymer composition and a power cable comprising the polymer composition,” US9587043B2, 2010.

[10] N. G. McCrum, C. P. Buckley, and C. B. Bucknall, *Principles of polymer engineering*, 2nd ed. Oxford Universtity Press, 2011.

[11] J. M. G. (John M. G. Cowie and V. (Valeria) Arrighi, *Polymers : chemistry and physics of modern materials*, 3rd ed. CRC Press, 2008.

[12] S. Nilsson, T. Hjertberg, and A. Smedberg, “Structural effects on thermal properties and morphology in XLPE,” *European Polymer Journal*, vol. 46, no. 8, pp. 1759–1769, Aug. 2010, doi: 10.1016/j.eurpolymj.2010.05.003.

[13] J. P. Coates, “The interpretation of infrared spectra: Published reference sources,” *Applied Spectroscopy Reviews*, vol. 31, no. 1–2, pp. 179–192, Jan. 1996, doi: 10.1080/05704929608000568.

[14] B. Crist and J. M. Schultz, “Polymer spherulites: A critical review,” *Progress in Polymer Science*, vol. 56, pp. 1–63, May 2016, doi: 10.1016/j.progpolymsci.2015.11.006.

[15] T. Andritsch, A. Vaughan, and G. C. Stevens, “Novel insulation materials for high voltage cable systems,” *IEEE Electrical Insulation Magazine*, vol. 33, no. 4, pp. 27–33, Jul. 2017, doi: 10.1109/MEI.2017.7956630.

[16] M. Hao, A. Fazal, A. S. Vaughan, G. Chen, Y. Zhou, and C. Zhang, “The impacts of degassing on space charge characteristics and DC conductivity in semicon-bonded XLPE for HVDC cable applications,” in *2016 IEEE Conference on Electrical Insulation and Dielectric Phenomena (CEIDP)*, Oct. 2016, pp. 97–100, doi: 10.1109/CEIDP.2016.7785533.

[17] Frøydis. Oldervoll, “Electrical and thermal ageing of extruded low density polyethylene insulation under HVDC conditions,” NTNU, 2000.

[18] U. H. Nilsson and J.-O. Bostrom, "Influence of the semiconductive material on space charge build-up in extruded HVDC cables," in *2010 IEEE International Symposium on Electrical Insulation*, Jun. 2010, pp. 1–4, doi: 10.1109/ELINSL.2010.5549811.

[19] D. Fabiani *et al.*, "Polymeric HVDC Cable Design and Space Charge Accumulation. Part 1: Insulation/Semicon Interface," *IEEE Electrical Insulation Magazine*, vol. 23, no. 6, pp. 11–19, Nov. 2007, doi: 10.1109/MEI.2007.4389975.

[20] L. C. Sawyer and D. T. Grubb, *Polymer Microscopy*. Dordrecht, NL: Springer Netherlands, 1996.

[21] J. W. Carr and C. Feger, "Ultraprecision machining of polymers," *Precision Engineering*, vol. 15, no. 4, pp. 221–237, Oct. 1993, doi: 10.1016/0141-6359(93)90105-J.

[22] K. Q. Xiao and L. C. Zhang, "The role of viscous deformation in the machining of polymers," *International Journal of Mechanical Sciences*, vol. 44, no. 11, pp. 2317–2336, Nov. 2002, doi: 10.1016/S0020-7403(02)00178-9.

[23] M. Hasheminezhad and E. Ildstad, "Partial discharge inception of interface voids versus mechanical surface pressure," in *2010 International Conference on High Voltage Engineering and Application*, Oct. 2010, pp. 397–400, doi: 10.1109/ICHVE.2010.5640742.

[24] Z. Yuanxiang, W. Yunshan, W. Ninghua, and S. Qinghua, "Effect of surface topography and morphology on space charge packets in polyethylene," *Journal of Physics: Conference Series*, vol. 183, no. 1, p. 012009, Aug. 2009, doi: 10.1088/1742-6596/183/1/012009.

[25] D. J. Lacks and R. Mohan Sankaran, "Contact electrification of insulating materials," *Journal of Physics D: Applied Physics*, vol. 44, no. 45, p. 453001, Nov. 2011, doi: 10.1088/0022-3727/44/45/453001.

[26] A. Moyassari, M. Unge, M. S. Hedenqvist, U. W. Gedde, and F. Nilsson, "First-principle simulations of electronic structure in semicrystalline polyethylene," *The Journal of Chemical Physics*, vol. 146, no. 20, p. 204901, May 2017, doi: 10.1063/1.4983650.

[27] S. le Roy, G. Teyssèdre, and C. Laurent, "Modelling space charge in a cable geometry," *IEEE Transactions on Dielectrics and Electrical Insulation*, vol. 23, no. 4, pp. 2361–2367, Aug. 2016, doi: 10.1109/TDEI.2016.7556514.

[28] R. Guffond, A. Combessis, and S. Hole, "Contribution of polymer microstructure to space charge, dielectric properties and electrical conduction," in *2016 IEEE Conference on Electrical Insulation and Dielectric Phenomena (CEIDP)*, Oct. 2016, pp. 141–144, doi: 10.1109/CEIDP.2016.7785655.

[29] Y. v. Serdyuk, "Computer modelling of electrophysical phenomena in high voltage insulation," Dept. of Electric Power Engineering, Chalmers University of Technology, 2004.

[30] S. le Roy, G. Teyssedre, C. Laurent, G. C. Montanari, and F. Palmieri, "Description of charge transport in polyethylene using a fluid model with a constant mobility: fitting model and experiments," *Journal of Physics D: Applied Physics*, vol. 39, no. 7, pp. 1427–1436, Apr. 2006, doi: 10.1088/0022-3727/39/7/014.

[31] M. Taleb, G. Teyssèdre, S. le Roy, and C. Laurent, "Charge injection and extraction in metal/polyethylene contact through an exponential distribution of surface states," in *2010 Annual Report Conference on Electrical Insulation and Dielectic Phenomena*, Oct. 2010, pp. 1–4, doi: 10.1109/CEIDP.2010.5724063.

[32] C. Kittel, *Introduction to Solid State Physics*, 8th editio. New York, NY, USA: Wiley & Sons, New York, NY (2004), 2009.

[33] D. A. Neamen, *An introduction to Semiconductor devices*. New York, NY, USA: McGraw-Hill, Inc., 2006.
[34] L. A. Dissado and J. C. Fothergill, *Electrical degradation and breakdown in polymers*, 1st ed. London, UK: P. Peregrinus Ltd., 1992.
[35] G. Teyssedre and C. Laurent, "Charge transport modeling in insulating polymers: from molecular to macroscopic scale," *IEEE Transactions on Dielectrics and Electrical Insulation*, vol. 12, no. 5, pp. 857–875, Oct. 2005, doi: 10.1109/TDEI.2005.1522182.
[36] T. J. Lewis, "Electrical Effects at Interfaces and Surfaces," *IEEE Transactions on Electrical Insulation*, vol. EI-21, no. 3, pp. 289–295, Jun. 1986, doi: 10.1109/TEI.1986.349063.
[37] A. Hoang, Y. v. Serdyuk, and S. Gubanski, "Charge Transport in LDPE Nanocomposites Part II—Computational Approach," *Polymers*, vol. 8, no. 4, p. 103, Mar. 2016, doi: 10.3390/polym8040103.
[38] H. Boukhari and F. Rogti, "Simulation of Space Charge Dynamic in Polyethylene Under DC Continuous Electrical Stress," *Journal of Electronic Materials*, vol. 45, no. 10, pp. 5334–5340, Oct. 2016, doi: 10.1007/s11664-016-4723-y.
[39] C. Laurent, G. Teyssedre, and S. le Roy, "A discussion on charge transport and electroluminescence in insulating polymers," in *Proceedings of 2005 International Symposium on Electrical Insulating Materials, 2005. (ISEIM 2005).*, 2005, vol. 1, pp. 7-15 Vol. 1, doi: 10.1109/ISEIM.2005.193306.
[40] S. le Roy, G. Teyssedre, C. Laurent, and P. Segur, "Numerical modeling of space charge and electroluminescence in polyethylene under dc field," in *Annual Report Conference on Electrical Insulation and Dielectric Phenomena*, 2002, pp. 172–175, doi: 10.1109/CEIDP.2002.1048763.
[41] S. le Roy, G. Teyssedre, C. Laurent, and P. Segur, "Numerical model for studying dynamic space charge behavior in polyethylene," in *Proceedings of the 7th International Conference on Properties and Applications of Dielectric Materials (Cat. No.03CH37417)*, 2003, vol. 3, pp. 859–862, doi: 10.1109/ICPADM.2003.1218557.
[42] S. le Roy, P. Segur, G. Teyssedre, and C. Laurent, "Description of bipolar charge transport in polyethylene using a fluid model with a constant mobility: model prediction," *Journal of Physics D: Applied Physics*, vol. 37, no. 2, pp. 298–305, Jan. 2004, doi: 10.1088/0022-3727/37/2/020.
[43] J. Tian, Y. Zhou, and Y. Wang, "Simulation of space charge dynamics in low-density polyethylene under external electric field and injection barrier heights using discontinuous galerkin method," *IEEE Transactions on Dielectrics and Electrical Insulation*, vol. 18, no. 5, pp. 1374–1382, Oct. 2011, doi: 10.1109/TDEI.2011.6032805.
[44] Y. v. Serdyuk, S. M. Gubanski, and A. S. I. Mohammad, "Computer simulation of space charge dynamics and electric fields in HVDC cable insulation," in *Proc. XV Int. Symp. on High Voltage Engineering*, 2007, pp. T8-405, [Online]. Available: http://proxy.lib.chalmers.se/login?url=http://search.ebscohost.com/login.aspx?direct=true&db=cat06296a&AN=clc.b1358267&lang=sv&site=eds-live&scope=site.
[45] J. L. Hartke, "The Three-Dimensional Poole-Frenkel Effect," *Journal of Applied Physics*, vol. 39, no. 10, pp. 4871–4873, Sep. 1968, doi: 10.1063/1.1655871.
[46] M. Ieda, G. Sawa, and S. Kato, "A Consideration of Poole-Frenkel Effect on Electric Conduction in Insulators," *Journal of Applied Physics*, vol. 42, no. 10, pp. 3737–3740, Sep. 1971, doi: 10.1063/1.1659678.
[47] N. Liu *et al.*, "An improved model to estimate trapping parameters in polymeric materials and its application on normal and aged low-density polyethylenes," *Journal of Applied Physics*, vol. 118, no. 6, p. 064102, Aug. 2015, doi: 10.1063/1.4928182.

[48] S. le Roy, H. Miyake, Y. Tanaka, T. Takada, G. Teyssedre, and C. Laurent, "Simultaneous measurement of electroluminescence and space charge distribution in low density polyethylene under a uniform dc field," *Journal of Physics D: Applied Physics*, vol. 38, no. 1, pp. 89–94, Jan. 2005, doi: 10.1088/0022-3727/38/1/015.

[49] O. Magen and N. Tessler, "On electrode pinning and charge blocking layers in organic solar cells," *Journal of Applied Physics*, vol. 121, no. 19, p. 195502, May 2017, doi: 10.1063/1.4983298.

[50] M. Kleefstra and G. C. Herman, "Influence of the image force on the band gap in semiconductors and insulators," *Journal of Applied Physics*, vol. 51, no. 9, pp. 4923–4926, Sep. 1980, doi: 10.1063/1.328366.

[51] D. M. Taylor and T. J. Lewis, "Electrical conduction in polyethylene terephthalate and polyethylene films," *Journal of Physics D: Applied Physics*, vol. 4, no. 9, p. 315, Sep. 1971, doi: 10.1088/0022-3727/4/9/315.

[52] S. le Roy, G. Teyssedre, and C. Laurent, "Charge transport and dissipative processes in insulating polymers: experiments and model," *IEEE Transactions on Dielectrics and Electrical Insulation*, vol. 12, no. 4, pp. 644–654, Aug. 2005, doi: 10.1109/TDEI.2005.1511090.

[53] F. Boufayed *et al.*, "Models of bipolar charge transport in polyethylene," *Journal of Applied Physics*, vol. 100, no. 10, p. 104105, Nov. 2006, doi: 10.1063/1.2375010.

[54] B. S. G. and R. H. F. T. E. Stern, "Further studies in the emission of electrons from cold metals," *Proceedings of the Royal Society of London. Series A, Containing Papers of a Mathematical and Physical Character*, vol. 124, no. 795, pp. 699–723, Jul. 1929, doi: 10.1098/rspa.1929.0147.

[55] R. H. Fowler and L. Nordheim, "Electron Emission in Intense Electric Fields," in *Semiconductor Devices: Pioneering Papers*, vol. 119, WORLD SCIENTIFIC, 1991, pp. 683–691.

[56] R. H. Good and E. W. Müller, "Field Emission," Berlin, Germany: Springer, Berlin, Heidelberg, 1956, pp. 176–231.

[57] M. Taleb, G. Teyssedre, S. le Roy, and C. Laurent, "Modeling of charge injection and extraction in a metal/polymer interface through an exponential distribution of surface states," *IEEE Transactions on Dielectrics and Electrical Insulation*, vol. 20, no. 1, pp. 311–320, Feb. 2013, doi: 10.1109/TDEI.2013.6451372.

[58] M. Fukuma, M. Nagao, and M. Kosaki, "Computer analysis on transient space charge distribution in polymer," in *Proceedings of 1994 4th International Conference on Properties and Applications of Dielectric Materials (ICPADM)*, 1994, vol. 1, pp. 24–27, doi: 10.1109/ICPADM.1994.413950.

[59] S. Delpino, D. Fabiani, and G. C. Montanari, "High Space Charge Dynamics in EVA-based Nanocomposite Flat Specimens," in *2008 Annual Report Conference on Electrical Insulation and Dielectric Phenomena*, Oct. 2008, pp. 137–140, doi: 10.1109/CEIDP.2008.4772807.

[60] M. A. Baldo and S. R. Forrest, "Interface-limited injection in amorphous organic semiconductors," *Physical Review B*, vol. 64, no. 8, p. 085201, Aug. 2001, doi: 10.1103/PhysRevB.64.085201.

[61] E. H. Doedens, N. B. Frisk, M. Jarvid, L. Boyer, and S. Josefsson, "Surface preparations on MV-sized cable ends for ramped DC breakdown studies," in *IEEE Conference on Electrical Insulation and Dielectric Phenomena (CEIDP)*, Oct. 2016, pp. 360–362, doi: 10.1109/CEIDP.2016.7785475.

[62] L. J. Brillson, *Surfaces and Interfaces of Electronic Materials*. Weinheim, Germany: Wiley-VCH Verlag GmbH & Co. KGaA, 2010.

[63] M. Meunier, N. Quirke, and A. Aslanides, “Molecular modeling of electron traps in polymer insulators: Chemical defects and impurities,” *The Journal of Chemical Physics*, vol. 115, no. 6, pp. 2876–2881, Aug. 2001, doi: 10.1063/1.1385160.

[64] M. Unge, C. Tornkvist, and T. Christen, “Space charges and deep traps in polyethylene - Ab initio simulations of chemical impurities and defects,” in *Proceedings of IEEE International Conference on Solid Dielectrics, ICSD*, Jun. 2013, pp. 935–939, doi: 10.1109/ICSD.2013.6619874.

[65] G. Teyssedre *et al.*, “Deep trapping centers in crosslinked polyethylene investigated by molecular modeling and luminescence techniques,” *IEEE Transactions on Dielectrics and Electrical Insulation*, vol. 8, no. 5, pp. 744–752, Oct. 2001, doi: 10.1109/94.959693.

[66] Y. Jiang, Z. An, C. Liu, F. Zheng, and Y. Zhang, “Influence of oxyfluorination time on space charge behavior in polyethylene,” *IEEE Transactions on Dielectrics and Electrical Insulation*, vol. 17, no. 6, pp. 1814–1823, Dec. 2010, doi: 10.1109/TDEI.2010.5658233.

[67] H. Ghorbani, C. O. Olsson, A. Abbasi, and M. Saltzer, “Influence of press films on conduction in polyethylene plaque samples,” in *2016 IEEE International Conference on Dielectrics (ICD)*, Jul. 2016, vol. 2, pp. 1179–1182, doi: 10.1109/ICD.2016.7547828.

[68] L. Chen, T. D. Huan, Y. C. Quintero, and R. Ramprasad, “Charge injection barriers at metal/polyethylene interfaces,” *Journal of Materials Science*, vol. 51, no. 1, pp. 506–512, Jan. 2016, doi: 10.1007/s10853-015-9369-2.

[69] V. I. Arkhipov, E. v. Emelianova, Y. H. Tak, and H. Bässler, “Charge injection into light-emitting diodes: Theory and experiment,” *Journal of Applied Physics*, vol. 84, no. 2, pp. 848–856, Jul. 1998, doi: 10.1063/1.368146.

[70] D. Blossey, “One-dimensional Onsager theory for carrier injection in metal-insulator systems,” *Physical Review B*, vol. 9, no. 12, pp. 5183–5187, Jun. 1974, doi: 10.1103/PhysRevB.9.5183.

[71] P. R. Emtage and J. J. O’Dwyer, “Richardson-Schottky Effect in Insulators,” *Physical Review Letters*, vol. 16, no. 9, pp. 356–358, Feb. 1966, doi: 10.1103/PhysRevLett.16.356.

[72] J. C. Scott and G. G. Malliaras, “Charge injection and recombination at the metal–organic interface,” *Chemical Physics Letters*, vol. 299, no. 2, pp. 115–119, Jan. 1999, doi: 10.1016/S0009-2614(98)01277-9.

[73] E. M. Conwell and M. W. Wu, “Contact injection into polymer light-emitting diodes,” *Applied Physics Letters*, vol. 70, no. 14, pp. 1867–1869, Apr. 1997, doi: 10.1063/1.118716.

[74] M. A. Abkowitz, H. A. Mizes, and J. S. Facci, “Emission limited injection by thermally assisted tunneling into a trap-free transport polymer,” *Applied Physics Letters*, vol. 66, no. 10, pp. 1288–1290, Mar. 1995, doi: 10.1063/1.113272.

[75] R. Guffond, A. Combessis, and S. Hole, “Polymer electrical property simulation using genetic model,” in *2018 IEEE 2nd International Conference on Dielectrics (ICD)*, Jul. 2018, pp. 1–4, doi: 10.1109/ICD.2018.8468403.

[76] R. Guffond, A. Combessis, and S. Hole, “Contribution of polymer microstructure to space charge, dielectric properties and electrical conduction,” in *2016 IEEE Conference on Electrical Insulation and Dielectric Phenomena (CEIDP)*, Oct. 2016, pp. 141–144, doi: 10.1109/CEIDP.2016.7785655.

[77] M. Hasheminezhad and E. Ildstad, “Application of contact analysis on evaluation of breakdown strength and PD inception field strength of solid-solid interfaces,” *IEEE Transactions on Dielectrics and Electrical Insulation*, vol. 19, no. 1, pp. 1–7, Feb. 2012, doi: 10.1109/TDEI.2012.6148496.

[78] S. M. Hasheminezhad, E. Ildstad, and A. Nysveen, “Breakdown strength of solid|solid interface,” in *2010 10th IEEE International Conference on Solid Dielectrics*, Jul. 2010, pp. 1–4, doi: 10.1109/ICSD.2010.5568229.

[79] A. Haddad and D. F. Warne, *Advances in high voltage engineering*, Pbk. ed. Stevenage, UK: Institution of Engineering and Technology (IET), 2004.

[80] P. Zhang, G. Fitzpatrick, T. Harrison, W. A. Moussa, and R. J. Zemp, “Double-SOI Wafer-Bonded CMUTs With Improved Electrical Safety and Minimal Roughness of Dielectric and Electrode Surfaces,” *Journal of Microelectromechanical Systems*, vol. 21, no. 3, pp. 668–680, Jun. 2012, doi: 10.1109/JMEMS.2012.2189358.

[81] M. Taleb, G. Teyssedre, and S. le Roy, “Role of the interface on charge build-up in a low-density polyethylene: Surface roughness and nature of the electrode,” in *Annual Report - Conference on Electrical Insulation and Dielectric Phenomena, CEIDP*, Aug. 2009, pp. 112–115, doi: 10.1109/CEIDP.2009.5377888.

[82] S. v Novikov, “Rough electrode surface: effect on charge carrier injection and transport in organic devices,” *Macromolecular Symposia*, vol. 212, no. 1, pp. 191–200, Apr. 2004, doi: 10.1002/masy.200450818.

[83] E. Doedens, E. M. Jarvid, C. Frohne, and S. M. Gubanski, “Enhanced charge injection in rough HVDC extruded cable interfaces,” *IEEE Transactions on Dielectrics and Electrical Insulation*, vol. 26, no. 6, pp. 1911–1918, Dec. 2019, doi: 10.1109/TDEI.2019.008213.

[84] E. Doedens, E. M. Jarvid, R. Guffond, and Y. v. Serdyuk, “Space Charge Accumulation at Material Interfaces in HVDC Cable Insulation Part I—Experimental Study and Charge Injection Hypothesis,” *Energies*, vol. 13, no. 8, p. 2005, Apr. 2020, doi: 10.3390/en13082005.

[85] E. Doedens, E. M. Jarvid, Y. v. Serdyuk, R. Guffond, and D. Charrier, “Local surface field- and charge distributions and their impact on breakdown voltage for HVDC cable insulation,” in *International Conference on Insulated Power Cables (Jicable)*, 2019, p. F2.24.

[86] R. W. Hare, R. M. Hill, and C. J. Budd, “Modelling charge injection and motion in solid dielectrics under high electric field,” *Journal of Physics D: Applied Physics*, vol. 26, no. 7, pp. 1084–1093, Jul. 1993, doi: 10.1088/0022-3727/26/7/012.

[87] N. Koenigsfeld, R. Kalish, A. Cimmino, D. Hoxley, S. Prawer, and I. Yamada, “Effect of surface roughness on field emission from chemical vapor deposited polycrystalline diamond,” *Applied Physics Letters*, vol. 79, no. 9, pp. 1288–1290, Aug. 2001, doi: 10.1063/1.1383803.

[88] Y. Chang, Z. Guo, A. Koneru, and Y. Wang, “Surface roughness realized and evaluated in different dimensional range and its effect on field emission behavior,” *Vacuum*, vol. 136, pp. 36–39, Feb. 2017, doi: 10.1016/j.vacuum.2016.11.020.

[89] A. M. Mahdy, H. I. Anis, and S. A. Ward, “Electrode roughness effects on the breakdown of air-insulated apparatus,” *IEEE Transactions on Dielectrics and Electrical Insulation*, vol. 5, no. 4, pp. 612–617, 1998, doi: 10.1109/94.708280.

[90] J. Domińczuk and A. Krawczuk, “Comparison of Surface Free Energy Calculation Methods,” *Applied Mechanics and Materials*, vol. 791, pp. 259–265, Sep. 2015, doi: 10.4028/www.scientific.net/AMM.791.259.

[91] M. Żenkiewicz, “Methods for the calculation of surface free energy of solids,” *Journal of Achievements in Materials and Manufacturing Engineering*, vol. 24, no. 1, pp. 137–145, 2007.

[92] P. N. Murgatroyd, “Theory of space-charge-limited current enhanced by Frenkel effect,” *Journal of Physics D: Applied Physics*, vol. 3, no. 2, p. 308, Feb. 1970, doi: 10.1088/0022-3727/3/2/308.

[93] F. Boufayed *et al.*, “Numerical resolution of charge transport in cross-linked polyethylene by means of a bipolar model with a distribution of traps,” in *Proceedings of the 2004 IEEE International Conference on Solid Dielectrics ICSD 2004*, 2004, vol. 2, pp. 562–566, doi: 10.1109/icsd.2004.1350493.

[94] F. Boufayed *et al.*, “Simulation of bipolar charge transport in polyethylene featuring trapping and hopping conduction through an exponential distribution of traps,” in *Proceedings of 2005 International Symposium on Electrical Insulating Materials, 2005. (ISEIM 2005).*, 2005, pp. 340-343 Vol. 2, doi: 10.1109/ISEIM.2005.193557.

[95] T. Tanaka, “Space charge injected via interfaces and tree initiation in polymers,” *IEEE Transactions on Dielectrics and Electrical Insulation*, vol. 8, no. 5, pp. 733–743, 2001, doi: 10.1109/94.959692.

[96] B. Vissouvanadin *et al.*, “Impact of concentration gradient of polarizable species on the electric field distribution in polymeric insulating material for HVDC cable,” *IEEE Transactions on Dielectrics and Electrical Insulation*, vol. 18, no. 3, pp. 833–839, Jun. 2011, doi: 10.1109/TDEI.2011.5931072.

[97] L. A. Dissado *et al.*, “Characterizing HV XLPE cables by electrical, chemical and microstructural measurements on cable peeling: effects of surface roughness, thermal treatment and peeling location,” in *2000 Annual Report Conference on Electrical Insulation and Dielectric Phenomena (Cat. No.00CH37132)*, 2000, vol. 1, pp. 136–140, doi: 10.1109/CEIDP.2000.885246.

[98] J. C. Fothergill *et al.*, “Electrical, microstructural, physical and chemical characterization of hv xlpe cable peelings for an electrical aging diagnostic data base,” *IEEE Transactions on Dielectrics and Electrical Insulation*, vol. 10, no. 3, pp. 514–527, Jun. 2003, doi: 10.1109/TDEI.2003.1207480.

[99] N. Zebouchi, P. Carstensen, A. A. Farkas, A. Campus, and U. H. Nilsson, “Electric characterization of films peeled from the insulation of extruded HVDC cables,” in *CEIDP ’05. 2005 Annual Report Conference on Electrical Insulation and Dielectric Phenomena, 2005.*, 2005, pp. 79–82, doi: 10.1109/CEIDP.2005.1560625.

[100] J. Cao, C. Zhou, N. Liu, Y. Xu, G. Chen, and H. Wang, “Model to estimate the trapping parameters of cross-linked polyethylene cable peelings of different service years and their relationships with dc breakdown strengths,” *High Voltage*, vol. 1, no. 2, pp. 95–105, Jul. 2016, doi: 10.1049/hve.2016.0012.

[101] E. Doedens, E. M. Jarvid, S. Gubanski, and C. Frohne, “Cable surface preparation: chemical, physical and electrical characterization and impact on breakdown voltage,” in *International Symposium on HVDC Cable Systems (Jicable-HVDC)*, 2017, Accessed: Feb. 05, 2018. [Online]. Available: http://www.jicable-hvdc17.fr/program_eng.php.

[102] E. H. Doedens, “Characterization of different interface types for HVDC extruded cable applications.,” Department of Signals and Systems, 2018.

[103] A. Küchler, *High Voltage Engineering Fundamentals*. Berlin, Germany: Springer Berlin Heidelberg, 2000.

[104] M. A. Brown, G. Chen, A. S. Vaughan, and P. A. Norman, “High voltage performance of bulk, and amalgamated, PE insulation systems. Part II. Breakdown, morphology and lifetime,” *Journal of Physics D: Applied Physics*, vol. 36, no. 24, pp. 3197–3204, Dec. 2003, doi: 10.1088/0022-3727/36/24/016.

[105] Y. Wei, M. Liu, W. Han, G. Li, C. Hao, and Q. Lei, “Charge Injection Characteristics of Semi-Conductive Composites with Carbon Black-Polymer for HVDC Cable,” *Polymers*, vol. 11, no. 7, p. 1134, Jul. 2019, doi: 10.3390/polym11071134.

[106] F. Baudoin, C. Laurent, S. le Roy, and G. Teyssedre, “Charge packets modeling in insulating polymers based on transport description,” in *2012 Annual Report Conference*

on Electrical Insulation and Dielectric Phenomena, Oct. 2012, pp. 665–668, doi: 10.1109/CEIDP.2012.6378868.

[107] S. Delpino *et al.*, "Feature article - Polymeric HVDC cable design and space charge accumulation. Part 2: insulation interfaces," *IEEE Electrical Insulation Magazine*, vol. 24, no. 1, pp. 14–24, Jan. 2008, doi: 10.1109/MEI.2008.4455499.

[108] Z. Li, N. Liu, S. Gabriel, and G. Chen, "Thermal ageing and its impact on charge trap density and breakdown strength in polyethylene," in *2016 IEEE Conference on Electrical Insulation and Dielectric Phenomena (CEIDP)*, Oct. 2016, pp. 907–910, doi: 10.1109/CEIDP.2016.7785587.

[109] A. P. S. Tiwana and C. C. Reddy, "Life estimation using damage equalization method and step-stress breakdown tests," *IEEE Transactions on Dielectrics and Electrical Insulation*, vol. 23, no. 4, pp. 2311–2318, Aug. 2016, doi: 10.1109/TDEI.2016.7556508.

[110] M. Sato, A. Kumada, K. Hidaka, T. Hirano, and F. Sato, "Quantum chemical calculation of hole transport properties in crystalline polyethylene," *IEEE Transactions on Dielectrics and Electrical Insulation*, vol. 23, no. 5, pp. 3045–3052, Oct. 2016, doi: 10.1109/TDEI.2016.7736868.

[111] E. Doedens, E. M. Jarvid, R. Guffond, and Y. v. Serdyuk, "Space Charge Accumulation at Material Interfaces in HVDC Cable Insulation Part II—Simulations of Charge Transport," *Energies*, vol. 13, no. 7, p. 1750, Apr. 2020, doi: 10.3390/en13071750.

[112] D. Min and S. Li, "Simulation on the influence of bipolar charge injection and trapping on surface potential decay of polyethylene," *IEEE Transactions on Dielectrics and Electrical Insulation*, vol. 21, no. 4, pp. 1627–1636, Aug. 2014, doi: 10.1109/TDEI.2014.004271.

[113] I. A. Tsekmes, D. van der Born, P. H. F. Morshuis, J. J. Smit, T. J. Person, and S. J. Sutton, "Space charge accumulation in polymeric DC mini-cables," in *2013 IEEE International Conference on Solid Dielectrics (ICSD)*, Jun. 2013, pp. 452–455, doi: 10.1109/ICSD.2013.6619768.

[114] D. Fabiani *et al.*, "HVDC Cable Design and Space Charge Accumulation. Part 3: Effect of Temperature Gradient [Feature article]," *IEEE Electrical Insulation Magazine*, vol. 24, no. 2, pp. 5–14, Mar. 2008, doi: 10.1109/MEI.2008.4473049.

[115] COMSOL AB, "COMSOL Multiphysics (R), v. 5.3." COMSOL, Inc, www.comsol.com, Stockholm, Sweden, 2018, [Online]. Available: www.comsol.com.

[116] C. Laurent, G. Teyssedre, S. le Roy, and F. Baudoin, "Knowledge-based modelling of charge transport in insulating polymers: From experiments to model optimization," in *2009 IEEE 9th International Conference on the Properties and Applications of Dielectric Materials*, Jul. 2009, pp. 1–8, doi: 10.1109/ICPADM.2009.5252265.

[117] The MathWorks Inc, "MATLAB Version 9.5.0.944444 (R2018b)." The Mathworks, Inc. Natick, MA, USA, Natick, Massachusetts, 2018.

[118] E. Doedens, E. M. Jarvid, C. Frohne, and S. M. Gubanski, "Enhanced charge injection in rough HVDC extruded cable interfaces," *IEEE Transactions on Dielectrics and Electrical Insulation*, vol. 26, no. 6, pp. 1911–1918, Dec. 2019, doi: 10.1109/TDEI.2019.008213.

[119] G. Blaise and W. J. Sarjeant, "Space charge in dielectrics. Energy storage and transfer dynamics from atomistic to macroscopic scale," *IEEE Transactions on Dielectrics and Electrical Insulation*, vol. 5, no. 5, pp. 779–808, 1998, doi: 10.1109/94.729703.

[120] Y. Zhuang *et al.*, "Effect of ground electrode on charge injection and surface potential of corona charged polyethylene film," *Journal of Electrostatics*, vol. 90, pp. 139–146, Dec. 2017, doi: 10.1016/j.elstat.2017.10.004.

[121] Y. Zhuang, G. Chen, and M. Rotaru, “Charge injection in gold ground electrode corona charged polyethylene film: Surface potential decay and corona charging current measurement,” in *2011 - 14th International Symposium on Electrets*, Aug. 2011, pp. 125–126, doi: 10.1109/ISE.2011.6085014.

[122] E. Doedens, A. Johansson, E. M. Jarvid, S. Nilsson, M. Bengtsson, and J. Kjellqvist, “Effects of inclusions of oxidized particles in XLPE on treeing phenomena,” in *2012 Annual Report Conference on Electrical Insulation and Dielectric Phenomena*, Oct. 2012, pp. 597–600, doi: 10.1109/CEIDP.2012.6378851.

[123] E. Reyes-Gómez, L. E. Oliveira, and M. de Dios-Leyva, “Shallow impurities in semiconductor superlattices: A fractional-dimensional space approach,” *Journal of Applied Physics*, vol. 85, no. 8, pp. 4045–4049, Apr. 1999, doi: 10.1063/1.370309.